Periodic cellular aluminum structures for space applications: From casting to additive manufacturing

THÈSE N^{O} 8611 (2018)

PRÉSENTÉE LE 18 MAI 2018

FACULTÉ DES SCIENCES TECHNIQUES DE L'INGÉNIEUR
PROGRAMME DOCTORAL EN SCIENCE ET GÉNIE DES MATÉRIAUX

ÉCOLE POLYTECHNIQUE FÉDÉRALE DE LAUSANNE

POUR L'OBTENTION DU GRADE DE DOCTEUR ÈS SCIENCES

PAR

Florian Thibaut GALLIEN

acceptée sur proposition du jury:

Prof. P. Muralt, président du jury
Prof. V. Gass, Prof. A. Mortensen, directeurs de thèse
Dr T. Ghidini, rapporteur
Prof. J. Banhart, rapporteur
Prof. R. Logé, rapporteur

ÉCOLE POLYTECHNIQUE
FÉDÉRALE DE LAUSANNE

Suisse
2018

Acknowledgements

A PhD is often seen as a long and lonely journey of one person but in reality, such a big challenge would be impossible without the help of a bunch of people with contributions at different levels. On my side, this chapter of my life could not be closed without the support of the following persons.

I would like to thanks first the jury who took time to evaluate my work and decided to give me the title of Dr., namely Prof. John Banhart, Prof. Roland Logé and Dr. Tommaso Ghidini. I appreciated a lot the discussion raising interesting points especially for future works. I would like to thanks my directors of thesis, Prof. Volker Gass and Prof. Andreas Mortensen, for their priceless supervisions, their trust and support making this project possible.

I would like to thanks the wonderful people at the ATMX workshop for all the work done for me during this thesis, often on short delays. Thanks to all the colleagues either from the LMM (Gio, Martin, Maité, Ana, Gabi, Hamed, Jérome, ..) or from the Space Center (Grégoire, Martine aka Maman, Camille, Christophe, Stefano, Federico, Stéphane, Sarah aka Jojo, Yannick, Gilles, Tobias, ...) for all the nice time shared and the good memories. I know you will miss my "grande gueule".

Being a non-conventional PhD between two countries, I would like to thanks also the crazy ESA people (Laurent, Adrian, Graham, Ana, Max, Romain ...) for the time spent on machine training, compassion for staying late in the lab, and also (and especially) for the beers at Escape. A special thanks to Andrew for its supervision on the ESA side, sorry if sometimes I woke you up after lunch.

A big thanks to my dance fellows either from the hip hop or the salsa, it will be too long to list all of you but without you, I certainly would become crazy (I mean more than what I am naturally).

A huge big up to my close friends in Lausanne, making my integration in Lausanne easier, sharing good moment, always cheering me up when it was necessary, and spending a lot's of time eating. This is for you Jo, Marina and Ludwin.

Enfin un très grand merci à mes parents, Philippe et Sylvie, qui ont fait de moi ce que je suis aujourd'hui et qui ont toujours cru en moi peu importe mes choix. Ce diplôme est aussi le votre. Merci aux frangin et frangines (Boubou, Banane et Minouche) pour tout.

A special thanks for a special friend who was always by my side even before starting the PhD. Thanks for the awesome moment (dancing, escape games, dinner, ...) but thank you even more in all the period I felt bad being always present whenever it was. This is for you Mary.

And last but not least. Thanks to my love, the one and only, Kristina who spent more than the half of the PhD supporting me on daily basis and giving me the sweet touch necessary in my life during this journey to successfully obtain this diploma.

Lausanne, 18 Avril 2018 F. G.

Abstract

Mass is one of the crucial parameters for hardware that has to be placed in Earth orbit. Due to its harsh environment, a material with highest specific properties is desired to achieve space missions. The rise and development of new technologies, such as additive manufacturing (AM), opened new opportunities in part-design complexity, periodic cellular structures (PCS) being one of them. The present thesis investigates the potential implementation of PCS in space applications, particularly for structures and micro-meteoroids and orbital debris (MMOD) impact shields. This was achieved in three steps:

Four different types of AlSi12 PCS manufactured by selective laser melting (SLM) were tested under quasi-static compression to measure the mechanical properties dependency versus topology and to characterize the failure mode. Properties ranging from 3 to 4 GPa for the compressive modulus, 5 to 12 MPa for the yield stress, 12 to 20 MPa for the plateau stress, and 2 to 8 MJ/cm^3 for the absorbed energy were obtained. An unexpected failure mode was observed when compared to classical cellular metals, namely a brittle failure occurring by global shearing. A predictive failure criterion was established based on topology considerations and correlated to most of the reported results in the literature. A preliminary test campaign on tensile specimens was performed to compute numerical models that were fed into a finite element analysis. Good agreement with experimental data was shown, and the importance of microplasticity effects in this class of material was highlighted.

An alternative process was developed to produce AlSi12 PCS by investment casting. The process is based on replication of a polymer preform used to build a NaCl mold. It was observed that the quality of the final cast part depends mainly on the grain size of the salt, with an optimum identified for distributions between 125 and 180 µm. Optimization of the process allowed to reduce the drying time by a factor 6. Main process parameters include a drying temperature of 80°C and infiltration at 660°C under 300 mbar. From this process, PCSs having an energy absorption capacity of 15 MJ/m^3 with an efficiency of 80% were produced.

Hypervelocity impact tests were conducted on cast PCS and stochastic structures. The objective being to hit the structures with a 2mm-diameter aluminum sphere at velocities close to 7 km/s. Influence of the sample topology, the orientation, and the bumper material was assessed. Stochastic structures successfully stopped the projectile in all configurations. The beneficial effect of the bumper was measured reducing the crater depth from 20 mm to 14 mm. This type of structure exhibited a comparable areal density (0.8 g/cm^2) to simple Whipple shield design. PCS poorly performed in mitigating the impact as the debris passed through all the structures, independently of the test configuration due to the open-channels present.

PCS are good candidates to be used in space hardware, but their design and the manufacturing process need to be carefully chosen depending on the specific application. AM PCS are suitable for structural application with a high compressive modulus and yield stress. Cast PCS would perfectly fit in shock absorbers. A more random design would be preferable for MMOD shielding applications.

Keywords: hypervelocity impact, periodic cellular structure, stochastic structure, AlSi12, selective laser melting, casting, failure criterion, space application, compression testing.

Résumé

La mise en orbite terrestre d'une charge utile n'est pas chose aisée due à l'hostilité de l'environnement spatial et de la grande quantité d'énergie nécessaire pour y parvenir. Cette dernière étant directement liée à la masse, le développement de matériaux avec des propriétés spécifiques toujours plus élevées est nécessaire à la réussite des missions spatiales. Le développement de nouvelles technologies, comme la fabrication additive, a ouvert le champ des possibles en termes de complexité de design, les structures cellulaires périodiques (SCP) étant un bel exemple. Cette thèse examine la possibilité d'inclure les SCP dans diverses applications spatiales, et plus particulièrement pour des applications structurelles et de protection contre les impacts de micrométéorites et de débris orbitaux (MDO). Pour cela, cette étude a été menée en trois étapes :

Différents types de SCP ont été produites en AlSi12 par fabrication additive pour être testées en compression quasi-statique afin de mesurer les propriétés mécaniques et de caractériser le mode de rupture. Les propriétés sont : un module de compression entre 3 et 4 GPa, une contrainte élastique entre 5 et 12 MPa, une contrainte de plateau entre 12 et 20 MPa et une énergie absorbée entre 2 et 8 MJ/m^3. Le mode de rupture observé est une rupture fragile par cisaillement et un critère de rupture a été établi pour prédire ce dernier, basé sur des considérations topologiques et confirmé par une bonne partie des résultats reportés dans la littérature.

Un procédé de coulée a été développé pour fabriquer des SCP en AlSi12. Le procédé est basé sur la réplication d'une préforme sacrificielle en polymère utilisée pour la confection du moule en sel NaCl. La qualité de la pièce coulée est surtout définie par la taille des grains de sel utilisé pour mettre en forme le moule ; avec un optimum entre 125 et 180 µm. L'optimisation du procédé a permis de réduire le temps de séchage d'un facteur 6. Les paramètres principaux sont une température de séchage de 80°C et une infiltration réalisée à 660°C sous une pression de 300 mbar. Á partir de ce procédé, des SCP ayant une capacité d'absorption d'énergie de 15 MJ/m^3 avec une efficacité de 80% ont pu être produites.

Une campagne de tests d'impact à très haute vitesse a été réalisée sur des pièces coulées, périodiques et stochastiques. Le but du test est d'impacter les structures avec une bille d'aluminum de 2 mm de diamètre à des vitesses proches de 7 km/s. Toutes les structures stochastiques ont réussi à arrêter le projectile, peu importe la configuration. Les effets bénéfiques du « bumper » se sont traduits par une profondeur de cratère réduite de 20 à 14 mm. En revanche, toutes les SCP ont été entièrement traversées par le projectile, indépendamment de la configuration. Ce résultat s'explique par la présence de canaux ouverts créés par la structure elle-même et empruntés par les débris pour atteindre l'autre côté de la pièce.

Ainsi, les SCP sont de bons candidats pour être utilisés dans des composant spatiaux, à condition de bien définir le design et le procédé de fabrication en fonction de l'application désirée. Les SCP fabriquées par impression 3D seraient adaptées à des applications structurelles ; les SCP coulées seraient propices à une utilisation en tant que absorbeurs de chocs alors qu'un design plus aléatoire pourrait être désiré pour la protection contre les impacts de MDO.

Mots clefs : impact hypervéloce, structure périodique cellulaires, AlSi12, fabrication additive, procédé de coulée, critère de rupture, structure stochastique, application spatiale, test de compression.

Contents

List of Figures

List of Tables

1 Introduction

> " Access to our space environment represents a real treasure for humanity. It benefits many areas of our activities, including science, exploration, and the acquisition of knowledge to ensure a safe and rewarding future for following generations. "
>
> (Claude Nicollier, Astronaut [1])

Nowadays, almost everyone depends on space on a daily basis without even realizing it. In telecommunication, in entertainment broadcasting, in global navigation, in weather forecasting or also in Earth monitoring, spaceborne assets and their applications are ever present. Since the first satellite placed in orbit on October 4th, 1957 by USSR to the launch of a Tesla Roadster beyond Mars by SpaceX on February 6th, 2018 (Figure 1.1), the underlying principle to access Earth orbit has remained the same, namely chemical propulsion. Based on the third Newton's law, this principle is governed by the rocket mass and the exhaust gas velocity providing the necessary thrust to reach Space, first described by Tsiolkovsky in 1903 leading to the following equation:

$$m_{prop} = m_{dry}(e^{\frac{\Delta v}{v_e}} - 1) \tag{1.1}$$

where m_{prop} is the propellant mass required to obtain a change in velocity of Δv, m_{dry} is the dry mass corresponding to the rocket mass without the propellant, and v_e the exhaust gas velocity. From this equation, it can be seen that the required propellant is proportional to the dry mass (rocket and payload) and exponentially dependent on the velocity change to be provided for orbital injection (about 7.5 km/s for low Earth orbit and 11.2 km/s to go beyond Mars). A crucial parameter driving the design of any spacecraft or satellite is its mass. Structural topology optimization has been performed over the last decades since Sputnik, to achieve the highest specific properties possible, currently aluminum honeycomb sandwich structures are state of the art.

The space environment is harsh for any object placed in orbit due to high-temperature gradients, high-vacuum, solar radiations and the presence of Micro-Meteoroid and Orbital Debris (MMOD) moving at high relative velocities. Reparation in Space is impossible (or extremely costly as for the Hubble space telescope). Therefore, extensive characterization campaigns need to be performed on-ground to assess the reliability of materials and systems.

The rise and development of new technologies such as additive manufacturing (commonly 3D-printing) opened up a new realm in terms of design complexity. Periodic cellular structures (PCS) fall into this category. These structures can consist of a precise assembly of struts and nodes leading to an optimization of specific mechanical properties and a reduction of the mass. PCS structures could be likely candidates for structures, shock absorbers or MMOD mitigation shields in Space applications. Whatever their uses, the performance and the failure modes of PCS need to be understood under different load state (compression or impacts). Also, different production processes have to be well-controlled and characterized in order to obtain reliable, reproducible and upscalable production methods.

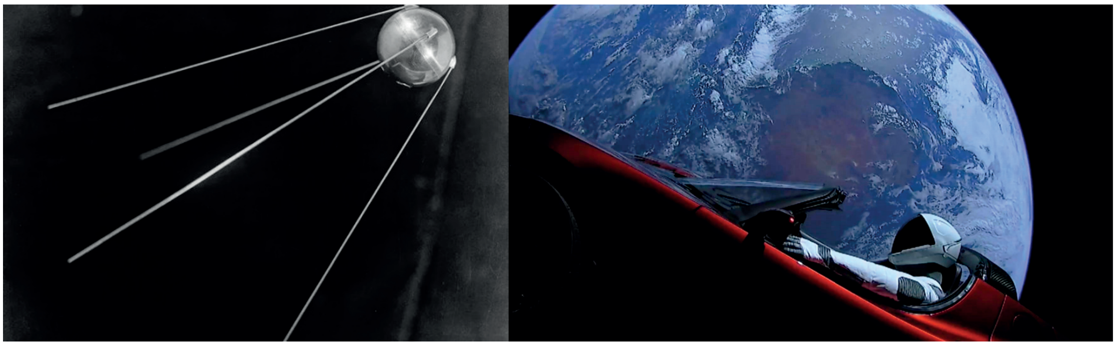

Figure 1.1 – First man-made object placed in Earth orbit in 1957, Sputnik-1 (left, credit to Sovfoto/UIG via Cetty) and Tesla Roadster launched in Space in 2018 (right, credit to SpaceX).

1.1 Motivation and Objectives

It was noted that periodic cellular structures have been extensively investigated in terms of topology and properties. However, no failure criterion was found to predict the failure mode although widely observed in different studies. Also, being mainly produced by additive manufacturing, parts are usually limited in size and bulk material availability, especially for aluminum alloys (interesting for Space applications due to low mass density). Other production methods include various sandwich structures alternating skins and simple (one or two) cell layers, not taking into account the full potential of this specific class of material. A process to produce PCS as an alternative to additive manufacturing is lacking. Finally, even if some hypervelocity impact tests have been conducted on cellular materials, namely stochastic foam or honeycomb; no data could be found in the literature regarding the behavior of PCS under impact.

The objectives of the present thesis are:

- Establish a criterion to predict the failure mode of periodic cellular structures under compression.
- Develop an investment casting process to produce PCS.

- Characterize PCS under hypervelocity impact testing to assess the MMOD shielding performances.

To succeed, this thesis explores the production of periodic cellular structures in an aluminium casting alloy (Al-12Si) by two freeform manufacturing methods, one being additive manufacturing the other investment casting. Additional comparison is also made with a stochastic aluminium cellular structure produced in prototypic industrial production by the Constellium company (Voreppe, France). The structures thus produced were tested in compression and in conditions simulating impact with MMODs, and their deformation behaviour simulated by finite element modeling, to show that, according to the process with the ensuing metal microstructure, and the structure, play important roles in defining their performance.

1.2 Thesis structure

In Chapter 2, the characterization of four different types of periodic cellular structures additively manufactured in AlSi12 is described using optical microscopy, 3D-tomography, and quasi-static compression testing. A preliminary tensile test campaign of the bulk alloy was conducted to measure the solid metal properties implemented then in a finite elements analysis. A failure criterion is finally established to predict the preferred deformation and failure modes of PCS.

In Chapter 3, an extensive description of the developed casting process is given as well as the optimization steps performed to define each process parameter value. Cast parts were characterized in the same way as the PCS described in Chapter 2.

In Chapter 4, a comparison between the mechanical properties of PCS manufactured by AM and casting is made to determine the influence of bulk alloy properties and structural topology.

In Chapter 5, a hypervelocity ballistic impact test campaign is conducted on cast PCS and stochastic foam to characterize their MMOD shielding performances.

The remainder of this chapter presents a review of the literature on questions relevant to this work.

1.3 Literature review

1.3.1 General introduction on additive manufacturing

Additive manufacturing (AM) has opened a new world of possibilities for enhanced part design complexity by switching from a top-down solutions (traditional manufacturing by matter substraction) to a bottom-up method (building up from preliminary base materials); a standard was released for general definitions of the process (ISO/ASTM 52900).

The following description of AM processing is based on the work of Gibson et al. [2] and can be divided into several steps:

1. A 3D CAD model is built either with a specifically dedicated software or by scanning an existing part.
2. The CAD model is converted into the standard STL format for AM, which is a volumetric representation of the outer surface consisting of an assembly of triangles (other more exotic machine specific formats also exist).
3. The STL file (or other file types for some cases) is transferred to the machine, where it is sliced, transforming the 3D volume into a stack of parallel adjoining 2D surfaces.
4. Machine parameters are adjusted for manufacturing depending on the material and the technology used.
5. Fabrication of the part is performed in a nearly fully-automated way.
6. The build is removed from the machine, and optional post-process machining can be performed to obtain the final desired part.

Polymers are additively manufactured in different ways depending on their composition. Thermoplastic polymers (characterized by melting upon temperature increase) can be printed by Fused Deposition Modeling (FDM) which consists of extruding layers of molten material on top of one another. Polylactic Acid (PLA) and Acrylonitrile Butadiene Styrene (ABS) are the most wide spread polymers used for this process. Another way to produce 3D-parts made out of thermoplastic polymers, usually with Polyamide-12, also known as PA2200, is Selective Laser Sintering (SLS), which is a powder-bed based process. A layer of powder material is placed on the building plate in the machine, and then a laser precisely heats selected spots to sinter a specific region along the surface. Once complete, another layer of powder is applied on top of the previous layer, and the selected area sintering starts again. Thermoset polymers (which undergo thermal degradation by heating) require an energy input to activate polymer reticulation and change state from liquid to solid; this input can be delivered by laser, UV or visible light. Non-reticulated liquid polymers are poured into a tank and layers are reticulated onto a moving building plate (by illumination processes such as Stereolithography (SLA) or Digital Light Processing (DLP)). The resin can also be precisely deposited layer by layer with an inkjet head and reticulated right after deposition (Material Jetting, known as MJ).

Ceramics can also be manufactured by powder-bed based freeform processes, either by SLS or by binder jetting. The latter consists of joining powder by depositing a binder (in a process similar to MJ); the resulting part is a green body, which requires subsequent binder removal and sintering steps.

Metals can be additively produced by Selective Laser Melting (SLM) or by direct energy deposition. The former is similar to SLS with higher energy input to melt the powder (instead of sintering it). The concept of the latter is close to FDM, but instead of extruding material, tracks of metals are deposited by feeding powder into a laser or an electron beam; this process can be seen as a successive application of welds. Figure 1.2 fives a schematic diagram of the different additive manufacturing methods and their corresponding materials and machine manufacturers.

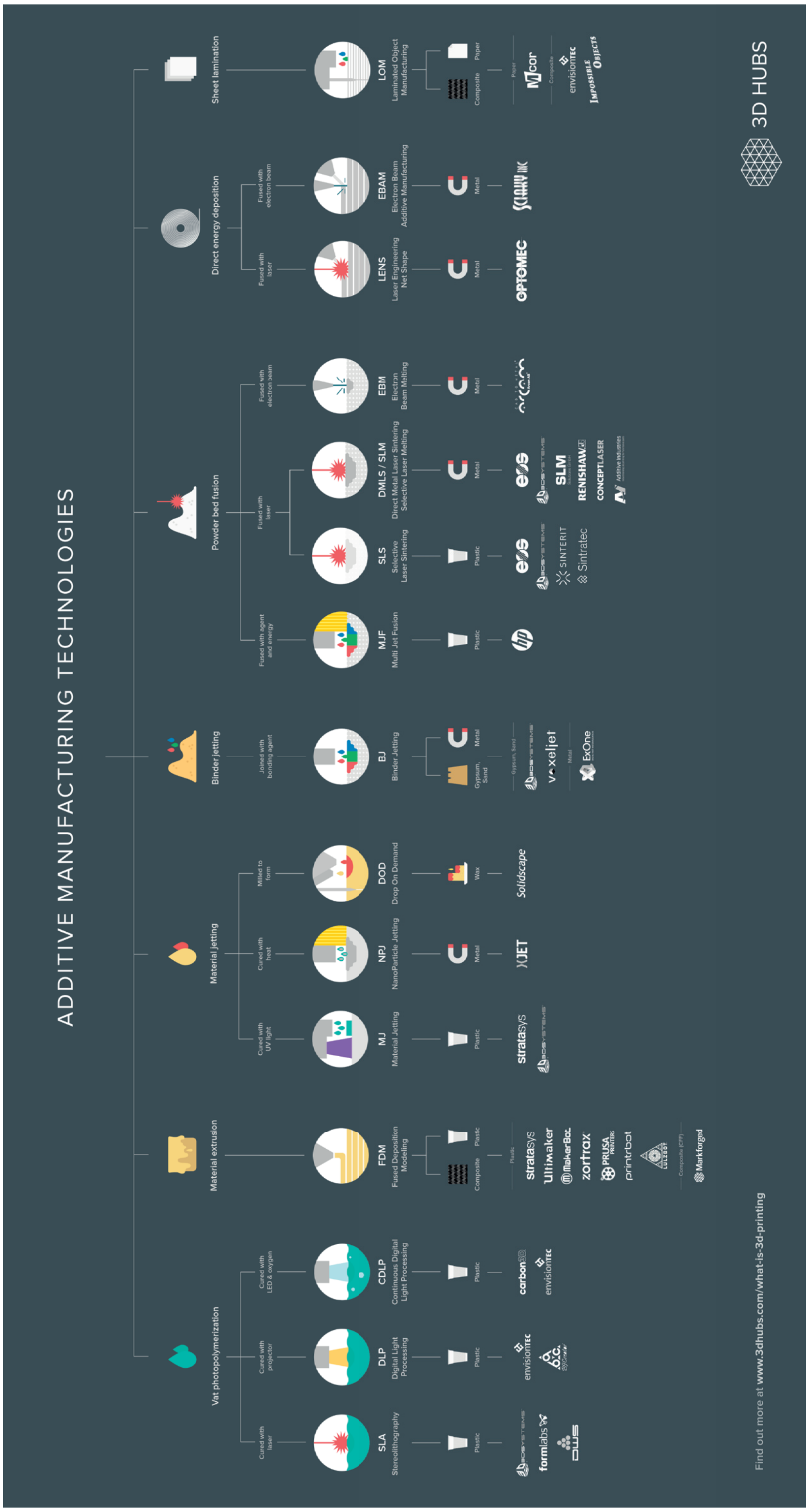

Figure 1.2 – Schematic diagram of the different available AM technologies [1]

---

[1] credit to https://www.3dhubs.com/knowledge-base/additive-manufacturing-technologies-overview

1.3.2 Selective laser melting

Process description, manufacturability and defects

Selective laser melting (SLM) is a powder-bed based process which builds a 3D solid volume from atomized powder of the desired material (mean size distribution typically in the tens of µm) [2]. More specifically a layer of powder is evenly dispersed on a plate in a moving working chamber under inert atmosphere. Next, a scanning laser beam selectively fuses the material. The working chamber is then moved slightly downward, a new layer of powder is spread, and a new laser pass is performed fusing the top layer sufficiently to bond it with solid material in the underlying layer. This step is repeated until the final part is complete. Figure 1.3 shows a sketch of the SLM process.

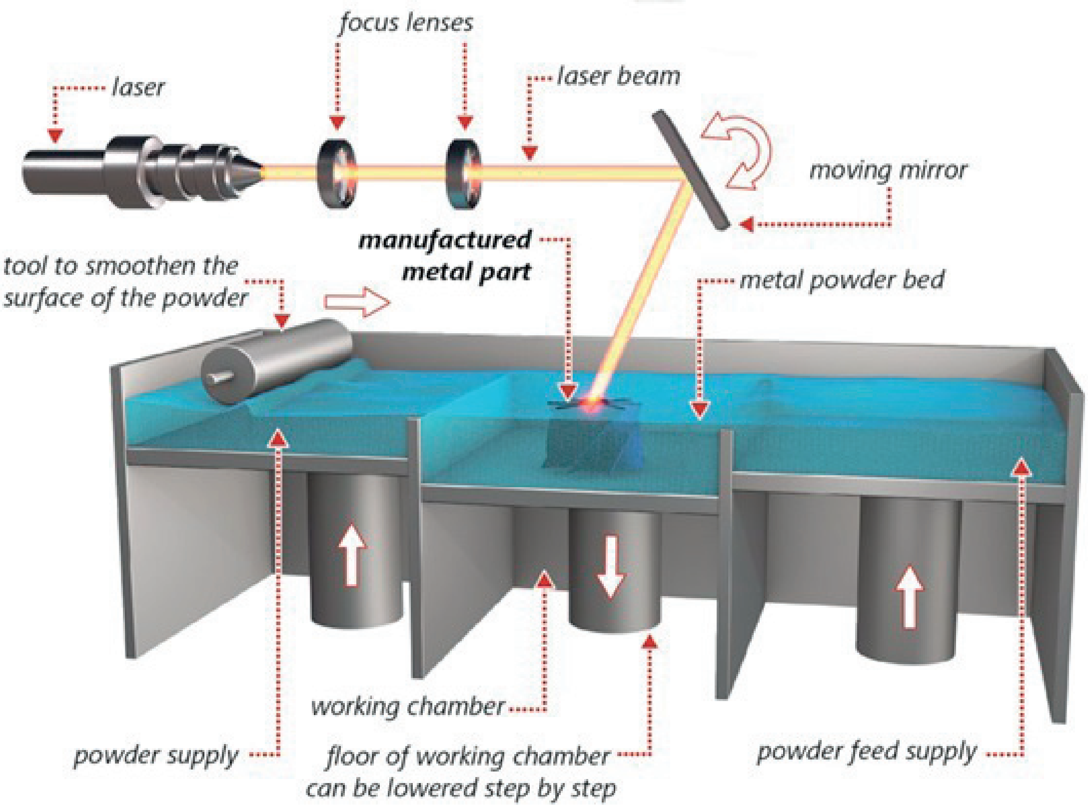

Figure 1.3 – Sketch of SLM process [2]

The main feature of 3D-printed metals is the presence of half-cylindrical features in the microstructures, which reveal the laser tracks during manufacturing. Due to the complex mixing of heat and mass transfer phenomena occurring during the process [3, 4], the shapes and sizes of these features depend on a large numbers of parameters that are either machine related (laser power, laser beam diameter, layer thickness, scanning speed, scanning islands, hatch spacing, hatch rotation angle and beam offset) or material related (melting temperature, laser absorptivity, thermal conductivity and heat capacity). The scanning speed is the speed at which the laser scans

---

[2] credit to https://www.empa.ch/web/coating-competence-center/selective-laser-melting

the sample surface to build the sample. The hatch spacing corresponds to the space between two parallel melt pools inside the same layer. The hatch rotation angle is the angle introduced between scannind directions of two successive layers. The beam offset corresponds to the hatch displacement in between two successive layers compared to a reference line. The (scanning) islands are the layer subdivision, each associated with different laser tracks orientations. Figure 1.4 schematically represents the above-mentioned machine-related parameters. Powder size and shape distribution play a major role in the density of the final part. It has been demonstrated that fine particles are required to optimize part properties (such as density, mechanical strength, and surface roughness) whereas large particles set the layer thickness and tend to increase ductility [5]. A good correlation was found between the powder layer density and the part density [6].

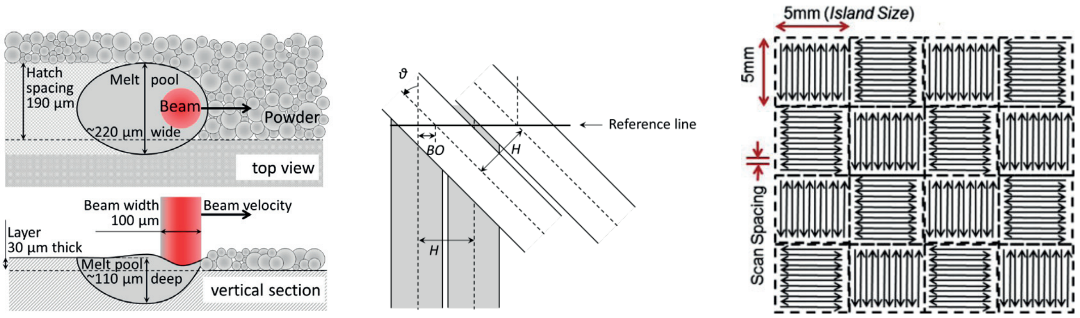

(a) (b) (c)

Figure 1.4 – (a) Melt pool characteristics showing the definition of hatch spacing, layer thickness, melt-pool width and depth. Typical values for AM AlSi12 are shown [7]. (b) Schematic representation of hatch spacing (H), rotation angle (ϑ) and beam offset (BO) [7]. (c) Schematic representation of scanning islands strategy (number given as order of magnitude) [8]

Selective laser melting is characterized by a high degree of freedom in terms of final part design complexity. Nevertheless, some topology constraints exist, which are imposed by the technique itself. SLM is a complex process due to the violent interaction between laser and powder/bulk metal, which involves a large temperature gradient, metal vaporisation, complex melt-pool geometries and overheating [9–11]. Design guides have been established to anticipate the limitations at the design stage or to orient the part in the machine [12]. Main restrictions come from the smallest features printable (about 0.2 mm for strut diameter [13, 14]), the part's dimensional deviations from the original design [15, 16] and the critical overhang angle (defined to be between 20° and 45° to the horizontal [12, 13, 17, 18]). The latter restriction is solved by adding support structures which also improve the solid metal thermal properties by preventing warping of the part; lower thermal conduction in the powder bed can lead to excessive thermal stresses [19]. In addition to topological constraints, SLM induces different microstructural defects that can be classified into three categories.

Gas-induced porosity appears when dissolved or adsorbed gas is present in the melt-pool and cannot reach the surface before (rapid) solidification due to the high-cooling rate imposed by the process. This type of pore is relatively small (under 100 µm) and a spherical shape. The entrapped gas (mostly hydrogen) originates from solid solution in the powder, gas adsorption or moisture. The last cause can be prevented by heat-treating the powder or preheating the powder layer before melting by using a fraction of the nominal laser power [20]. Inert gas trapped in the powder during the atomization process can also contribute to the final porosity. Gas porosity is usually evenly dispersed within the solid part.

Process-induced porosity is introduced in the part during the interaction of the laser with the powder and is characterized by a high shape factor and large sizes (up to 1 mm) compared to the previously defined gas-induced pores. The main factor controlling the characteristics of this defect is the energy density E_n defined by the combination of four process parameters (equation 1.2),

$$E_n = \frac{P}{VHL} \tag{1.2}$$

where P is the laser power, V is the scanning speed, H is the hatch spacing, and L is the layer thickness. An excessive energy density leads to partial (or full) vaporization of the metal and formation of a keyhole (a well-known problem in laser welding application [21]), whereas insufficient energy density leads to lack of fusion due to insufficient overlapping between melt-pools [22, 23]. These defects are less present than gas-porosity but more detrimental to mechanical performance.

Inclusion of other elements (for example iron into aluminum or tungsten into titanium) primarily occurs due to contamination of the powder itself or by insufficient cleaning of the machine between the printing of different materials. Another type of inclusion is oxide, especially for aluminum due to its high affinity with oxygen. Two sources of oxide have been identified; namely the residual oxygen present in the inert atmosphere and the oxide layer present on the powder surface. AM defects can be seen on Figure 1.5.

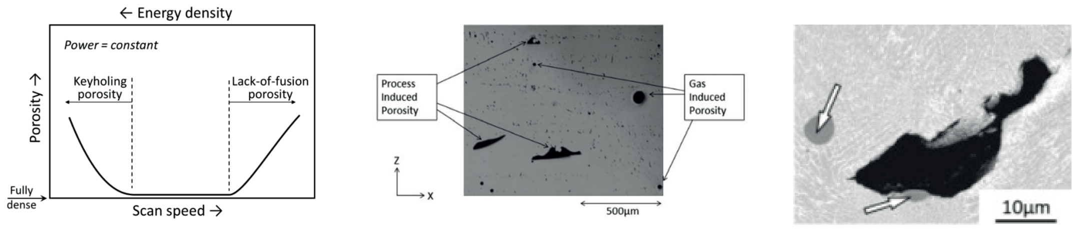

(a) (b) (c)

Figure 1.5 – (a) Influence of the energy density on process-induced porosity (keyhole and lack of fusion) [7]. (b) Micrography of gas-porosity and process-induced porosity (keyhole and/or lack of fusion) in a Ti6Al4V parts [24]. (c) Oxide inclusion and induced porosity shown by arrows in an AlSi10Mg part [25]

SLM of Aluminum-Silicon alloys

Aluminum-silicon alloys represent 80% of aluminum casting alloys and exhibit high aptitude for welding, making them good candidates for additive manufacturing. In particular, AlSi10Mg, AlSi12Mg, and AlSi12 alloys, which have been extensively studied, are the focus of several reviews [6, 26, 27]. Nevertheless, high oxygen affinity, poor powder flowability, high laser reflectivity and thermal conductivity make the additive manufacturing of aluminum challenging.

The selective laser melting process as applied to aluminum (and metals in general) induces as already mentionned very high solidification rates (in the order of 10^6 °K/s [28, 29]) so the resulting microstructure is very fine (less than a micron) [30]. In the case of AlSi alloys, this rapid cooling induces an off-eutectic structure with a cellular solidification structure of primary aluminum surrounded by a fibrous network of fine-scale eutectic [31, 32]. The cell size is related to the thermal gradient during solidification; the higher this gradient, the finer the structure. Therefore, the size of the cells is not homogeneous in the melt-pools, decreasing from the border (about 0.7 µm) towards the center (about 0.4 µm). A heat-affected zone (HAZ) can be observed under the newly produced melt-pool; it contains a eutectic globular Si structure instead of a continuous fibrous network as shown in Figure1.6a [33]. The crystallographic texture is also influenced by the thermal gradient, which creates columnar grains oriented towards the centerline of the laser track; <100> directions dominate at the center while <110> and <111> are preferentially present at the border (Figure 1.6b).

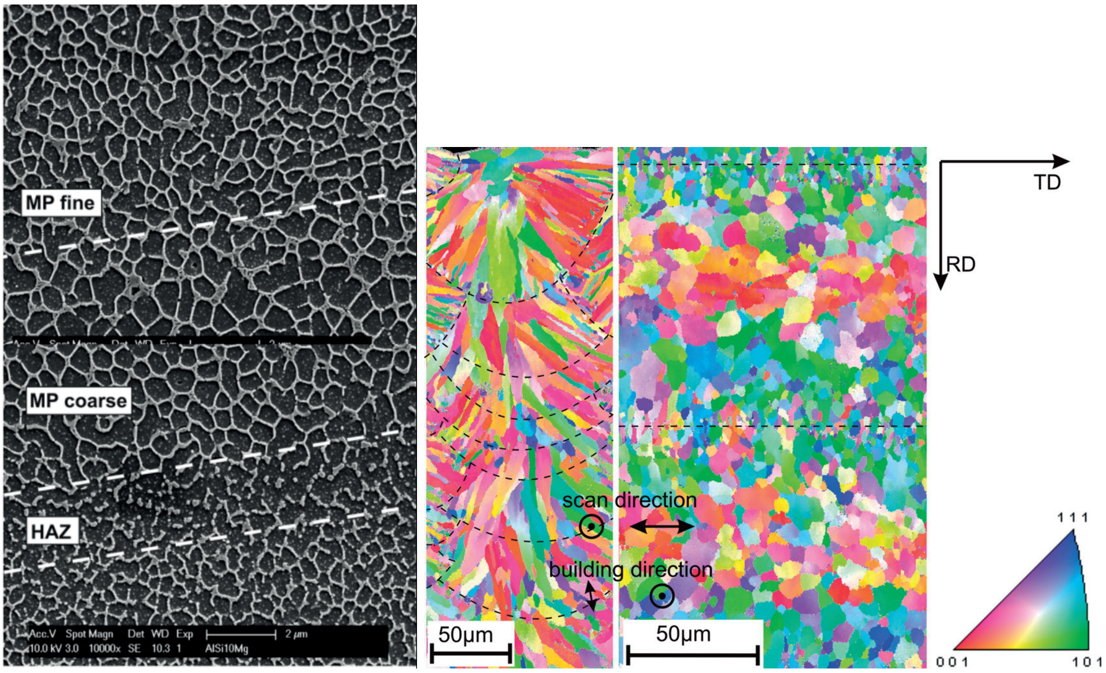

(a) (b)

Figure 1.6 – (a) SEM image of AlSi10Mg built by SLM. MP fine and MP coarse represent the primary aluminum cells surrounded by fibrous silicon of finer and larger sizes respectively. HAZ highlights the heat-affected zone induced by the deposition of the next layer. (b) EBSD image showing the grains orientation induced by the laser beam from the [33]

The fine microstructure of aluminum-silicon alloys produced by SLM leads to higher yield and ultimate tensile strength while lowering the ductility compared to their conventionally cast counterparts. Table 1.1 shows the reported mechanical properties of aluminum-silicon alloys produced by SLM that have been reported in literature. Different process parameters could explain the measured value dispersion.

Table 1.1 – Mechanical properties of AlSi alloys produced by SLM reported in the literature; the yield strength σ_y; the ultimate tensile strength σ_{UTS}; the failure strain ϵ_f. Letters in brackets represent the sample orientation during building while Z is the building direction

	σ_y [MPa]	σ_{UTS} [MPa]	ϵ_f [%]	Hardness [HV]	Ref
AlSi10Mg	-	360 (Z) 420 (XY)	-	145	[34]
	-	396 (Z) 391 (XY)	5.6 (Z) 3.5 (XY)	127	[35]
	-	330	1.4	-	[36, 37]
AlSi12Mg	236	434	4.6	-	[13]
AlSi12	225 (XY)	360 (XY)	5	-	[38]
	200-220	370-420	3.9-4.4	-	[39]

The failure mode of such alloys is influenced by the melt-pool structure and tensile sample orientation. For vertically manufactured samples, cracks that initiate at large pores and then propagate inside the melt-pools boundaries until fracture have been observed (Figure 1.7) [26, 35, 40]. Purcek and al [41] demonstrated that coarser silicon particles dispersed into AlSi12 alloys lead to lower mechanical properties. Microhardness tests performed at the melt-pools border confirmed this trend (Figure 1.8) [25].

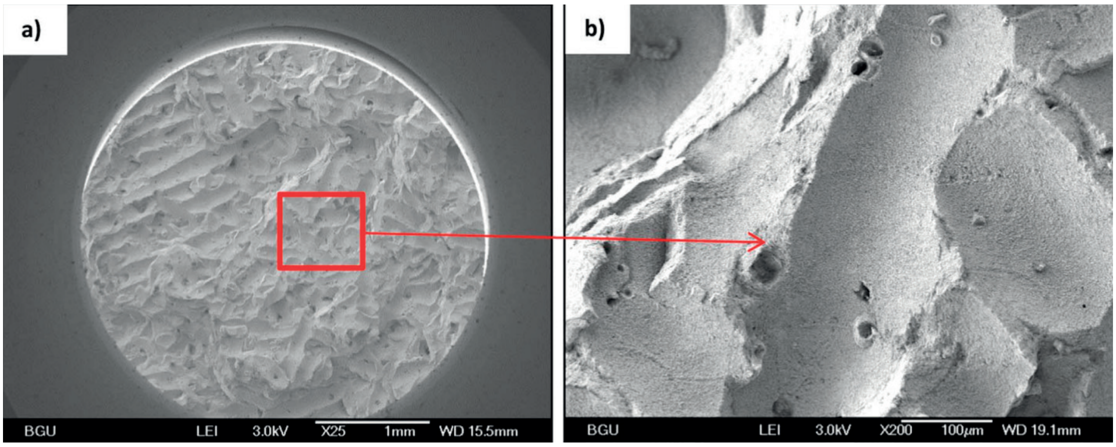

Figure 1.7 – SEM fracture surface images of sample manufactured along the building machine direction revealing inter melt-pools fracture at a) low and b) high resolution [40]

1.3.3 Cellular materials

Cellular materials and especially cellular metals have the piqued interest of the scientific community for some time due to their specific combination of cellular material characteristics (low density, high specific stiffness, high energy-absorption and damping capacity) with characteristics of metals (high flow-stress, toughness, electrical and thermal conductivity). Research on cellular metals mostly started on closed-porosity metal foam, produced mainly by blowing a gas into molten metal or by mixing it with a foaming agent. Technologies then evolved and opened the

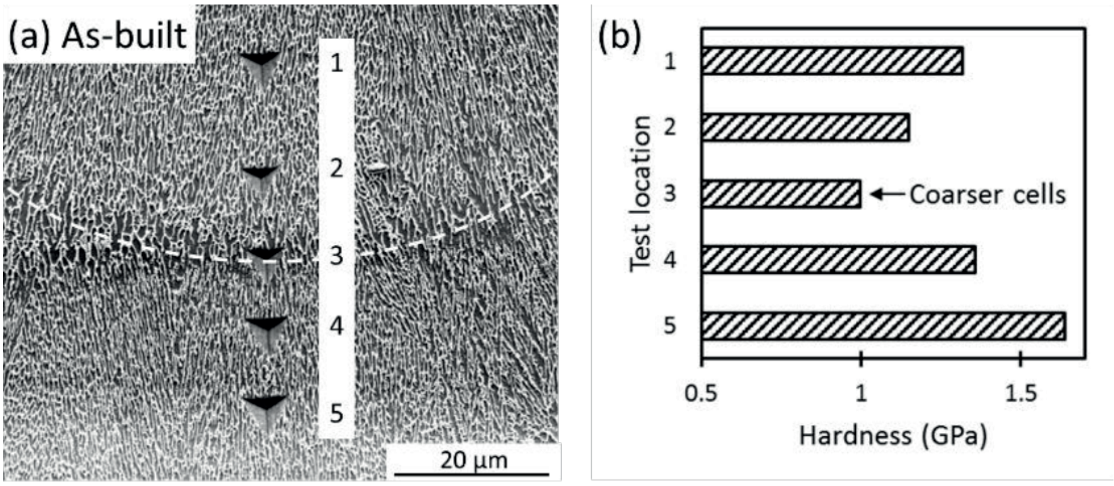

Figure 1.8 – (a) Microhardness tests performed across the melt-pools border on AlSi10Mg produced by SLM and (b) their corresponding measured values [25].

possibility to produce cellular metals in a wide range of topologies and bulk materials (steel, copper, gold, lead, titanium, aluminum, magnesium). Nowadays, cellular metals can be classified according to their porosity (open or closed) and their structures (stochastic or periodic). Several reviews discuss the manufacturing of cellular metals [42–48], ; Figure 1.9 shows a taxonomy of the wide range of manufacturing routes available to produce such structures [47] while Table 1.2 lists references associated with some of the manufacturing processes.

Gibson and Ashby studied extensively cellular materials in general [42, 110] including their behavior in deformation and therefore under compression. A standard deformation pattern has been identified for cellular material uniaxial deformation, which can be divided into three parts: (i) an elastic regime corresponding to a linear deformation of the material until the yield stress is reached, (ii) a roughly constant stress regime where deformation takes place over a wide range of strain (characteristic of a cellular material) and (iii) a densification regime in which pores start closing resulting in a rapid increase of the stress. In porous metals, yield occurs at low applied stress due to the presence of high stress-concentration sites within pore walls or metals. The initial slope of the stress-strain curve is often influenced by macroscopic stress inhomogeneity; therefore a more precise method for measurement of the Young's modulus is to use load/unload cycles [42, 111]. The predominant mode of deformation of cellular materials under compression (except for some precisely manufactured lattice truss structures) is bending of the struts or cell walls. Yielding of porous metals has been investigated by several authors under different test configurations [112–121]. The main characteristic of a metal foam under compression, which differs from bulk metals, is the large deformation at almost constant pressure corresponding with metals to plastic deformation and gradual reduction of porosity. Pore collapse typically occurs in compression testing by successive failure of narrow-band of material roughly orthogonal to the loading direction. Once a band is dense, deformation switches to another band until a full column of dense material is present, marking the onset of the third regime [83, 110, 122–133]. During this plateau phase, the deformation can be either smooth and constant, or alternate up and down with a constant mean value (Figure 1.10). Concerning the dynamic response of a metal foam to loading (compression at high strain-rate), even if conclusions are not unanimous among the

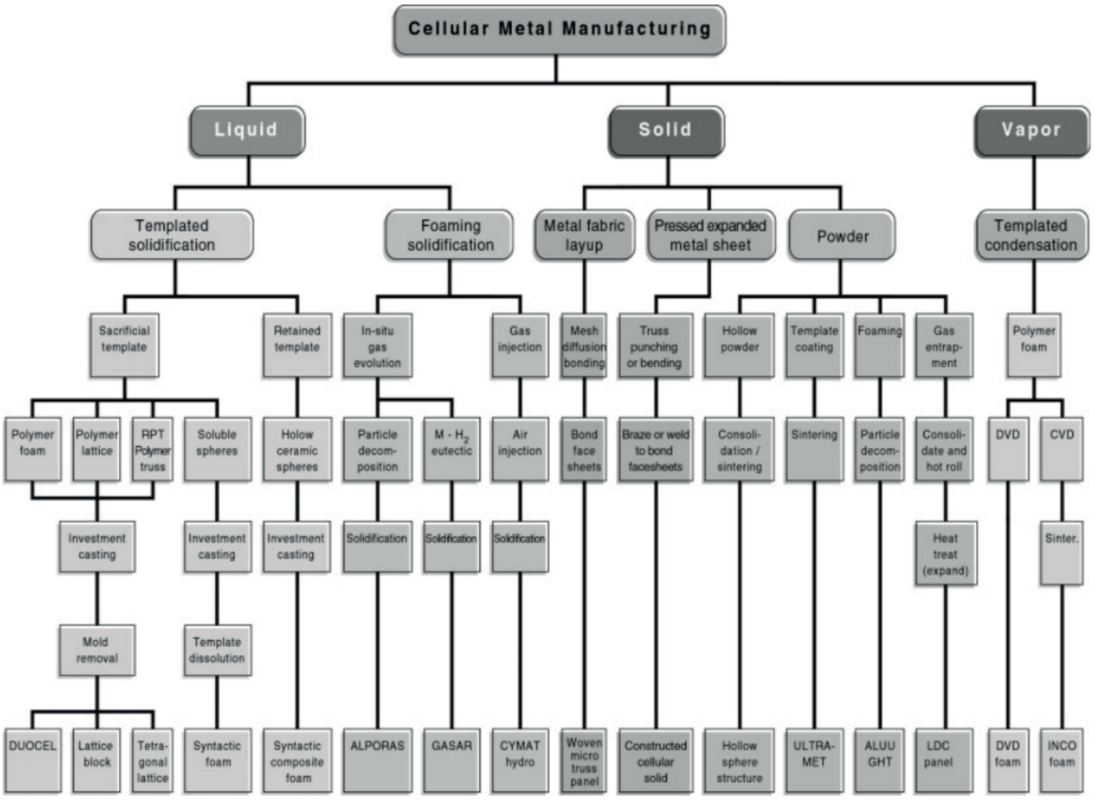

Figure 1.9 – A taxonomy of cellular metal manufacturing processes [47].

papers, the generally accepted observation is an increase of the strength by increasing the strain rate [127, 134–139]. This behavior can come from the intrinsic strain-rate dependency of the bulk metals [140–143] (not a major factor for aluminium-based foam [144]), from microinertia effects that depend on the cell morphology [144–146] or from the formation and propagation of a shock front at very high strain-rate [136, 140, 147–149].

A common way to measure the mechanical properties of cellular materials is to compare them to the properties of the solid material making the foam. Extensive work, later confirmed by experiments, was performed by Ashby and Gibson [42, 110] and led to scaling laws for some properties such as Young's modulus E, Plateau stress σ_{pl} and Densification strain ϵ_D as a function of the relative density of the cellular material (Equation 1.3 to 1.5), namely:

$$\frac{E}{E_s} = (0.1 \text{ to } 4)(\frac{\rho}{\rho_s})^{(1.8 \text{ to } 2.2)} \tag{1.3}$$

$$\frac{\sigma_{pl}}{\sigma_{y,s}} = (0.25 \text{ to } 0.35)(\frac{\rho}{\rho_s})^{(1.5 \text{ to } 2)} \tag{1.4}$$

Table 1.2 – Manufacturing routes to produce metallic cellular materials

Process	References
Closed porosity	
Blowing gas	[49–52]
Foaming agent	[53–55]
Phase change (Gasar/Lotus)	[56–59]
Packing/sintering of hollow spheres	[60–62]
Open porosity	
Investment casting	[63–66]
Deposition on polymer preform	[67–73]
Sintering of particles/fibers	[74–76]
Dealloying	[77–79]
Powder-based space holder	[80–82]
Preform infiltration	[83–88]
Periodic cellular structures	
Investment casting	[89–95]
Weaving and joining wires	[47, 96–99]
Sheet metals processes	[47, 100–103]
Additive manufactured	[104–108]
Electroplating	[109]

$$\epsilon_D = (1 - (1.4 \text{ to } 2)\frac{\rho}{\rho_s}) \tag{1.5}$$

where E is the Young's modulus, $\frac{\rho}{\rho_s}$ the relative density, σ_{pl} the plateau stress, σ_y the yield stress and ϵ_D is the densification strain. The s subscript is associated with the strut/cell wall (dense) solid material properties. Based on bending theory, these equations are valid for relative densities up to 0.3; denser structures possess struts with lower aspect ratios estimated to yield under more complex states of stress. This type of structure is susceptible to side effects; the size of the sample can influence its mechanical properties when sample and pore dimensions come close to one another. Studies have shown that a sample to cell size ratio of at least seven would be sufficient to neglect this phenomenon [42, 150].

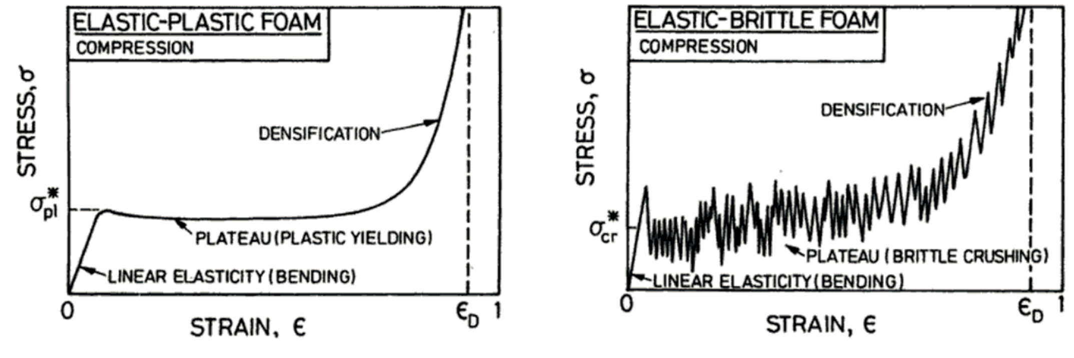

(a)

(b)

Figure 1.10 – Typical compression stress-strain curves of cellular materials with high ductility (a) and brittle (b). Images adpated from [110]

1.3.4 Metallic periodic cellular structures

Periodic cellular structures (PCS) are a specific class of cellular material, which consists of a precisely defined assembly of struts. Pin-jointed struts assumption were used to analytically estimate the properties of such assemblies [151, 152]. The response to loading of these structures is greatly influenced by the deformation mode of the struts, namely bending (leading to bending-dominated structures) or stretching (leading to stretch-dominated structures). Two criteria were established by Maxwell [153] (in 2D and 3D) to predict the preferred deformation mode of the structures according to the number of struts s and nodes n in a unit cell (Equation 1.6 and 1.7); if respected, the stretch-dominated behavior is expected, keeping in mind that the condition is necessary but not sufficient.

$$s - 2n + 3 \geq 0 \quad \text{in 2D} \tag{1.6}$$

$$s - 3n + 6 \geq 0 \quad \text{in 3D} \tag{1.7}$$

A generalization of Maxwell's criteria was then proposed by Calladine [154], to take into account the presence of mechanism and self-stress states in a pin-jointed assembly of struts. Deshpande and al. [152] demonstrated that, for structures with nodes similarly situated in the lattice, a struts connectivity of 12 (6 in 2D) is sufficient to obtain stretch-dominated structures. In planar lattices, two different type of strain-producing mechanisms were characterized, namely a periodic and a macroscopic [151]. The importance to differentiate these collapse mechanisms was emphasized by the analysis of a network which was predicted to fail by bending but finally appeared rigid. Planar Kagome lattice exhibits a rigid behavior in all directions despite a connectivity of 4, explained by the presence of only periodic strain-producing mechanism [151]. Hutchinson and al. extensively studied the deformation of Kagome lattice and developed a method to analyze the periodic strain-producing mechanism using Bloch's theorem [155]. Finally, even if Kagome lattice exhibits the same effective stiffness as the fully-constrained triangular lattice, it was reported that the former is more susceptible to topological imperfections [156]. In 3D, it was reported that no polyhedron are able to fill the space by replication and being rigid at the same time. Therefore, stretch-dominated structures are obtained only by a combination of two different polyhedra, themselves compliant with Maxwell's criterion [152].

The relative density is the most important parameter descriinge the cellular material, and periodic cellular structures are no exception to this; almost every property can be scaled to it [42]. Looking at the mechanical properties, significant differences have been observed in the scaling models comparing the stretch and the bending-dominated behaviors. Equation 1.8 refers to bending-dominated structures, and 1.9 refers to stretch-dominated lattices regarding the Young modulus and the yield stress:

$$\frac{E}{E_s} = (\frac{\rho}{\rho_s})^2 \qquad \frac{\sigma_y}{\sigma_{ys}} = (\frac{\rho}{\rho_s})^{1.5} \tag{1.8}$$

$$\frac{E}{E_s} = \frac{\rho}{\rho_s} \qquad \frac{\sigma_y}{\sigma_{ys}} = \frac{\rho}{\rho_s} \tag{1.9}$$

where subscript s corresponds to (dense) solid bulk material properties. Figure 1.11 compares different lattice structure performances with baselines extracted from the two previous relations. In stochastic cellular material, deformation and failure are governed by strut-bending, attributed to the low struts connectivity (about 3-4) [111]. This deformation mode is associated with constant flow pressure over a large range of strain, which could be beneficial for energy-absorption applications. On the contrary, some specific lattice structures may exhibit a stretch-dominated behavior characterized by a higher initial stiffness at equivalent relative density but followed by yield softening. Therefore, using this type of structure would be more advantageous in structural applications.

Metallic periodic cellular structures are manufactured according to various production methods such as:

- Weaving or joining wires [47, 96–99] or using sheet metal processes [47, 100–103]. These methods are cost-effective; however, the need to bond the different layers using a third material, can be detrimental for the properties. Also samples are often limited to a few layers in thickness.
- Investment casting [89–92, 157, 158], which imposes relatively large cells (above 10 mm) and is costly. Issues on molten metal flow and mold removal were observed and led to missing struts in the structure. Molds were produced in ceramics or salt by replication of a preform, or directly 3D-printed.
- Electroplating of a sacrificial preform [109], leading to the lightest structures manufactured (relative densities from 10^{-2} to 10^{-4})

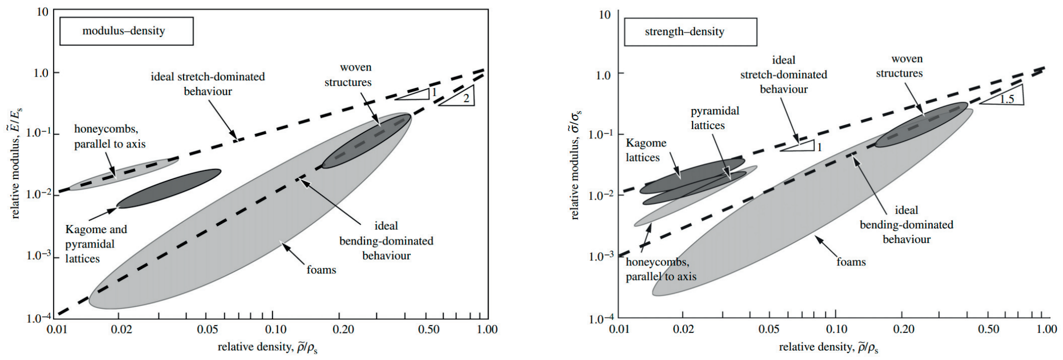

(a) Relative modulus-relative density plots on logarithmic scales for various cellular structures, including PCS. The exponent difference in equations 1.8 and 1.9 is shown with the two baselines resulting in slopes of 2 and 1, respectively.

(b) Relative stress-relative density plots on logarithmic scales for various cellular structures, including PCS. The exponent difference in equations 1.8 and 1.9 is shown with the two baselines resulting in slopes of 1.5 and 1, respectively.

Figure 1.11 – Comparison of relative modulus and strength plotted against relative density [111]

- Additive manufacturing by selective laser or electron beam melting [104–108], limited by process manufacturability (smallest features, overhang angle, unmelted powder removal).
- Binder jetting of metal oxides followed by a reduction step [159], limited by the green body strength to withstand the depowdering step, and volume shrinkage during sintering.

The base alloys used are mainly stainless steel (316L), titanium (Ti6Al4V) and aluminum-silicon. A wide selection of cell topologies were already characterized such as body-centered cubic [160–166], face-centered cubic [13, 160], simple cubic [167, 168], diamond [104, 105, 107, 107, 169] rhombic [163, 170], auxetic [163, 170], rhombicuboctahedron [171], 3D-Kagome [99, 101, 172] or octet-truss [160, 170, 171, 173–179]. The latter is the most manufactured and studied in the literature. Deshpande and al. extensively studied all the possible deformation mode of the struts depending on the load-state and estimated scaling relations for the Young modulus, the shear modulus and the yield stress. The anisotropy was also characterized and it is estimated that octet-truss structures are twice stiffer in the <111> direction with respect to the <100> orientations. [180]. Recent studies investigated the manufacturability of more exotic periodic structures based on surface and topology optimizations leading to continous shell mesostructures [36, 162, 178].

Deformation behaviors of lattice structures have been now extensively recorded and it appears that, in addition to the classical band-collapse failure observed in stochastic foams under compression [13,36,37,98,99,109,181], samples also exhibit failure by shearing [13,37,165,165–167], as shown in Figure 1.12. Despite the large amount of studies observing one or the other mechanism, no clear criteria could be found to predict and explain the underlying reason of the obtained failure mode.

Inherently linked to the topology of the unit cell, periodic cellular structures exhibit a high anisotropy in their mechanical properties. Xu and al. [160] numerically showed that the com-

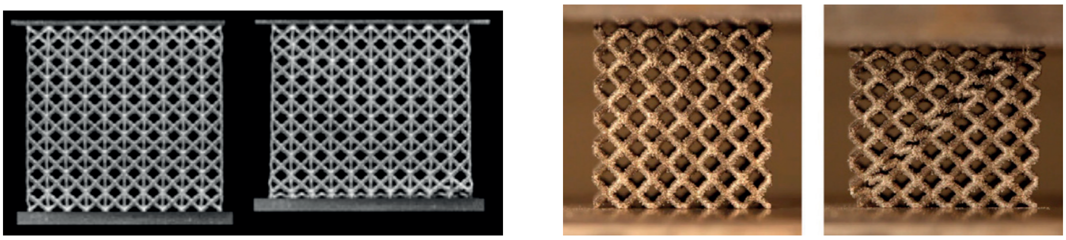

(a) (b)

Figure 1.12 – (a) Images of a FBCCZ sample before and after failure by band collapse, manufactured in AlSi12Mg by SLM with a relative density of 16% [13]. (b) Images of a BCC sample before and after failure by sliding between planes, manufactured in AlSi10Mg by SLM with a relative density of 22% [37].

pressive modulus can be five time higher along an orientation with respect to another one, the stiffer direction is aligned with the struts axis. Figure 1.13 shows the calculated anisotropy for various unit cell topologies. This strong impact of anisotropy on the mechanical properties was experimentally characterized by compression testing on body-centered cubic structures at different orientations, manufactured by electron-beam melting in Ti6Al4V alloy; again emphasizing the importance of the strut axis on the properties [161]. Attempts at mitigating the anisotropy by inducing disparities in struts diameter or combining two different topologies were performed [160]. Finally, anisotropy was measured in periodic structures between two directions that are topologically equivalent (belonging to the same direction family). Octet-truss structure exhibited a stiffness 20% higher in the horizontal directions compared to the vertical building direction. This was associated to the overmelting of the horizontal struts during the manufacturing process [171].

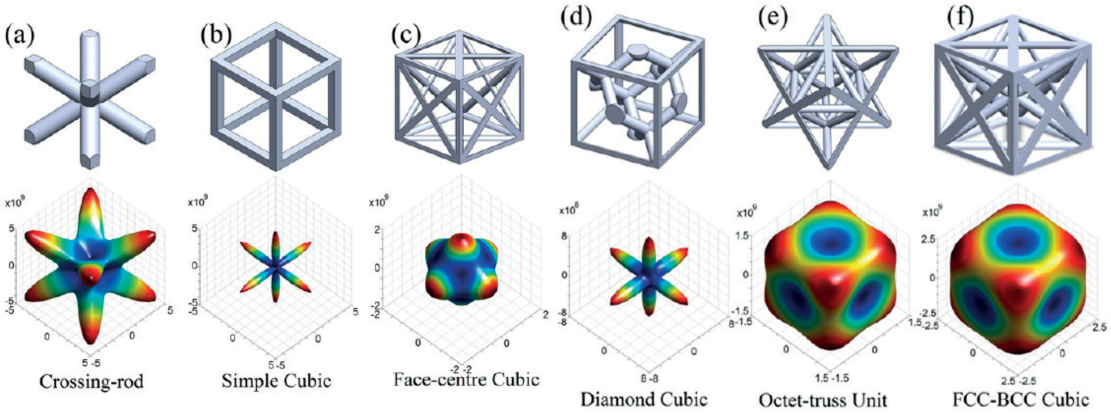

Figure 1.13 – Effective compressive modulus anistropy calculated for different cell topologies with the corresponding CAD models: (a) Body-centered cubic BCC, (b) Simple cubic, (c) Face-centered cubic FCC, (d) Diamond cubic, (e) Octet-truss, and (f) combination of FCC with BCC. Adapted and reproduced from [160].

In parallel to the topology and the relative density, other parameters have an impact on PCS performance. As for their stochastic counterparts, PCS are susceptible to side effects, but to a lesser extent. It was reported that numerical simulations [163] and experimental data [182] agreed on a sample-cell size ratio of 3-4 to avoid any side effect. At constant relative density, it was also demonstrated that cell size has a small effect on the mechanical properties; the smaller the cell size, the stronger the structure. This relation was explained by the bulk alloy characteristics; a smaller cell size leads to smaller cross-sections and therefore faster laser pass. This increase in laser scanning speed induced a slightly faster cooling rate responsible for a finer microstructure, itself responsible for higher mechanical properties [183].

Manufacturability inspections were conducted to assess the limitations of additive manufacturing of PCS, as well as the impact of processing parameters on their mechanical properties. The deviations from CAD design while using standard machine parameters was described, highlighting the necessity to adjust wisely the parameters to obtain the highest fidelity of the final part [164]. It has been shown that laser power as a positive influence on the mechanical properties while an optimum was observed regarding the laser scan speed. These results have been explained by the obtained strut topology and porosity while tuning these two parameters [165]. A study performed on the manufacturability of Ti6Al4V lattice structures defined that the critical overhang angle is 30°, the maximum bridge length is 1 mm, the minimum hole diameter is 0.1 mm, and the minimum wall thickness is 0.1 mm [160]. Finite element analysis usually model the struts as perfect rods leading to overestimation of the actual mechanical properties. An attempt was made to catch more accurately with 3D-tomography the geometrical defects induced by the SLM process to improve the correlation between simulations and experimental data. Geometrical defects were separated into three categories, namely (i) strut undersizing, (ii) strut thickness variation, and (iii) strut waviness. An interesting result from the study is that geometrical imperfections might be responsible for the observed failure mechanism (band or shear-collapse). It was shown that the same structures can fail according to two different mechanisms depending on the defects content in it [171]. Figure 1.14 shows an example of the change in failure mode as a function of the difference between horizontal and diagonal strut diameters in an octet-truss structure.

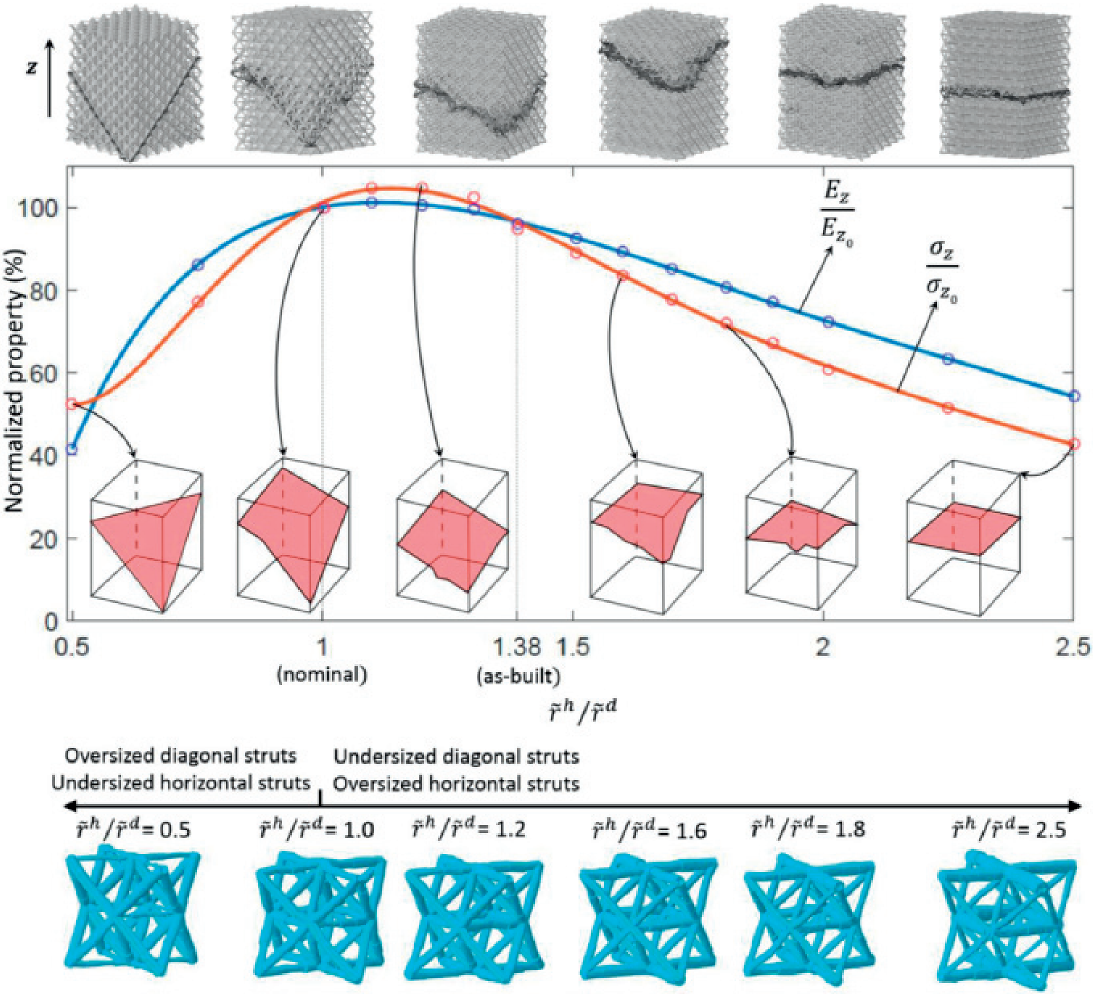

Figure 1.14 – Normalized Young modulus and compressive strength as a function of the difference between the horizontal and diagonal strut diameter. Top sketches show failure mode through computations, highlighting the variation from shear to band-collapse. Reproduced from [171].

1.3.5 Ceramics processing

The following section summarizes the exhaustive book published by T.A. Ring [184]. All references to chapter number in the next sections are related to the one of the book. The manufacturing of ceramics can be divided into several steps:

1. The base material powder is produced
2. The powder is transformed into a ceramic suspension or paste (with a high volume fraction of particles)
3. The green body is shaped from dry powder, suspension or paste
4. The green body is dried, relieved of its binder, and sintered to obtain the final ceramic part

Powder is the base component of ceramic manufacturing and a narrow size distribution with a mean particle diameter of 5 µm is often desired. Several different methods can produce a ceramic powder depending on the material, the size distribution, the reaction kinetics or the production costs. Particles can be made by transforming an initial solid material into powder using chemical reactions, usually in parallel with the emission of liquid or gas. For example, calcium oxide (CaO) can be produced by thermal decomposition of calcium carbonate ($CaCO_3$), alumina (Al_2O_3) by oxidation of aluminum (Al) or silicon nitride (Si_3N_4) by nitridation of silicon (Si) (Chapter 5). Instead of starting with a solid, the powder synthesis step can be initiated from a liquid in which the desired particles are precipitated. This process involves supersaturating a solution to cause particle nucleation followed by crystal growth (Chapter 6). The next main production route is based on gaseous reactants; gases are heated to induce chemical reactions leading to nucleation, growth and aggregation of solids. Quenching is performed at the end to stop the reaction and freeze the particle distribution. This is the case for silicon tetrachloride ($SiCl_4$) in combination with oxygen to produce silica (SiO_2) or for titanium tetrachloride ($TiCl_4$) with water vapor (H_2O) to create titanium oxide (TiO_2) (Chapter 7). Another way to produce ceramic powder is to dry small droplets of liquid into fine particles by atomization or spray drying (Chapter 8). Finally, nearly all produced and naturally available powders need to be downsized by comminution and classified to obtain the final desired size distribution (Chapter 4).

The next (optional) ceramic manufacturing process step is to shape the obtained powder into a ceramic suspension or a paste. Particles are mixed into a solvent specifically selected for its good wettability on the powder. Particle surface roughness also plays a role in the process; the smoother the surface, the easier the wetting. Deagglomeration is then performed to break any possible aggregates, either by comminution or ultrasonification. Recombination into clusters is prevented by adsorption of the solvent itself, of an ion, of a surfactant or of a polymer (Chapter 9). Finally, the colloidal stability of the suspension is established by electrostatic or steric stabilization to prevent particles from combining after colliding due to random thermal or fluid motions. A stabilized colloidal suspension is optimal for reaching a high packing density for a single component ceramic powder. For multicomponent ceramic powder, the segregation between different components is prevented by destabilizing the suspension (by adjusting the pH or adding surfactants/polymers) to reach the percolation limit that locks the particles in place (Chapter 10). Colloidal stabilization is not permanent and possesses a limited life expectancy that limits the time available to shape the green body before detrimental effects on the final ceramic part are observed. This "shelf-life" is linked to particle sedimentation driven by a balance between buoyancy, Brownian diffusion, gravitational and drag forces in the solvent. The settling is influenced by several parameters such as particle density, size, shape, size distribution and volume fraction as well as solvent density (Chapter 11).

Green bodies are shaped directly from dry ceramic powder or from an intermediate ceramic suspension/paste. In all cases, a good understanding of the base component rheology is crucial for a good final part quality, whether it is dictated by the powder flowability for dry particles, the viscosity for ceramic suspension or the visco-elastic behavior of ceramic paste (Chapter 12). Table 1.3 shows a non-exhaustive list of processes that can be used to shape green bodies as a function of the base material available (dry powder, suspension or paste) (Chapter 13).

Several steps are performed to complete the ceramic manufacturing process; drying, binder

Table 1.3 – Green body shaping processes as a function of the base component (dry powder, ceramic suspension or ceramic paste)

Dry powder	Ceramic suspension	Ceramic paste
Die pressing Isostatic pressing	Slip casting Filter pressing Sedimentation Centrifugal casting Dip coating	Extrusion Injection molding Tape casting

removal and sintering. The drying step consists of removing any residual solvent present from the preparation of the ceramic suspension or paste. A constant drying rate is first observed corresponding to the rearrangement of the particles inside the green body until a rigid network is formed, and then a decreasing drying rate is seen associated with removal of the remaining solvent (as shown in Figure 1.15). Internal stresses during the drying step are caused by a capillary pressure gradient, escaping solvent pressure gradient or differential thermal expansion and can lead to warping or cracking of the green body. Precise control of the drying rate is crucial to prevent these defects from occurring (Chapter 14). Binders are polymers incorporated into the dry powder, ceramic suspension (or paste) to enhance the green body strength during shaping. Thermal degradation later eliminates the binders under an oxidizing atmosphere used to remove any residual carbon. Degradation of polymers occurs during endothermic or exothermic reactions involving a significant amount of released volatiles; this process leads to thermal and pressure gradients that can later cause the formation of defects into the part (Chapter 15). At this stage, the green body relieved of its binder is in its most fragile state and needs to be handled with care. The last step before obtaining a ceramic part is sintering, which densifies and imparts the structural integrity upon the green body by heating to high temperatures close to the melting point. The driving force is the reduction of the inner (pore) surface area. Application of pressure during sintering can help to further increase the density and/or speed the process, and post-process grain refinement by heat treatment can be performed to improve the mechanical properties (Chapter 16).

1.3.6 Hypervelocity impact testing

Since the first satellite launch on October 4th, 1957 by the ex-USSR, Sputnik-1, an ever-increasing number of man-made objects have been put into orbit, bringing with them their sets of undesired orbital debris. In addition to natural micro-meteoroids, these debris present a threat for space missions, especially for the safety of astronauts during manned-missions [185]. Orbital objects are hazardous due to their very high speeds ranging from 1 to 15 km/s for debris in low earth orbit (LEO) and up to 72 km/s for micro-meteoroids [186, 187]. Objects larger than 10 cm, mostly localized on LEO (Figure 1.16) and composed of fragmentation debris [188], can be tracked from the ground and cataloged. Being impossible to shield, the debris trajectories are anticipated, and avoidance maneuvers are performed when possible (for example for the ISS or the Space Shuttle). In 1978, by examining the constant augmentation of debris in LEO, Kessler and Cour-Palais described a theoretical catastrophic scenario in which collisions occur in a cascading effect leading to an exponential augmentation of objects, preventing the use of some

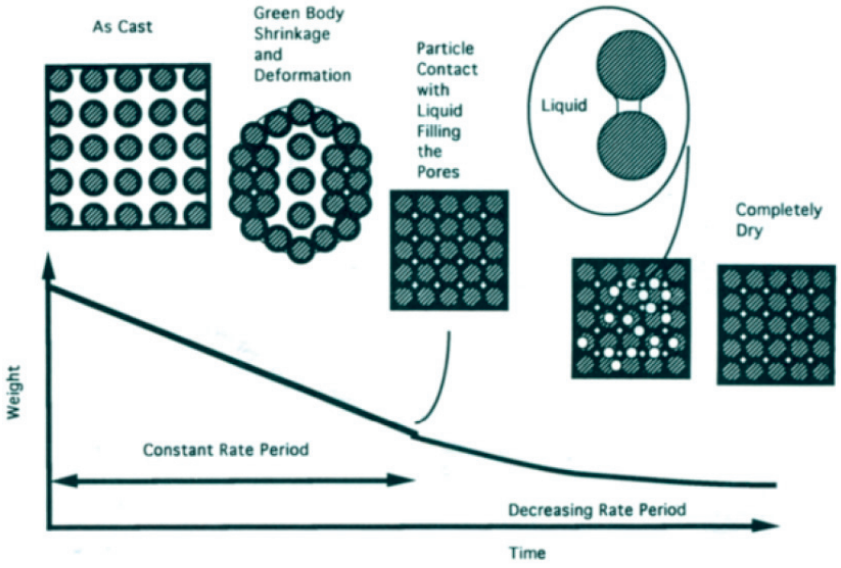

Figure 1.15 – Schematic representation of the green body weight loss according to the drying time with its associated shrinkage (Chapter 14)

orbits for years [189]. Two events confirmed this hypothesis leading to two sharp increases in the amount of debris (Figure 1.16), namely an anti-satellite missile test performed by China in January 2017 and a collision between two satellites (Iridium 33 and Kosmos-2251) which happened in February 2009. These events increased the total number of orbital debris larger than 10 cm by 3000 and 2000, respectively. Therefore, to prevent this situation from escalating into what is called the Kessler prediction, mitigations plans have been adopted by space agencies to limit the amount of additional debris in orbit [190, 191]. In addition to observable objects, it is estimated that hundreds of thousands of smaller debris gravitate around the Earth; engineering models have been developed to estimate the size distribution of this class of debris [192, 193].

Micro-meteoroids and small orbital debris (MMOD) are invisible to ground-based radar stations. The threat is then mitigated by shielding placed over spacecraft and satellites. The multiple-stage light gas gun concept has been developed to assess the shield performances by reproducing the high-velocities observed in space [194, 195]. The underlying principle is simple compared to the velocity reached by the projectile. A highly pressurized gas (generated either by compression or with the use of explosive charge) is allowed to expand into a pump tube pushing a piston. This piston compresses the gas (usually hydrogen or helium) until specific pressure is reached; at this point, a diaphragm is ruptured and the gas pushes forwards the projectile sitting in a sabot. At the exit of the barrel, the projectile and the sabot are separated by the combined action of residual atmosphere in the chamber and a stopper plate. Figure 1.17 shows a schematic of a two-stage light gas gun. This configuration enables velocities up to 10 km/s [196]. The integrity of the projectile before impact is verified with RX flashes, the velocity is measured with optical laser barriers, and the test is recorded with high-speed cameras.

---

[3] http://www.esa.int/Our-Activities/Operations/Space-Debris/Analysis-and-prediction

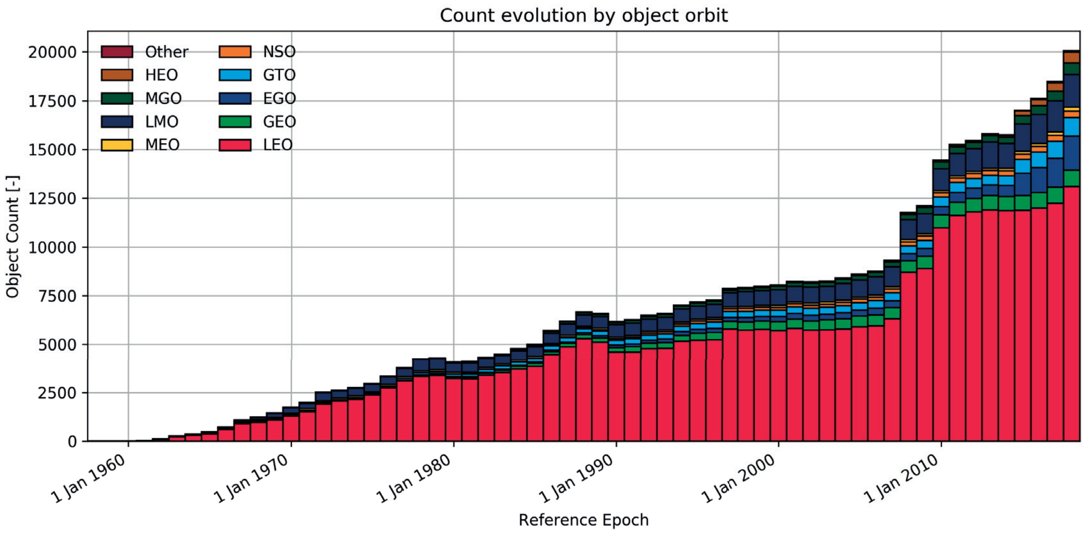

Figure 1.16 – Time evolution of orbital debris bigger than 10 cm according the orbits [3]

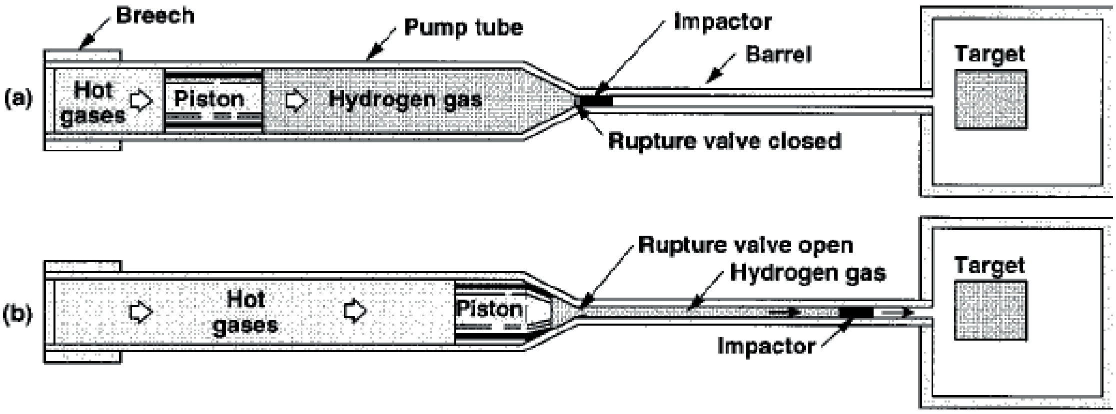

Figure 1.17 – Sketch of a two-stages light gas gun [195]

Due to the high energy required to place an object into Earth's orbit, spacecraft are limited in mass. Monolithic shielding was consequently defined as an unacceptable option and a new concept was to spread the impact load over a larger area to decrease the required protection thickness. This was achieved by adding what it is know as a bumper layer with an interspace, leading to the so-called Whipple shield configuration. Studies on the interaction between an Al thin plate and an Al projectile at high velocities showed that: (i) at speeds below 3 km/s, the bumper has no effect on the projectile integrity and the shielding performance is not improved compared to monolithic protections; (ii) between 3 and 6.5 km/s, shock pressure at impact induces fragmentation and partial melting of the projectile; (iii) for velocities above 6.5 km/s, the impactor is estimated to be fully molten with potential vaporization and at this stage no further improvement is seen compared to a bulk shield [186,197,198]. From hypervelocity impact tests, Ballistic Limit Curves

(BLC) are drawn by plotting the critical Al projectile diameter able to perforate the shield as a function of the velocity, as shown in Figure 1.18. A study on the debris cloud morphology following impact with the bumper showed that a transition could be observed from wide to confined depending on the projectile diameter, the plate thickness, and the impact velocity [199]. Figure 5.21 p.149 highlights the difference and shows the debris clouds after impacts for a set of different parameters.

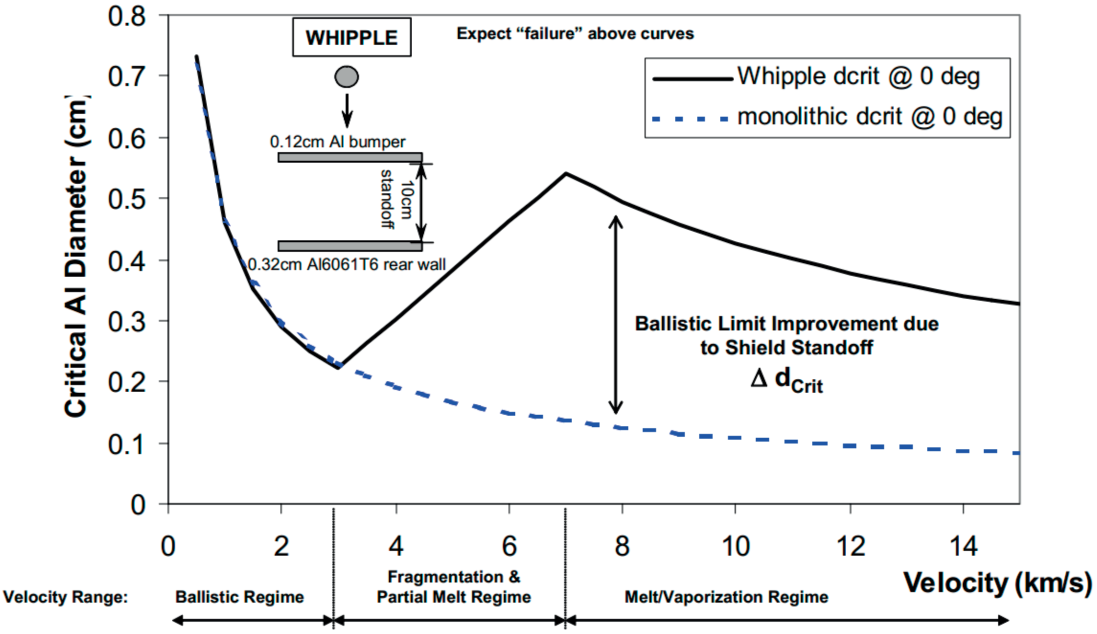

Figure 1.18 – Ballistic limit curve for equal mass monolithic and whipple shields. Monolithic target is 0.44 cm thick Al 6061-T6. Whipple shield consists of 0.12 cm thick Al 6061T6 bumper followed at 10 cm by 0.32 cm thick Al 6061T6 rear wall [186].

Based on empirical data, Ballistic Limit Equations (BLE) have been established to estimate the performance of a specific shield configuration at various velocities [186, 187, 197, 200–205]. BLE were also numerically estimated with the hypothesis that the solid is transformed into a liquid for such high loadings [206, 207] and this estimation followed by the development of a predictive software by NASA [208].

Further improvements of Whipple shield configurations led to the introduction of the multi-shock shield concept, in which more than one bumper is placed in front of the rear wall; preliminary tests were performed with Al plates as additional shock absorbers but were later replaced by high-strength fabrics such as Nextel$^{\H{o}}$ and Kevlar$^{\H{o}}$ [186, 187, 197, 200–202, 205]. Currently on the ISS, more than 100 different multi-shock shields were designed depending on the ISS module to protect from MMOD impacts; most of the designs are based on Nextel$^{\H{o}}$ and/or Kevlar fabric$^{\H{o}}$ [192].Finally, investigations were performed to determine if Al foams could be used as MMOD shields, with promising results [207, 209–215]. Figure 1.20[4] shows different tested

---

[4] adapted from https://ares.jsc.nasa.gov/orbital-debris/hvit/shield-development/shield-development.html

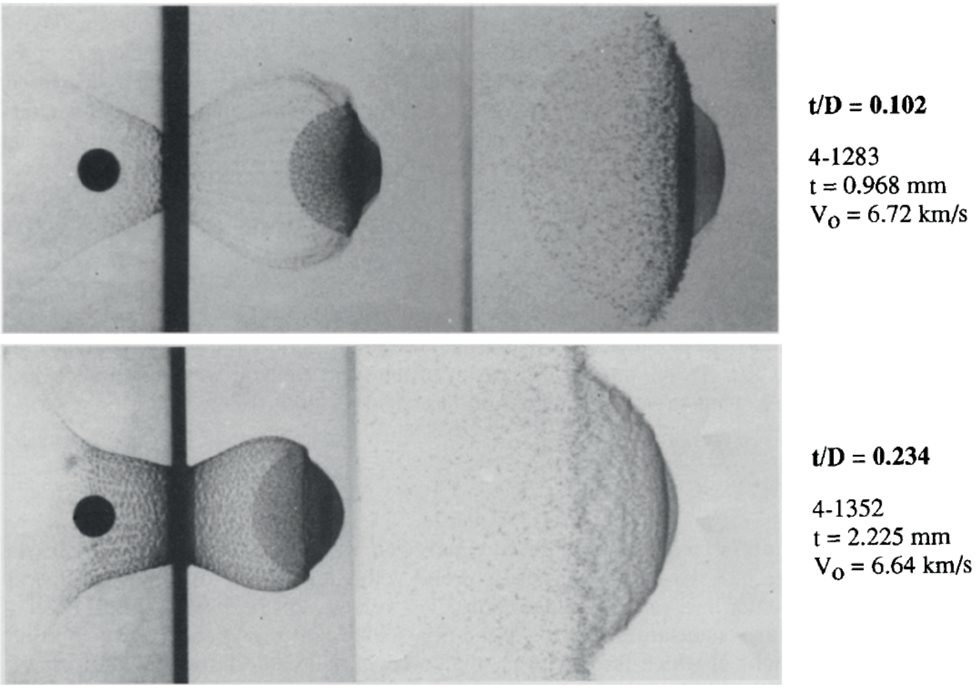

Figure 1.19 – Composite images of 9.53 mm diameter 2017-T4 Al sphere impacting 6061-T6 Al bumper with various thicknesses. Impact velocities were kept constant [199].

shield configurations including a comparison between an Al honeycomb panel and a Duocel^{ő} Al foam core sandwich structure.

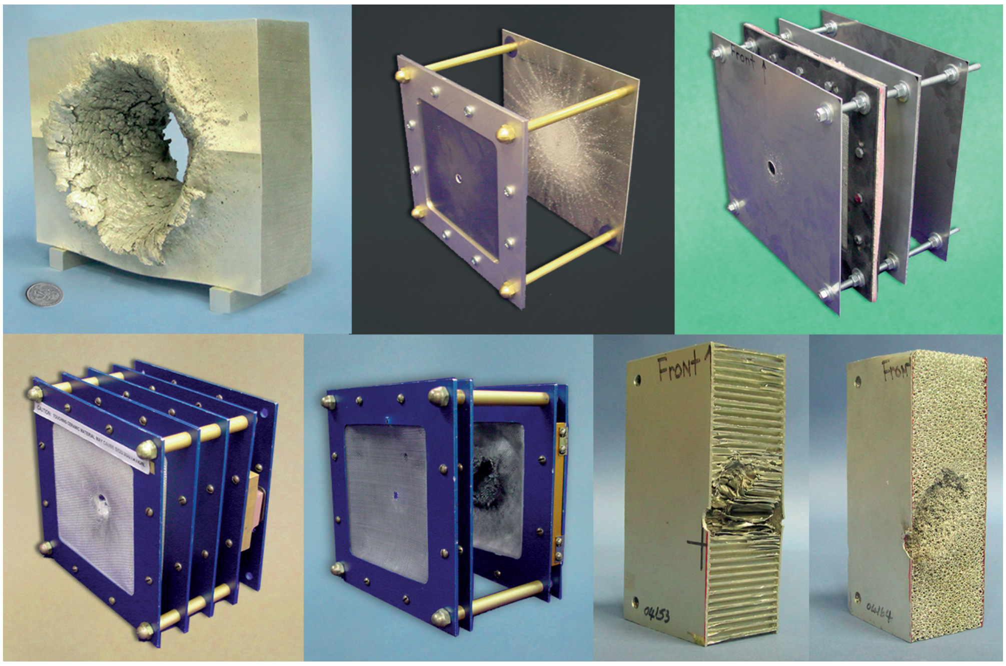

Figure 1.20 – Various shield configurations. Top: monolithic, whipple, stuffed whipple. Bottom: multi-shock, mesh double bumper, honeycomb panel, metallic foam. Reproduced from [216].

.

2 Additively manufactured AlSi12 PCS: Microstructure, mechanical properties and failure mode

2.1 Introduction

Periodic cellular structures (PCS) are topologically improved porous structures exhibiting better mechanical properties by at least one order of magnitude compared to their stochastic counterparts. Starting to be widely investigated in literature either for the manufacturability [164, 217, 218], the design [161, 178], the mechanical properties [91, 98, 99, 104–109, 181, 219], the failure mode [13, 143, 162, 181] or the defects influence [167, 171]; no clear explanation was reported concerning one of the two underlying deformation mechanism, namely a global shearing (the other being the classical band-collapse mechanism also observed for stochastic structures). This chapter aims to answer this question and to establish a failure criterion of PCS under compression. Four different types of PCS manufactured in AlSi12 by SLM were tested in compression. Samples were characterized regarding topology, microstructure, defects, mechanical properties and failure mode. In addition to mechanical tests, finite elements analysis were performed with the implementation of bulk material numerical models obtained through a preliminary tensile test campaign on the bulk alloy.

2.2 Material, process, and samples

All the part were additively manufactured by selective laser melting of an AlSi12 aluminum alloy. The reason is based on availability at the subcontractor facilities (Inspire AG, St-Gallen, Switzerland) and the fact that, being one of the first Al alloy printed, it is very well-known in terms of manufacturing and properties. In addition, this choice also eases the procurement of raw material for the cast PCS (see Chapter 3) with the goal of comparing the two processes. This section presents the raw material characteristics (the powder) as well as the parameters used for the build and finally the samples manufactured.

2.2.1 Powder characteristics

The raw material used during this test campaign is a near-eutectic aluminum-silicon alloy of composition shown in Table 2.1 which was atomized into powder. Important parameters for the process, the particle size distribution and the flowability of the powder are assessed using the dynamic flowability measurement method [220], the Table 2.2 summarizes these characteristics.

Table 2.1 – Initial powder material composition (all the numbers are in percentage of mass). SLM-cube sample stand for composition analysis perform in house by the company providing the additive manufactured samples, Inspire AG – innovation center for additive manufacturing (icams), St-Gallen, Switzerland.

Condition	**Al**	**Si**	**Cu**	**Fe**	**Mn**
DIN EN 1706	base	10.5–13.5	0.05	0.5	0.001–0.4
Powder certificate	base	10.5 – 13.5	0-0.05	0-0.55	0-0.35
SLM-cube sample	base	12.3	0.002	0.127	0.002
Condition	**Mg**	**Zn**	**Cr**	**Ni**	**Ti**
DIN EN 1706	0.05	0.1	-	-	0.15
Powder certificate	0-0.05	0-0.10	-	0-0.05	0-0.15
SLM-cube sample	0.0007	<0.001	0.022	0.008	0.006

Table 2.2 – Volume-based analysis (q3) of particle size distribution, and flowability parameters "avalanche angle" and "surface fractal" of the AlSi12 powder

	d10	**d50**	**d90**	**avalanche angle**	**surface fractal**
AlSi12 powder	16.4 µm	37.4 µm	76.4 µm	47.2 ± 4.8°	1.8 ± 0.2

2.2.2 Machine parameters

The SLM machine that was used is a ConceptLaser type M2, equipped with a fiber laser of wavelength 1,070 nm, operated in the continuous mode, with a maximum average power of approx. 190W at the build platform. The beam has a M^2 of < 1.3 and a measured $D4\sigma$-diameter of 90 µm in the focal plane (Gaussian mode). All samples were produced with a nominal laser power of 200W, a slice thickness of 30 µm, and a volume energy density of about 60 J/mm^3. No island scanning strategy was used, which is in contrast to the conventional scanning strategy used with ConceptLaser machines. Therefore, the scanning strategy applied for each layer was to make all the laser tracks parallel. The following layer is rotated by 90° (X and Y directions thus becoming Y and X respectively), keeping in mind that the building direction is along the Z direction. Figure 2.1 shows a schematic view of the scanning strategy during the build. An external perimeter is added to the struts. Manufacturing was performed by Inspire AG.

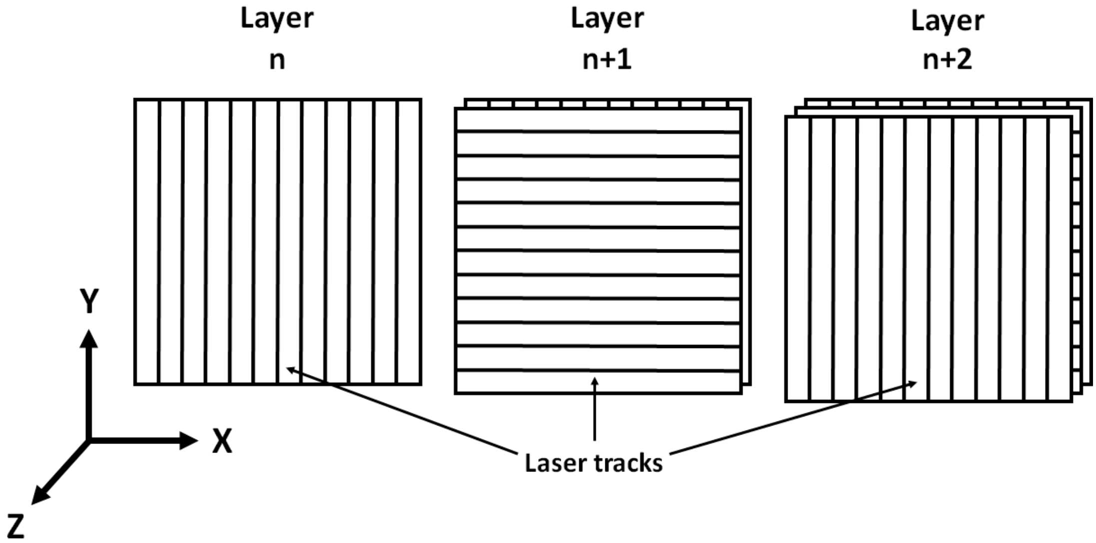

Figure 2.1 – Schematic of the no island strategy with 90° rotation angle in between two successive layers (defined as n, n+1 and n+2).

2.2.3 Samples

Four different structures were chosen and designed for this study namely: (i) the so-called diamond (Di) structure, which is an assembly of octahedrons, (ii) the body-centered cubic (BCC) and (iii) the face-centered cubic (FCC) structures, where as their names imply that nodes are where atoms are situated in those crystal structures, and (iv) the octet-truss (Oct) structure consisting of an octahedron surrounded by 8 tetrahedra. Topology selection was made on crystallographic considerations (for BCC, Di, and FCC) and on interest in literature (for Oct) [180]. Figure 2.2 shows a CAD model of a unit cell for each of these four structures. In order to have a reference for comparison, all the structures were designed to have a 30% relative density, leading to different struts diameter (0.69 mm for Oct, 0.85 mm for FCC, 0.91 mm for BCC and 1.01 mm for Di) with a preliminary cell size fixed to 4 mm side. In order to avoid any side effects, one sample consists of repetition in each direction of 8 preliminary cells [110]. Sizing of the sample was based, on one hand, on the need to avoid side effect (sufficient repetition of unit cells in the three directions, here 8) and, on the other hand, the resolution restrictions imposed by the process itself which are the shortest bridges possible keeping a struts diameter of at least 0.5 mm. Therefore, a trade-off was done and, keeping some margins, it came out the previously defined sample size characteristics. Five samples of each structure were finally manufactured in five different jobs (one job consisting of one sample of each structure, Figure 2.3). It is good to notice that more sample could have been manufactured in one job looking at the available working volume of the machine but the limitation came from the data management of input STL files which tend to be large (several hundreds of Mo) for this specific kind of repetitive structures.

During the manufacturing of the PCS, separate tensile specimens were built for bulk material properties investigations. For each job, tensile samples were built along the three different directions (X,Y,Z), the building direction in the additive layer manufacturing process being the Z-direction. For samples manufactured along the Z-axis, two types of sample were produced, namely a cylinder (60 mm with a diameter of 5 mm) and a directly printed (non-machined) dogbone (with a gauge length of 30 mm and a diameter of 2 mm named Zr hereafter). The dogbone shape couldn't be manufactured directly by SLM for the X and Y directions due to the need for support material for heat extraction and for prevention of warping during the process [11, 13, 17–19, 217]. Therefore, each job contains four different types of tensile sample (X, Y, Z and Zr). Three samples of each type were built leading to 12 tensile specimens for each job for a total of 60 samples. The final dogbone shape of the cylinder samples before testing was produced by post-process machining; unfortunately the same geometry as the Zr sample was impossible to give (samples breaking while manufacturing the gauge), therefore a diameter of 3 mm (instead of 2 mm) was given to the gauge diameter for the same length of 30 mm.

To conclude, four different PCS and four different types of tensile specimen were tested. For each PCS, four samples were tested under the same conditions; for the tensile specimen, at least 9 samples of each type were tested. All the samples (PCS and tensile) of the Job 5 were kept untested and used for metallographic analysis. Table 2.3 summarizes the content of one job.

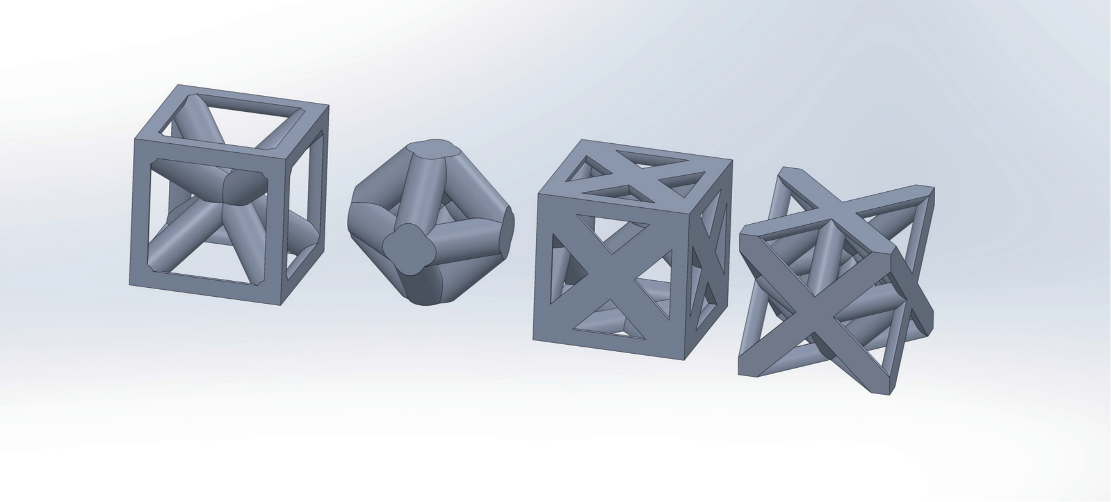

Figure 2.2 – CAD models of the four preliminary cells (from left to right: body-centered cubic, diamond, face-centered cubic and octet truss)

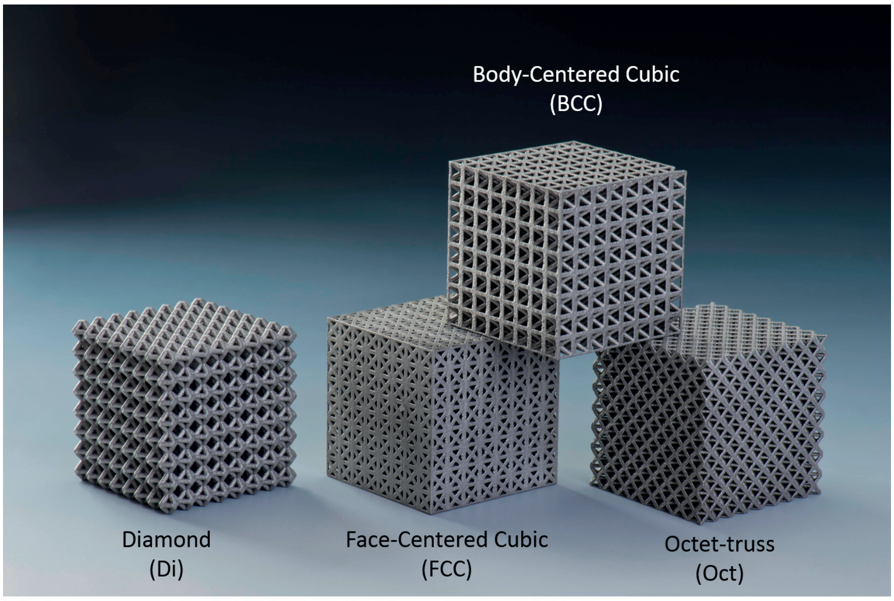

Figure 2.3 – AlSi12 PCS samples produced by SLM (corresponding to one job)

Table 2.3 – Features of each job performed (for a total of 5). Nomenclature column refers to the terminology used in the test

Part	Quantity	Description	Nomenclature
BCC PCS	1	32x32x32 mm3 8x8x8 unit cells 30% relative density	BCC
Diamond PCS	1		Di
FCC PCS	1		FCC
Octet PCS	1		Oct
X Cylinder	3	60x5 mm3 cylinder according X direction	X
Y Cylinder	3	60x5 mm3 cylinder according Y direction	Y
Z Cylinder	3	60x5 mm3 cylinder according Z direction	Z
Z Dogbone	3	60x5 mm3 for the head 30 mm gauge length, 2 mm diameter according the Z direction	Zr

2.3 Experimental method

2.3.1 Metallographic preparation

This section describes the protocol followed to prepare the (PCS and tensile) samples for metallographic and microstructural analysis. The extraction of the region of interest to be investigated was performed by sawing on an Accutom-50 machine manufactured by the Struers Company (Westlake, Ohio, USA). The wheel selected is a 10S15 with a rotation speed of 3500 rpm for a cutting speed of 0.03 mm/s. Once the region of interest had been cut out from the sample, it was embedded into resin for metallographic preparation. The resin used is an Epofix-2 Resin

Table 2.4 – Parameters used for the polishing of specimen

Step	Nap reference	Particle distribution	Time	Load (per sample)	Lubricant
1	MD-Dac	6 µm	6 min	30 N	blue
2	MD-Dac	3 µm	4 min	30 N	red
3	MD-Nap	1 µm	1 min	20 N	red
4	MD-Nap	1/4 µm	1min30s	20 N	red
5	OP-Chem	OP-S	2 min	15 N	none

with its hardener provided by the Struers company. The ratio is 20:3 in volume (20 volumes of resin for 3 volumes of hardener). Once it is immersed in the resin, vacuum cycles were performed on the samples to remove any residual air trapped inside. The cycles consist of spending three times 5 min at 0.2 bar using a CitoVac equipment (Struers). The mix is cured at ambient temperature during 12h. Samples are then processed for grinding by means of a Labopol-25 equipment (Struers). Five different Grit sizes of SiC paper was used (180, 320, 800, 1200, 2000). The grinding starts with the coarsest abrasive nap (180) to finish with the finest one (2000). During each step, all the scratches are made in the same direction, and then the sample is rotated to 90°; each step ends once the scratches from the previous one are removed. Finally, samples are polished. This is done on a Tegra-Pol 35 instrument with an automatic Tegra Force 5 head both manufactured by Struers. Each time decreasing the particle size, the polishing is performed in 5 steps starting from a 6 µm diamond particles distribution to finish with a SiO_2 colloidal suspension. All the steps are performed with a rotation speed of 150 rpm with both the head and the nap spinning in the same direction, all the other parameters are summarized in the Table 2.4 [1]. In between each step, samples were sonicated to remove trapped particles. Once polished, specimens were optionally etched with an HF 1% aqueous solution during 10-15 s.

The microstructure of the bulk material was observed by optical and scanning electron microscopy. Optical microscopy was performed on an inverted Leica DMI 5000 M microscope in bright field (Leica, Wetzlar, Germany). The SEM images were taken on a Teneo Microscope (FEI, Hillsboro, Oregon, United States of America). When samples were to be investigated by SEM, a sputtering of Au-Pd was performed in order to increase the surface conductivity of both the sample and the embedding resin, in order to reduce the charging effect. A conductive path with silver paint and copper tape was made to ground the surface.

2.3.2 3D-Tomography

3D tomography was performed using a Phoenix v|tome|x m300 machine (GE Sensing & Inspection Technologies GmbH) at ESTEC (ESA, Noordwijk, The Netherlands) on selected specimen before testing. This investigation provided information on the porosity and the inclusions introduced by the SLM process. The parameters used for the scans were a voltage of 230 kV, a current of 60 µmA on a molybdenum target with an acquisition time of 1s per frame for a total of 1000 frames over a full rotation of the sample. The voxel size was set to be 30 µm for the

---

[1] All the consumables are manufactured by Struers

PCS and 20 µm for the tensile specimen. No filter was used during scanning. Auto Optimiser and Switch options were turned on during the scans, decreasing the probability of obtaining ring artifacts during specimen reconstruction. The reconstruction of the part based on the X-ray scans was performed using the embedded software Phoenix datos|x reconstruction v.2.1.0 - RTM (GE Sensing & Inspection Technologies GmbH) and further analysis was executed using the VGStudio Max v.2.2.1 software (Volume Graphics, Heidelberg, Germany).

3D tomography allows the characterization of the sample topology and the defects content. Quantification of these defects was performed by the mean of 3D representation of the part in gray levels. The defect analysis is performed based on the use of two gray scale thresholds (in addition of that defining the sample isosurface), the lower threshold defining porosity as all voxels of lower intensity, the upper one giving inclusions for voxels of intensity above its value.

2.3.3 Mechanical properties

Tensile specimen

The machine used to perform the test was produced by Zwick Roell (Ulm, Germany); it is equipped with a load cell of 63kN. The extensometer has a gauge length of 10 mm for samples with a diameter of 2 mm (Zr samples) and a gauge length of 15 mm for samples with a diameter of 3 mm (the rest), in order to keep a constant ratio of 5 between gauge length and sample diameter, so as to be compliant with the standard [221]. The test was strain-controlled with a strain rate of 10^{-3} s^{-1}. The (engineering) strain was computed by dividing the extensometer displacement by the gauge length (15 mm for X,Y,Z samples and 10 mm for Zr samples). The (engineering) stress was computed by dividing the load by the initial tensile sample cross-section. The Young modulus is calculated as the slope of the first linear regime between 30 and 100 MPa. The yield stress is defined as the stress corresponding to 0.2% plastic strain. The ultimate tensile stress (UTS) corresponds to the maximum stress reached before necking or failure. The failure strain, as its name implies, stands for the strain at which the specimen failed. The strain-hardening (Hollomon) exponent and strength coefficient were estimated by plotting the true stress-true strain curves on a log-log scale and fitting a line to the data.

PCS samples

The compression PCS tests were performed on a Zwick/Roell Z100 tensile/compression machine with a load cell of 100kN at ESA facilities. Stainless-steel compression platens were used. Loading (to 5kN) and unloading (free of charge) cycles were performed while tightening the platens to ensure alignment and parallelism. This was repeated until, free of load, platens were not able to move. Compression platens were coated black in order to avoid any disturbing reflections during the test recorded by the stereo-camera set-up (Figure 2.4a). Then, a set of specifically designed stickers was glued on the front faces of both platens as well as on some aluminum plates coated black beforehand and stuck to the platens with double face tape. The aluminum plates are set on the four different corners of the space reserved for the sample and in the same plane as that where the sample front surface should be. Stickers are then put on the nodes (on a fraction or on all of them) of the front sample surface (figure 2.4b). Global and local sample deformation were measured with the stereo-camera set-up, enabling the tracking of the glued markers within a precision of ±5 µm in all three directions. Digital image correlation (DIC) was automatically performed on the Pontos software provided by the GOM company (Braunschweig, Germany). The stickers on the aluminum plates acted as an extensometer. Following the ISO standard on compression of cellular metals [222], the test was performed in a strain-controlled mode with a nominal value of 10^{-3} s^{-1}. Compression was stopped when the load dropped by at least 50% of the maximal load in between two successive data points. For 12 samples, the tests were performed with the inclusion of periodic loading and unloading cycles, conducted in order to measure the evolution of the compressive modulus with increasing plastic strain [42, 111]. For the last of each series of four samples, the test was conducted under monotonic loading. The initial compressive modulus was computed as the slope of the initial linear regime of deformation in monotonic loading. The yield stress was calculated as the stress at 0.2% of plastic deformation, while the maximal stress was obtained at the peak of the stress-strain curve. The failure strain was taken at the end-point of the stress-strain curves. The absorbed energy was calculated by integration of the stress-strain curve. The energy absorption efficiency is defined as the ratio between the measured and the ideal energies, the latter estimated by multiplying the maximal stress with the failure strain. To obtain an estimation of the compressive modulus free of misalignment effects or microplasticity (localized plasticity occurring during the initial linear deformation regime) [42, 111], Young's modulus values measured during successive unloading/reloading cycles were extrapolated to zero strain by fitting data points using a power law model, $E(\epsilon) = E_0 + A\epsilon^n$ where E_0 is the extrapolated uniaxial (Young's) compressive modulus and ϵ is the strain. A and n are parameters computed by quadratic least square regression to fit the data using dedicated built-in Matlab module.

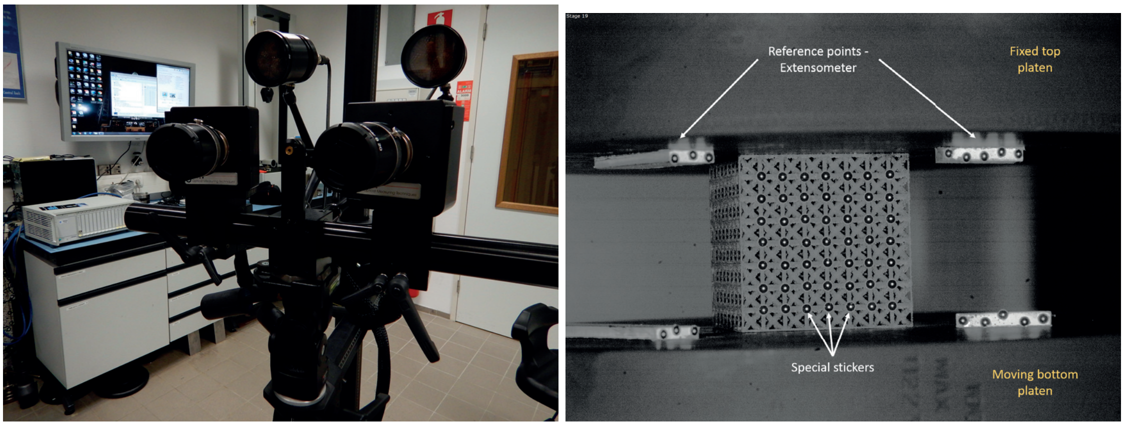

(a) (b)

Figure 2.4 – (a) Stereo-camera set-up for test recording and DIC, (b) Platens, sample and markers configuration for DIC

2.4 Results

2.4.1 Tensile specimens

Microstructure

As expected from the literature review [6, 26, 27], melt-pools (corresponding to laser tracks) can be observed in the tensile specimen. Figure 2.5 shows the microstructure of samples after etching for the four different types of samples (X, Y, Z, and Zr). Light areas correspond to a coarser microstructure, highlighting (but not necessarily defining) the border between two laser tracks. Orange regions correspond to finer structures and show the interior of melt-pools. Differences in color intensity between two different samples come from the etching and slightly different optical microscope parameters and are not necessarily related to differences in microstructure. No clear difference can be seen in terms of microstructure between X and Y directions or between Z and Zr directions

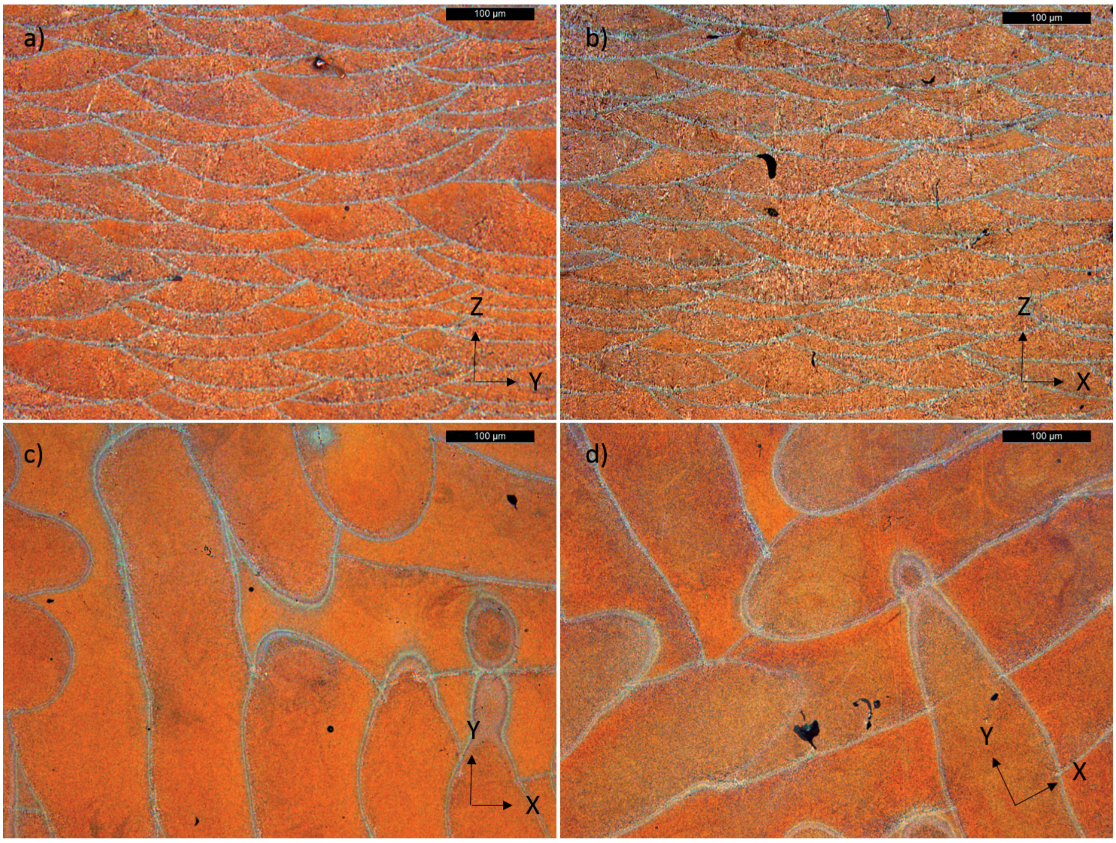

Figure 2.5 – Microstructure for the four different types of sample: a) X, b) Y, c) Z and d) Zr. Axis represent the direction in-the plane, Z being the building direction. The scale bar corresponds to 100 µm

Scanning electron imaging was performed on the specimen to examine in more details the microstructures. Figure 2.7 shows the border region of a tensile specimen that was built along the X and the Z direction. The microstructure consists of primary aluminum cells surrounded by a network of fibrous eutectic. In both cases, three distinct regions can be highlighted (in agreement with the literature [33]):

- Melt-pool cores with fine cellular structure (MP)
- Coarse cellular structure at the border (CR)
- Heat affected zone composed of globular eutectic particles (HAZ)

EDX was performed on the microstructure to analyze the composition of the network and reveals, as expected [31, 32], that silicon is mainly present in these regions (Fig. 2.8)

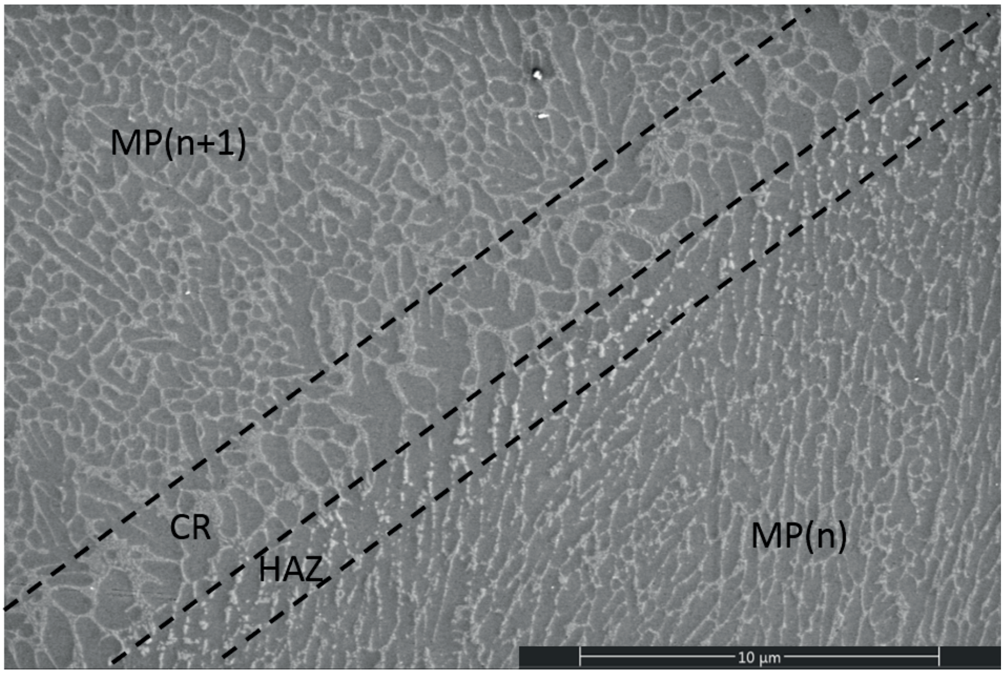

Figure 2.6 – SEM images of tensile specimen according the X direction. MP(n) stands for melt pool number n, CR for coarser regions and HAZ for heat affecting zones.

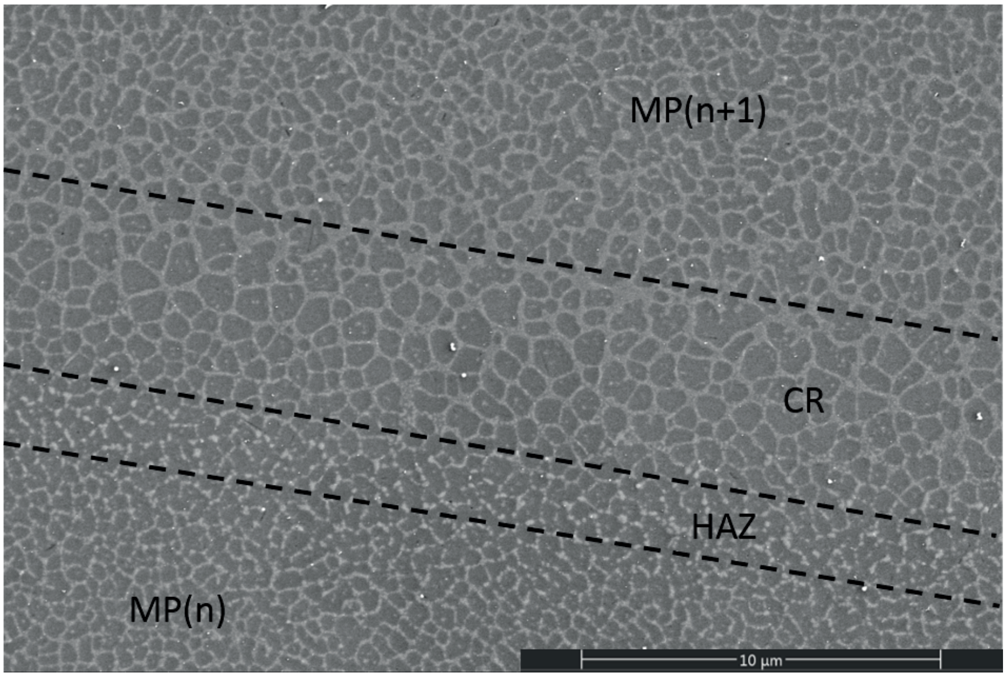

Figure 2.7 – SEM images of tensile specimen according the Z direction. MP(n) stands for melt pool number n, CR for coarser regions and HAZ for heat affecting zones.

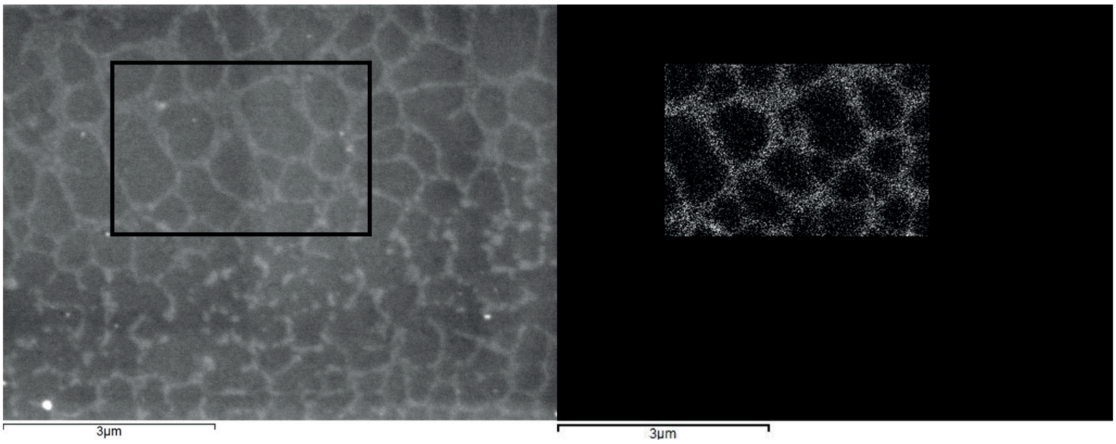

Figure 2.8 – EDX analysis of the microstructure. SEM images of the region of interest, close to a melt pool border (left). Silicon sprectrum of the selected area represented by the black rectangle (right)

Defects

Additive manufactured metals including aluminum can present different manufacturing defects which can be classified into two categories of porosity, namely (i) gas-induced defects (gas porosity [20]) and (ii) process-induced pores (keyhole/lack of fusion [21–23]). An example of each of these two defects can be seen in Figures 2.9 a) and b). Figure 2.9 c) shows an inclusion that is present within the material; its iron-based character was verified by EDX on an area shown by the white rectangle. Finally, Fig. 2.9 d) reveals the presence of oxide supported by the difference in oxygen contents shown in the two spectra (already reported in literature [25]). Contents of porosity and inclusions were automatically estimated with 3D-tomography. It has to be kept in mind that the resolution being 40 µm, the contents of defects could have been underestimated by lack of detection of small defects. Figure 2.10 shows on example of the output of a CT-scan; defects are highlighted and differences in gray level can be observed. The analysis was performed on two different samples per type per job. The CT-scan was performed before post-machining the X,Y and Z sample into the dogbone shape (starting from a cylinder). The scan focused on the 30 mm which are in the center of each specimen. Only iron-based inclusions could be quantified due to the insufficient density difference between aluminum and aluminum oxide. Table 2.5 shows the results of defect quantification according to the type of sample (X, Y, Z or Zr) or the job in which it was produced. No significant difference can be observed either in terms of sample type or batch number.

Table 2.5 – Porosity and inclusion contents for tensile samples according the type and the job

	Pores		Inclusions	
	[%]	[µm]	[%]	[µm]
X	0.05 ±0.02	130 ±6	0.13 ±0.11	149 ±3
Y	0.04 ±0.01	162 ±22	0.26 ±0.15	160 ±24
Z	0.06 ±0.02	236 ±66	0.34 ±0.29	164 ±29
Zr	0.11 ±0.01	182 ±17	0.47 ±0.22	164 ±10
Job 1	0.06 ±0.03	206 ±77	0.37 ±0.25	176 ±22
Job 2	0.08 ±0.04	169 ±36	0.23 ±0.13	154 ±8
Job 3	0.06 ±0.04	191 ±82	0.39 ±0.34	164 ±27
Job 4	0.06 ±0.03	160 ±24	0.35 ±0.26	153 ±14
Total	0.06 ±0.03	173 ±49	0.29 ±0.21	158 ±18

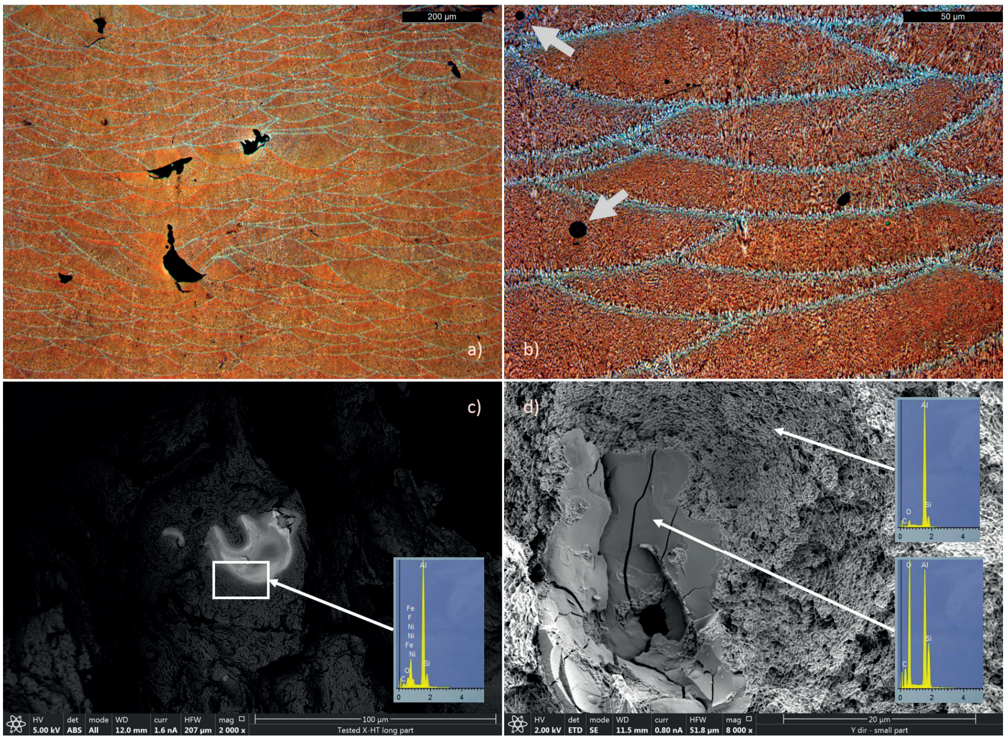

Figure 2.9 – Micrograph of additive manufactured AlSi12 by SLM. a) Examples of process-induced defects (keyhole/lack of fusion) with a x100 magnification. b) Examples of gas-induced defects (showed by arrows) with a x500 magnification. The building direction is going from the bottom to the top of the images. c) Example of Iron-based inclusion associated with the map spectrum revealing the composition. d) Example of oxide inclusion with the two points spectrum showing the difference in oxygen contents.

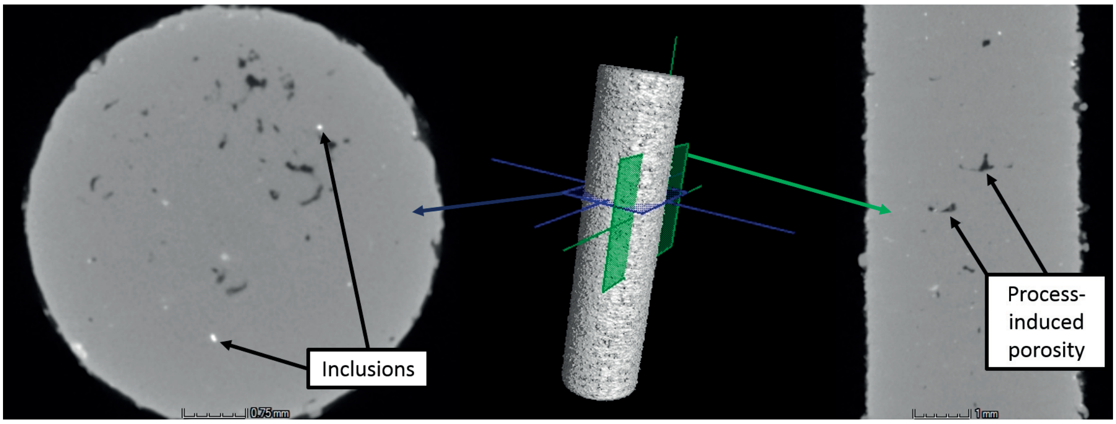

Figure 2.10 – 3D CT-scan of a Z tensile sample before machining of its gauge section. 3D volume situated at the center and the two different cut planes (blue and green) associated to their respective orientation on left and right. Inclusions appear in bright spots whereas porosity is black.

Mechanical properties

Figure 2.11 shows the tensile stress-strain curves for all the different sample types and directions tested. Table 2.6 summarizes the mechanical properties extracted from the test campaign; nominal properties of cast AlSi12 are added for comparison. As expected [34], SLM introduced anisotropy in the mechanical properties, induced by the presence of the mesoscale melt-pools feature. A difference between the two different samples built in the Z direction can be noticed, especially looking at the dispersion of the specimens.

Table 2.6 – Tensile properties of 3D-printed AlSi12 manufactured by SLM compared with cast bulk alloy properties found in literature. The variation (±) corresponds to the standard deviation with at least 9 samples tested for each sample types.

	Young's Modulus **[GPa]**	Yield Stress 0.2% **[MPa]**	Ultimate Tensile Stress **[MPa]**	Failure strain **[%]**	Strain-hardening exponent **[]**	Strength coefficient **[MPa]**
X	69 ±1	300 ±10	411 ±23	3.5 ±0.8	0.19 ±0.01	789 ±14
Y	71 ±5	305 ±9	424 ±28	4.1 ±1.0	0.19 ±0.01	788 ±12
Z	69 ±3	266 ±2	397 ±28	2.9 ±0.8	0.25 ±0.01	972 ±16
Zr	66 ±5	242 ±14	378 ±14	2.8 ±0.6	0.26 ±0.02	955 ±33
Bulk alloy [2]	71	131	290	3.5	-	-

---

[2] Data taken from matweb website under the name Aluminum 413.0-F Die Casting Alloy

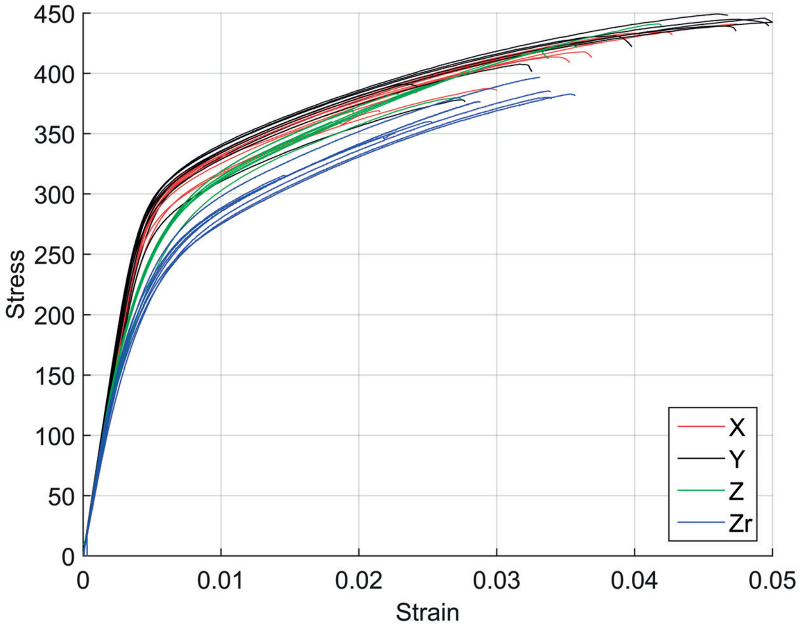

Figure 2.11 – Strain-stress curves of the tensile specimen according the direction X and Y and the two types of samples for the Z direction (Z and Zr specimen)

Fracture surfaces

Optical and SEM images were taken to investigate the fracture surfaces of broken AlSi12 alloy tensile specimen produced by SLM. Figure 2.12 shows the main difference between samples manufactured along the building direction (Z and Zr) compared to the samples oriented orthogonal to it (X and Y). X and Y samples broke with a fracture surface at an angle between 30 and 40° with the loading direction, whereas Z and Zr samples mostly break with a fracture surface normal to the sample axis. Higher magnification (Figure 2.12 e)) shows that fracture occurred between two melt-pools for vertically oriented samples (Z and Zr), confirmed by scanning electron images as shown in Figure 2.13 (consistent with the observation made by Rosenthal and al. [40]). The latter figure also shows magnifications of previously described defects. For the sake of readability, two different defects are shown on the X (and Y) orientations (process-induced porosity and iron-base inclusions) whereas two other types of defects are highlighted on Z (and Zr) samples. Nevertheless, it has to be kept in mind that all of these defects were present in all the samples regardless the orientation. Investigation of secondary fracture of Z and Zr specimens showed that crack tends to preferentially propagate in the HAZ, avoiding the eutectic particles which do not form a fibrous network anymore in this specific region (Figure 2.14).

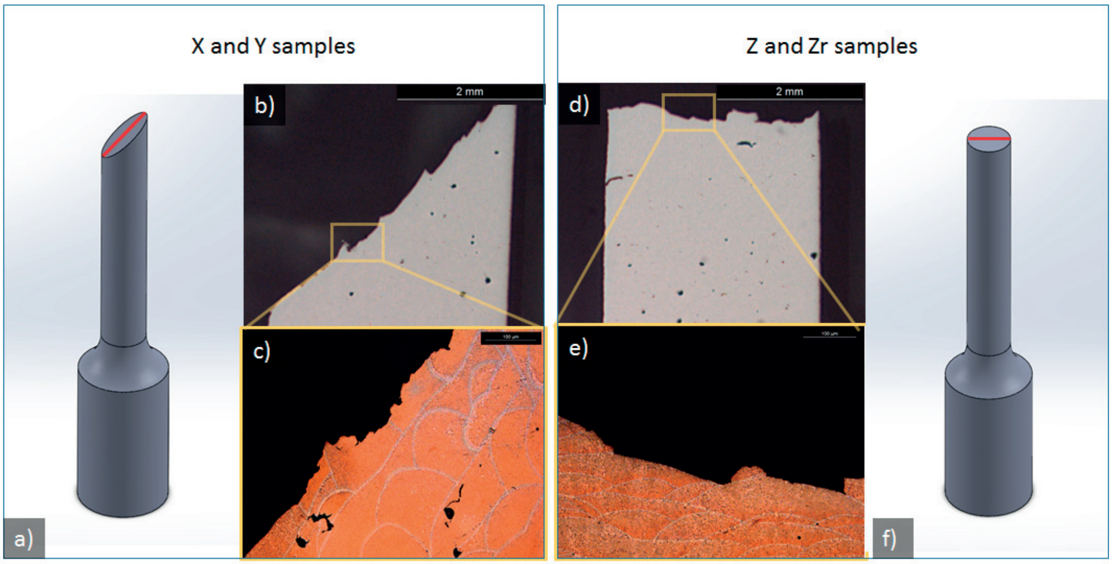

Figure 2.12 – Sketch views of the investigated cross-sections in red for X/Y and Z/Zr samples (a) and f) respectively). Optical microscopy of fracture surfaces at low magnification (b) and d)) and at higher magnification highlighting the melt-pools feature (c) and e)).

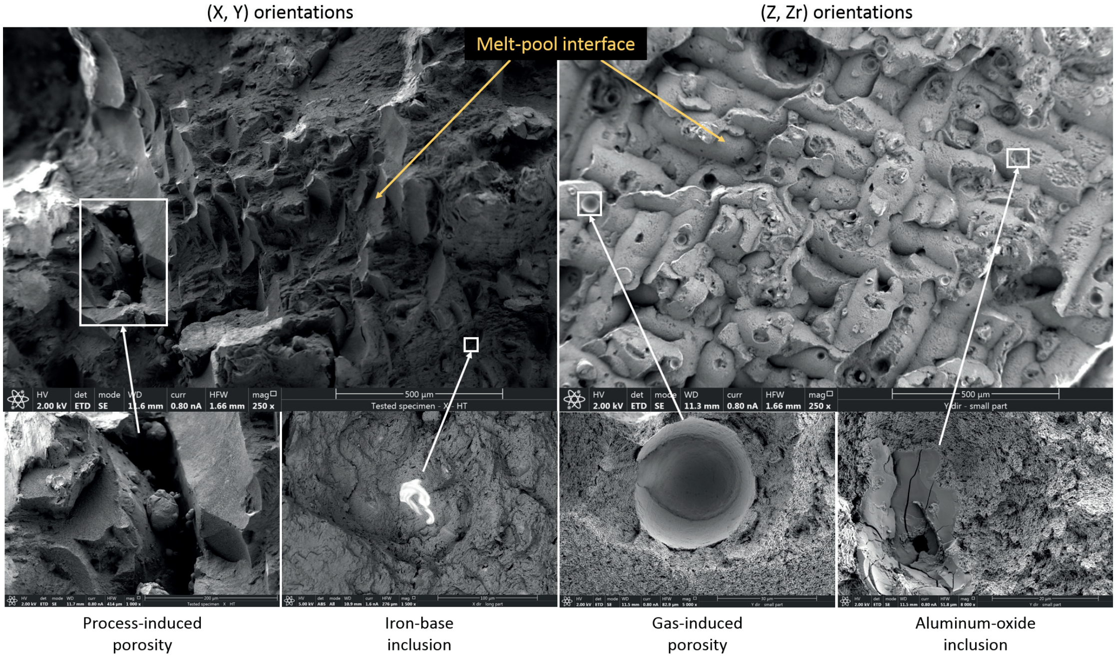

Figure 2.13 – Fracture surfaces, SEM imaging, of additive manufactured AlSi12 tensile specimen according the X (and Y) orientations (top left) and Z (and Zr) orientations (top right). Evidence of inter-melt-pools fracture is highlighted. Bottom rows shows an example of the four main types of defects present in this kind of part. From left to right: process-induced porosity (keyhole/lack of fusion), iron-base inclusion, gas-induced porosity, and aluminum oxide inclusion.

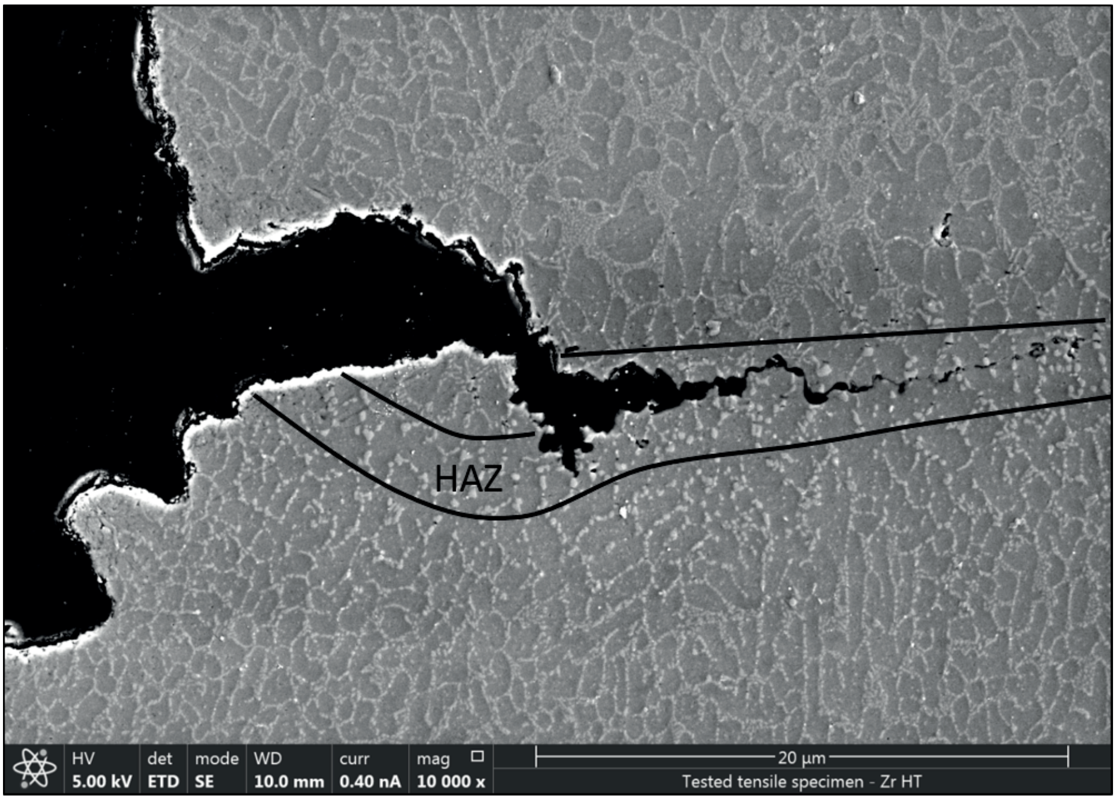

Figure 2.14 – SEM pictures of Z (and Zr) samples after tensile failure viewed from above (left) exhibiting dimples and from the side (right), which shows the preferential crack growth path inside the HAZ.

2.4.2 PCS

Microstructure

Being build at the same time as previously described tensile specimens, the microstructure of the metal within the PCS is expected to be similar to that found in tensile samples, with the presence of melt-pool borders, process- and gas-induced defects, inclusions, and alumina. One finds indeed that the microstructure is again composed of primary aluminum cells surrounded by fibrous eutectic of the same scale. Nevertheless, two noticeable differences can be observed. The first consists in the orientation of the scale-like shape of the melt-pool borders; while it was strictly defined by the building direction for the tensile specimens, in the PCS, the lower outer layers of overhang struts appeared to be aligned along the strut axis and not along the vertical direction. Figure 2.15a shows the optical microstructure of struts belonging to the Diamond structure, aligned with a [110] direction. The second difference comes from the fact that horizontal struts trap extra powder underneath by sintering. The sintered powder can be recognized by still having the microstructure produced by the atomization process, which is coarser than that present in additively manufactured alloy and appears in white. It can be noticed that sintered powder seems to concentrate a high fraction of gas porosity. Figure 2.15b shows the powder sintered under the horizontal struts of BCC structures. The difference in heat conduction between solid metal and powder layer explained the misaligned first layer and the sintered powder [217].

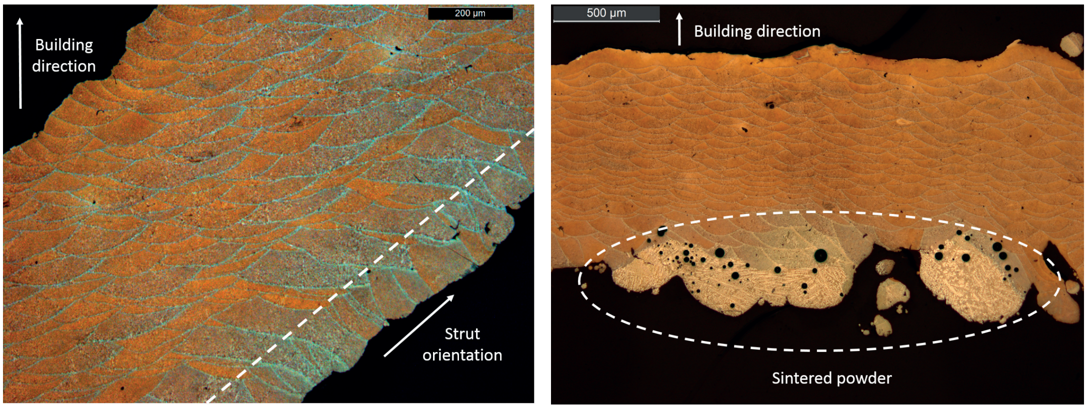

(a) (b)

Figure 2.15 – a) Misalignment of the lower outer layer of overhang strut in Di structures along the [110] direction. b) Sintered powder under a BCC horizontal strut containing a high fraction of porosity

Defects

After the additive manufacturing process, the same defects as found in the bulk material were observed in PCS. The quantification method is therefore the same as that used before, based on 3D-tomography. Except for the PCS presenting an additional source of inclusions with a bigger size, in the range of a millimeter and coming from the sandblasting post-process (hard-steel pellets are used to smoothen the sample surface). Some of these pellets were trapped after plastically deforming the struts. The scan was performed on the entire sample volume on all 16 samples (job 5 excluded). The space between struts was not counted as porosity as the algorithm looks only for closed porosity. The separation of inclusions coming from sandblasting or from powder contamination is done by measuring their diameters. Since a clear gap (from 0.4 mm to 0.6 mm) is present on the inclusion distributions, the limit was set at 0.5 mm. Table 2.7 summarizes the output of the defect analysis. Concerning the porosity, there is no noticeable difference between different structures or jobs except for the FCC structures, which tend to have slightly more porosity. Regarding inclusions, FCC structures also tend to trap more sandblasting pellets, whereas no clear difference can be noticed regarding powder contamination.

Table 2.7 – Average porosity and inclusions contents according structure and job. Uncertainty represents the standard deviation.

	Pores		Sand-blasting inclusions		Powder contamination	
	[%]	[µm]	[%]	[µm]	[%]	[µm]
BCC	0.05 ±0.02	130 ±6	0.01 ±0.01	766 ±232	0.13 ±0.11	149 ±3
Di	0.04 ±0.01	162 ±22	0.02 ±0.005	871 ±139	0.26 ±0.15	160 ±24
FCC	0.11 ±0.02	236 ±66	0.22 ±0.3	861 ±66	0.34 ±0.29	164 ±29
Oct	0.06 ±0.01	182 ±17	0.03 ±0.01	767 ±103	0.47 ±0.22	164 ±10
Job 1	0.06 ±0.03	206 ±77	0.15 ±0.28	732 ±179	0.37 ±0.25	176 ±22
Job 2	0.08 ±0.04	169 ±36	0.03 ±0.04	796 ±102	0.23 ±0.13	154 ±8
Job 3	0.06 ±0.04	191 ±82	0.15 ±0.28	886 ±162	0.39 ±0.34	164 ±27
Job 4	0.06 ±0.03	160 ±24	0.02 ±0.005	836 ±147	0.35 ±0.26	153 ±14
Total	0.06 ±0.03	173 ±49	0.06 ±0.15	817 ±148	0.29 ±0.21	158 ±18

Mechanical properties

During this test campaign, a total of 16 PCS samples were tested in quasi-static compression, four samples per type of structure. For each test, the load-displacement data were recorded; the load is measured by the load cell, and the displacement deduced from the markers glued on auxiliary aluminum plates, themselves fixed on the compression platens. From the raw data, stress-strain curves were extracted, as shown in Figure 2.16. For three samples per type, compression was performed with the inclusion of periodic unloading/loading cycle. This allows the possibility to estimate the compressive modulus evolution with plastic strain. Figure 2.17 shows the results of this study and plots also the fitting models extracted from it (see Section 2.3.3). Table 2.8 summarizes the mechanical properties obtained from the compression tests.

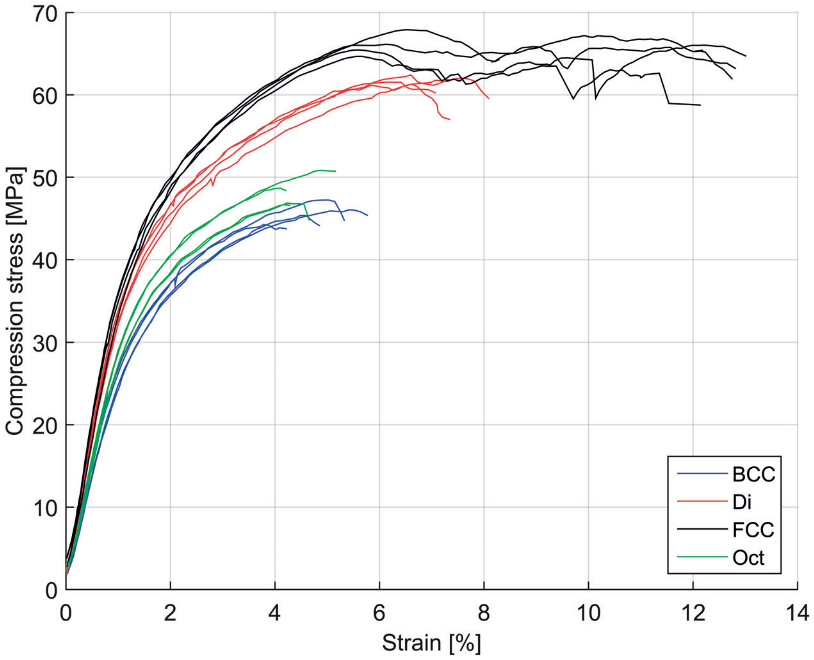

Figure 2.16 – Stress-strain curves of quasi-static compression tests performed on PCS built by additive manufacturing (SLM) of AlSi12 alloy

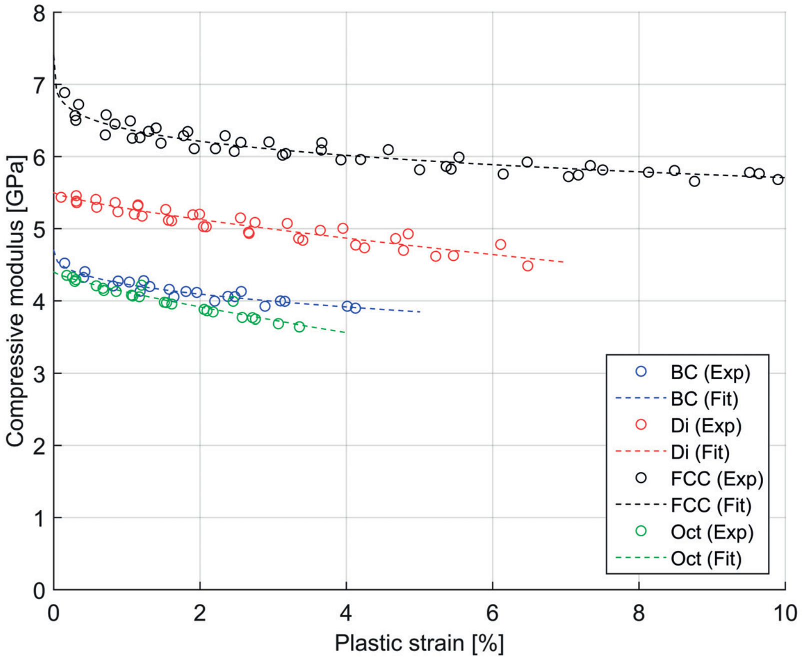

Figure 2.17 – Evolution of the compressive modulus with plastic strain for different types of PCS. Dashed lines represent fits to the experimental data (defined in Section 2.3.3)

Table 2.8 – Average mechanical properties of PCS. Uncertainty represents the standard deviation.

		BCC	Di	FCC	Oct
Relative density	**[%]**	30.6 ± 0.2	29.8 ± 0.2	32.2 ± 1.2	30.8 ± 0.4
Compressive modulus	**[GPa]**	2.9 ± 0.2	3.8 ± 0.1	4.0 ± 0.3	3.0 ± 0.1
Extrap compressive modulus	**[GPa]**	4.7 ± 0.3	5.5 ± 0.4	7.4 ± 0.4	4.4 ± 0.2
Yield stress 0.2%	**[MPa]**	28 ± 1	36 ± 1	38 ± 1	32 ± 1
Maximal stress	**[MPa]**	46 ± 2	62 ± 1	66 ± 1	48 ± 2
Failure strain	**[%]**	5.0 ± 0.7	7.5 ± 0.4	12.7 ± 0.4	4.6 ± 0.4
Absorbed energy	**[J/cm3]**	1.8 ± 0.3	3.7 ± 0.2	7.3 ± 0.3	1.7 ± 0.2
Energy absorption efficiency	**[%]**	76 ± 1	80 ± 1	87 ± 1	75 ± 1
Hollomon exponent	**[ ]**	0.35 ± 0.01	0.29 ± 0.01	0.32 ± 0.02	0.32 ± 0.01

Failure mode

DIC allows the tracking of specific markers glued on the sample front face during the compression tests, with a precision of ± 5 µm. The failure mode was then characterized for the different types of PCS. The same pattern was observed independently of the structure, namely a homogeneous global deformation until the last few percents of deformation, where upon failure occurred by shearing in between two planes. The difference between the structures is in the angle characterizing this shear planes. Figure 2.18 to 2.21 show the stress-strain curves with corresponding images recorded during the tests.

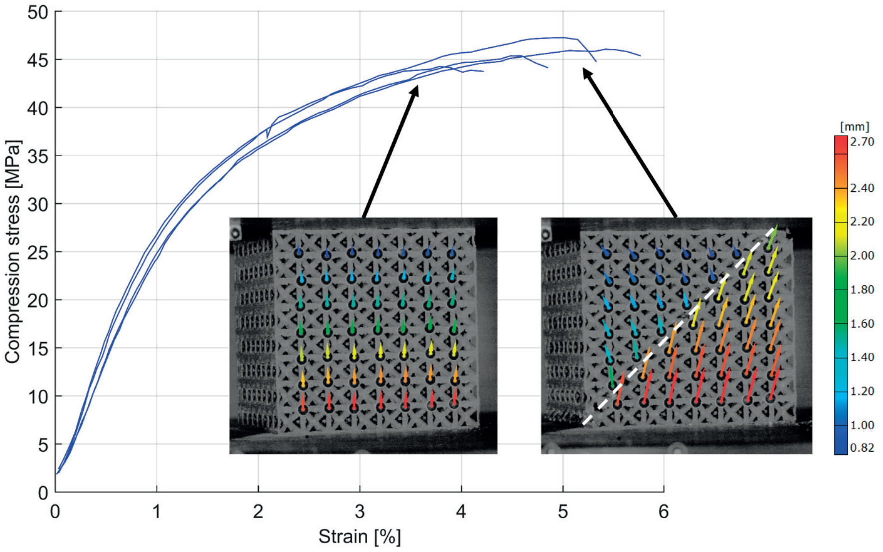

Figure 2.18 – Stress-strain curves of BCC samples with image extracted from DIC analysis before failure (left image) showing homogeneous deformation and after failure (right image) highlighting the shear failure mode. Reference plane is the top sample surface.

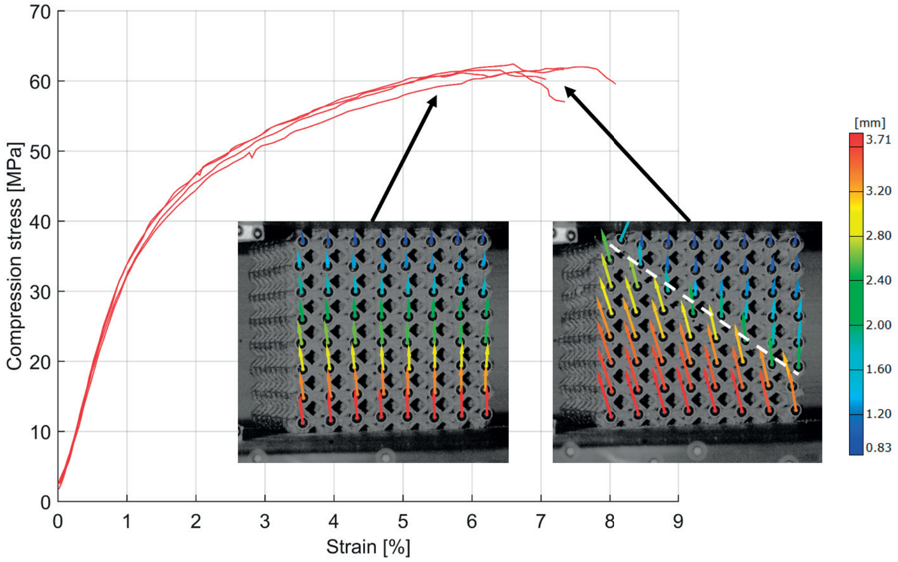

Figure 2.19 – Stress-strain curves of Di samples with image extracted from DIC analysis before failure (left image) showing homogeneous deformation and after failure (right image) highlighting the shear failure mode. Reference plane is the top sample surface.

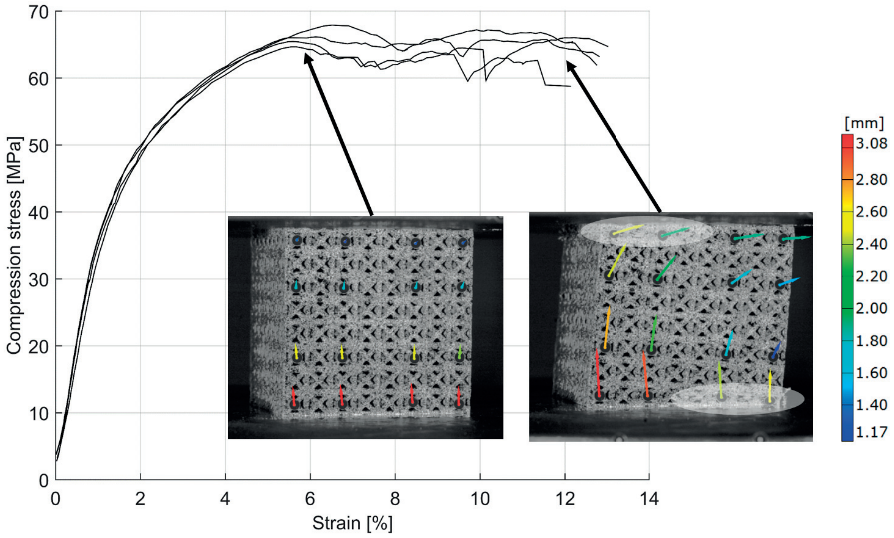

Figure 2.20 – Stress-strain curves of FCC samples with image extracted from DIC analysis before failure (left image) showing homogeneous deformation and after failure (right image) highlighting the shear failure mode. Reference plane is the top sample surface.

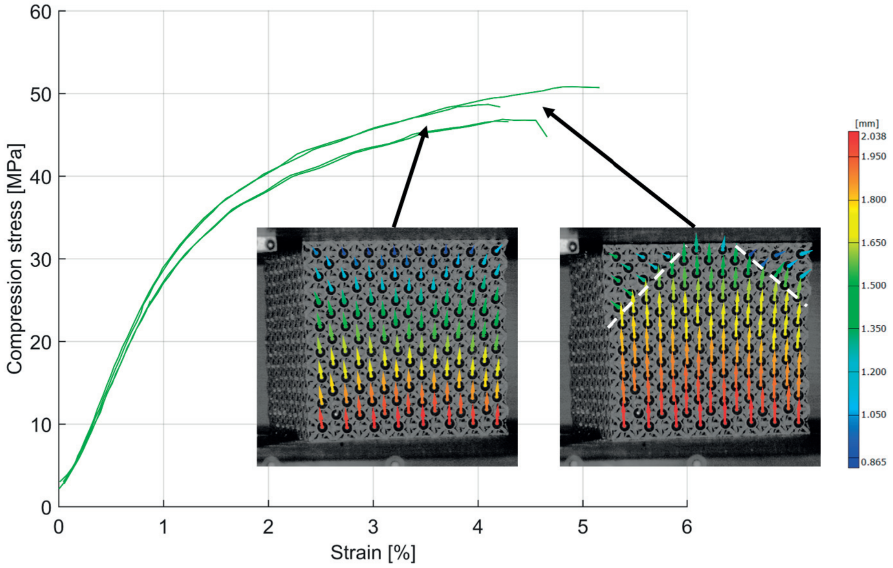

Figure 2.21 – Stress-strain curves of Oct samples with image extracted from DIC analysis before failure (left image) showing homogeneous deformation and after failure (right image) highlighting the shear failure mode. Reference plane is the top sample surface.

An analogy with crystallographic planes was made to characterize the shear planes leading to failure, which appeared to be straightforward for three out of the four different PCS types. For BCC samples, all samples failed with an angle of 45° characteristic of the $\{110\}$ plane family (also observed in literature [13, 181]). FCC samples failed by rotation of the core induced by the collapse of two horizontal half-planes, belonging to the $\{100\}$ plane family. Oct structures failed according to several planes all belonging to the $\{111\}$ plane family (consistent with the observation of Liu and al. [171]).

At first glance, Di samples seemed to fail according to a less well-defined planar surface. Further investigations were then performed to characterize the shear surface better. The cells involved in the failure were recorded on 3D-tomography cut views, one for each cell layer. On each 2D views, a combination of two different collapse orientations was, either horizontal or with a 45° angle as shown in Figure 2.22. The recorded failure surface was then analyzed using the dedicated built-in Matlab module. It is concluded that the shearing occurred in a combination of different planes orientations, which appeared to be the $\{111\}$ plane family (roughly 60% of the surface), $\{100\}$ (roughly 30% of the surface), and the rest being either the $\{110\}$ plane family or more exotic orientations. Figure 2.23 shows an example of the surface discretization performed in Matlab and the resulting outcome with the different plane orientations associated with the surface. Finally, typical failure modes for the different PCS are summarized in Figure 2.24 with pictures of the corresponding failed sample.

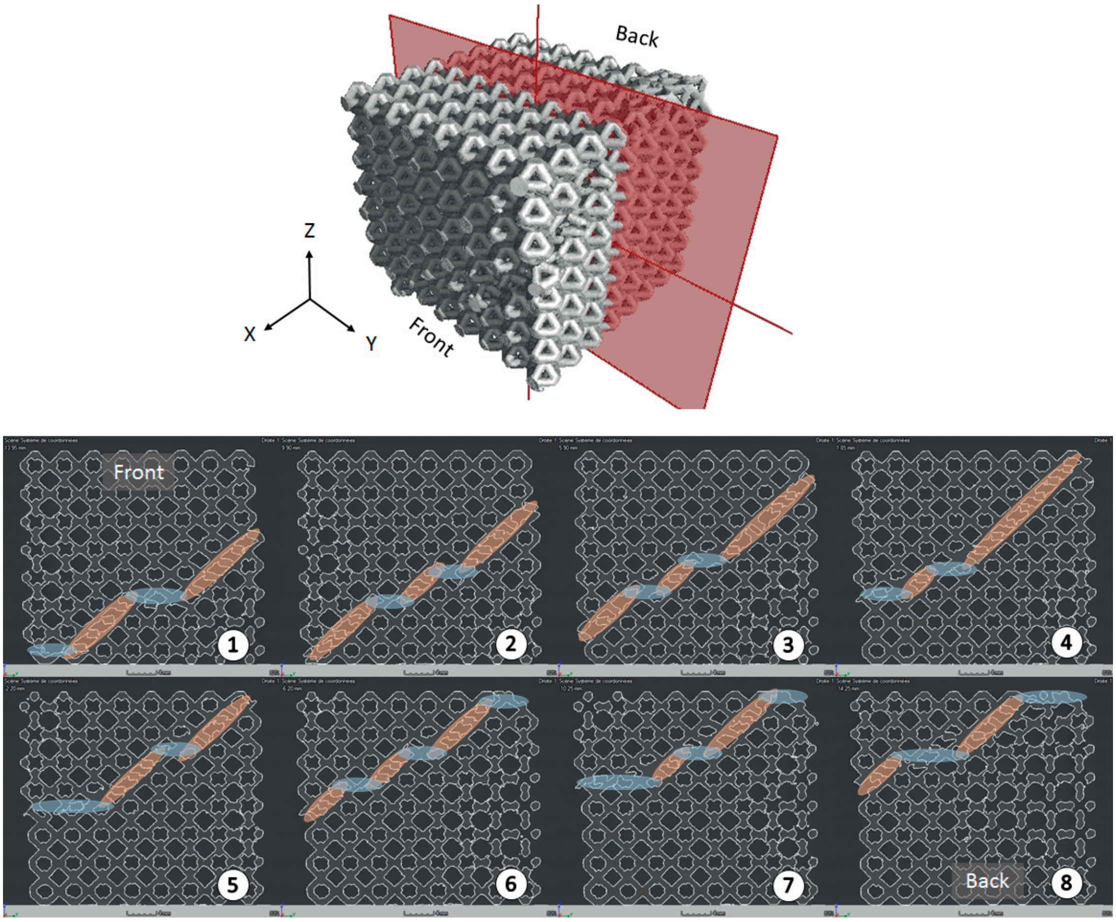

Figure 2.22 – CT-scans cutaway views of a Di sample performed with a horizontal sweep from front to back. Red plane shows an example of cross-section performed. Numbers represent the cell layer investigated from 1 (front) to 8 (back). Fracture is highlighted in transparent red (45°) and blue (horizontal)

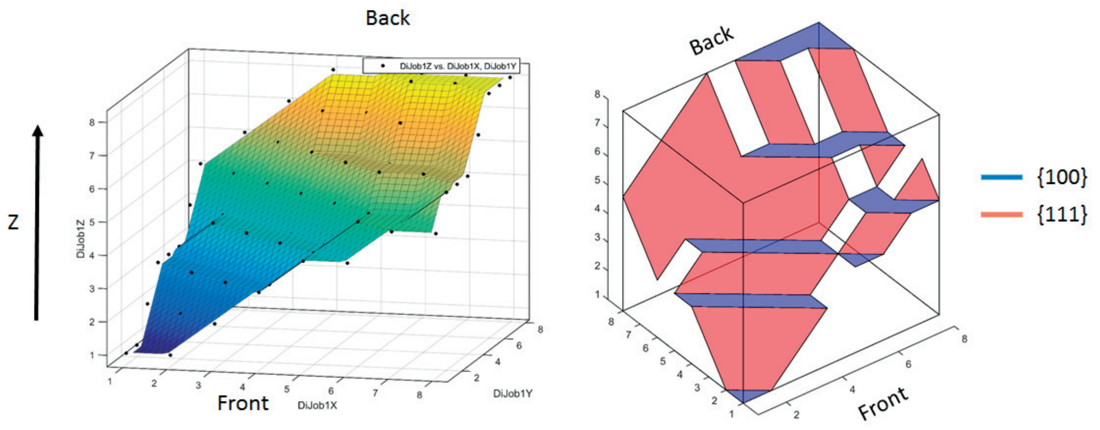

Figure 2.23 – Fracture surface discretization in Matlab (left) and the resulting associated plane orientations (left)

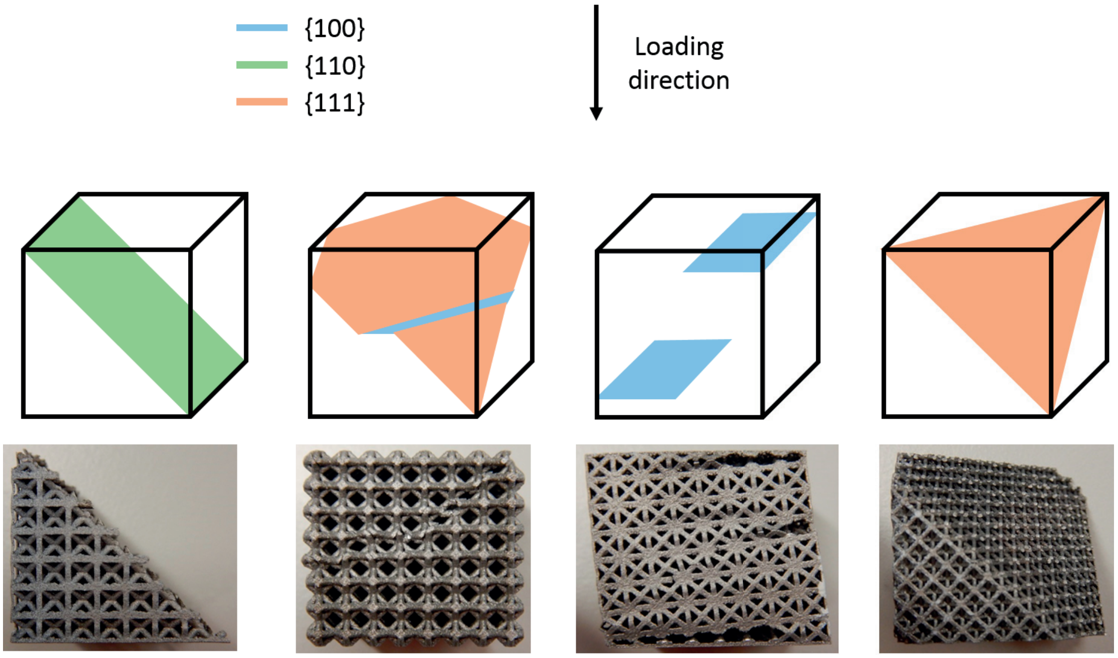

BCC Di FCC Oct

Figure 2.24 – Typical failure modes of PCS with a corresponding pictures of failed samples. Color code highlight the associated crystallographic plane orientations

Fracture surface

For almost all samples, fracture surfaces could not be observed as the sample was not split into two or more separate parts. Nevertheless, some BCC and Oct samples failed this way allowing for fracture surface observation. Post-mortem samples pictures (Figure 2.25) show that failure occurred at the junction between struts and nodes. SEM imaging (Figure 2.26) shows evidence of failure by bending, resulting in two distinct regions on the strut fracture surface. One corresponds to compressive friction leading to the smearing of the surface, and the other shows failure in tension. For the latter, the exact same characteristics are present compared to the tensile specimens, meaning failure preferentially along the melt-pool border with the presence of porosity (gas and process induced), alumina and steel inclusions.

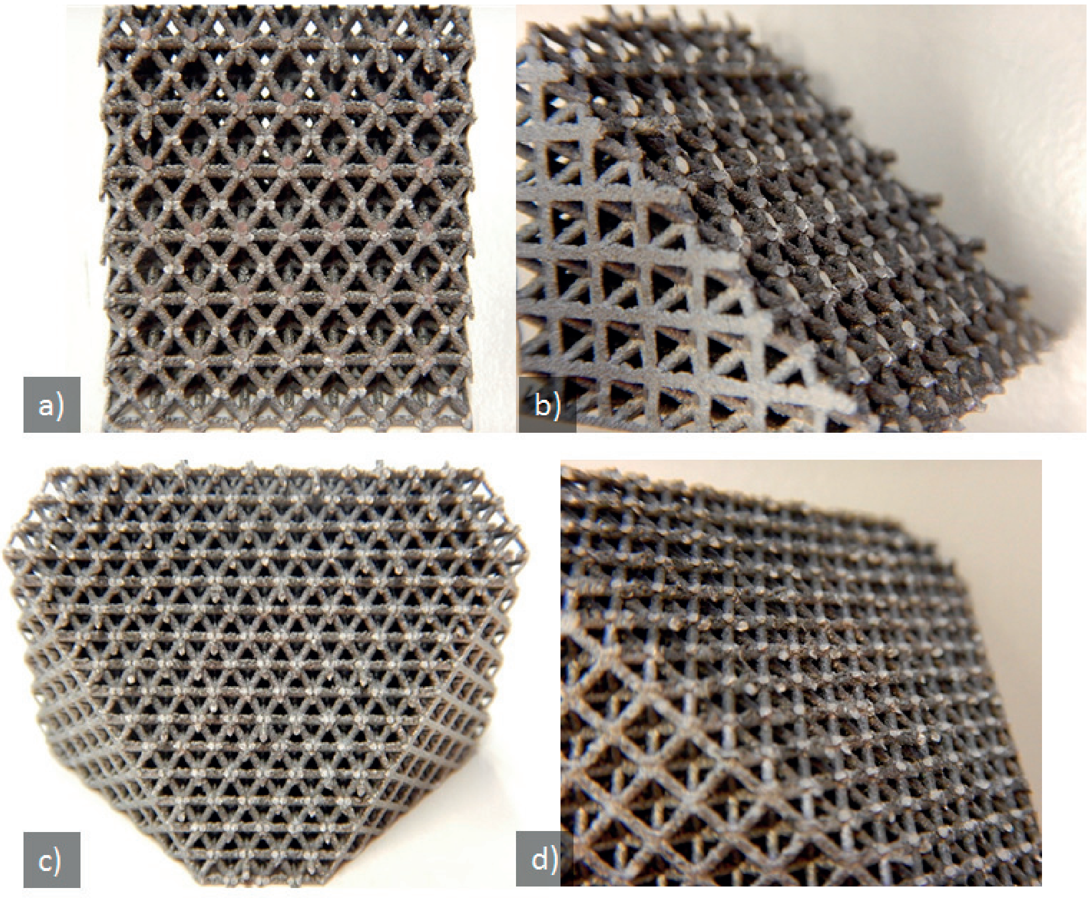

Figure 2.25 – Fracture surface photos of a BCC sample (a) and b)) and an Oct sample (c) and d))

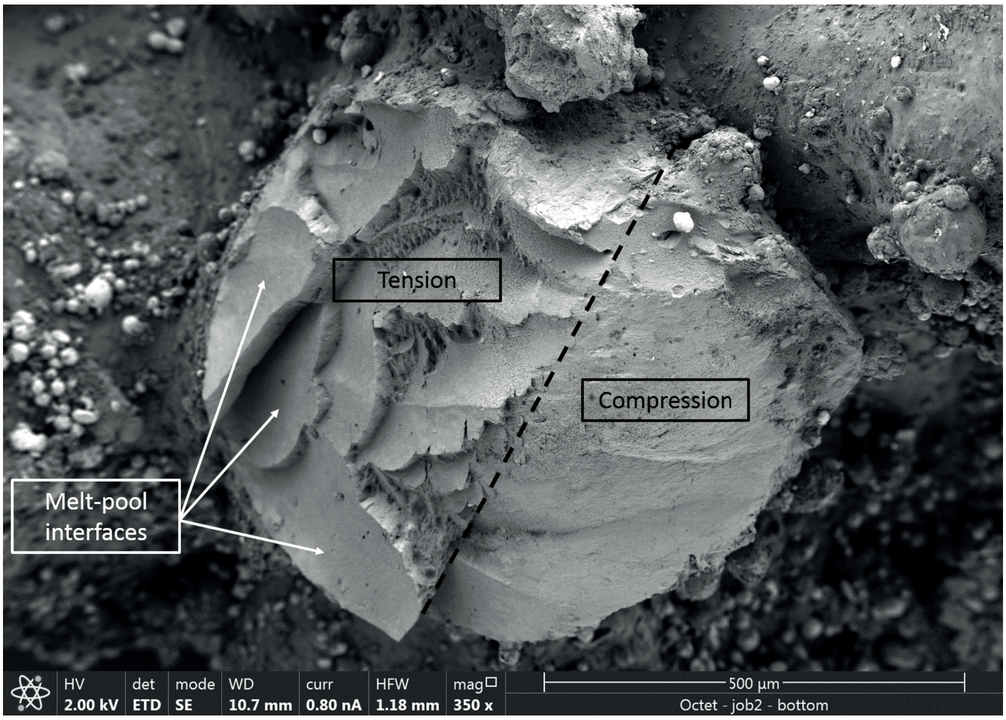

Figure 2.26 – Fracture surface of a broken strut in an Oct sample. Dashed black line shows the limit between the two different modes of failure, namely compression and tension. Melt-pool interfaces can be observed in the tension area (in white)

2.5 Finite element analysis

All the finite element simulations were performed on the ABAQUS 6.14-1 software (Dassault systemes, Vélizy-Villacoublay, France) with mesh built in an automatic way.

2.5.1 Numerical models

From the previously extracted mechanical properties of the bulk material in three directions, numerical models were built and used to perform finite element analysis of PCS. The model is based on the combination of an elastic regime represented by the Young modulus E (Equation 2.1) and a plastic regime defined by the Hollomon equation with the two coefficients K and n (Equation 2.2). The two regimes are joined at the intersection defined by Equation 2.3 and 2.4 for the strain and stress respectively.

$$\sigma = E\epsilon \tag{2.1}$$

$$\sigma = K\epsilon^{n} \tag{2.2}$$

$$\epsilon_{int} = (\frac{E}{K})^{\frac{1}{n-1}} \tag{2.3}$$

$$\sigma_{int} = K(\frac{E}{K})^{\frac{n}{n-1}} \tag{2.4}$$

By injecting the strain at which yielding occurs during experiments into the Hollomon equation, the yield stress is given by Equation 2.5. Table 2.9 summarizes the measured and the estimated yield stress for the four different types of samples.

$$\sigma_{y,model} = K(\frac{\sigma_{y,real}}{E} + 0.002)^n \tag{2.5}$$

Table 2.9 – Intersections points and yield stress estimation error for the material models

Direction	ϵ_{int}	σ_{int}	$\sigma_{y,real}$	$\sigma_{y,model}$	$\Delta\sigma_y$
	[%]	[MPa]	[MPa]	[MPa]	[%]
X	0.4	276	300	301	0.5
Y	0.4	280	305	306	0.2
Z	0.4	239	266	272	2.4
Z raw	0.3	215	242	248	2.7

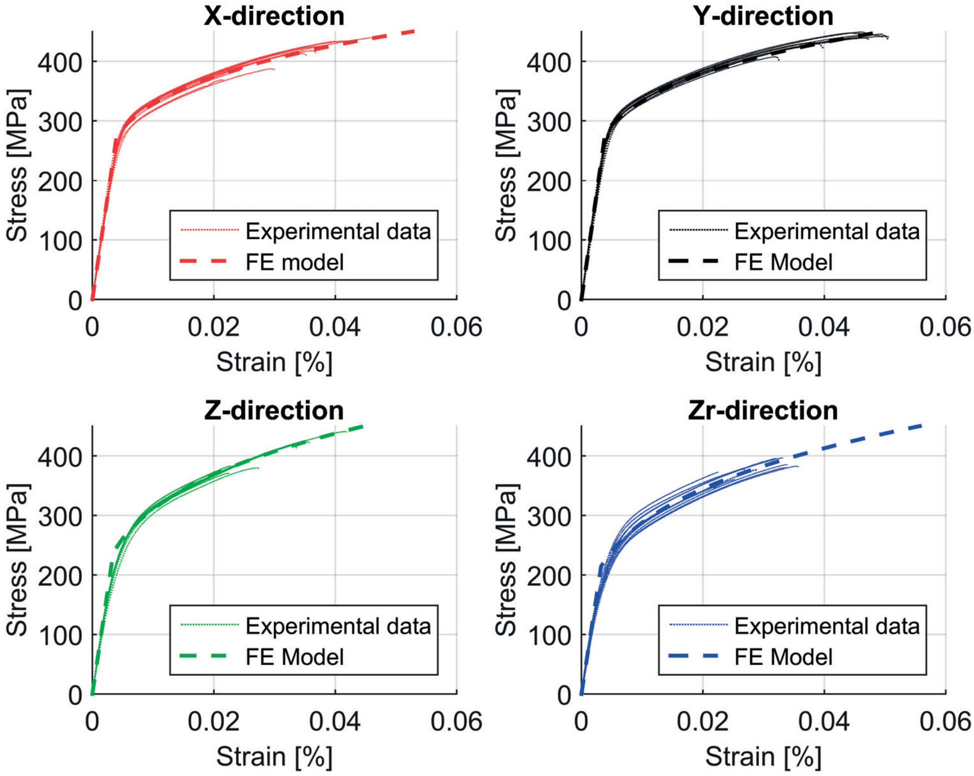

Figure 2.27 – Material models implemented in FE analysis compared to the experimental data for every directions

2.5.2 Mesh convergence

In order to define how many elements across the smallest features are necessary, a mesh convergence analysis was performed. This consists in measuring the influence of the element size on the mechanical properties calculated by the simulation. Only the approximate size of the element was changed, all the other parameters remaining the same. Table 2.10 summarizes the parameters kept constant for the different structures. The maximal number of elements across the smallest features in models varies between each PCS due to the difference in computation time from 6 (BCC, FCC), 7 (Oct) to 8 (Di). Figure 2.28 shows the obtained stress-strain curves from the simulation for the different PCS along the range of element sizes. The calculation was performed on one-eighth of a unit cell using three symmetry plans. The strain was applied to the top face while all other surfaces unconstrained by symmetry remain stress-free. The mesh was automatically built by setting the desired approximate element size.

From the curves, three mechanical properties were extracted, namely the Young modulus, the yield strength, and the final stress defined as the stress once the maximal strain is reached (extracted from experimental data); these values were used to study the convergence of the model. Computation time was also added to the analysis. Figure 2.29 shows the evolution of the four predefined variables for the different structures, varying the number of elements. A trade-off

Table 2.10 – Parameters kept constant for the different structures during the mesh convergence study

	BCC	Di	FCC	Oct
Strut diameter [mm]	0.91	1.01	0.85	0.69
Unit cell size [mm]	4			
Element type	Tetrahedral quadratic (10 nodes)			
Maximal strain imposed [%]	6	9	14	6
Material model	AlSi12 Zraw (see Section 2.5.1)			

was done choosing the number of elements in final computations between mechanical properties accuracy and required computation time. The number of elements was selected close to the intersection between the different curves. The table 2.11 shows the number of elements chosen and the corresponding approximate size (relative to the unit cell size) for each structure.

Table 2.11 – Number of element and approximate element size (relative to strut diameter) for each structure

Structure	**Number of elements**	**Approximate element size**
BCC	3	0.20
Di	5	0.16
FCC	3	0.20
Oct	3	0.28

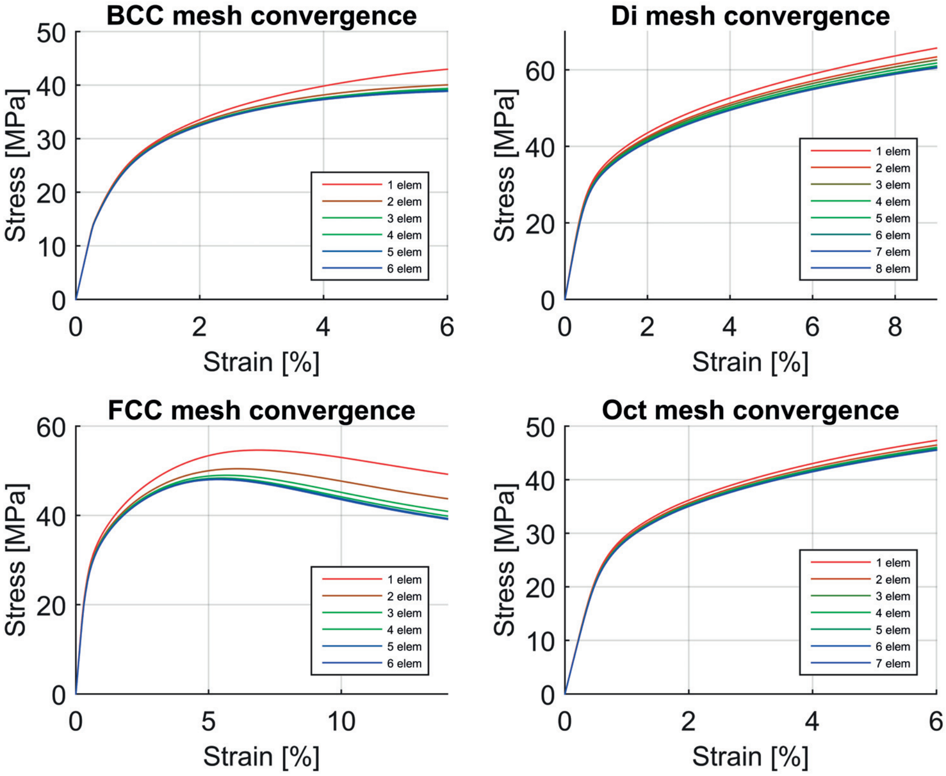

Figure 2.28 – Stress-strain curves for convergence analysis varying the number of elements across the smallest features for the different PCS

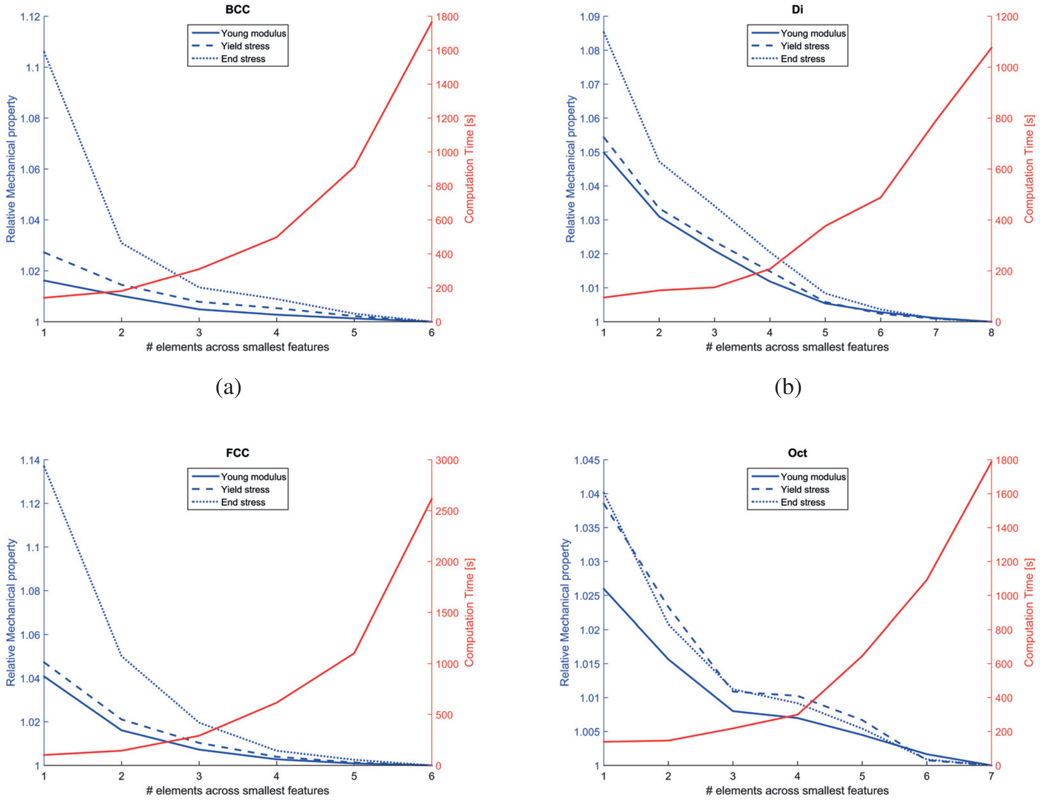

(a) (b)

(c) (d)

Figure 2.29 – Evolutions of the compressive modulus, the yield stress, the maximal stress and the computation time versus the number of elements across the smallest features present in the model for a) BCC, b) Di, c) FCC and d) Oct structures

2.5.3 Size effect

Based on previous studies, hierarchical structures such as metallic foam and more generally cellular materials can exhibit a size effect on certain properties when the sample becomes only a few unit cells wide. It has been shown that such a size effect on mechanical properties of metallic foams can be neglected when the number of cells is higher than 7-8 in all directions [42, 145]. Morrish and al. observed that periodic diamond structures manufactured in Ti6Al4V alloy by electron beam melting exhibited a lower susceptibility to size effect than stochastic foam, with a threshold of 3-4 cells [182], and confirmed by simulations [163]. Simulations were performed to estimate the limit for our specific structures. CAD models of each unit cell were designed, and numerical models of the bulk metal properties (see Section 2.5.1) were associated with the corresponding orientation of the struts. Horizontal struts were associated with X and Y models while vertical struts were matched with Zr model. An intermediate numerical model averaging the X and Zr model was computed to be associated with struts neither horizontal nor vertical. Then, CAD model consisting of a repetition of n unit cells in all three directions were built. Due to computational capacities, the maximal number of repetitions n was set to 6. Parts were then meshed, using the element sizes previously defined and simulations were run, consisting of a monotonic displacement of the upper face equals to the failure strain obtained experimentally (6% for BCC and Oct, 9% for Di and 14% for FCC). The reaction force of the upper face, corresponding to the load which would be required to deform the part, was recorded during the simulation and then the load-displacement curves were extracted, further converted into strain-stress curves.

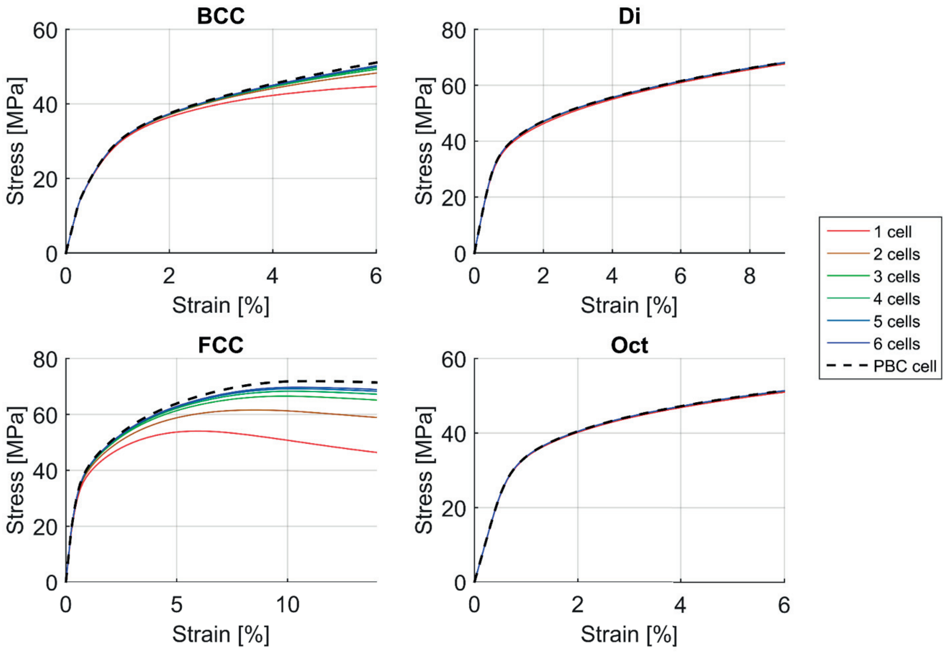

Figure 2.30 – Stress-strain curves convergence analysis according the number of elements across the smallest features for the different PCS

In order to estimate the properties of an infinite number of cells (n → ∞), a simulation was done on a unit cell with periodic boundary conditions (PBC) in the X and Y directions, meaning that the displacement of nodes on one face (X or Y) needs to correspond to the displacement of its corresponding nodes on the opposite face [223]. Figure 2.30 shows the results for the four different PCSs. It can be already seen that the size effect can be null (Di and Oct) or non-negligible (FCC). Four different mechanical properties were calculated from the stress-strain curves obtained from the simulations to estimate the size effect. The three already calculated for the mesh convergence study and the absorbed energy corresponding to the area under the curves. Figure 2.31 shows the evolution of the four properties according to the number of unit cells for each PCS. All the properties are shown as the ratio with the properties obtained for infinite structure expressed as a percentage.

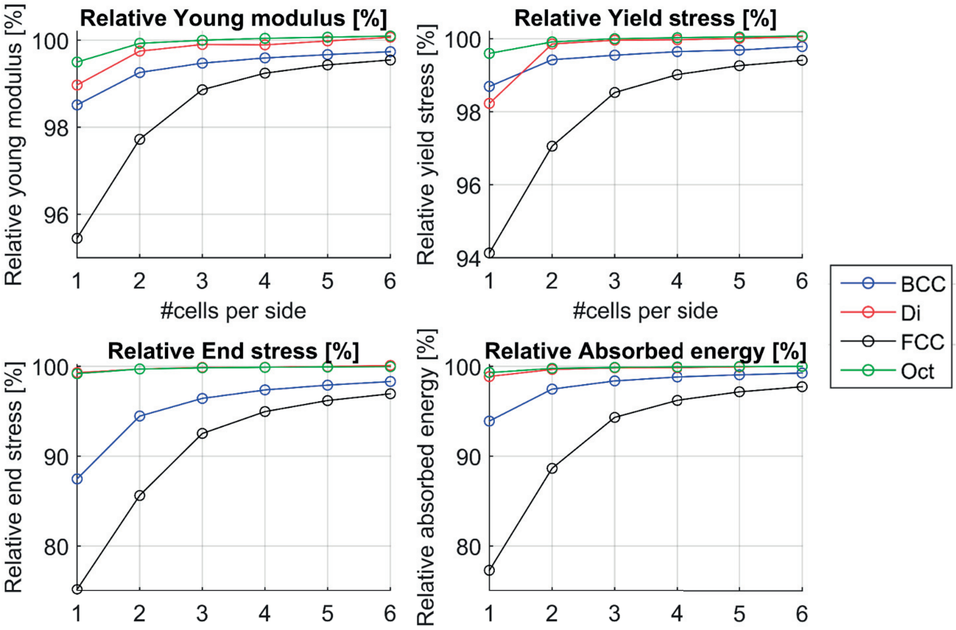

Figure 2.31 – Stress-strain curves convergence analysis according the number of elements across the smallest features for the different PCS

On one hand, two structures (Di and Oct) seem to be insensitive to size effect as a repetition of 2 unit cells is enough to obtain at least 99.5% of the properties estimated with the infinite model. On the other hand, two structures undergo a relatively large size effect, especially the FCC structure. Steady-state is reached at 3-4 cells per side for BCC and 5-6 repetitions for FCC leading to properties of at least 97% of the estimated infinite structures. This size effect was associated with buckling of vertical struts, present only in BCC and FCC structures.

2.5.4 Comparison with experimental data

The FE models were then confronted with experimental data for validation; Figure 2.32 shows the comparison. The model used was the one estimated in the case of a fictive infinite structure applying periodic boundary conditions to the faces parallel to the displacement. It can be observed that the models fit very well the experimental data during plastic deformation while overestimating properties in elastic regime. This deviation can be explained by the absence of microplasticity in the CAD models and naturally occurring (at local stress concentration sites; see below) in cellular materials [83, 224]. For the FCC structure, after 6% of deformation, a drop in the mechanical properties was not predicted by the calculations.

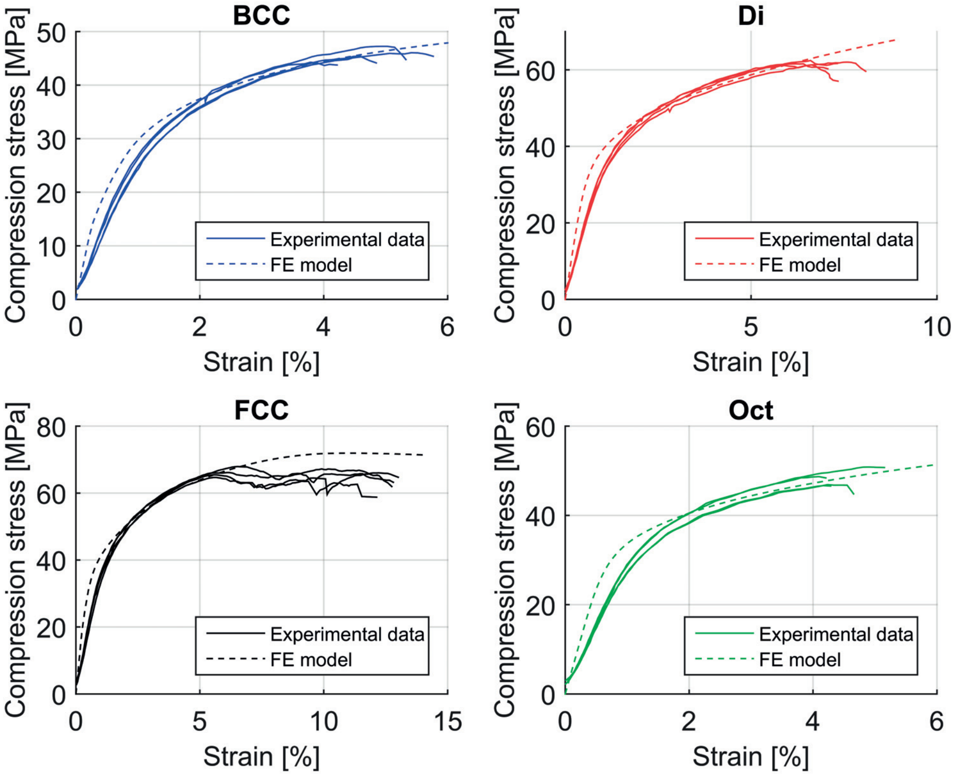

Figure 2.32 – Comparison between FE models and experimental data of additive manufactured PCS

2.6 Discussion

2.6.1 Defects influence

At first glance, a paradoxical observation can be made on the FCC structures looking at the porosity content on one hand (Section 2.4.2) and the mechanical properties on the other hand (Section 2.4.2). The strongest structure is at the same time the most porous. This is explained by looking at the spatial distribution of the porosity. FCC structures contain the most significant amount of sintered powder (resulting in the highest relative density, namely 32%) due to the large fraction of horizontal struts. This trapped powder contains gas porosity which is then counted as belonging to the FCC structure by CT-scans analysis, but at the same is located in not (or weakly) constrained regions. It has also been observed that larger process-induced pores tend to be located at the node centers which are less constrained than the struts. Therefore, the effect of the higher porosity content in FCC structures is minimized by the fact that porosity tends to be partially located in low-stress regions. Figure 2.33 shows an optical microscopy image highlighting the two previously described features.

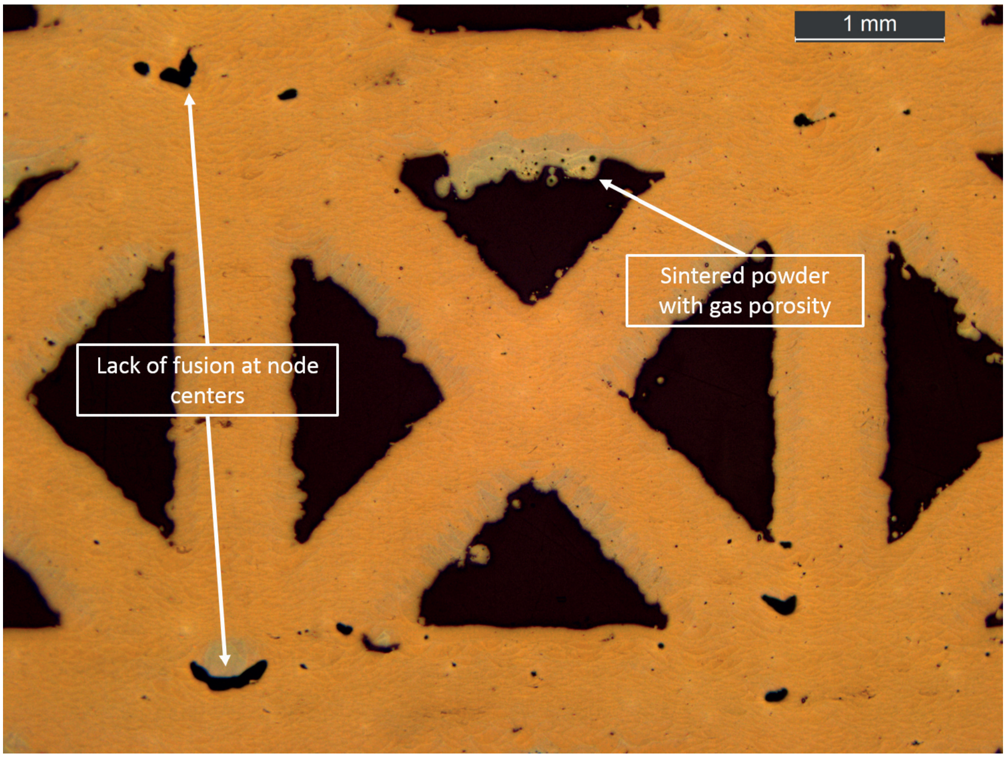

Figure 2.33 – Optical microscopy of FCC structure (x18.75) highlighting the lack of fusion at node centers and gas porosity in sintered powder.

2.6.2 FEA calculations and compressive modulus

The deformation of additive manufactured PCS in AlSi12 differs from that of conventional cellular materials in, in that the structure break in a brittle mode at the beginning of the plateau regime instead of deforming over a large range of strain before densifying. Finite element analysis predictions are in good agreement with the experimental data (Figure 2.32) implying that the preliminary tensile test campaign captured well the behavior of the bulk material. This result is supported by two observations. Firstly, the mesostructure (microstructure) is one (three) order(s) of magnitude in size smaller than the bar and strut diameters. Therefore, the strut material behavior is well-described by the "average" material behavior measured in larger tensile bars. Secondly, defect characteristics and contents being also the same between tensile and PCS specimen, their influence was also well-captured and implemented in the numerical models. Nevertheless, the fitting of the simulation is not perfect in two regions. The first is in the linear regime, where the models overestimate the stiffness. This deviation is due to the way the models were built by slightly overestimating the flow stress in the region around the transition from elastic to plastic deformation, and also because the initial slope of the stress-strain curves is well-known to be marred by effects such as misalignment between the platens and the sample surfaces, or localized plasticity. The second difference between test data and simulations is seen on the FCC structures, more precisely past 6% of deformation. This can be explained by the fact that experimentally, this structure tends to show local cell collapse with an ensuing global rotation of the structure. In the FE analysis, periodic boundary conditions are applied to unit cells, and therefore the global deformation mode is no longer appropriately described past 6% strain.

Finite element simulations were conducted to calculate the PCS compressive modulus in an ideal case free of any misalignment and microplasticity effects. Experimentally, this result is produced by estimating the extrapolated compressive modulus [42]. A good correlation between the two different modulus values for each PCS structure was found, emphasizing the importance of inhomogeneous deformation and microplasticity in the early stages of deformation of this class of material, as shown in Table 2.12.

Table 2.12 – Comparison between compressive modulus (in GPa) estimated by finite element analysis and extrapolated from its evolution according plastic strain on experimental data

Structure	Extrapolated	Finite element
BCC	4.7	5.1
Di	5.5	6.0
FCC	7.4	7.7
Oct	4.4	4.9

2.6.3 Failure mode

From experimental data, PCSs exhibited the same overall failure mode, this being a sliding between two planes (see Section 2.4.2). A hypothesis is proposed based on this result, namely that the sliding occurs in between planes with the highest surface density. The decision was then made to calculate the surface density evolution in PCS unit cells along different directions. To limit the calculations that have to be performed, the choice was made to focus on the unit cell strut orientations: <100>, <110> and <111> directions.

Table 2.13 summarizes the different struts orientations for each PCS. The surface density evolutions were numerically calculated using Matlab. Three different CAD models per PCS type were designed corresponding to unit cells oriented along the three directions of interest. For the rest of the calculations, it was decided to aligned the unit cell main orientation with the vertical, as shown in Figure 2.34. Then, for each unit cell, the surface density evolution was calculated by sweeping a horizontal mesh grid along the vertical direction and counting the mesh points belonging to the structure, later transformed to surface density.

In addition to the comparison of the average surface density with the designed relative density of

Table 2.13 – Strut orientations in each PCS type

Struture	**Struts orientations**
BCC	<100><111>
Di	<110>
FCC	<100><110>
Oct	<110>

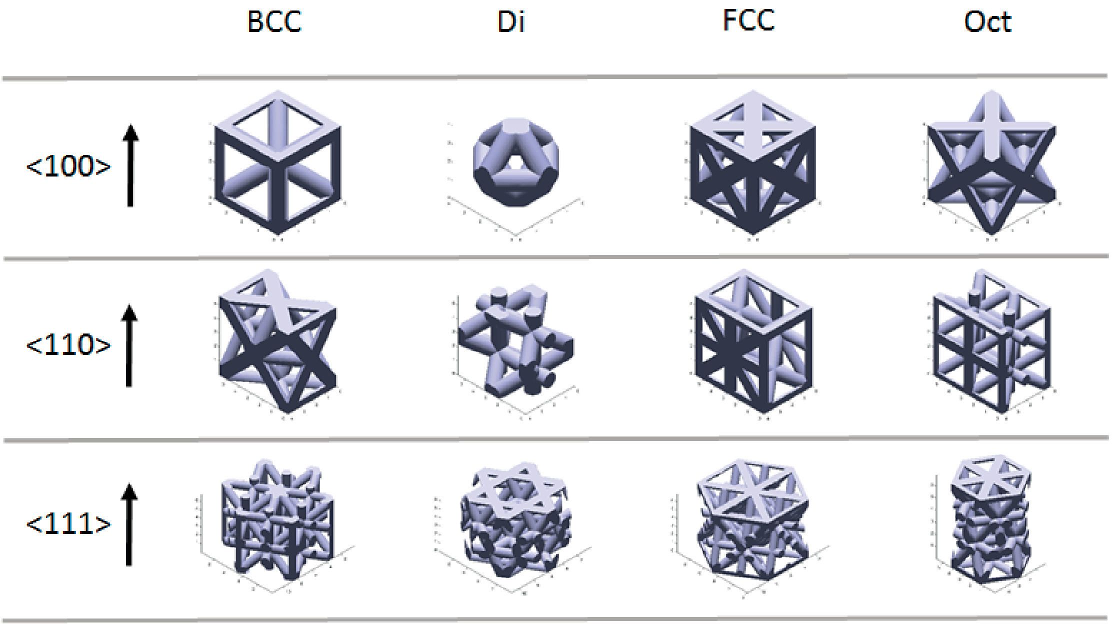

Figure 2.34 – Unit cell CAD models of PCS for the three different directions aligned to the vertical

30%, analytical calculations were performed to assess the veracity of the Matlab script. Equations were established to estimate the maximum surface density ρ_{max} and the surface density in the region where it stays constant ρ_{cst}. These equations could be established for two out of the three directions of interest, where struts formed an interconnected network. Equations 2.6 and 2.7 show the general relation to calculate the two previously described surface densities where d is the strut diameter and a the unit cell size. Table2.14 summarizes the corresponding coefficient values for each pair of PCS type and direction.

$$\rho_{max} = A\frac{d}{a} - B(\frac{d}{a})^2 \tag{2.6}$$

$$\rho_{cst} = C(\frac{d}{a})^2 \tag{2.7}$$

The surface density evolutions of experimental data were also calculated based on CT-scans. First, the registered 3D volume was oriented according to the desired orientation. Then, cross-sections

Table 2.14 – Calculated coefficients corresponding to the analytical maximum and constant surface density

		A	B	C
BCC	<100>	2	1	$\pi(\frac{1}{4}+\sqrt{3})$
	<110>	$\frac{1+2\sqrt{3}}{\sqrt{2}}$	$\frac{7}{4}+\frac{\sqrt{3}}{2}$	$\frac{\pi}{2}(\sqrt{3}+1)$
Di	<100>	$2\sqrt{2}$	2	$\pi\sqrt{2}$
	<111>	$\sqrt{6}$	2	$\pi\frac{3\sqrt{2}}{4}$
FCC	<100>	$2(\sqrt{2}+1)$	$(\sqrt{2}+1)^2$	$\pi(\frac{1}{4}+\sqrt{2})$
	<111>	$\sqrt{6}$	$\frac{3}{2}$	$\frac{3\pi}{4}(1+\sqrt{2})$
Oct	<100>	$2\sqrt{2}$	2	$\pi2\sqrt{2}$
	<111>	$2\sqrt{6}$	6	$\pi\frac{3\sqrt{2}}{2}$

were taken sweeping along the direction of interest. Finally, obtained images were binarized and processed by Matlab to estimate the experimental surface density. Figures 2.35 to 2.38 show the result obtained from the surface density calculation campaign, compared to analytical and experimental verification points. The powder sintering under horizontal struts (described in Section 2.6.1) can be seen on the experimental surface density evolution along the (001) direction by breaking the symmetry of the general pattern around the maximum peaks.

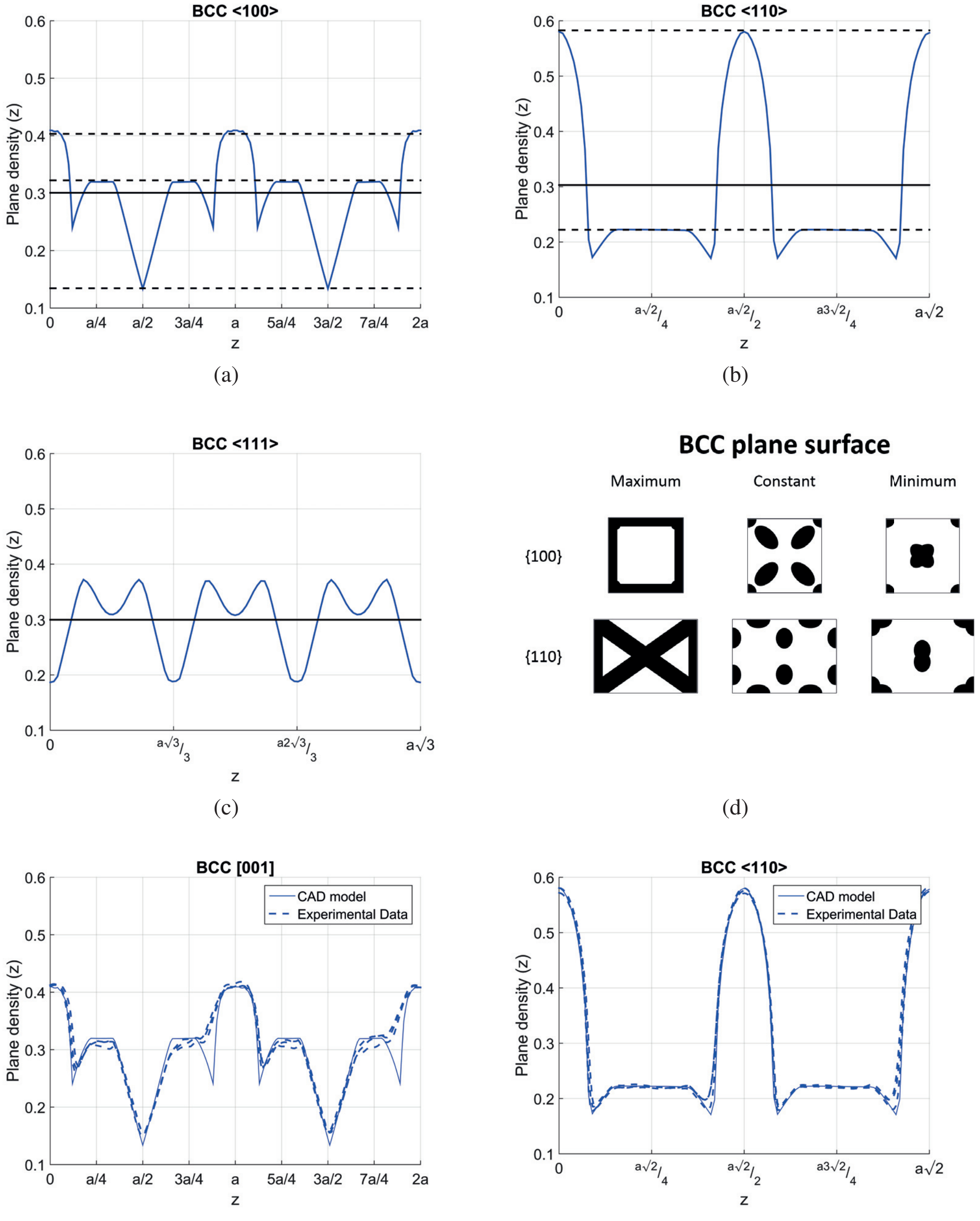

(a) (b) (c) (d) (e) (f)

Figure 2.35 – Surface density evolution for the BCC structure along (a) <100> directions, (b) <110> directions and (c) <111> directions. (d) Cut views corresponding to the maximum, the constant and the minimum value of the surface density for the {100} and {110} planes. Black dashed lines represent analytical estimation, and solid lines stand for the average surface density. Comparison of real and calculated surface densities for the BCC structures according (e) the [001] direction (with evidence of sintering effect) and (f) the <111> directions.

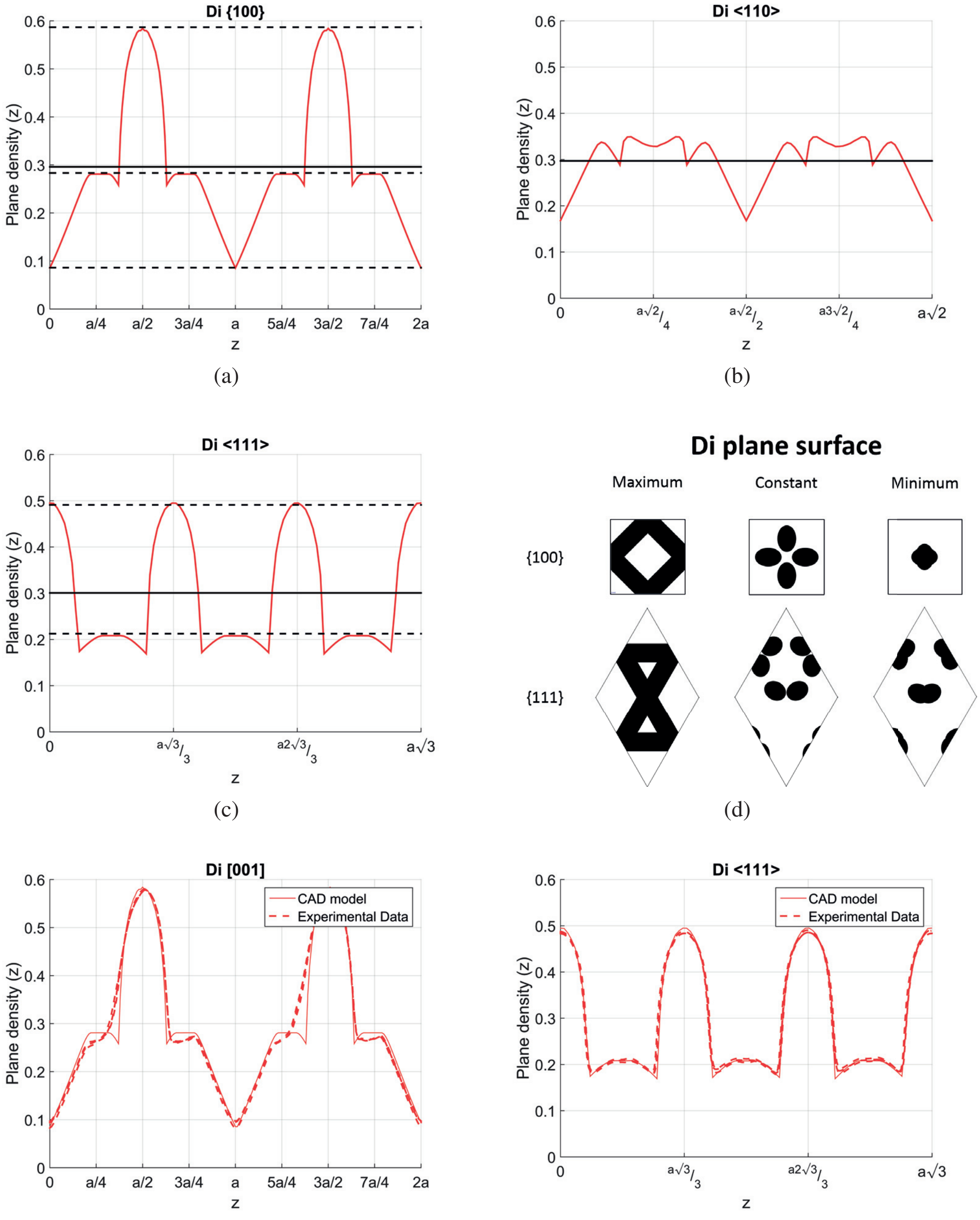

(a) (b)

(c) (d)

(e) (f)

Figure 2.36 – Surface density evolution for the Di structure along (a) <100> directions, (b) <110> directions and (c) <111> directions. (d) Cut views corresponding to the maximum, the constant and the minimum value of the surface density for the {100} and {111} planes. Black dashed lines represent analytical estimation, and solid lines stand for the average surface density. Comparison of real and calculated surface densities for the Di structures according (e) the [001] direction (with evidence of sintering effect) and (f) the <111> directions.

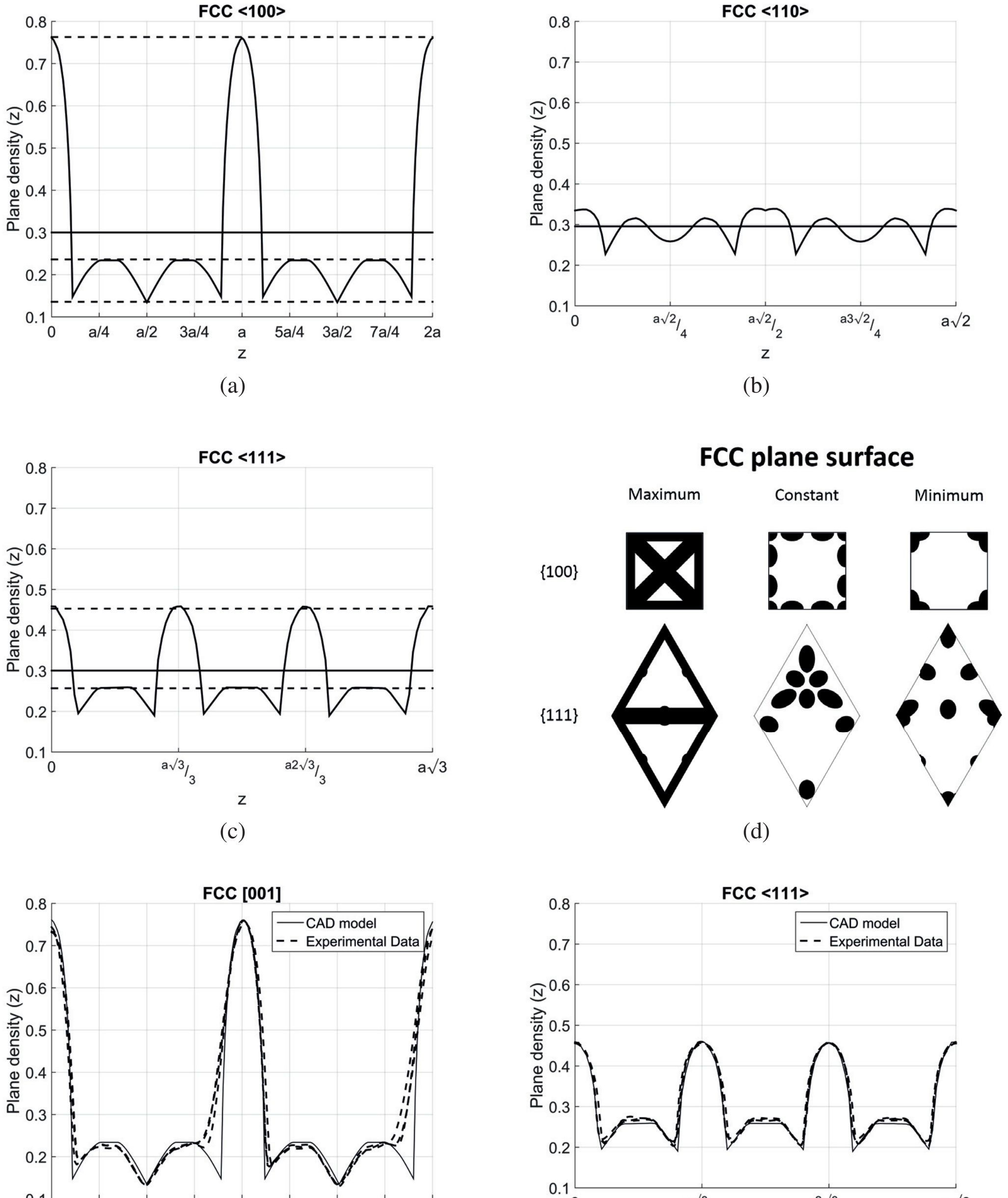

(a) (b) (c) (d) (e) (f)

Figure 2.37 – Surface density evolution for the FCC structure along (a) <100> directions, (b) <110> directions and (c) <111> directions. (d) Cut views corresponding to the maximum, the constant and the minimum value of the surface density for the {100} and {111} planes. Black dashed lines represent analytical estimation, and solid lines stand for the average surface density. Comparison of real and calculated surface densities for the FCC structures according (e) the [001] direction (with evidence of sintering effect) and (f) the <111> directions.

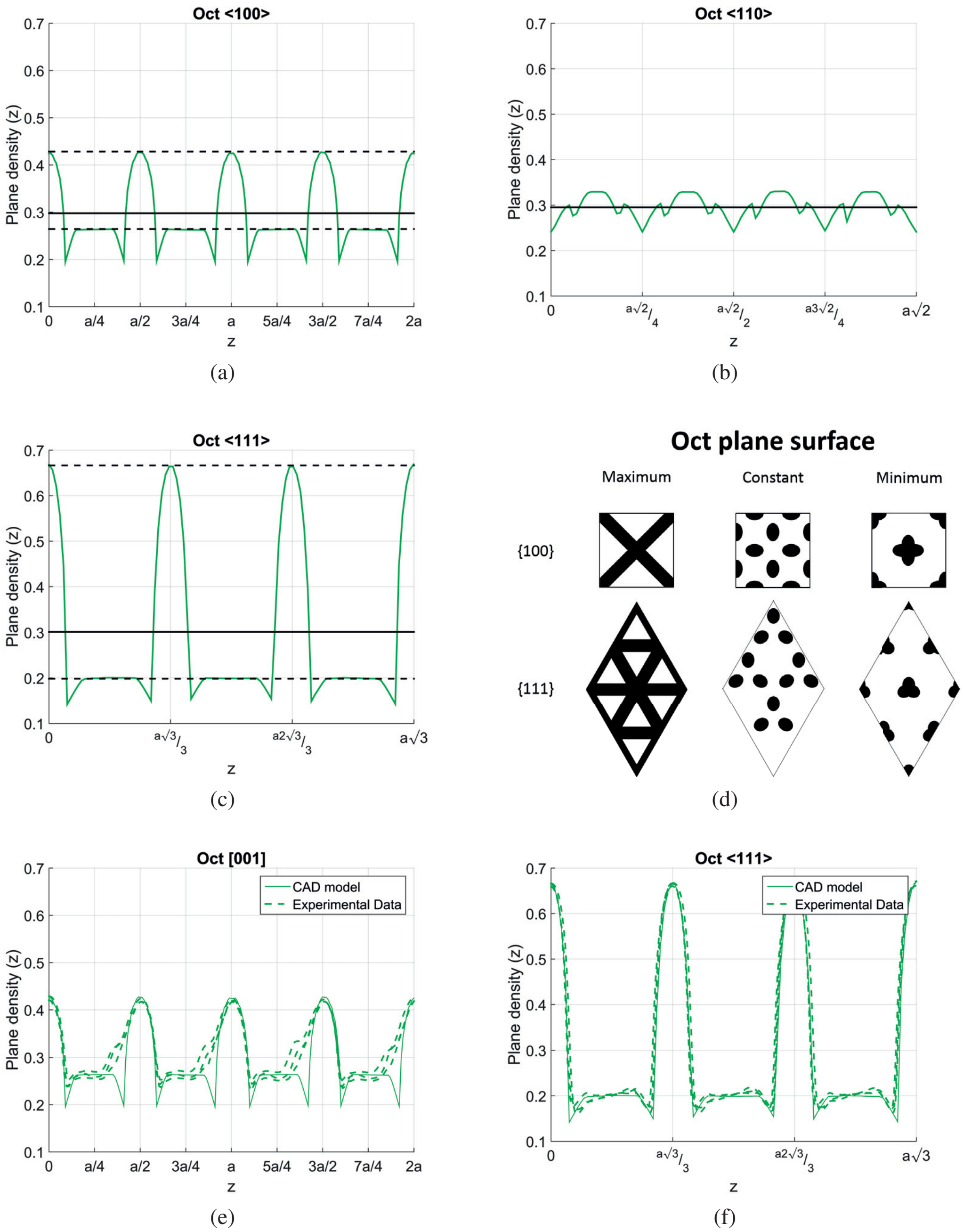

(a) (b) (c) (d) (e) (f)

Figure 2.38 – Surface density evolution for the Oct structure along (a) <100> directions, (b) <110> directions and (c) <111> directions. (d) Cut views corresponding to the maximum, the constant and the minimum value of the surface density for the {100} and {111} planes. Black dashed lines represent analytical estimation, and solid lines stand for the average surface density. Comparison of real and calculated surface densities for the Oct structures according (e) the [001] direction (with evidence of sintering effect) and (f) the <111> directions.

The hypothesis made on the PCS failure mode is based on the assumption that the failure is driven by the inhomogeneity of the surface density. The choice was then made to compare the surface density standard deviations. Table 2.15 shows the standard deviation for every PCS type and direction combinations. Three structures exhibited a clear direction of maximal surface density deviation (standard deviations twice as high as for other directions), namely <110> for BCC structures, <100> for FCC structures, and <111> for the Oct structures. These results are in a good agreement with the observed failure surface on samples under compression (see Section 2.4.2). Concerning the Di structure, two directions competed in terms of surface density variations, which correspond to the two sliding planes present in the failure surface of such structure, namely <100> and <111>. Nevertheless, a difference can be observed between numerical estimations and experimental results regarding the predominant failure plane of Di structures. Numerical results give almost parity between the two directions whereas experimental data highlight a dominance of the <111> directions (about 60%). Therefore, in addition to the surface density, the stiffness and mechanism of the interconnected struts networks were investigated. Struts in planes normal to the <111> direction form a 2D Kagome lattice, and struts normal to the <100> direction are assembled into a 2D square lattice, as shown in Figure 2.39. The connectivity of the two different lattices is Z=4, therefore no explanation on the <111> predominance can be made on this side. However, it has been demonstrated by Fleck and al. [151, 155] that the Kagome lattice is stiffer than the square lattice due to the presence of a macroscopic strain-producing mechanism of the latter. This then explains the observed preferential shear along the {111} planes for the Di structures and validates the initial hypothesis on the PCS failure modes.

Table 2.15 – Standard deviations (in %) of surface density according the structures and the directions

		Structure			
		BCC	Di	FCC	Oct
Direction	<100>	7	14	19	7
	<110>	14	5	3	3
	<111>	6	13	9	18

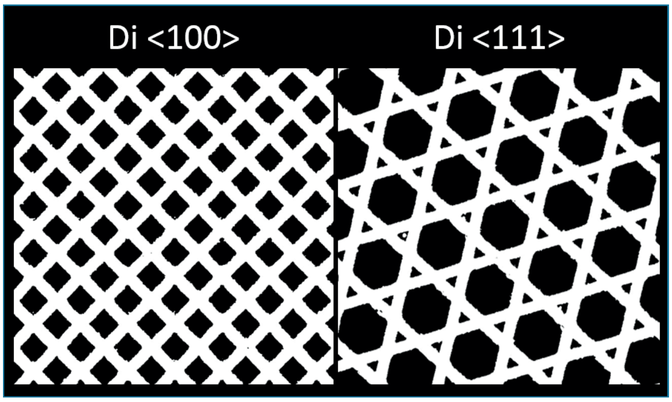

Figure 2.39 – 3D-tomography cut views of Di sample corresponding to <100> (left) and <111> (right) normal directions

To conclude, it has been demonstrated that the compressive failure mode by global shearing of

PCS is governed by uneven mass distribution along different directions, the direction exhibiting the highest variation being that normal to the failure planes. In the case where two directions present close variations, the failure surface is a combination of the two and failure takes place preferentially along the plane including the stiffer interconnected 2D struts network. This result is supported by the observations made on BCC structures [13, 162, 181] and on Oct structures [143].

2.6.4 Fracture

Fracture in BCC and Octet structures mainly occurred by a rupture in bending of struts at nodes junctions (see Section 2.4.2). This result can be explained by three factors. Firstly, the stress-concentration present at the struts hinges with the nodes might induce local stresses reaching the bulk metals strength. Then, from the surface density evolution study (see Section 2.6.3), it can be observed that a local minimum is present close to the struts, as shown in Figure 2.40 for the BCC <110> direction and Oct <111> direction. This minimum surface density induces higher stress in the corresponding plane which might lead to failure.

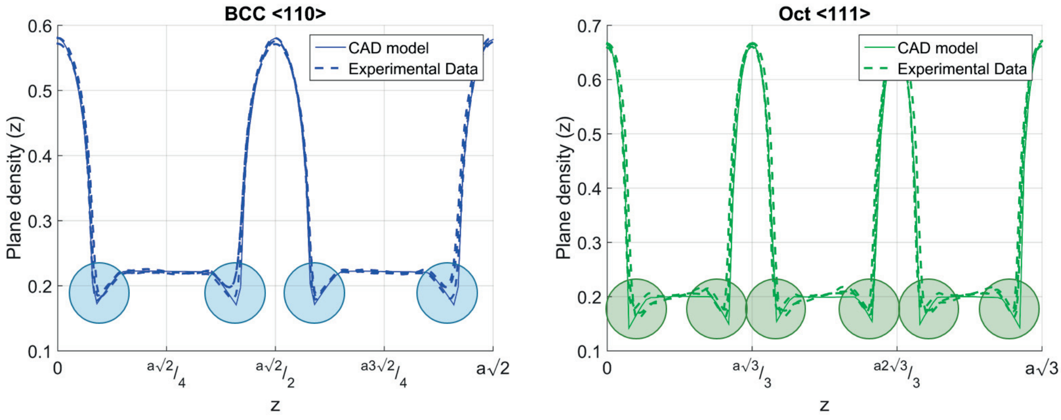

Figure 2.40 – Numerical and experimental surface density evolution for BCC <110> direction (left) and Oct <111> direction (right). Circles highlight the minimum at the junction between struts and nodes

Finally, it has been observed in this study (Section 2.4.1) and reported in the literature [25, 40] that melt-pool interfaces are preferential crack paths in SLM metals. In BCC and Oct PCS, the overhang angle induces a misalignment of the lower outer layer, being aligned to the strut orientation instead of the building direction. This places the bulk metal in the most detrimental configuration to sustain the tension induced by bending, the tension being orthogonal to the preferential fracture plane. Figure 2.41 shows the situation for a BCC structure.

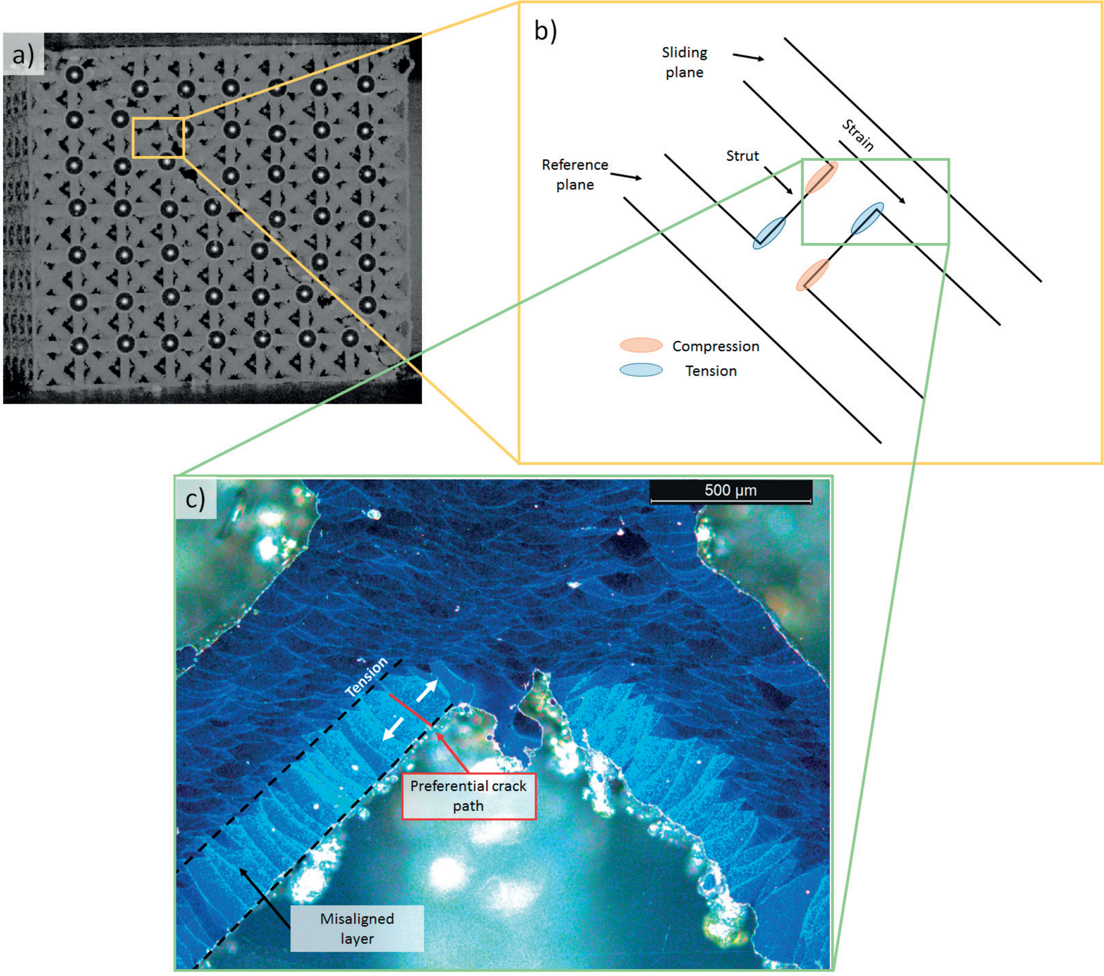

Figure 2.41 – a) Broken BCC sample. b) Sketch of stress states at the junction between sliding planes and strut. c) Optical microscopy highlighting the combination of tensile load state and preferential crack path, i.e. along the melt-pool interface

2.7 Conclusion

In this chapter, quasi-static compression tests were performed on four different types of PCS manufactured in AlSi12 by SLM in parallel of tensile test on the bulk alloy. PCS deformations were recorded by the use of digital image correlation, and 3D-tomography analysis was conducted for defects and topology investigation. Several conclusions were made from this study:

- Tensile test campaign showed consistency with the literature regarding the mechanical properties, the defects, and the fracture surfaces [6, 25–27, 35, 38–40, 225]. Numerical models were extracted from the campaign to be used in FE calculations.
- Significant difference could be observed between different structure topologies emphasizing the importance of the design regarding the structural performances. Brittle failure was

associated with the intrinsic brittleness of the bulk solid material associated with the existence of planes of weakness delimited by melt-pools contours.

- Finite element simulations are in a good agreement with experimental data as concerns plastic deformation. Divergence in the linear regime highlight the importance of microplasticity or misalignment in this class of material.
- The observed global shear failure mode of PCS under compression is explained by topological considerations: sliding failure planes are normal to the direction presenting the highest surface density variation, and including interconnected strut network. If more than one plane family can be identified, the fracture preferentially takes place in the plane exhibiting the highest planar stiffness.
- Fracture occurs by strut bending at the junction with nodes, promoted by a minimum surface density and a preferential alignment to the crack path, along the melt-pool interfaces.

Additively manufactured metals exhibit mechanical property anisotropy due to the presence of the mesostructure related to the process. Further analysis might be required to assess the impact of this anisotropy on the PCS deformation under compression.

3 Investment casting of PCS

The previous chapter describes the test campaign performed on additively manufactured periodic cellular structures (PCS) by selective laser melting (SLM) and explains their failure mode based on topology considerations. In this chapter, the feasibility of producing equivalent structures by investment casting is investigated. This investment casting process is based on the replication of a sacrificial polymer preform by using a water-leachable mold made of common table salt.

The detailed manufacturing procedure is described, from the manufacturing of the preform to the casting of the PCS. The selection of the process parameters is then highlighted with a focus on the reasoning behind the choice of specific parameter values. To conclude, metallographic and mechanical tests results are given, which document main characteristics of cast PCSs produced by the process that was developed here.

3.1 Process description

3.1.1 Overall process sequence

Figure 3.1 shows the overall casting process sequence. For each step, two series of section references are given; red and blue numbers correspond respectively to step description and step optimization.

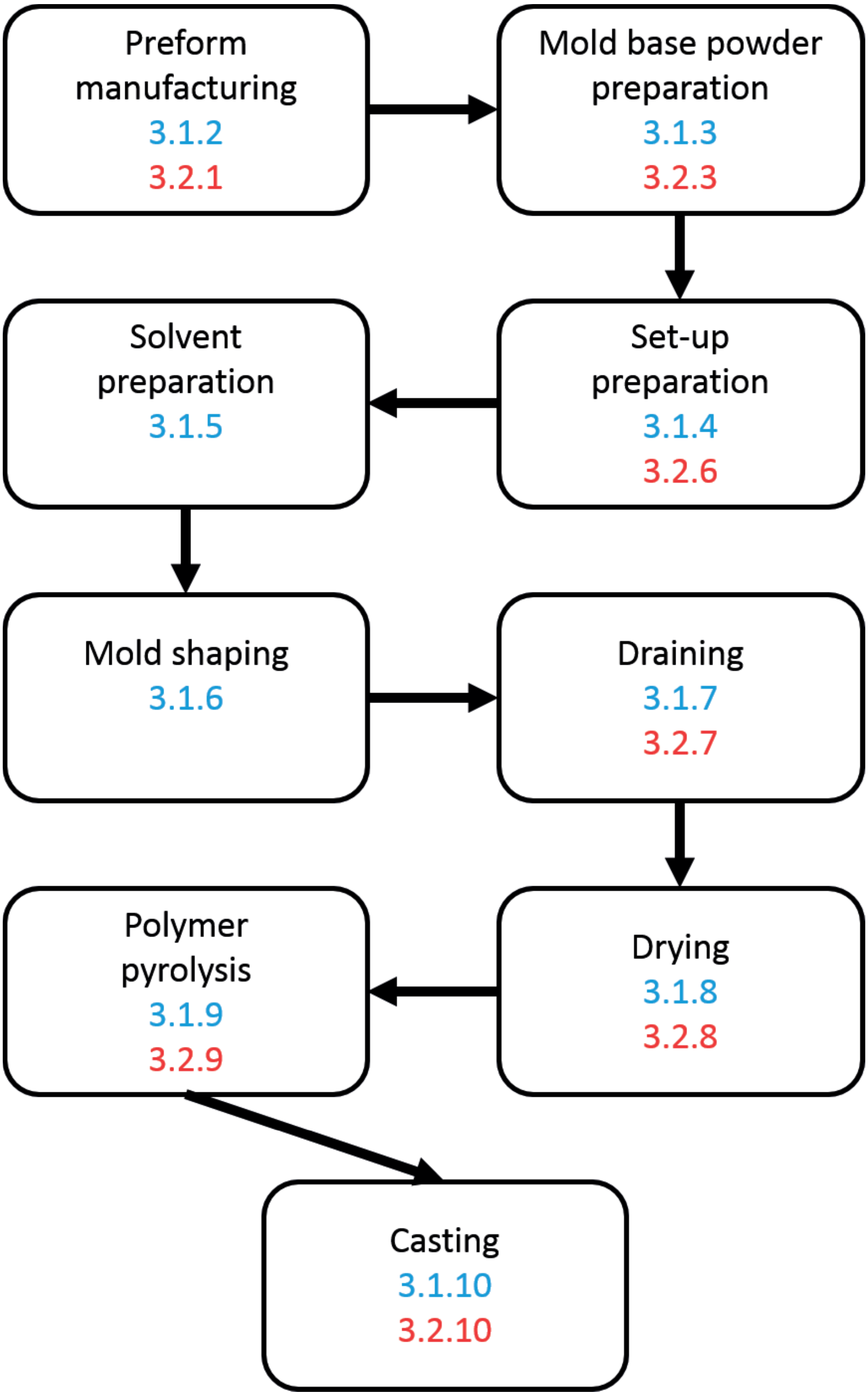

Figure 3.1 – Process sequence presenting the steps performed to cast PCS. Section references for step description are in blue and section references for step optimization are in red

3.1.2 Preform fabrication

The sacrificial preform is manufactured by additive manufacturing of a polymer directly to the shape of the desired metallic part. The shape of the final parts being predefined, only the selection of the polymer and its corresponding manufacturing process remained as variables to be defined. Process development focused on a preform printable in-house at EPFL on existing equipment using polylactic acid (PLA) by fused deposition modeling (FDM) (see Section 3.2.1 for further details on preform selection). Due to manufacturing constraints, the cell size was increased from 4 mm to 6 mm and only the Di structure polymer preform showed satisfactory results regarding CAD fidelity, keeping the targeted relative density of 30%. The manufacturing of the preform was already a challenge by itself, regarding the topology required, the presence of horizontal struts (or struts with a high overhang angle). This led to finding the right settings for the best final resolution of the printed preforms, requiring to tune dozens of parameters on the machine. Critical parameters were identified and a preliminary campaign was performed to find the best configuration, other parameters being kept at their nominal value [226]. These parameters are the extruder and bed temperatures, the printing speed (more precisely the perimeter printing speed as the struts are small enough to contain only perimeters), the bridge printing speed and flow rate, and finally the extrusion multiplier which scales the amount of matter extruded for a given horizontal displacement. Table 3.1 shows the parameters value coming from this study.

Table 3.1 – Printer settings for the manufacturing of PLA preform

Setting	Value
Extruder temperature	200°C
Bed temperature	50°C
Printing speed (except bridges)	15 mm.s^{-1}
Printing speed (bridges)	10 mm.s^{-1}
Bridge flow ratio	0.7
Extruder multiplier	0.85

3.1.3 Mold base powder preparation

The base material for the mold used in this work is sodium-chloride (NaCl) salt powder. The main parameter (and later found to be the most influential on the cast quality) is the NaCl grain size distribution. Therefore, the preparation of the base material for the molds consists of producing the optimal grain size distribution, defined to be in between 125 and 180 µm (more details of the selection can be found in section 3.2.3). Several batches of salt, from three different manufacturers, were investigated:

- **Fluka :** provided by Fluka company (branch of Sigma-Aldrich company, St-Louis, USA)
- **CP1 :** procured by Les Salines Suisses (Bex, Switzerland), can be in the commercial shape or delivered already milled (so-called CP1 Milled).
- **MARSEL :** provided by Zoutman (Gent, Belgium).

Apart from the commercially available CP1 salt, all batches exhibited a size distribution which overlapped the desired one; therefore, the salt went into a sieving process. Salt batches were identified by the provider's name (Fluka, CP1 and MARSEL). Concerning the commercially available CP1 salt (not milled), due to a size distribution larger compared to the interesting range, the salt went to a preliminary milling step consisting of pushing the grains through a mesh with a rammer. The mesh size used was defined as the upper limit of the distribution of interest, namely 180 µm. The obtained powder was then sieved like the three others batches and named CP1.

Preparation of the salt started with a heating to 250°C for 10 min in air to remove residual moisture. It then was poured into the sieving machine, an analysette 3 PRO produced by Fritsch (Idar-Oberstein, Germany) after cooling to ambient conditions for 5 min. The mesh sizes used were 125 and 180 µm, the finest being at the bottom. The sieving was performed on 300-400 g batches for 10 min with a vertical amplitude of 0.3 mm. Figure 3.2 shows the set-up during the extraction of salt powder. The separated salt was then stored in glass bottles preheated to 120°C for 2h to reduce moisture content.

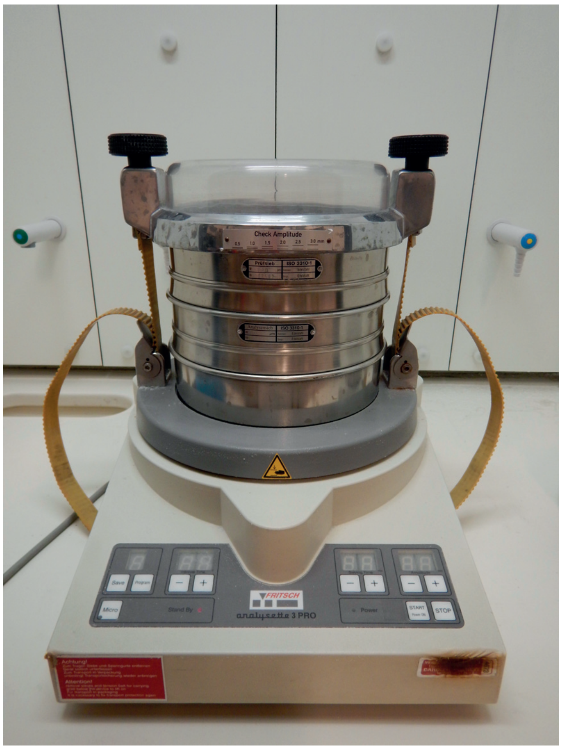

Figure 3.2 – Sieving equipment for the extraction of the 125-180 µm salt powder distribution

3.1.4 Set-up preparation

Five different parts are required for each set-up; namely a frame structure with a circular open base plate as well as four identical cylindrical segments to close the structure (Fig. 3.3). The parts were made out of acrylonitrile butadiene styrene (ABS) by FDM in the AFA-Workshop at EPFL.

A square piece of filter fabric held in place with kapton tape was placed on top of the grid to prevent the salt exiting the set-up during shaping and draining. Where the cylindrical segments come into contact with the base, a layer of paraffin film was applied to the kapton tape. To further improve the sealing of the base, a second layer of kapton was applied under the grid (Fig. 3.4a).

The same filter fabric was fixed to the inner part of the cylindrical segments to prevent cracking of the mold during segment removal once the mold has been drained (Fig. 3.4b). The frame and the segments could then be assembled. Kapton tape was used to hold the set-up in place. In order to minimize the probability of leaks during shaping, care had to be taken to leave no gaps between the segments and the frame structure (Fig. 3.5). Four set-ups were assembled as one batch. During the course of the thesis, 5 batches in this final configuration were produced.

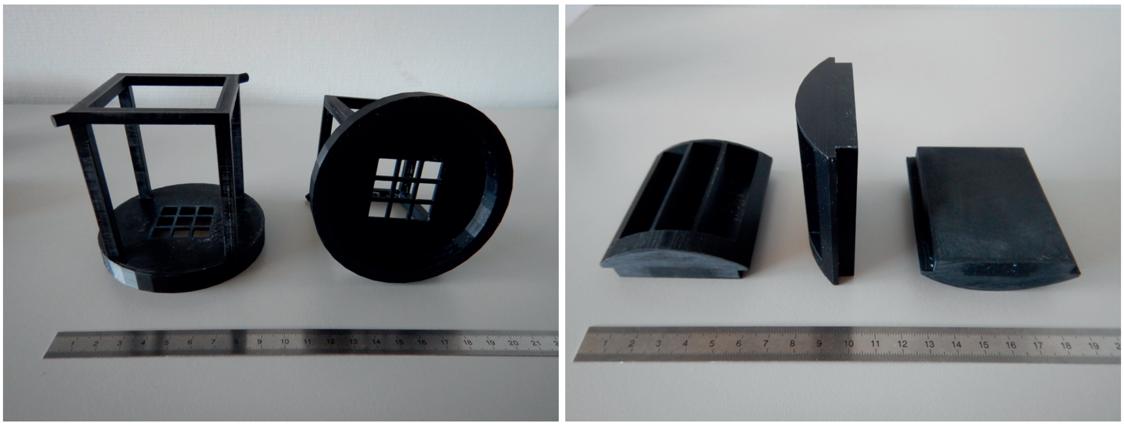

(a) (b)

Figure 3.3 – (a) Side and bottom views of the frame with its base, (b) Front, side and back views of the cylindrical segments

(a) (b)

Figure 3.4 – (a) frame (side and bottom views) and (b) cylindrical segments (front, side and back views) ready for assembly

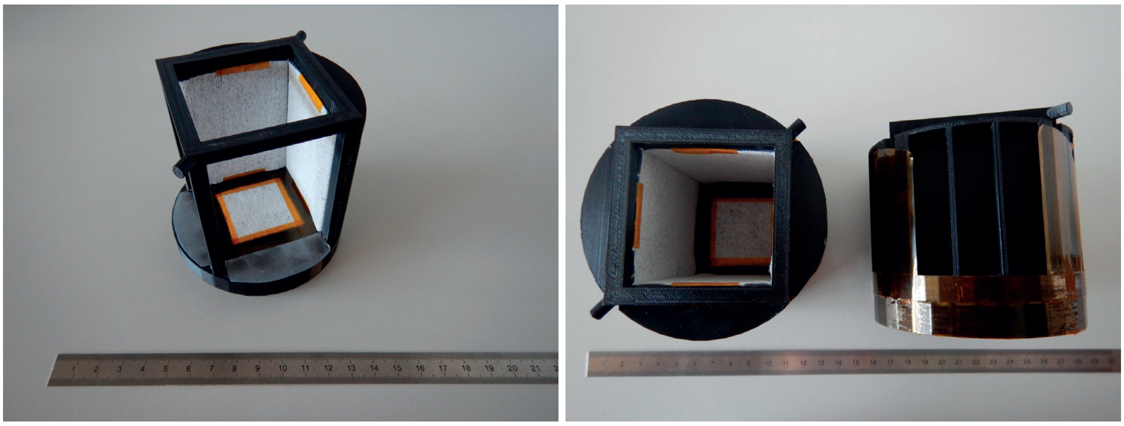

(a) (b)

Figure 3.5 – (a) Set-up half assembled and (b) fully assembled (top and side views).

3.1.5 Solvent preparation

The solvent used during the process was fabricated by mixing supersaturated water with salt and dish-washing soap (bought at Migros, Switzerland under the brand Handy). The water was supersaturated with salt by mixing 700-800 mL of hot water with at least 400 g of salt (to make sure that the quantity was well above the solubility in water, this being 391.2 g/L at 100°C). The salt used for this step was the commercially available CP1. The solution was then kept on a hot plate at 80°C and magnetically stirred for 12h. Soap was added to the solution to reduce surface tension and improve the wettability of the preform, one droplet (about 50µL) for every 50 mL of water corresponding to 0.1 % in volume. The solution was cooled down to ambient temperature and then filtered to remove excess salt.

3.1.6 Mold shaping

Once the set-up was ready, the mold could be produced. We to call this step "mold shaping" to differentiate it from the casting of the metallic part. For vibration packing, a simple homemade shaker (using an electrovalve actuator) was used at 50 Hz with a vertical amplitude measured at about 0.1 mm (Figure 3.6).

The assembled set-up was placed in a glass cup to confine the solvent, which could otherwise leak during the shaping process (Figure 3.7a) before pouring the solvent (150 mL) into the cavity. The 3D-printed preform was then rinsed (but not dried) with ethanol and immediately but slowly placed into the solvent filled cavity (Fig. 3.7b). The preform was gently shaken by hand to remove any residual air trapped inside the structure. Centering of the preform inside the set-up was accomplished by aligning the infiltration canals on the diagonals with the corresponding corners of the set-up (Figure 3.8a). Dry salt (grain size 125-180 µm) was then added in several steps, with 180-200 g used per shaping process. One such step consists of distributing 8 g of salt with a spatula uniformly around the perimeter of the preform; the whole set-up (including glass cup) was then vibrated for 30 s. To further enhance the uniformity of the salt distribution, the

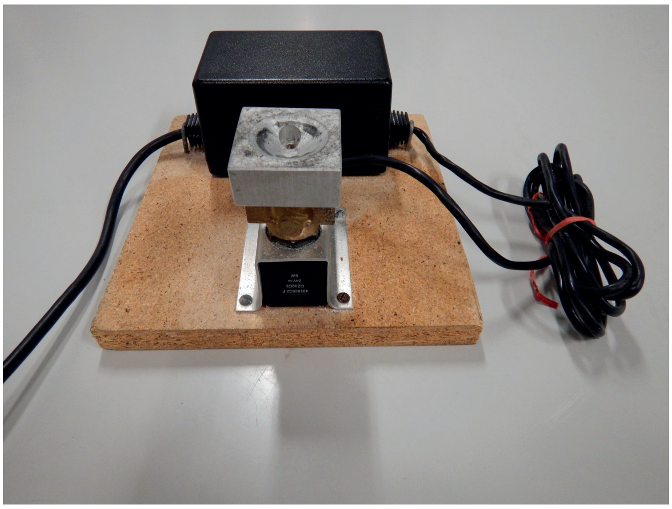

Figure 3.6 – Homemade shaker for vibration packing

whole set-up was rotated by 90° between each step (Figure 3.9). It is recommended to manually hold the preform in place during vibration; details on vibrating time requirements can be found in Section 3.2.5. This step was repeated until the salt reached a level 5 mm below the top of the infiltration canals (Fig. 3.8b). It is to be noted that, during the shaping process, excess solvent was removed in order to keep its level touching the infiltration canals, as illustrated in Figure 3.9. In this thesis, four mold shapes were produced in one batch.

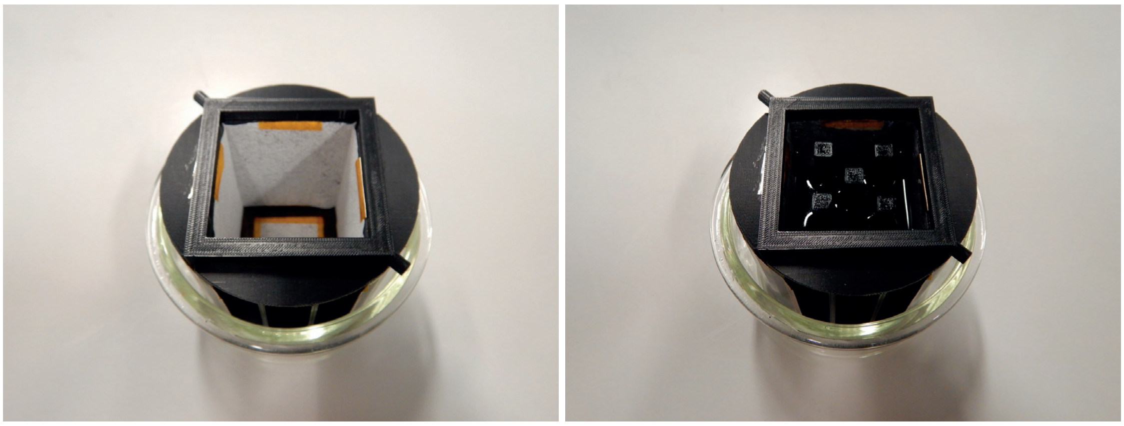

(a)

(b)

Figure 3.7 – (a) Set-up placed in a glass cup to confine any leaks and (b) set-up containing the preform with 150 mL of solvent

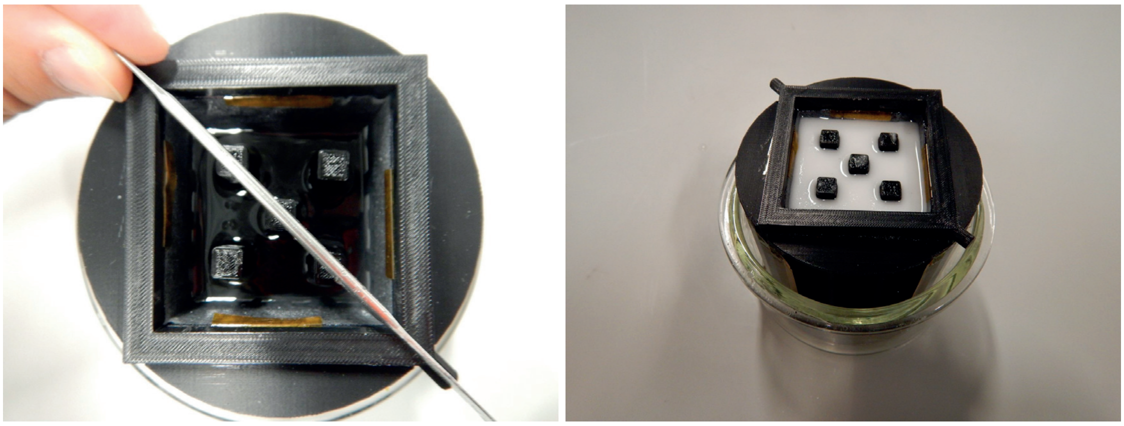
(a)

(b)

Figure 3.8 – (a) Placing and centering of the preform inside the set-up and (b) mold fully shaped before draining

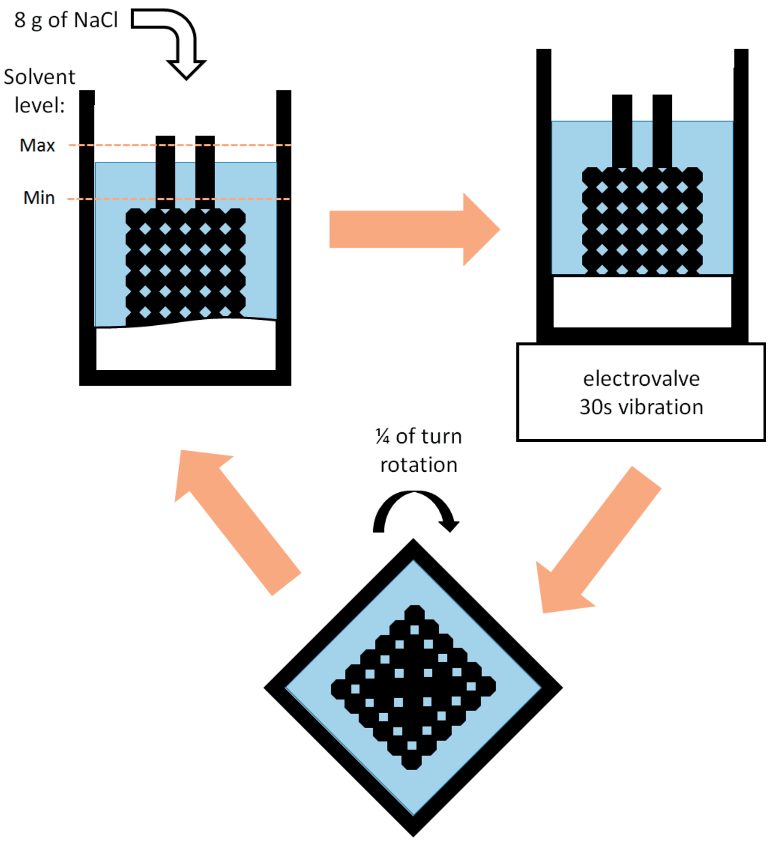

Figure 3.9 – Sketch of the cycle to be repeated in order to shape the mold

3.1.7 Draining

This step allows a fraction of the solvent present in the wet mold to be drained right after shaping. This strengthens the green body, easing removal of the cylindrical segments. Whilst maintaining the set-up in a vertical position, the kapton layer under the grid was carefully removed, opening the access to the filter fabric that keeps the salt from flowing out (Figure 3.10).

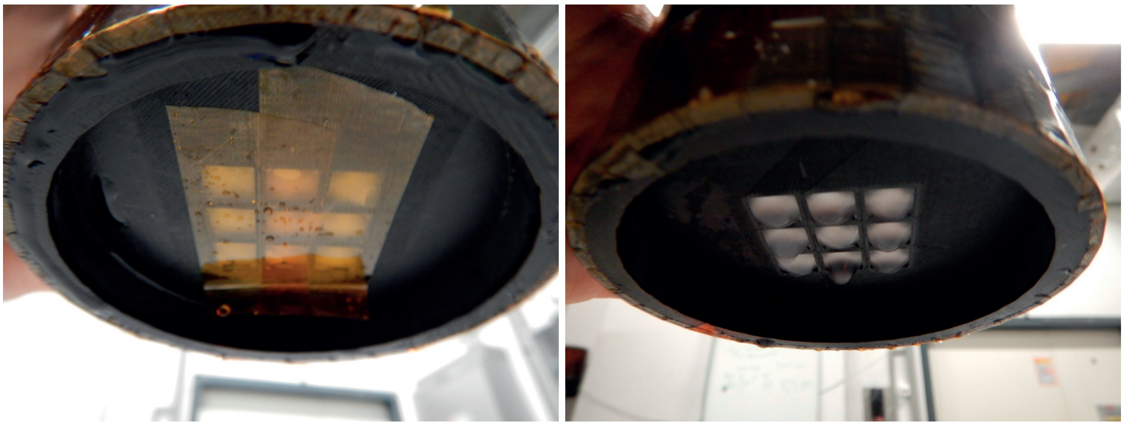

(a) (b)

Figure 3.10 – Removing the kapton layer under the grid of the set-up before draining, (a) grid bottom with and (b) without kapton layer.

Once the Kapton layer was removed, the set-up was delicately placed on absorbent paper to enhance draining. Manually, a slight pressure was applied to the top of the set-up to guarantee good contact between the grid and the absorbent paper. The absorbent paper needed to be changed five times to keep a good draining efficiency (details are shown in Section 3.2.7). The following times of this repeated step were determined to be sufficient, taking into account the specific absorbent paper used: 30 s, 2 min, 5 min, 10 min and 20 min respectively. The segments could then be carefully removed radially one by one after cutting the kapton tape (Figure 3.11a). At this time, the paraffin could be removed from the set-up (Figure 3.11b). Finally, the vertical edges of the salt mold were removed delicately using a sharp knife, to later ease the removal of the mold from the base once the drying step was over.

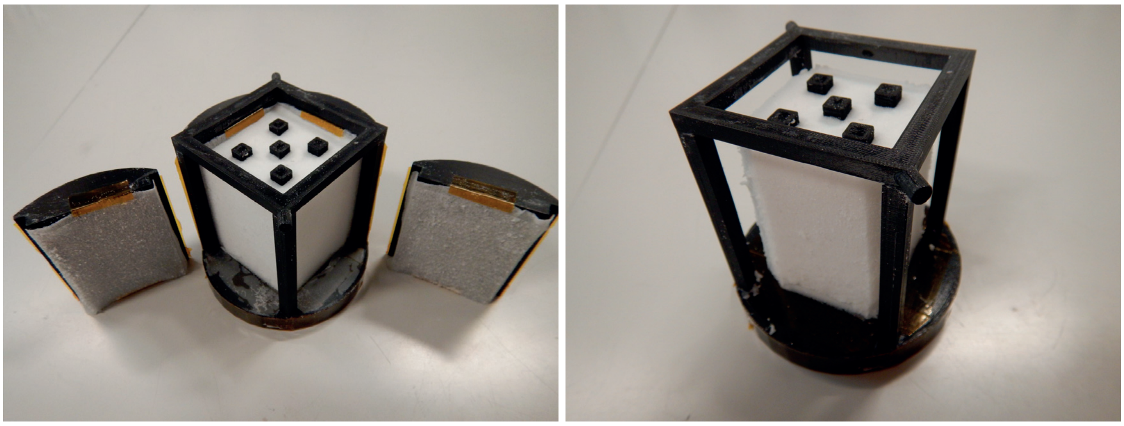
(a) (b)

Figure 3.11 – (a) Removing of the cylindrical segments after draining and (b) mold ready to be dried (with vertical edges removed)

3.1.8 Drying

To remove all the remaining solvent to the mold, the latter was dried in an oven at 80°C in air. Also, the salt dissolved in the solvent precipitated upon drying and acted as a bond between the individual salt grains. This step was the most time-consuming in the process, as it is based on diffusion.

A top-opened Elite oven (Elite Thermal Systems Ltd, Leicestershire, United Kingdom) was used as shown in Figure 3.12a. To keep moisture from accumulating and to add air circulation, a shaped copper tube (8 mm outer diameter, 5 mm inner diameter and 6 m in length) was inserted around the inner wall at the bottom of the oven; it was connected to laboratory compressed air at 1 bar. This tube had to be long enough to insure the circulated air did not cool the molds. Inside the oven, a refractory brick was placed in front of the pipe end, diverting the air flow and supporting a steel interface grid. The green bodies were placed onto the grid, one batch at a time (four units), always two on top of each other (Figure 3.13). Care had to be taken while placing the samples inside the cavity, and a gap (in our case at least 5 cm) was maintained between the set-ups and the inner faces of the oven to reduce undesirable temperature gradient effects (Figure 3.12b). Although the temperature was set to 80°C, it was measured to be only 75° inside the oven in between the set-ups, likely because the oven remains open during drying. Total drying of the molds took 4 to 6 days. During this time, the set-up positions were swapped two by two on a daily basis, between bottom and top layers. Twice a day (10 h to 14 h intervals), the set-ups were weighted. The process step was considered complete once the mass difference between two consecutive measurements fell below 0.01 g (Figure 3.15). Once removed from the set-up, the filter fabric was peeled off from the bottom of the mold and a small layer of salt carefully scratched away until the preform was revealed.

(a) Oven used for mold drying

(b) Molds inside the oven for drying

Figure 3.12 – Drying of the molds

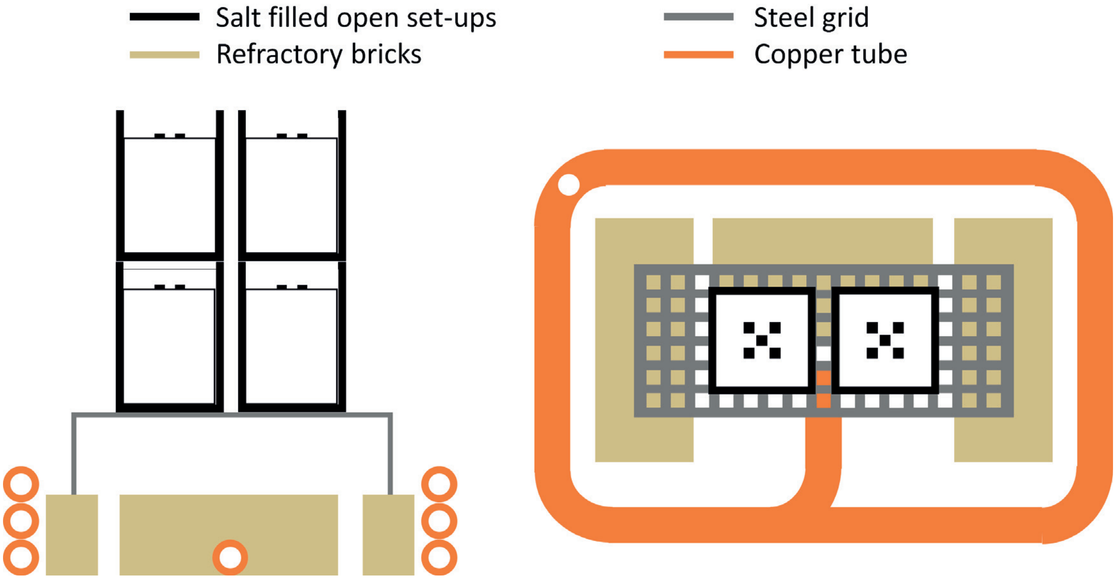

Figure 3.13 – Front (left) and top (right) schematic views of the oven configuration during molds drying.

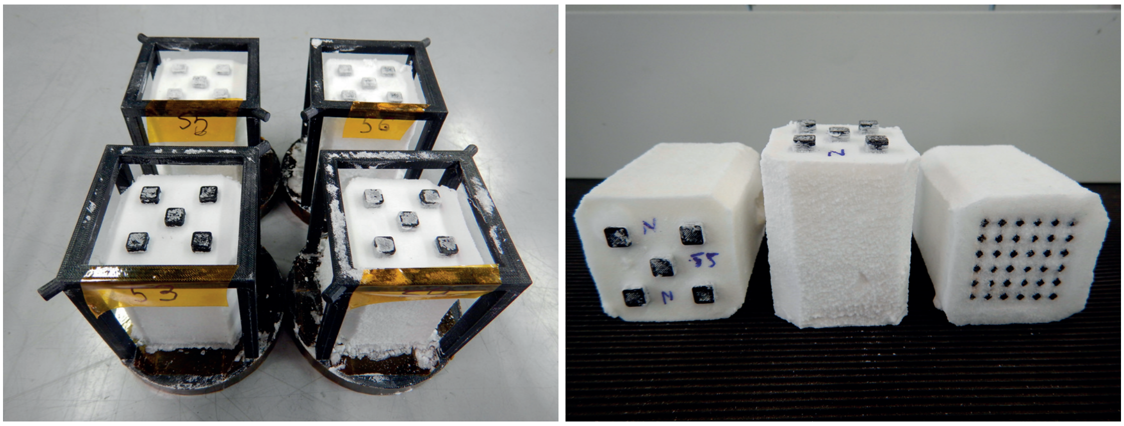
(a) (b)

Figure 3.14 – Removal of fully dried molds from the set-ups

3.1.9 Polymer pyrolysis

The polymer preform is removed from the mold by burning it in a pyrolysis step. The same oven was used in the same configuration as described in Section 3.1.8. Now, the 1 bar air flux brought additional oxygen necessary for the complete combustion of the polymer. As shown in Figure 3.15a, a thermal profile was performed first bringing the molds to 380°C with a ramp of 5°C/min and dwelling there for 1 h, then increasing the temperature to 750°C with the same temperature rise rate and holding this hot state for 3 h. At this stage, all residual carbon was oxidized and any ashes were flushed into the ventilation system above the oven. The oven was then switched off and allowed to cool slowly over a period of 6 h to minimize thermal shock. Below 50°C, the molds could be removed and cleaned. Due to the lower polymer density in the infiltration canals (larger 3D-printed surfaces have this property), small salt growths could sometimes be seen on the inner surfaces of the canals. Holding the mold upside-down to prevent them from falling in, these growths were scratched away carefully using a sharp tool (Figure 3.15b).

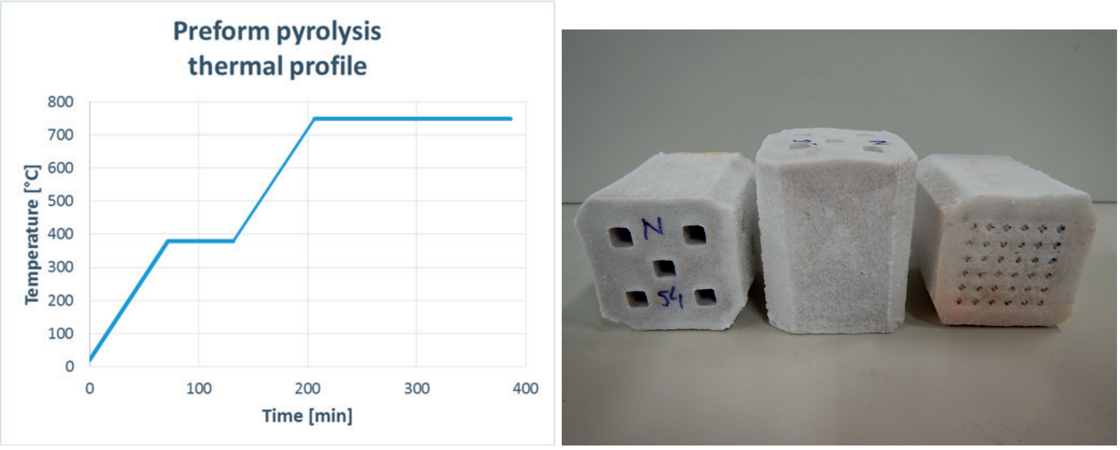

(a) (b)

Figure 3.15 – (a) Thermal time profile used for polymer pyrolysis and (b) molds after preform removal before casting

3.1.10 Casting

The molds were infiltrated with molten AlSi12 aluminum alloy during the casting step of the process. A cast iron chamber of slightly conical shape (1.4°) with an inner diameter of 14 cm at the bottom, a height of 20 cm and a wall thickness of 8 mm was manufactured to this end. The chamber included a 10 mm-thick milled flange with 16 M6 threaded holes (Fig. 3.16).

(a) (b)

Figure 3.16 – Chamber manufactured for the casting of AlSi12 aluminum alloy into the salt molds from (a) top and (b) side views

A matching circular steel lid, 19 cm in diameter and having a thickness 5 mm was also manufactured, and bolted to the chamber through holes added on the outer rim to accommodate M6 16 mm fasteners (DIN912/ISO4762 12.9 Black steel). A 8 mm hole was drilled in the center of the disk to allow the welding of a 50 cm long steel feed-through tube. This feed-through served to pull a vacuum from the chamber and pass a thermocouple for temperature monitoring. At the end of the tube a brass T-section was crimped to separate the vacuum and the sensing functions, the former achieved by crimping a copper tube (the U-shaped set of elements serving as a handle) and the latter achieved with a crimped airtight feed-through (Figure 3.17). The bottom surface of the lid was milled to improve chamber tightness.

Figure 3.17 – Lid manufactured for the casting of AlSi12 aluminum alloy into the salt molds

A graphite coating (Graphit 33, Kontakt Chemie, Iffezheim, Germany) was manually sprayed onto the inner walls of the chamber to favor the demolding of the part after casting, as shown in Figure 3.16a. The molds were then placed directly on the bottom of the chamber with the infiltration canals facing up (Figure 3.18a). A 10 mm layer of large grain salt (larger than 0.4 mm in diameter) was poured into the bottom of the chamber around the molds (Figure 3.18b). Then, fine grain salt (smaller than 125 µm) was added up to the level of the molds. In order to prevent local agglomeration of the fine salt, the pouring was interrupted 2 to 3 times and the chamber lightly manually rotated back and forth along its axis for 10 s (Figure 3.18c). A 12 cm sealed quartz-glass tube was sunk into the salt to accommodate the thermocouple and prevent its direct contact with the molten metal (Figure 3.18d).

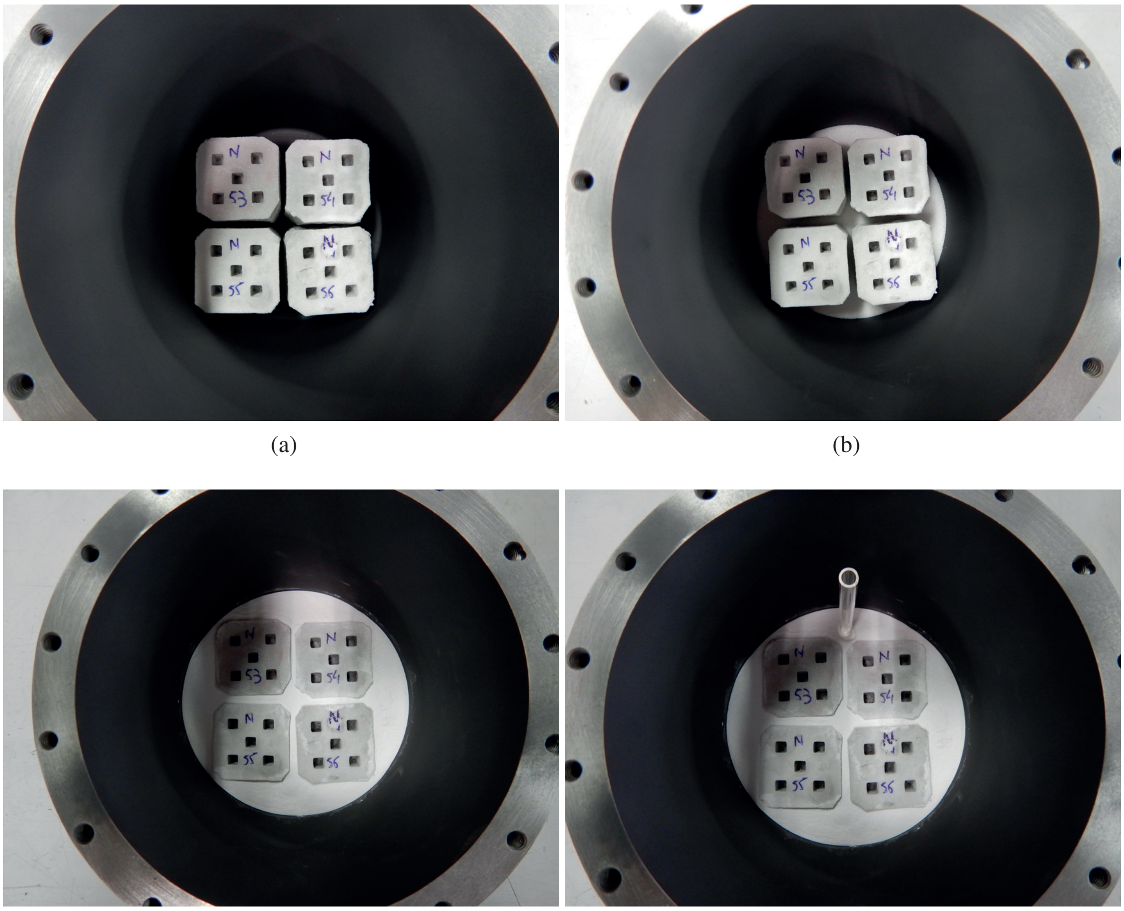

(a) (b)

(c) (d)

Figure 3.18 – Positioning and preparation of the molds into the casting chamber before infiltration. (a) Placing of the molds inside the chamber, (b) pouring of a 1 cm layer of large grain size salt (above 0.4mm), (c) chamber filled with finer grain size (below 0.125 mm) and (d) glass tube to protect the thermocouple

A 2 kg AlSi12 ingot was cut in two and its outer surfaces sanded down to eliminate any oil residue. The cleaned ingots were gently positioned in the chamber on top of the molds, being careful not to damage the fragile salt molds (Figure 3.19a). In order to seal the chamber, a multilayer ring was built up layer by layer on the flange. Here we started by applying a thermal paste (Dow Corning lubricant G-n, Dow Corning, Midland, Michigan, USA) with a paint brush obtaining a homogeneous 0.5 mm thick coating. A 0.2 mm thick graphite paper ring (Ucar Carbon Company, Parma, OH, United States) was added; a second layer of thermal paste applied; a second graphite ring was then added and a last coating of thermal paste completed the seal (Fig. 3.19b). The lid was then placed taking care to align the 16 through holes to the corresponding threads (Figure 3.19c). Holding the lid in place, the seal was punched through using the 16 holes as guides, and a layer of thermal paste painted around them. All the M6 fasteners could then be inserted (with washers between head and lid) and tightened sequentially as shown in Figure 3.19d, one-eighth of a turn at a time to keep the lid parallel to the flange.

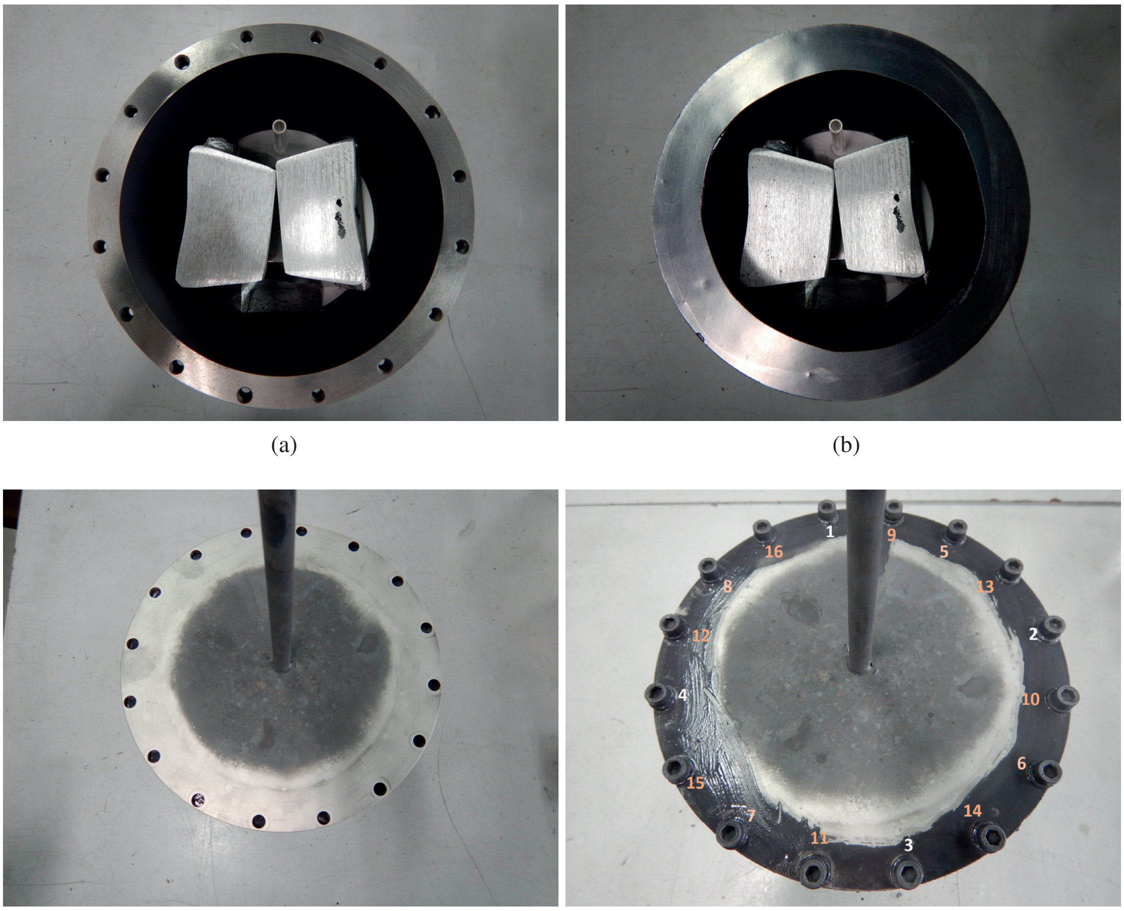

(a) (b)

(c) (d)

Figure 3.19 – Closing of the chamber before investment casting. (a) metal ingots are placed on top of the molds, (b) carbon joints and thermal paste are applied to the flange, (c) lid positioned on top of the chamber and (d) sealing of the chamber with 16 M6 fasteners (numbering shows tightening sequence)

Thermal insulation composed of two layers of silica wool with a total thickness of 10 mm was wrapped around the conical side of the chamber and secured with steel wires (Figure 3.20a). The test set-up was then connected to a vacuum pump (Adixen OME 25 S (Pfeiffer Vacuum, Asslar, Germany) as shown in Figure 3.20b, and placed in the oven (Figure 3.20c). Refractory bricks and silica wool were added to close the cavity as the oven was operated in open configurations (Figure 3.20d).

(a) (b)

(c) (d)

Figure 3.20 – Connection of the chamber to the vacuum pump and positioning inside the oven for casting. (a) 10 mm Silica wool wrapped around the chamber and maintained in place with steel wires, (b) connection of the chamber to the vacuum pump, (c) placing of the chamber into the oven and (d) closing of the oven with refractory bricks and silica wool.

The thermocouple was connected to a multimeter (54 II thermometer, Fluke company, Everett, WA, United States) before starting the slow extraction of air with the vacuum pump (about 200 mbar/min), slow extraction being used in order not to disturb the fine salt placed around the molds. A vacuum well below 10 mbar was maintained until infiltration, reading being taken on the pressure gauge located near the pump. The oven was then set to a temperature of 750°C, heating with a ramp of 5 to 10°C/min. Once, the temperature inside the chamber was near 660°C, the endothermic melting of the alloy melting caused it to drop by 50-60 °C before rising again, indicating that the entire mass of metal was now liquid. It was decided to wait until the 660°C reading was reached again before starting the infiltration.

At this time, the valve of the vacuum pump was closed and air allowed to slowly leak into the set-up until the residual vacuum read on the gauge was 300 mbar. The chamber was removed from the oven and positioned on a 60 mm-thick copper stack placed on an anvil (three 20 mm-thick disks were available in the laboratory, Figure 3.21a). As there is no silica wool under the base of the chamber, this configuration provided the heat sink necessary for the directional solidification of the casting (Figure 3.21d). Vacuum in the chamber was held at 300 mbar over the next 30 min until solidification was complete. Then the vacuum was switched off and the set-up allowed to cool down to ambient temperature (duration about 5 h).

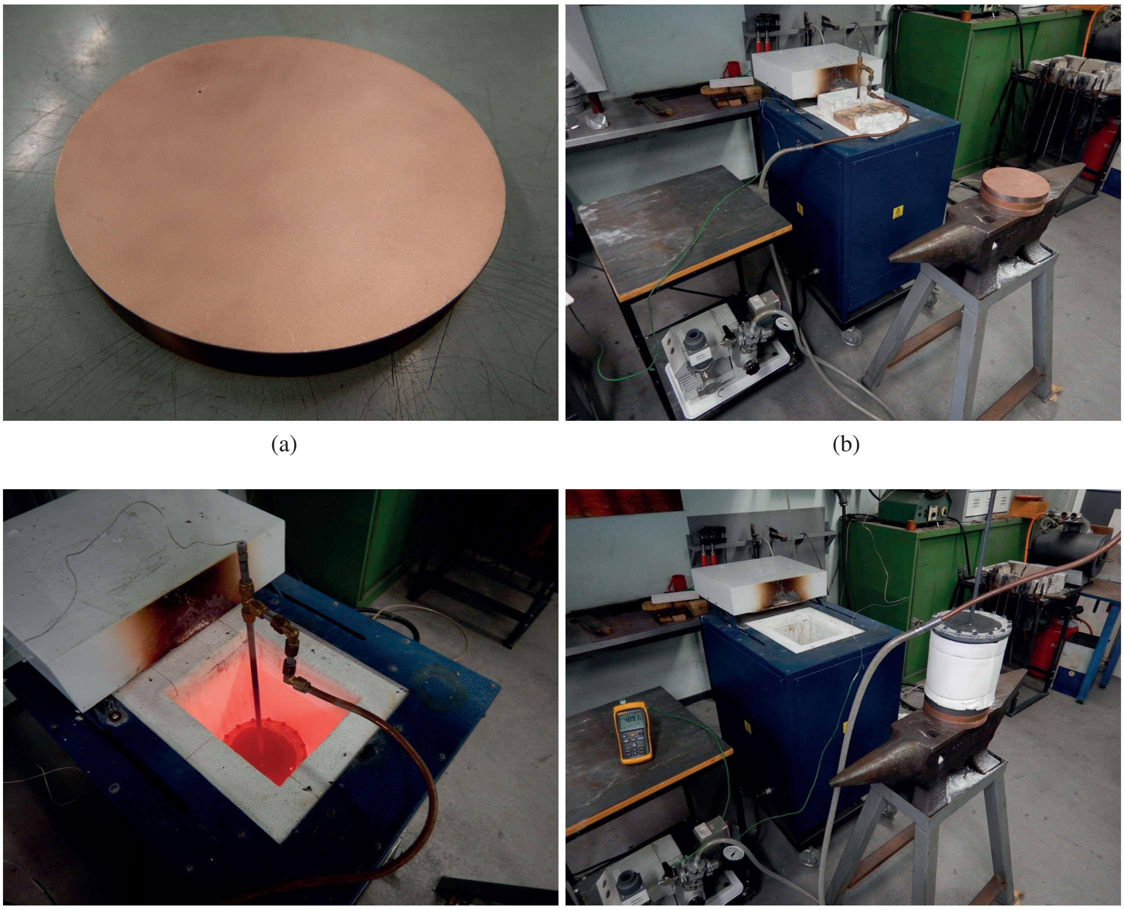

(a) (b)

(c) (d)

Figure 3.21 – Infiltration and cooling of the chamber. (a) Copper disk used as an heat sink, (b) Full casting set-up with cooling promoted by three copper disks and an anvil, (c) chamber right before cooling and (d) chamber during cooling.

Once the chamber reached ambient temperature, vacuum and thermocouple were disconnected (Figure 3.22a, white residues are from oxidation of thermal paste). After removing M6 fasteners, the lid could be lifted and care had to be taken not to damage the thermocouple as it slid out of its quartz tube (Figure 3.22b). After removing the seal from the flange, the casting was extracted from the chamber by tilting it over slowly. It was noted that the casting slid out easily due the graphite coating applied as well as the conical geometry of the chamber (Fig.3.22c). The fine salt around the molds was only lightly sintered, so care had to be taken while taking the casting and placing under a stream of hot tap water for 3 to 5 min, allowing the four samples to be revealed (Figure 3.22d). The thin alloy layer that was in contact with the bottom of the chamber was peeled off before the individual samples were separated from the bulk of the casting at the level of the infiltration canals.

Every time before re-use, the top of the flange and the bottom of the lid were carefully controlled and sand-blasted to ensure chamber tightness.

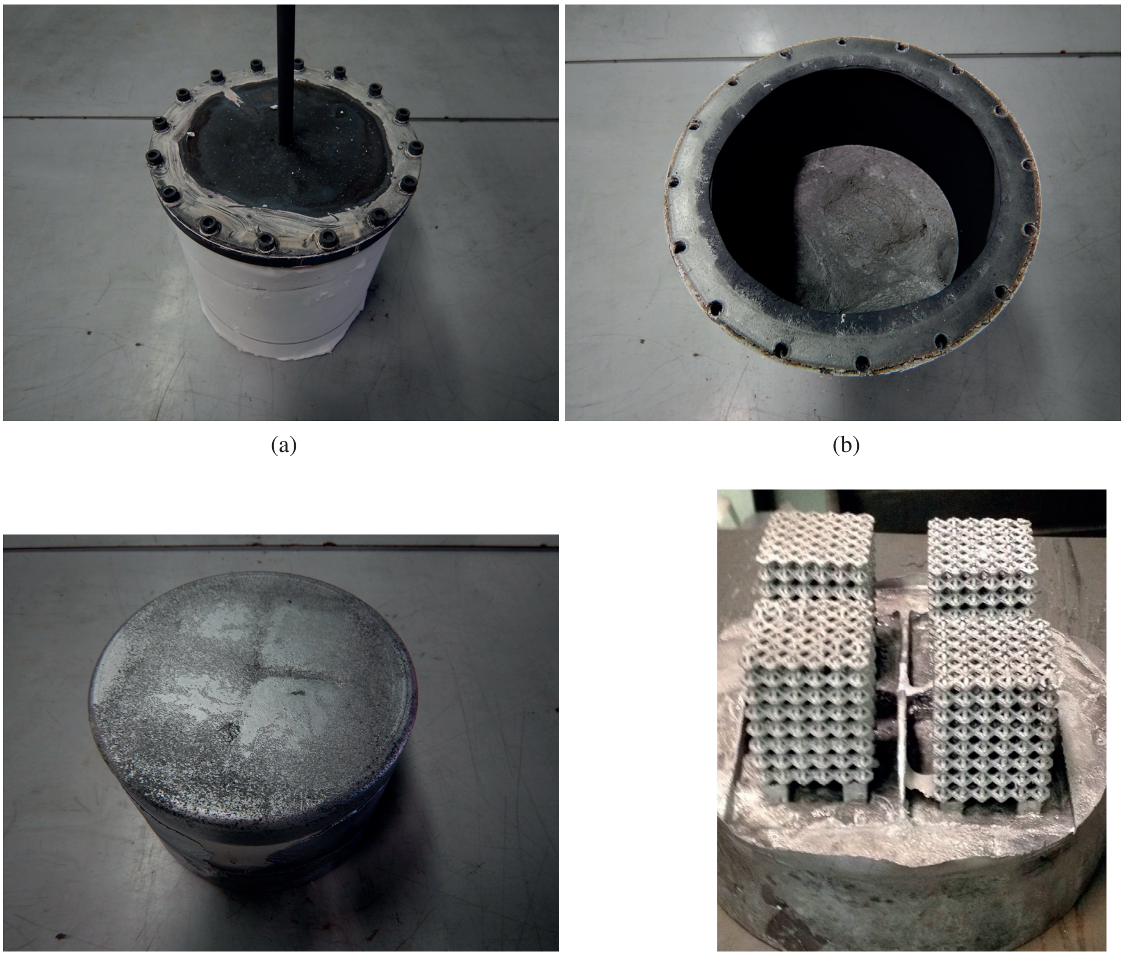

(a) (b) (c) (d)

Figure 3.22 – Opening of the chamber and extraction of the samples. (a) Chamber disconnected from the vacuum pump right after casting (whitish residues are thermal paste oxidation products), (b) opened chamber, (c) demolded casting and (d) samples still connected to the metal mass and gating

3.2 Process development

3.2.1 Preform fabrication

Six different materials and three different production methods were studied. The Fused Deposition Modeling (FDM) using our own 3D printer (Creatr 3D, Leapfrog, Alphen aan den rijn, The Netherlands), was investigated with PolyLactic Acid (PLA) and Acrylonitrile Butadiene Styrene (ABS). The second technology studied was Selective Laser Sintering (SLS) performed in the AFA-Workshop at EPFL on an EOS machine (EOS GmbH, Krailing, Germany), applied to PolyAmide 12 (PA2200) and Poly(Methyl MethAcrylate) (PMMA). It was decided to procure parts made through stereolithography (Envisiontec Inc, Deaborn, MI, USA and Formlabs, Somerville, MA, USA). Two different polymer preform sets were obtained without having access to their chemical composition as this information was considered proprietary by both suppliers. The main advantages and drawbacks of the different technologies are listed in Table 3.2.

Table 3.2 – Comparison in terms of advantages and drawbacks of the 3D printing methods investigated for the manufacturing of preforms

	Advantages	Drawbacks
FDM	- Best price - Relatively low mechanical properties of polymers (PLA) - No residues after burning (PLA)	- Topology restrictions - Lowest resolution - Residues after burning (ABS)
SLS	- Good resolution - Almost no restrictions in topology (except for powder removal) - No residues after burning (PMMA and PA2200)	- Relatively strong material (PA2200) - Depowdering of the part (for small unit cells) - Porosity of the part - Expensive technology
Stereo-lithography	- Best resolution - No restrictions in topology - No residues after burning (Envisiontec and Formlabs)	- Strong material (Envisiontec and Formlabs) - Expensive technology

Seven criteria were chosen to compare materials and technologies against each other. They are, in order of decreasing importance:

- **Flexibility:** user-friendliness of access to machine parameters.
- **Mold compatibility:** compliance between polymer and mold with respect to mold cracking.
- **Availability:** time to obtain redesigned preforms.
- **Pyrolysis residues:** minimum residues after pyrolysis.
- **Topology restrictions:** minimize structural design restrictions (bridges, overhang, smallest features).

- **Resolution:** Geometrical compliance between designed and manufactured parts.
- **Cost:** recurring and non-recurring costs.

Table 3.3 shows the trade-off matrix where the ranking for each criterion is from 1 (most advantageous) to 3 (most inconvenient). Ranking was obtained by addition of scores. As seen PLA by FDM was the best combination.

Table 3.3 – Trade-off matrix for polymer-manufacturing method selection

	FDM		SLS		Stereolithography	
	ABS	PLA	PMMA	PA2200	Envisiotec	Formlabs
Flexibility	1	1	2	2	3	3
Mold compatibility	1	1	1	1	2	2
Delivery delay	1	1	2	2	3	3
Burning-out residues	2	1	1	1	1	1
Topology restrictions	3	3	2	2	1	1
Resolution	3	3	2	2	1	1
Cost	1	1	2	2	3	3
Trade-off index	**12**	**11**	**12**	**12**	**13**	**13**

3.2.2 Sample sizing

In our case, sample size was driven by process parameters as well as the equipment available in the laboratory. On the process side, the drying time of the salt mold is critical. For example, a 150 cm^3 part takes 4 days to dry while this time is multiplied by 6 for a volume 2500 cm^3. The inner volume of our oven (Section 3.1.8) defines the maximum size of the infiltration chamber. It was decided to produce four samples simultaneously. Considering the maximum size of the molds able to fit in the chamber, the remaining cross-section for the samples was 40x40 mm^2 taking into account 5 mm of wall-thickness margin for the mold. The requirement to have full cells (cell size defined to be 6 mm, see Section 3.2.1 for further details) led to 6 x 6 cells in the horizontal plane. A height of 8 cells was chosen for each sample as they were manufactured to be tested in compression using cubic specimens. To ensure a homogeneous distribution of alloy, 20 mm long infiltration canals were added in five locations on top of each sample. Table 3.4 summarizes the size of the PCS sample preform and the inner part of the mold shaping set-up.

In order to estimate process parameters, a set of smaller samples (4 x 4 x 6 cells, 6 mm cell size, Diamond lattice) used with a smaller existing infiltration set-up were produced. This allowed to predetermine some critical elements such as salt grain size and infiltration pressure as well as the feasibility of the process in general.

Table 3.4 – Sample and set-up size definition based on lab equipment restrictions

	PCS	Inner part of set-up
X	36 mm (6 cells)	50 mm
Y	36 mm (6 cells)	50 mm
Z	68 mm (8 cells + infiltration canals)	70 mm

3.2.3 Salt grain size selection

The salt's grain size distribution is the main parameter influencing the quality of the mold replication process, i.e. the quality of the cast part. The denser the packing during the shaping process (see Section 3.1.6), the better the outcome of the final part. Mold integrity relies on the recrystallization of dissolved salt in the solvent acting as a bond between the salt grains. It was decided to trade-off between two characteristics:

- electrostatic forces; for small grain sizes (less than 90 µm) these tend to hinder dense packing.
- surface to volume ratio; needs to be kept sufficiently high to enhance bonding during salt precipitation upon drying

Four different batches of salt were investigated during this study:

- **Fluka :** provided by Fluka company (branch of Sigma-Aldrich company, St-Louis, USA).
- **CP1 Milled:** provided by Les salines suisse (Bex, Switzerland); milled (mean size distribution of 50 µm).
- **CP1:** procured from Les salines suisse (Bex, Switzerland); standard commercial cooking salt (mean size distribution of 250 µm); ground in our lab.
- **MARSEL :** provided by Zoutman (Gent, Belgium).

By sieving the salt with an amplitude of 0.3 mm for 10 min (See Section 3.1.3 for further details), different grain size distributions were obtained. Figure 3.23 shows scanning electronic microscope images of the four different salts with the same grain size distribution. Two trends could be observed, the shape factor and the surface roughness. The CP1 Milled and the Fluka had a more uniform grain shape, the former having a higher surface roughness than the latter.

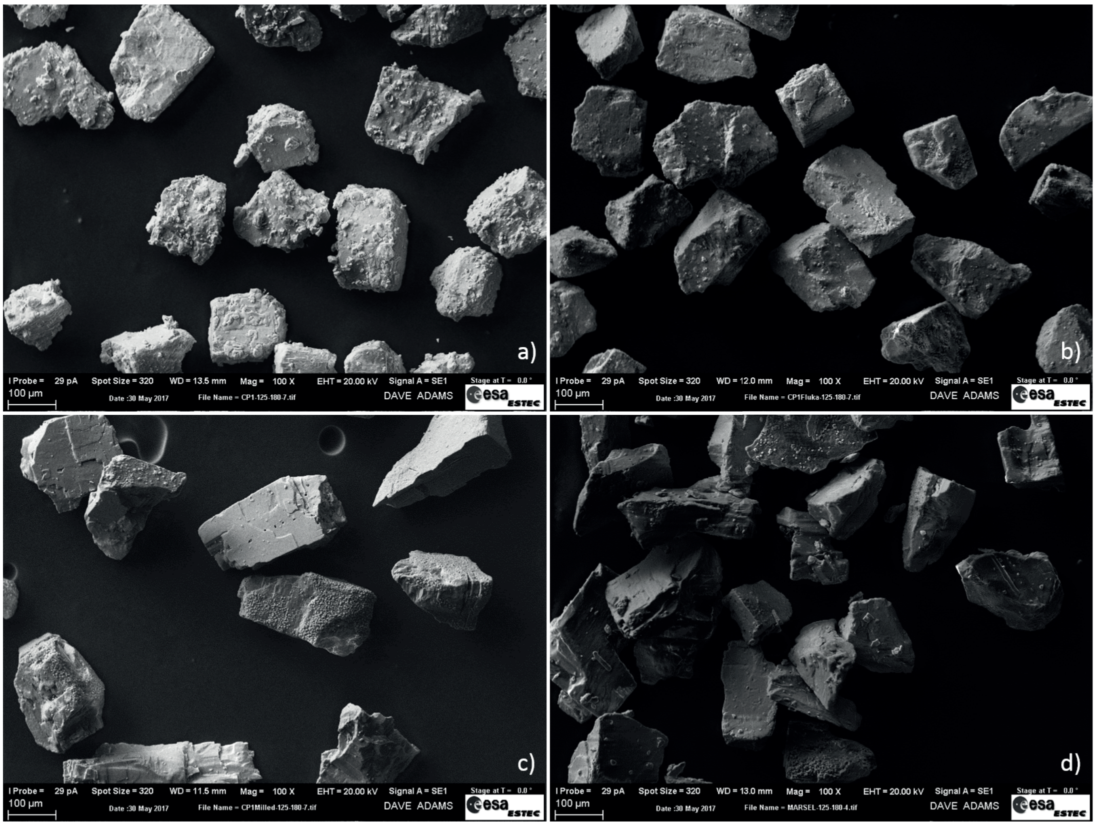

Figure 3.23 – SEM Images of the four different salts (x100), a) CP1, b) Fluka, c) CP1 Milled and d) MARSEL. The grain size distribution in these pictures is between 125 and 180 µm

Different salt samples were prepared from all batches with seven mean grain size intervals between 20 µm and 325 µm, and added into a solvent-filled glass tube. The tube had an outer diameter of 16 mm and a wall thickness of 1.7 mm. It was closed at one end with a layer of filter fabric and a layer of latex, placed on the shaker (section 3.1.6) to reflect as close as possible the mold shaping conditions.

To estimate the packing density, 20 mL of solvent (see Section 3.1.5) were poured into the tube and 5 g of salt sample added and shaken for 10 min. The packing density was derived from residual height of the powder measured with a caliper (Heng Liang company). The result was then normalized to the density of bulk salt, 2,16 g/cm^3 and expressed in percentage.

Additional packing occurs whilst draining; in order to estimate this, the latex was peeled off, the tube with the fabric filter placed on absorbent paper (for 10 min, displacing the tube every minute) and the difference in residual height measured. Figure 3.24 illustrates these process steps, which were conducted three times for every salt sample.

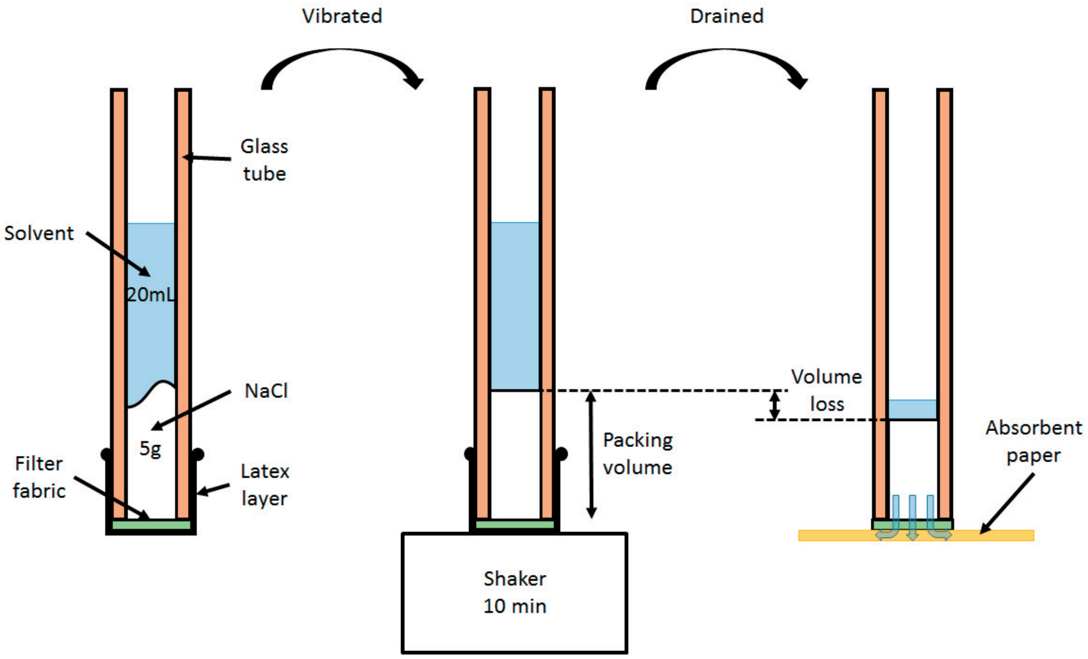

Figure 3.24 – Sketch of set-up used to define the relative packing density into solvent and volume loss during draining

Figure 3.25 shows the normalized packing density for different salt samples. It increases asymptotically to reach a maximum around 63% when NaCl particle sizes exceed 225 µm. First castings with a mold from NaCl with an average grain size of 220 µm showed unsatisfactory results with respect to the sample's overall aspect. Choosing an average grain size of 150 µm produced promising results (Figure 3.26). A plausible explanation for this difference is that the higher grain size in the first run hindered the homogeneous distribution of precipitated salt, leading to unwanted asperities in the casting.

Considering the influence of the grain shape, heterogeneous distributions (corresponding to a higher shape factor, CP1 and MARSEL) led to NaCl lower packing densities.

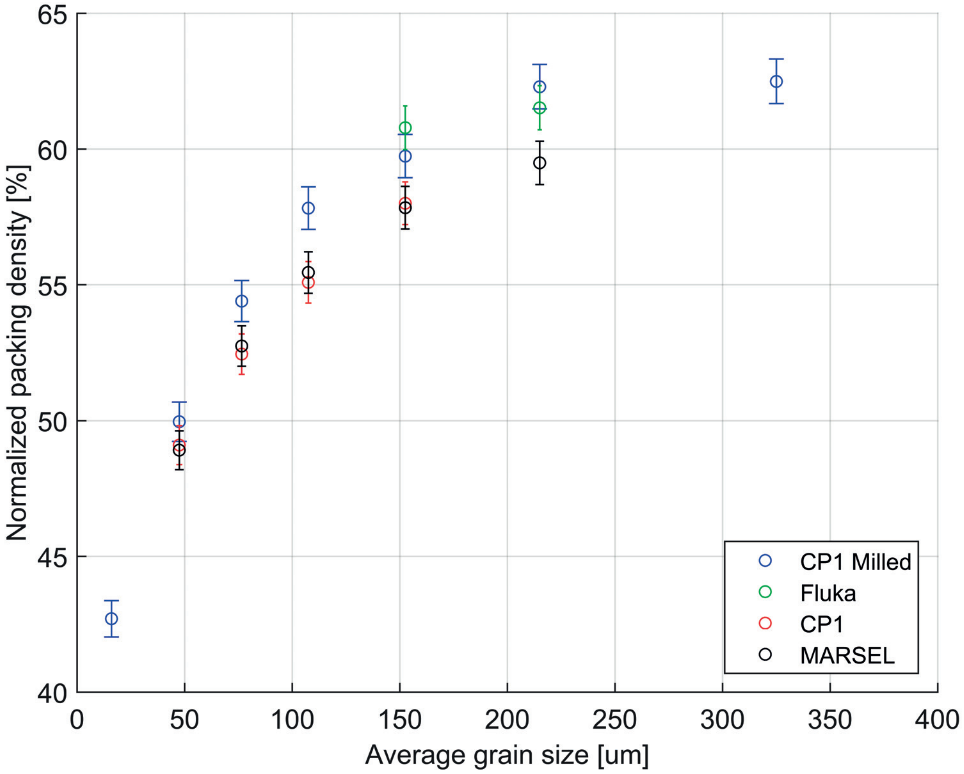

Figure 3.25 – Normalized vibrated salt packing density in solvent

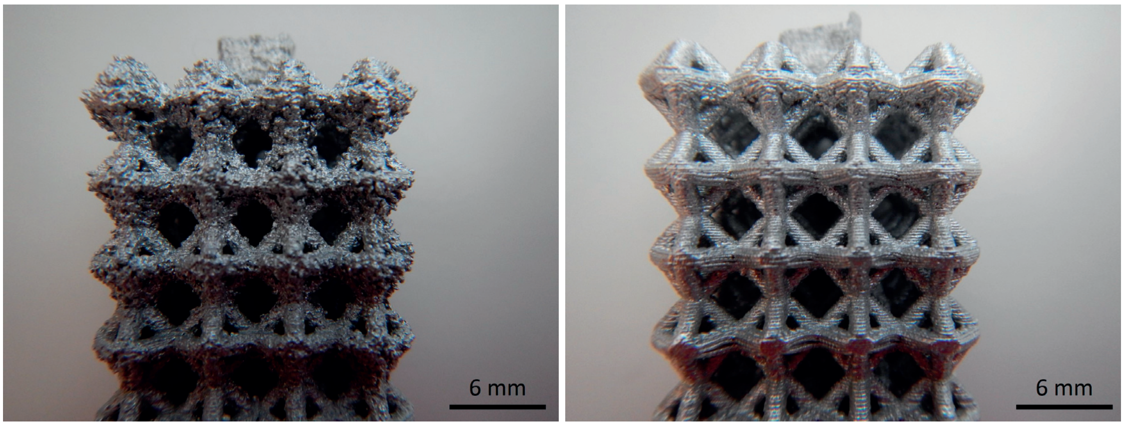

(a)

(b)

Figure 3.26 – Effect of reduced grain size on the quality of the cast part. (a) PCS cast with Fluka salt of average grain size 225 µm, (b) PCS cast with a Fluka salt of average grain size 150 µm

Figure 3.27 shows the volume loss during draining as a function of the grain size distribution. This result confirms the need to select large average grain sizes, so as to minimize volume loss.

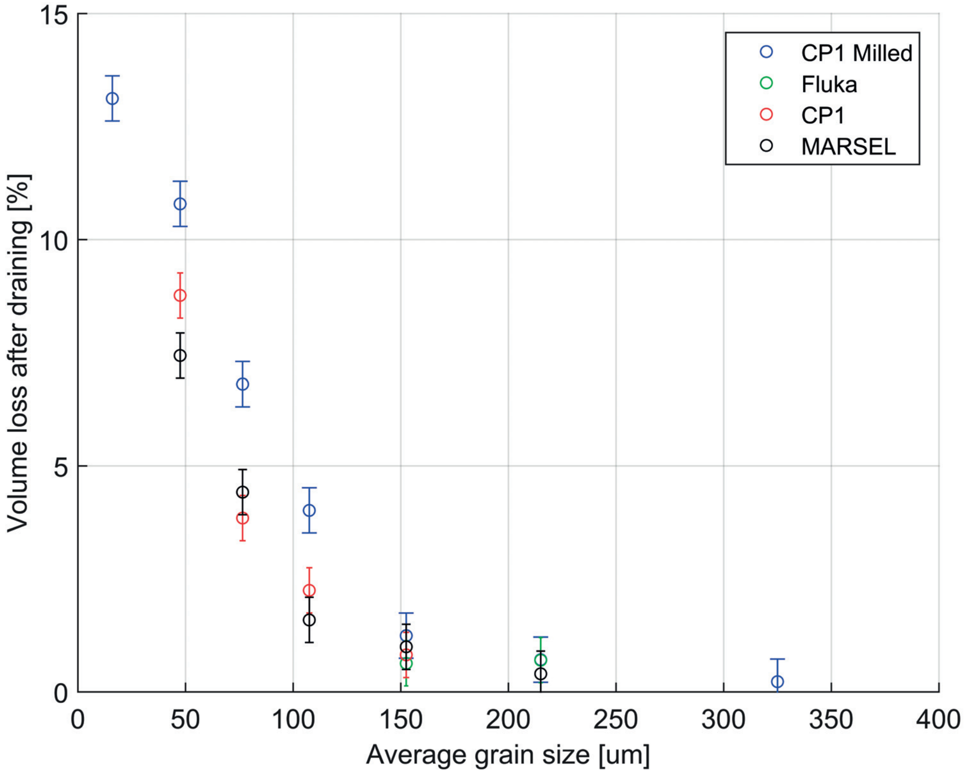

Figure 3.27 – Volume loss of vibrated salt packing during draining

To conclude, it has been found that an optimal average NaCl grain size of 150 µm allows a reasonably high packing density, a low volume loss after draining, whilst maintaining a good overall aspect of the final resulting cast sample. Thus, only salt retrieved between the 125 µm and the 180 µm sieves was used for the manufacturing of the full-size samples. This implied that a normalized packing density between 57 and 61% and a draining volume loss lower than 2% could be achieved.

3.2.4 Salt batches selection

All salt batches were sieved for 10 min at an amplitude of 0.3 mm in a stack with decreasing mesh sizes; 400, 250, 180, 125, 90, 63, 32 µm, respectively (see Section 3.1.3). The volume fraction in each sieve was weighed and normalized with respect to the total mass poured into the sieving machine Figure 3.28 shows the size distribution for different batches of salt.

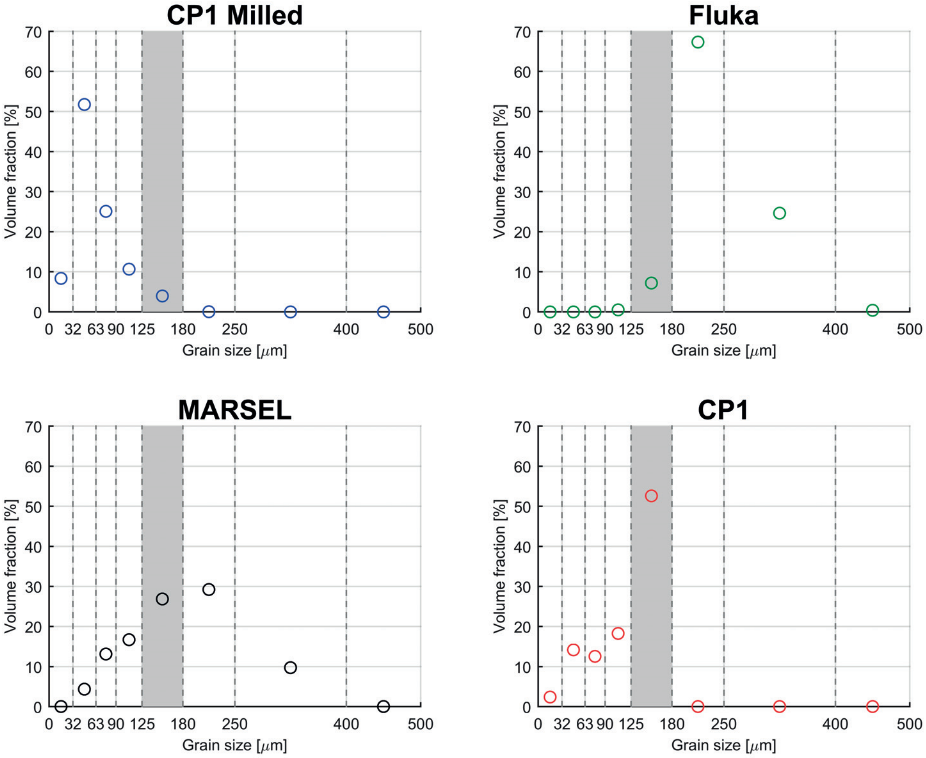

Figure 3.28 – Salt distributions according to batches. Dash lines represent the different mesh size available for the sieving process. The grey area represents the selected distribution used, [125-180] µm

As MARSEL and CP1 batches contained a significantly higher fraction of useful grain sizes (see Table 3.5), these two were mainly.

Table 3.5 – Volume fraction of selected grain size distribution (125 to 180 µm) for the different salt batches

CP1 Milled	4 %
Fluka	7 %
MARSEL	27 %
CP1	53 %

3.2.5 Determination of vibration time for packing

The time needed to achieve sufficient NaCl packing density was obtained by repeating the packing operation (Section 3.2.3) for different lengths of time and measuring the density; a 97% density was considered sufficient. It was observed that for all batches, 30 s of packing under vibration was sufficient (Figure 3.29).

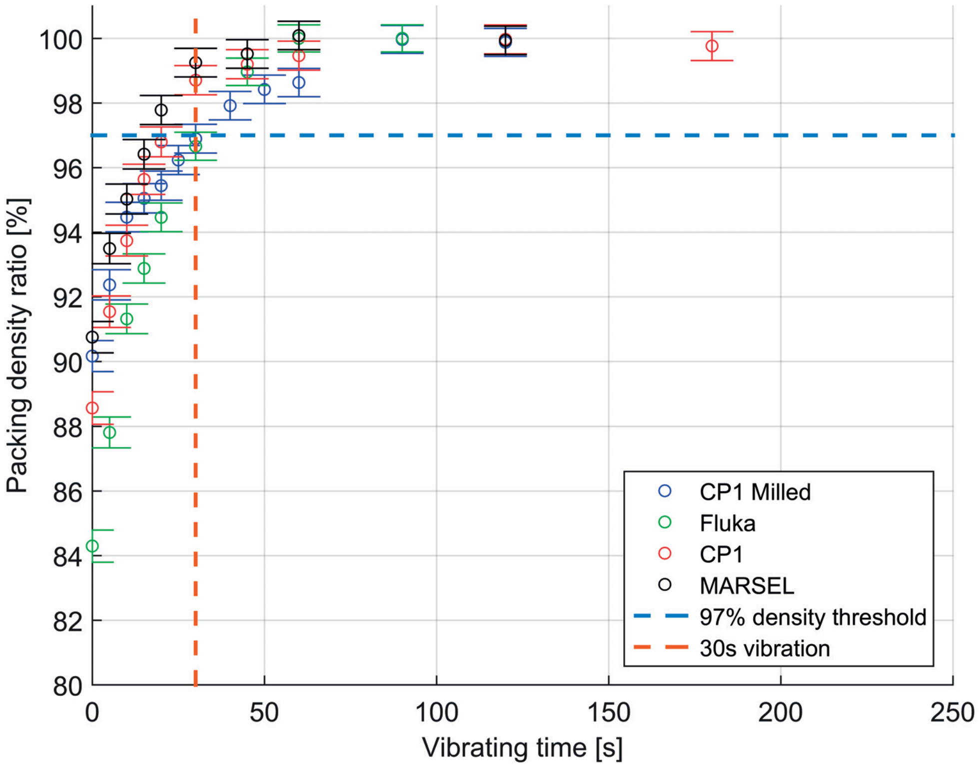

Figure 3.29 – Salt packing density evolution according time vibrated for the selected grain size distribution (125 to 180 µm)

3.2.6 Set-up development and optimization

The performance of the set-up (Section 3.1.4) relied on the capacity to drain the solvent through its base before removing the segments to accelerate drying of the mold. The set-up was designed and manufactured in ABS by FDM in several iterations to optimize shaping, maintaining inner dimensions of 50x50x70 mm^3 (Section 3.2.2).

The first design of the set-up showed a square bottom grid with a simple frame structure (4x4mm^2 struts). The main drawbacks were undersized struts that ruptured during shaping, and the square side plates that could not be well attached and maintained in place.

Increasing the struts to 7x7 mm^2 and changing the side plates to cylindrical segments (and widening the base accordingly) solved the previous drawbacks. This set-up still showed leaks around the segments and between the grid and the kapton tape.

The final design improved sealing by reducing the grid surface and thickening the base, allowing easier and more efficient taping when closing the set-up (higher pressure applied). Figure 3.30 shows the set-up design evolution.

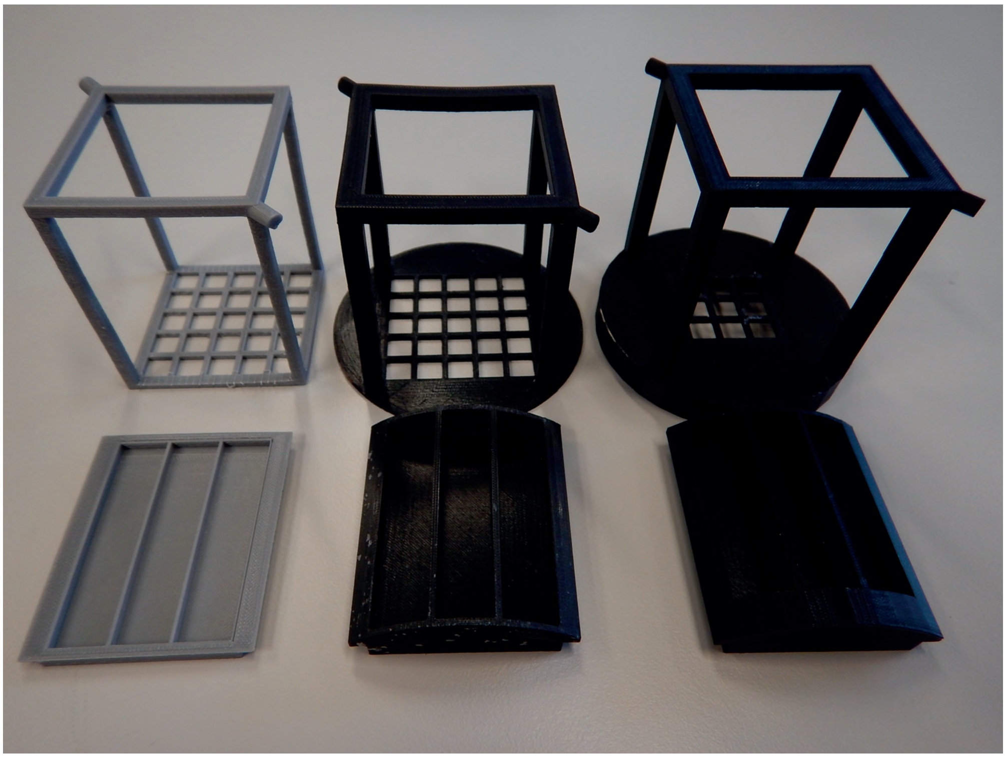

Figure 3.30 – Set-up design evolution from left to right.

3.2.7 Draining

To estimate the time at which cylindrical segments could be removed to accelerate drying (see Section 3.1.7), the set-up filled with salt and solvent was systematically placed on absorbent paper and removed after increasing time periods; structural integrity of the green body and solvent transferred to the paper were determined for each time period. Figure 3.31 shows these results. It was observed that after 37 min (cumulative time of the five periods, each period using a fresh absorbent paper), removal of the cylindrical segments was always possible without effect to the green body, Figure 3.31.

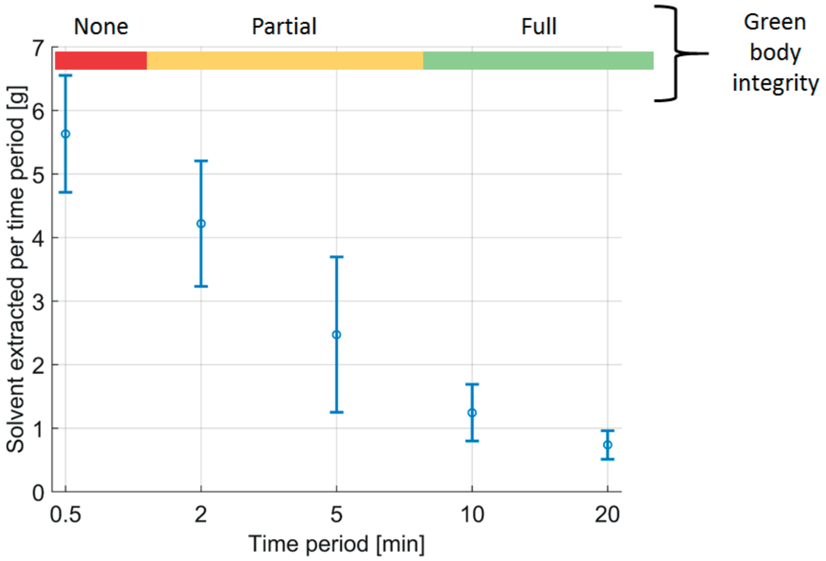

Figure 3.31 – Evolution of the solvent extracted per time period. Color bar represents the corresponding green body integrity from none (red) to full (green).

Note: systematic use of fresh absorbent paper enhances capillary action and diffusion of the solvent; a total weight loss of about 14 g corresponding to 12 mL could be achieved.

3.2.8 Drying optimisation

The set-up itself is designed to allow efficient drying of the molds through the base grid and removable cylindrical segments.

As discussed in Section 3.1.8, drying was viewed as complete once mass loss fell to less than 0.01 g after at least 10h. As the solvent's main composition is water and evaporation could lead to pore formation, the maximal temperature was set to 95 °C; however, at this temperature, it was observed that the ABS set-up was deformed. Repeated tests on ABS samples showed that creep was observed at temperatures higher than 85°C, thus it was decided not to exceed 80°C in this process step.

Although the literature for conventional drying of ceramics describes a gradual increase in temperature during the drying phase of a green body [227], no difference was observed in our cast parts when it was tried; so the temperature can be kept constant at 80°C during the whole drying process.

Ambient humidity also influences the total drying time via the partial vapor pressure in the atmosphere surrounding the molds. The impact of humidity was minimized by leaving the oven door open and creating an air flux (increased convection) by inserting a copper tube under the molds (see Section 3.1.6).

It was observed that the position of the molds in the oven had a significant influence on the quality of the final cast parts. Figure 3.32 shows directional defects (spikes) on a part that was positioned too close to the wall of the furnace. This effect is probably due to the higher temperature of the walls (peaks measured at 120°C), inducing an undesirable temperature gradient that increased the capillary pressure acting on the solvent, eroding channels in the salt that created these spikes. Centering the molds in the oven solved this issue (see Section 3.1.6).

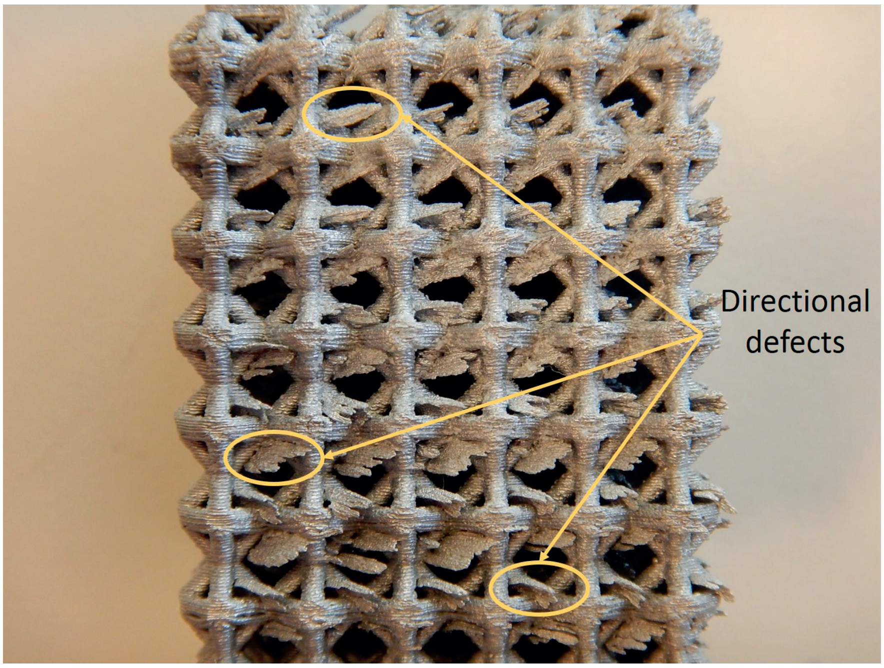

Figure 3.32 – Defects introduced by a temperature gradient during drying

3.2.9 Pyrolysis optimization

The preform ws removed from the mold by pyrolysis. In order to define the process parameters, each polymer's properties were measured using thermogravimetric analysis (TGA) in ESA's laboratory on a TGA/SDTA851 equipment (Mettler Toledo, Colombus, OH, United States). As can be seen on Figure 3.33, the polymer "degradation" temperature is always situated between 350°C and 450°C and the carbon oxidation threshold is clearly visible as these tests were conducted under normal air pressure. TGA tests were performed three times on each sample (5 mg) at different heating rates (5, 10 and 20°C/min); as expected [228], a higher heating rate causes the thermal degradation threshold to be higher. It can be noted that empty alumina crucibles were characterized beforehand to take into account any buoyancy effect that could influence the measurement.

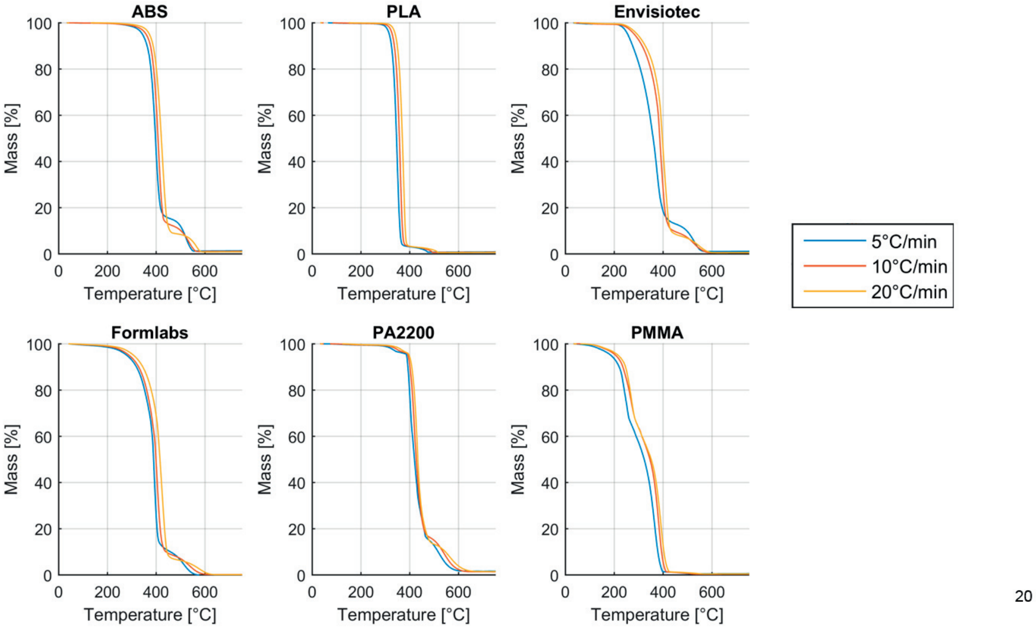

Figure 3.33 – TGA analysis of the 6 different polymers for several ramp. The targeted temperature was 750°C and under air atmosphere

The quality (integrity, polymer residue) of the molds was the main selection criterion for the polymer preform, all types were tested. It was observed that stereolitography resins tend to fracture the mold during pyrolysis, as shown in Figure 3.34.

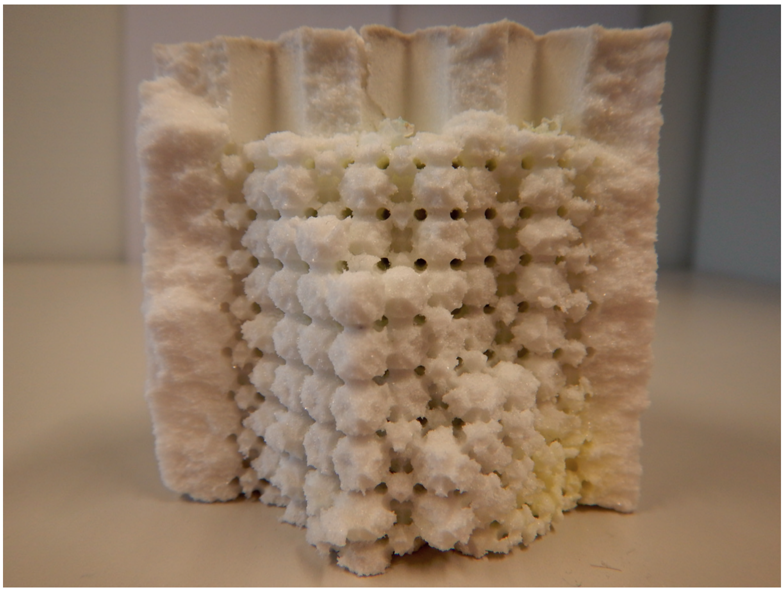

Figure 3.34 – Mold broken during the pyrolysis of a 6 mm Diamond structure made by stereolitography (Envisiotec); yellowish residues can be seen on bottom right corner.

PLA showed best results and was therefore used for the test campaign. For PLA, thermal decomposition takes place between 360°C and 380°C and carbon oxidation ends at 580°C. The thermal cycle described in section 3.1.9 showed satisfactory results. The upper temperature limit during pyrolysis is defined by the melting point of NaCl, namely 801°C. The air flux added during drying was maintained during pyrolysis to promote carbon oxidation.

3.2.10 Casting optimization

The infiltration temperature and pressure are the two main parameters that govern the casting process. A ramp of 5-10°C/min was selected for the heating of the chamber to the desired temperature of 650-670°C. As described in Section 3.1.10, the differential pressure was obtained with a vacuum pump. Five small samples (see section 3.2.2) were produced at different pressures; 100 mbar, 200 mbar, 300 mbar, 400 mbar and 500 mbar.

At 100 mbar differential pressure, no infiltration was observed; at 500 mbar, the metal infiltrated the mold's inner structure, effectively blurring the casting; the other samples were of better quality (Figure 3.35). As a pressure in the middle of the acceptable range, it was chosen to use 300 mbar as infiltration pressure.

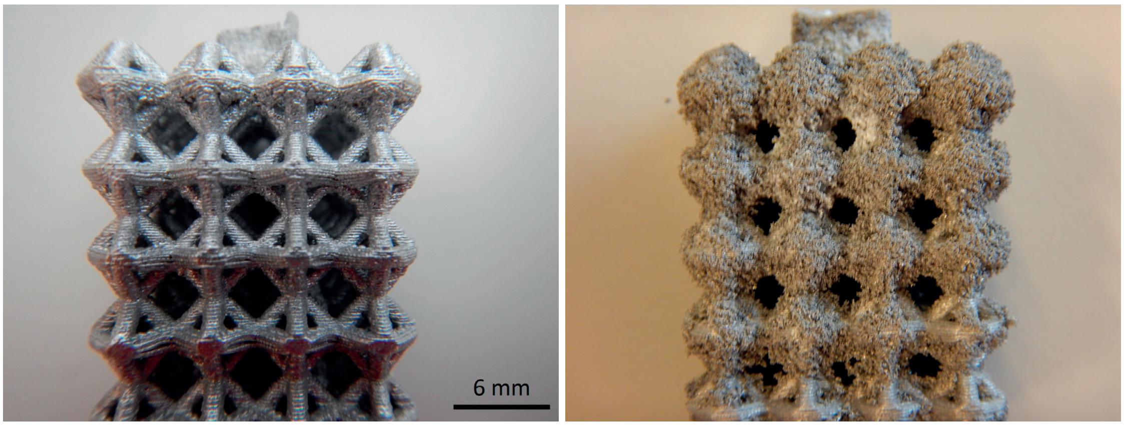

(a) (b)

Figure 3.35 – Influence of the infiltration pressure on the quality of the casting (125-180 µm Fluka salt), (a) with a pressure of 300 mbar and (b) with a pressure of 500 mbar

The first full-size parts cast exhibited solidification shrinkage indicating that cooling was not optimal. To solve this issue, the process was adapted (see section 3.1.10) as follows:

- (i) 10 mm-thick silica wool was wrapped around the chamber to insulate against lateral heat loss.
- (ii) a copper heat sink was placed between anvil and chamber to enhance thermal conductivity.

- iii) coarser salt was poured first into the chamber to form a layer (about 10mm high) that partially prevented the finer salt filler from moving under the molds at the bottom of the chamber; thus hindering the heat extraction.

These changes led to the successful suppression of solidification shrinkage within the cast PCS as shown in Figure 3.36.

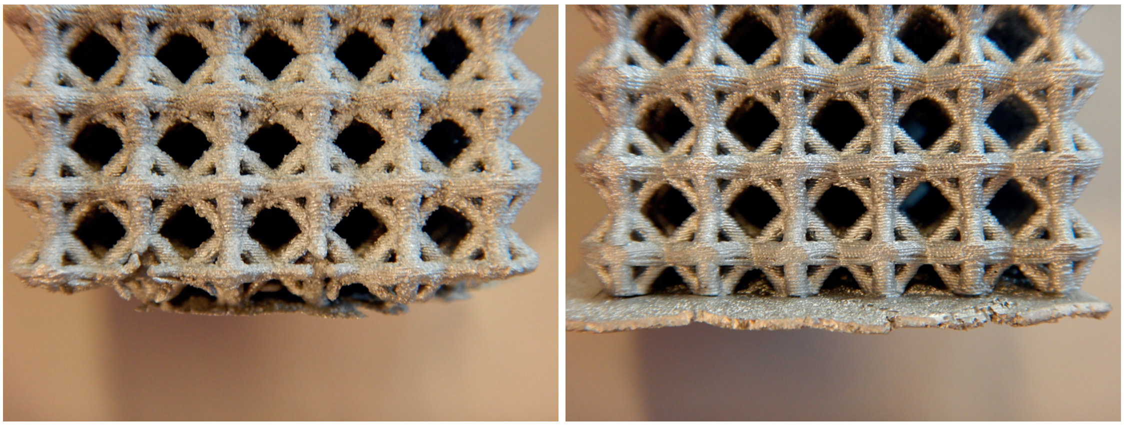

(a) (b)

Figure 3.36 – a) Solidification shrinkage highlighting the incapacity of the set-up to extract fast enough the heat from the bottom to promote directional solidification. b) Heat extraction sufficient to induce directional solidification and prevent solidification shrinkage.

3.3 Periodic cellular structures

This section describes the samples produced by the investment casting process and their characterizations. It focuses on (i) porosity, defects and topology, (ii) microstructure characterization, (iii) measurement of mechanical properties.

3.3.1 Experimental methods

Samples

Samples used in this study were Diamond type periodic cellular structures with a unit cell of side 6 mm and a targeted relative density of 30%. Specimens were cast in AlSi12 aluminum alloy by replication of a sacrificial polymer preform as described above in Sections 3.1 and 3.2). From the casting, samples were produced with a dimension of 36 x 36 x 48 mm^3 corresponding to 6x6x8 cells in each of the X,Y and Z directions, respectively. Samples were trimmed to shape by grinding of excess material from infiltration canals and solid bottom layer. For mechanical tests, the top and the bottom cell layers were removed rendering a 36 x 36 x 36 mm^3 (6 x 6 x 6 cells) cube as can be seen in Figure 3.37.

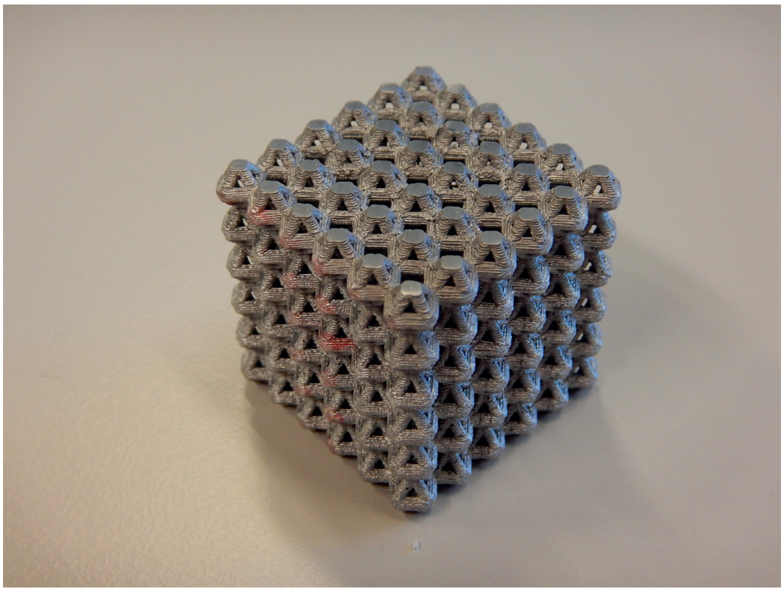

Figure 3.37 – Sample use for mechanical testing (quasi-static compression)

3D-Tomography: porosity, inclusions and topology analysis

A total of five samples were analysed by CT-scanning. 3D-tomography was performed in the exact same way as for the printed samples manufactured by SLM (see Section 2.3.2).

Metallography: microstructure analysis

Metallographic preparation and analysis were also performed in the exact same way as for the printed samples manufactured by SLM (see Section 2.3.1) except that no chemical etching was done on cast samples.

Quasi-static compression: mechanical properties

Compression tests were conducted in the exact same way as for the printed samples manufactured by SLM (see Section 2.3.3). The cast PCS showed significantly different behavior under test (Figure 3.41).

The plateau stress is defined as the mean stress value between 20 and 60% of deformation. The peak stress, as it names implies, is taken as the maximal stress reached before entering the plateau regime. The densification strain highlights the end of the plateau phase, and is defined as the strain at which the stress reached 1.3 times the plateau stress. As no rupture was observed in the cast sample, the absorbed energy was calculated up to the point when the densification strain was reached. The energy absorption efficiency is defined as the ratio between the measured and the ideal energies, the latter estimated by multiplying the peak stress with the densification strain ([222]).

3.3.2 Results

3D-Tomography: porosity, inclusions and topology

Table 3.6 shows porosity and inclusion quantifications for the five samples tested as well as the mean size of defects.

Table 3.6 – Average porosity and inclusion contents and mean sizes for the five different samples tested. ± stands for the standard deviation

	Porosity		Inclusion	
Sample	10^{-2}.[%]	[µm]	10^{-4}.[%]	[µm]
#1	1.3	168 ±83	0.3	194 ±60
#2	1.4	164 ±67	3.9	230 ±74
#3	3.1	200 ±123	0.7	234 ±108
#4	1.7	168 ±63	4.5	259 ±224
#5	1.7	188 ±100	9.5	236 ±124
All samples	1.8 ±0.7	178 ±89	3.8 ±3.7	231 ±120

The topology was characterized by analyzing the mass distribution inside samples. Specifically, the relative density of metal from the bottom to the top of the sample was measured.

An entire sample (6x6x6 cells) was divided into 6 different horizontal cell layers (6x6x1 cells). For each layer, the relative density was computed by binarizing the scan-images and counting the white pixels (showing solid aluminum). Results showed that the relative density is not homogeneous; it linearly increases by 0.4% per layer from the bottom to the top of the sample (Figure 3.38).

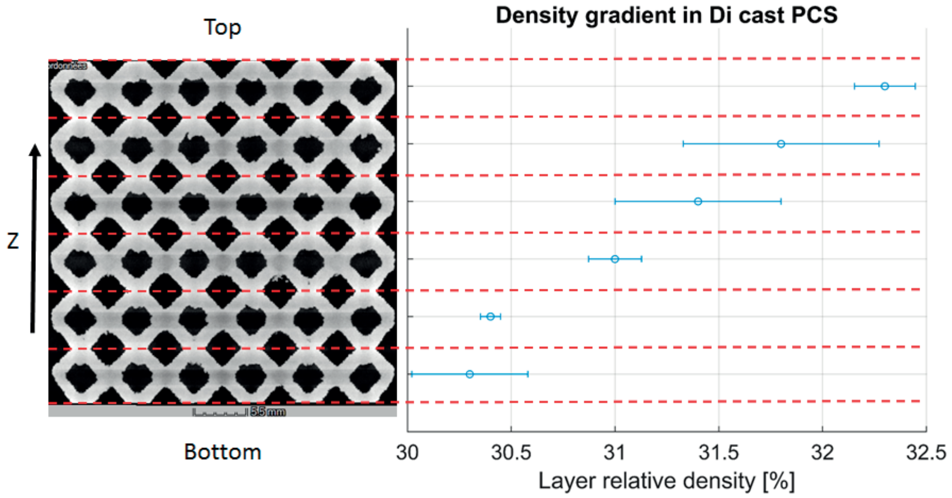

Figure 3.38 – Average relative density evolution in samples (right) and the corresponding image highlighting the layers extracted from a CT-scan

Metallography: microstructure analysis

Samples exhibited a standard near-eutectic aluminum-silicon microstructure (primary aluminum dendrites surrounded by eutectic; lamellar structures alternating aluminum and silicon platelets). A few primary silicon particles (100 µm) were also observed. The microstructure was homogeneous over the whole sample except at the top center (number 1 in Figure 3.39e)) where the eutectic interlamellar spacing is about twice as large as it is elsewhere (13 µm instead of 6 µm).

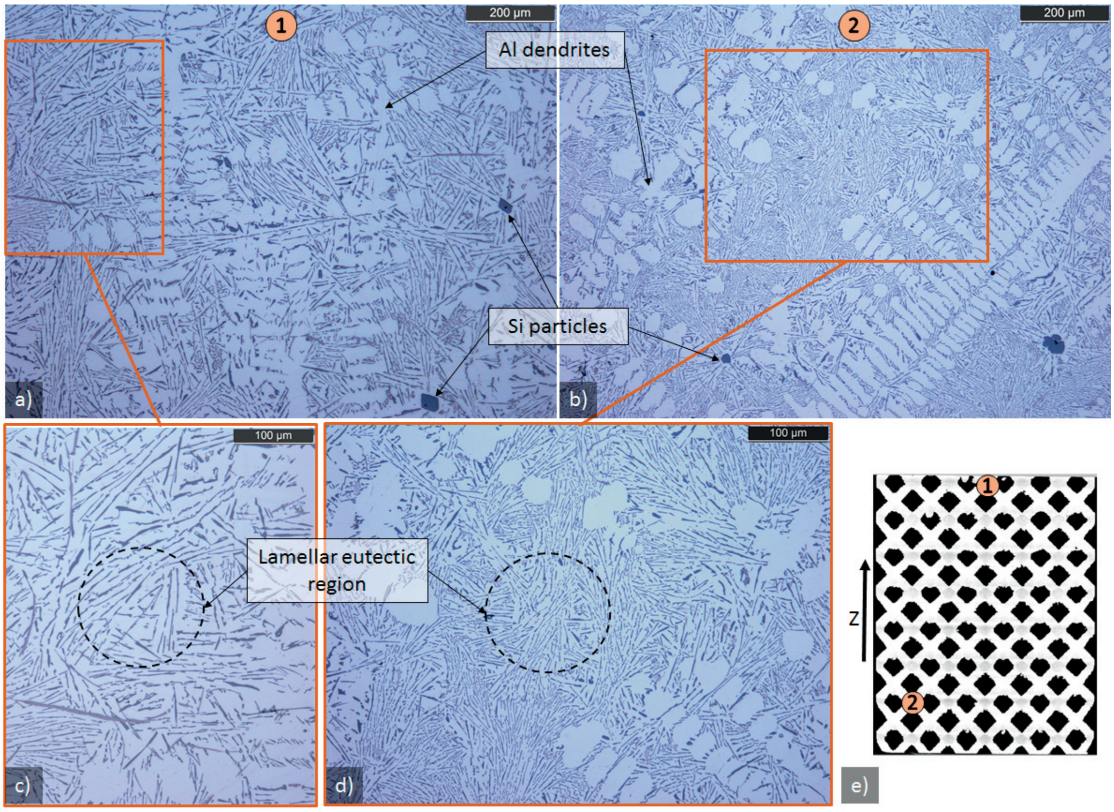

Figure 3.39 – Microstructure of AlSi12 cast PCS x100 (a) and b)) and x200 (c) and d)). Al dendrites, Si particles and lamellar eutectic regions can be observed. Position of the observed areas are displayed by numbers on the sample overview (e))

Deformation and failure mode

Our cast periodic cellular structures exhibited in compression a classical three phases deformation pattern, namely (i) a linear elastic regime defined by the compressive modulus calculated to be 1.2 GPa, (ii) deformation at almost constant stress characterized by a plateau stress measured at 20 MPa, (iii) densification after 77% of deformation. Table 3.7 summarizes the properties obtained from the mechanical test campaign performed.

The evolution of the compressive modulus is with strain shown in Figure 3.40. A dip is observed around 20% of plastic strain, and a relatively large dispersion is seen at high strain (above 40%).

Table 3.7 – Mechanical properties of cast diamond PCS under quasi-static compression. ± figures being the standard deviation. Averaged on four samples.

Relative density	[%]	31.3 ±0.5
Compressive modulus	[GPa]	1.2 ±0.2
Extrapolated compressive modulus	[GPa]	5.4 ±0.5
Yield stress (0.2%)	[MPa]	12 ±0.5
Peak stress	[MPa]	24 ±1
Plateau stress	[MPa]	20 ±2
Densification strain	[%]	77 ±5
Absorbed energy	[J/cm^3]	15 ±1
Energy absorption efficiency	[%]	80 ±2

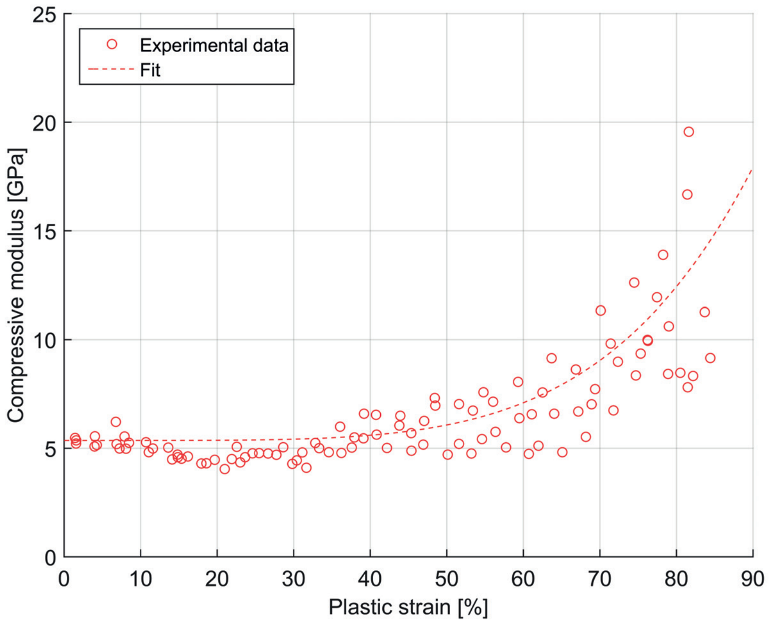

Figure 3.40 – Evolution of compressive modulus vs plastic strain for all four cast PCS samples.

Although densification of cast PCS occurred in different ways, the same overall pattern was observed; namely (i) homogenous deformation up to the peak stress (about 15% strain); (ii) local shearing /sliding between planes (roughly 30° to vertical); (iii) collapsing of top layers (at about 30% strain); (iv) shearing and collapsing until densification (above 40% strain). Figure 3.41 shows the stress-strain curves obtained and pictures of a sample at four different stages of compression.

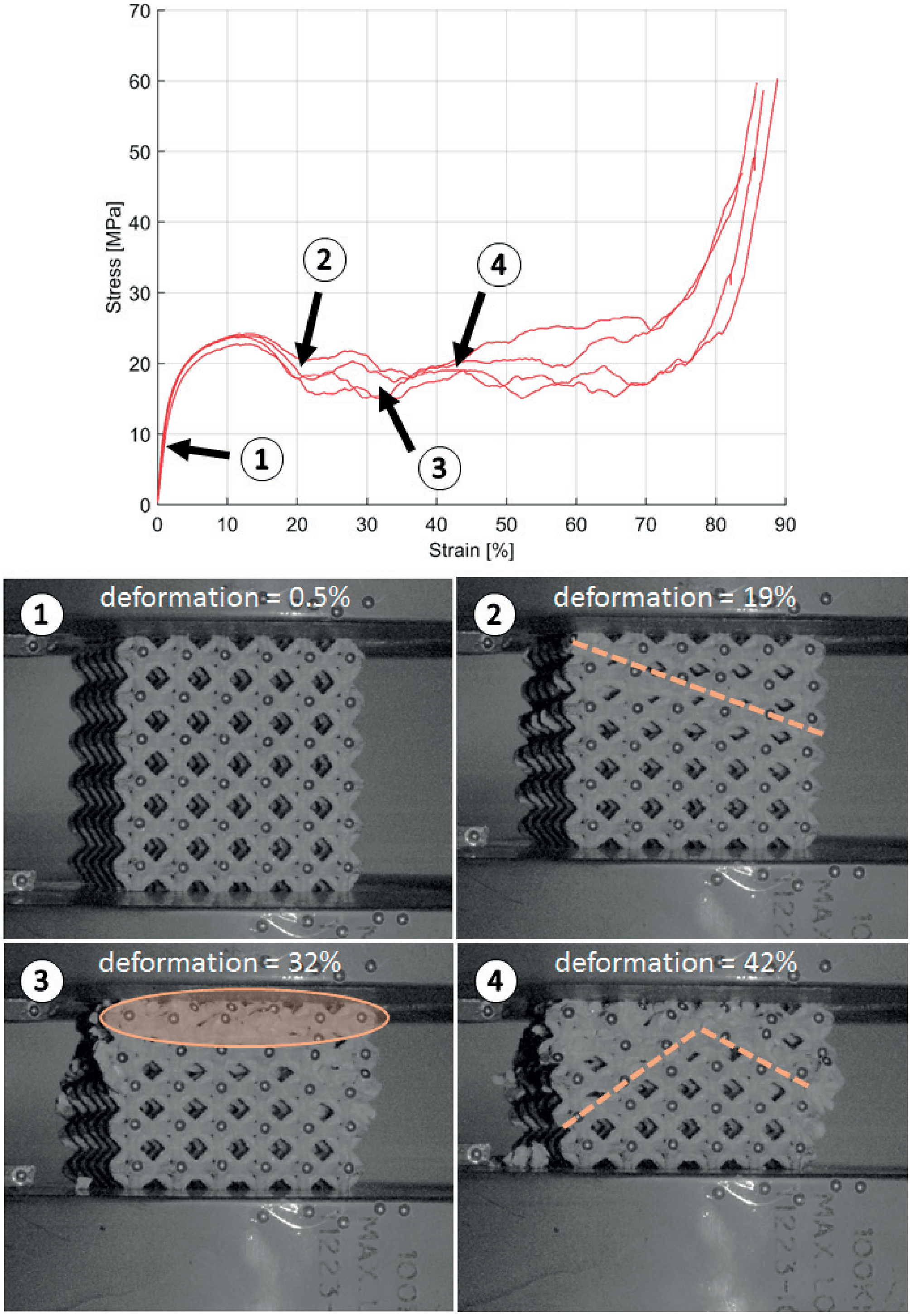

Figure 3.41 – Stress-strain curves of cast diamond PCS under quasi-static compression (top) and corresponding selected pictures of a sample at different strains. Dashed brown lines represent the sliding planes; highlighted area shows collapsed top cell layer.

3.3.3 Discussion

3D-tomography: Topology, pore and inclusion contents

Characterizing the uneven mass distribution showed that its origin is an increasing porosity in the mold along the vertical direction, present before casting. This porosity gradient was interpreted as being the result of the packing difference between bottom and top of the mold (more compact at the bottom), further enhanced by transport of NaCl during drainage to the bottom.

3D-tomography allowed the quantification of porosities and inclusions present within the cast PCS. The measured average pore content of 0.02% is comparable to observations made in similar bulk alloys [229]. As to inclusions, cast PCS exhibited only low concentrations of a denser element (probably Iron) in the range of $10^{-4}\%$ mass (estimated from the volume fraction obtained from 3D-tomography), although higher values were expected taking into account the Iron content present in the base alloy (0.75% mass). This difference can be explained by the fact that the detection method with CT-scans has a lower threshold in terms of minimal detectable inclusion dimension (expressed in voxels). Inclusions are only counted if the corresponding cluster exceeds 8 voxels (in our case a minimum size of 60 µm). Therefore, smaller clusters as well as iron in solid solution (up to 0.1% mass) can not be detected.

Microstructure: solidification rate estimation

The solidification rate was estimated by measuring the secondary dendrite arm spacing (SDAS) of primary Al dendrites. According to Caceres and al [230], a correlation can be drawn between this specific length and the solidification rate of the cast. Figure 3.42 shows an optical microscopy image of SDAS from which it was estimated that the SDAS for the cast samples produced is 25 µm (average of 575 SDAS measurements). Chen and al. [231] established a relation between cooling rate and SDAS given by the following equation,

$$SDAS = 40.5 R_C^{0.31} \tag{3.1}$$

where R_C is the cooling rate in °K/s and SDAS is in µm. In our case, the cooling rate is then estimated to be about 5 °K/s.

Deformation and densification

Ashby and al. [42] suggest that the compressive modulus of cellular materials should be determined by the slope of repeated load/unload cycles, as due to high-stress concentration sites and defects, microsplasticity occurs at low strain and decreases the apparent compressive modulus taht is measured from the initial slope of a compressive stress-strain curve. This was confirmed by comparing the extrapolated compressive modulus to the one calculated by finite elements analysis, 5.4 GPa and 6 GPa respectively; for comparison, the slope of the initial linear regime led to a far lower compressive modulus of 1.2 GPa.

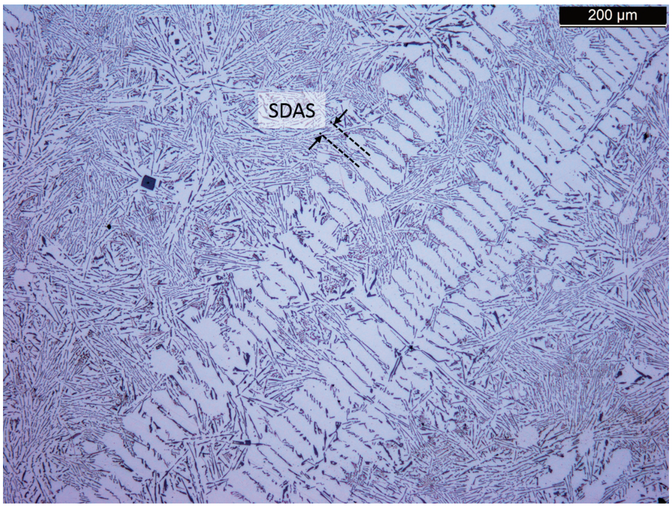

Figure 3.42 – SDAS on actual micrograph of metal within cast PCS x100.

Failure by shearing of PCS is explained in Chapter 2 (see section 1.6.2) for samples manufactured by SLM; high density planes drive the angle at which failure occurs. In diamond structures, two families of planes are similar in terms of surface density, namely the {100} and the {111} planes. This can be seen on the picture corresponding to 19% of deformation (Figure 3.43). Once densified, the shearing moved to another set of cells belonging with the same plane characteristics. This mode, alternating shearing and cell layer collapse, was also observed on additively manufactured PCS [165, 178].

Results with stereolithography preforms

Although stereolithographic preforms had the highest fidelity in terms of aspect, shape and resolution, it was a disappointment to notice systematic defect on the cast samples. Figure 3.44 shows these results and 3D-tomography investigation revealed that small cracks in the mold produced thin metal walls between cells. The cause of this phenomenon is probably the higher thermal expansion coefficient and higher Young's modulus of the resin compared to thermoplastics.

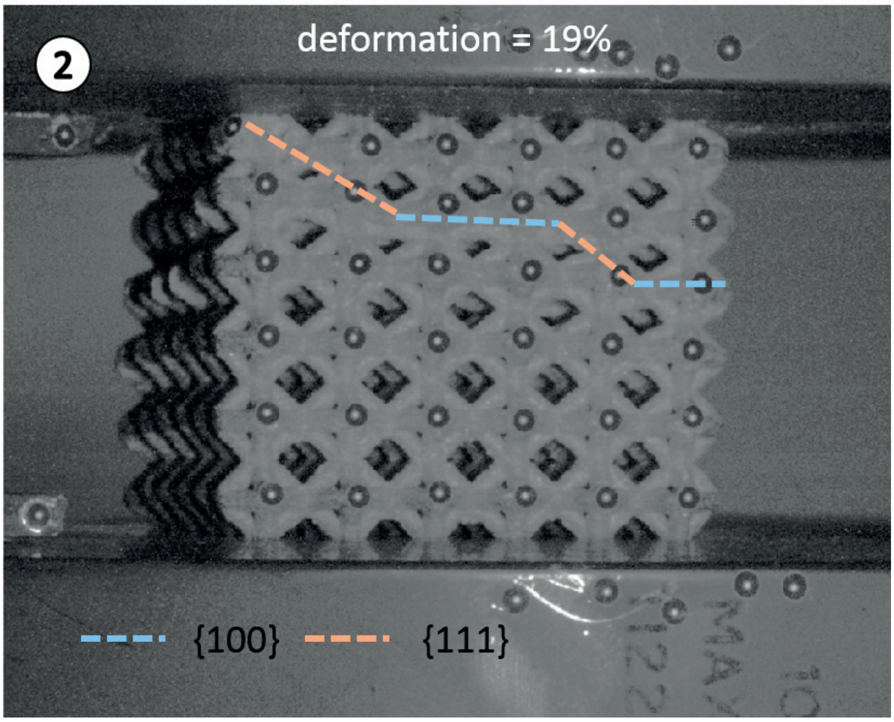

Figure 3.43 – Di PCS cast sample under compression at 19% deformation. Dash lines highlight the corresponding failure planes in terms of crystallographic plane families.

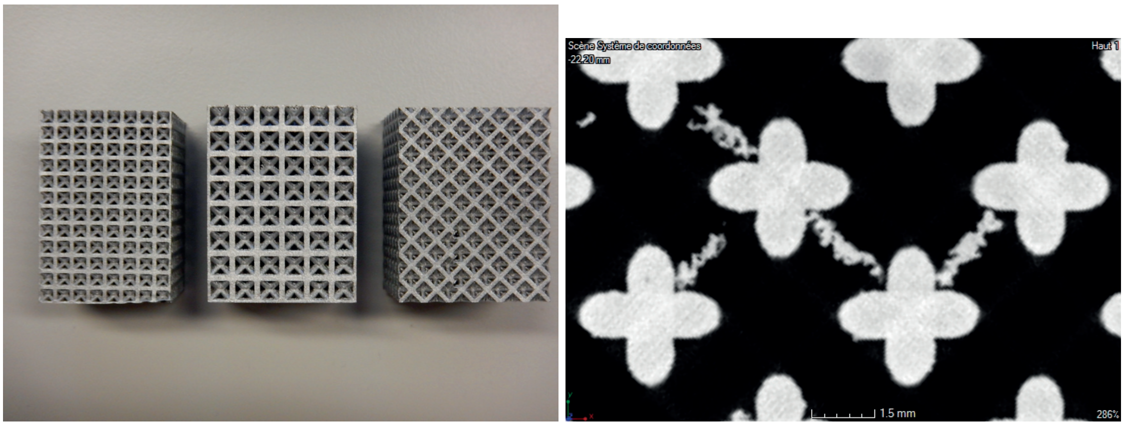

(a) (b)

Figure 3.44 – a) PCSs cast with stereolithographic preforms, from left to right, BCC 4 mm cell size, BCC 6 mm cell size and Oct 6 mm cell size. b) Evidence of mold cracking during the preform pyrolysis

3.4 Conclusion

In this chapter, it was demonstrated that investment casting of periodic cellular structures is feasible and a complete process was developed for this purpose. Extensive studies on a wide range of parameters, including the grain size distribution, packing vibration time or infiltration pressure and temperature, were performed for process optimization. The NaCl grain size distribution was found to be the main parameter influencing the process. The duration of the drying step could be greatly shortened by optimizing draining and exposing the surfaces of the green body. These resulted in a successful casting of Diamond PCS structures with a cell size of 6mm and a relative density of 31%. A Young's modulus was measured at 1.2 GPa and calculated to be 5.4 GPa without microplasticity effects. A plateau stress of 20 MPa and a densification strain of 77% were observed. This type of structure could be interesting for mechanical damping applications due to its high energy absorption capacity (15 MJ/m^3) and efficiency (80% of an ideal material). Nevertheless, the mold shaping process should be improved to allow stereolithographic preforms to be used as they present better shape and form fidelity, specifically compared to other 3D-printed polymers.

4 Additively manufactured vs. cast PCS

4.1 Introduction

Previous chapters characterized the mechanical properties of periodic cellular structures produced with two different manufacturing methods (casting and additive manufacturing). The influence of structure topology, bulk alloy and manufacturing process on the mechanical properties are compared in this chapter. Tests conducted on stochastic structures [232] were added to the comparison. The following nomenclature was adopted; namely AM PCS stands for structures manufactured by SLM (Chapter 2), Cast PCS for structures produced by investment casting (Chapter 3) and Stoch for stochastic structures provided by Constellium.

4.2 Microstructure and properties of bulk alloys

The AlSi12 alloy was selected in both processes used to produce PCS (casting and SLM). The high difference in cooling rate between the two processes induced a significant difference in the microstructure scale and morphology. On one hand, the low-cooling rate of the casting process(estimated at 5°K/s) produces a dendritic microstructure classical for this class of alloys, with a characteristic secondary dendrite arm spacing (SDAS) of ~ 25 µm. On the other hand, the high-cooling rate of the SLM process (order of magnitude: 10^6 °K/s) produces cellular structures with a characteristic cell diameter of ~ 0.5 µm. These observations are consistent with the relation established by Chen and al. [231]. Figure 4.1 compares the two different microstructures.

Manufacturing defects larger than 60 µm could be observed for both processes, using 3D-tomography. Whereas the porosity level (0.02% to 0.06%) was similar (within error margins), the volume of inclusions (mostly iron) was at least 100 times higher in SLM compared to cast microstructures. This highlights the necessity of high quality control during the additive manufacturing process, particularly concerning the powder purity, the chamber cleanliness as well as the post-processing steps.

Additively manufactured Al alloys exhibited higher strength than cast Al alloys due to their fine microstructure; this is clearly caused induced by the higher cooling rate. Finer microstructure leads to higher mechanical propeties [41]. The mechanical improvements compared to cast alloys are in the order of 60-100% for the yield stress and 25-40% for the ultimate tensile stress. No clear enhancements could be observed regarding the stiffness (as expected) or the failure strain. Despite higher mechanical properties, additive manufacturing of aluminum also introduced anisotropy in the metal structure, due to the presence of a mesoscale structure (melt-pool). This anisotropy was measured to be about 25% for the yield stress and 10% for the ultimate tensile stress, the vertical direction (Z) being always the weakest (consistent with [33, 233, 234]). A summary of bulk alloy properties can be found in Table 2.11 in Chapter 2.

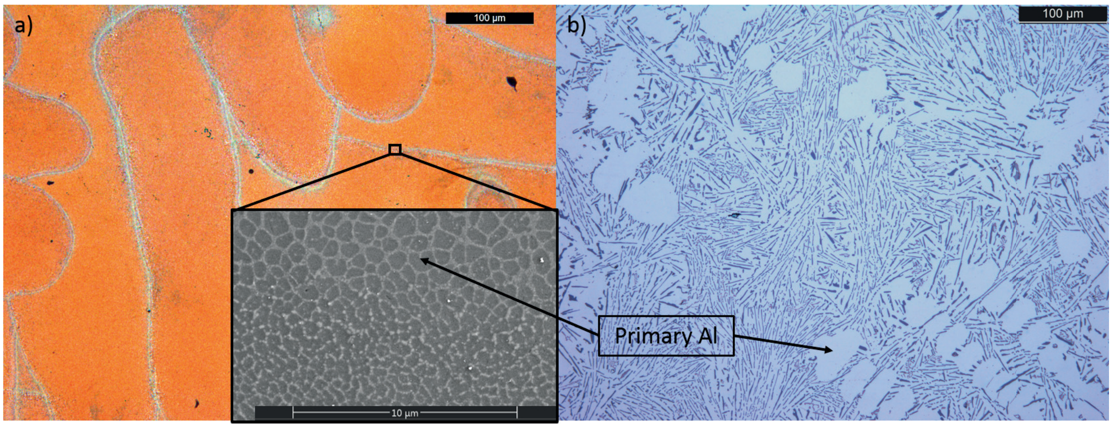

Figure 4.1 – AlSi12 microstructure produced by a) SLM with cellular primary Al and b) casting with classical dendritical structure. Optical images have the same magnification; the scale bar of optical micrographs represents 100 µm

4.3 Mass distribution

The homogeneity of the mass distribution in PCS was assessed by calculating the relative density of each cell layer along the building direction (Z). The calculations were performed by binarizing CT-scans images with a Matlab script and counting the white pixels. Figure 4.2 shows the results for the AM and Cast PCS. In AM PCS, all samples showed homogeneous densities, whereas for the Cast sample a gradient was observed (about 0.4% per cell layer) between bottom and top of the structure. Although the relative density was designed to be 30%, most parts showed higher values. For AM structures, this deviation is explained by the sintering of metal powder under horizontal struts [12–18, 168, 171] and the trapping of steel-pellets during post-process sand-blasting. For Cast structures, the density gradient as well as the higher relative density could be led back to varying conditions of the mold shaping process (see Section 3.1.6).

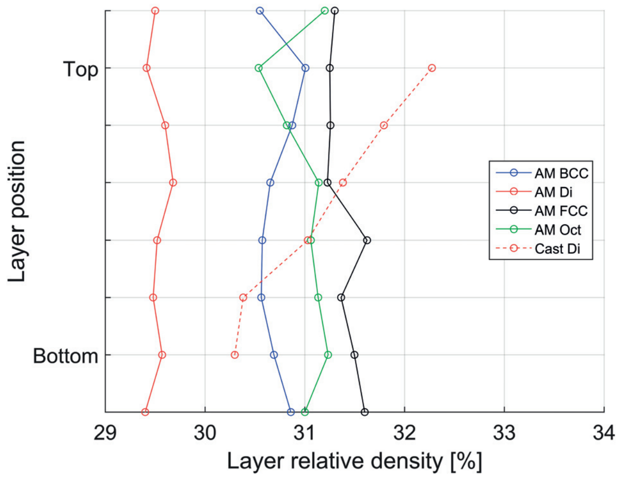

Figure 4.2 – Relative density per cell layer from the bottom to the top of the sample (being oriented along the building direction). Uncertainty was deliberately not shown for sake of readiness.

4.4 Cellular structure mechanical properties

4.4.1 Stochastic foam

A preliminary test campaign was performed on stochastic structures provided by Constellium [232]. The manufacturing method is based on investment casting of a NaCl salt preform. The main characteristics of these structures are a A357 bulk alloy with 2 mm to 8 mm-cylindrical pores and a relative density ranging from 20% to 40%. Quasi-static compression tests were conducted on the samples with the same settings as for our PCS (see Chapters 2 and 3). Cubic samples were cut out of larger slabs; the objective was to have a side length equal to ten times the characteristic pore size. Figure 4.3 shows an example of the samples for two different pore sizes. Only the results from stochastic structures with a 3 mm-pore and a relative density close to 30% are used in the following comparison.

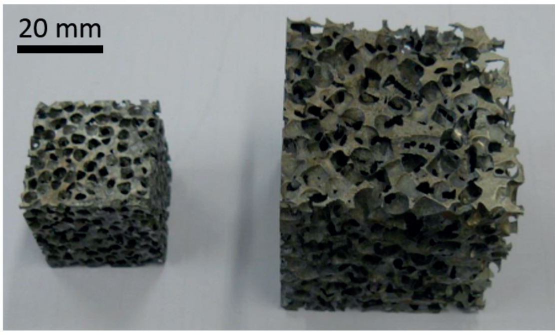

Figure 4.3 – Stochastic structure samples before compression test with a pore size of 3 mm (left) and 5 mm (right)

4.4.2 Mechanical properties and stress-strain curves

We consider the comparison valid for the following reasons:

- Base alloy of similar compositions, aluminum-silicon alloy (with a small amount of magnesium for the A357)
- Relative densities close to 30% for all the structures
- Compression test parameters identical regarding the strain rate and the compression platens

Table 4.1 summarizes all the mechanical properties and Figure 4.4 shows the stress-strain curves for the all different structures (AM PCS, Cast PCS and Stoch).

Table 4.1 – Comparison of PCS and stochastic structures mechanical properties. Uncertainties correspond to standard deviations.

		AM				Cast	
		BCC	Di	FCC	Oct	Di	Stoch
Relative density	[%]	30.6 ± 0.2	29.8 ± 0.2	32.2 ± 1.2	30.8 ± 0.4	31.3 ± 0.5	29.4 ± 2.3
Compressive modulus	[GPa]	2.9 ± 0.2	3.8 ± 0.1	4.0 ± 0.3	3.0 ± 0.1	1.2 ± 0.2	1.7 ± 0.4
Extrap. comp. modulus	[GPa]	4.7 ± 1	5.5 ± 1	7.4 ± 1	4.4 ± 1	5.4 ± 1	-
Yield stress	[MPa]	28 ± 1	36 ± 1	38 ± 2	32 ± 1	12 ± 1	5 ± 1
Peak stress	[MPa]	-	-	-	-	24 ± 1	-
Plateau stress	[MPa]	-	-	-	-	20 ± 2	12 ± 1
Maximal stress	[MPa]	46 ± 2	62 ± 1	66 ± 2	48 ± 2	-	-
Failure strain	[%]	5.0 ± 0.7	7.5 ± 0.4	12.7 ± 0.4	4.6 ± 0.4	-	-
Densification strain	[%]	-	-	-	-	76 ± 5	46 ± 1
Absorbed energy	[MJ/m^3]	1.8 ± 0.3	3.7 ± 0.2	7.3 ± 0.3	1.7 ± 0.2	14.8 ± 1.2	5.1 ± 0.5
Energy abs. efficiency	[%]	76 ± 1	80 ± 1	87 ± 1	75 ± 1	80 ± 2	61 ± 1

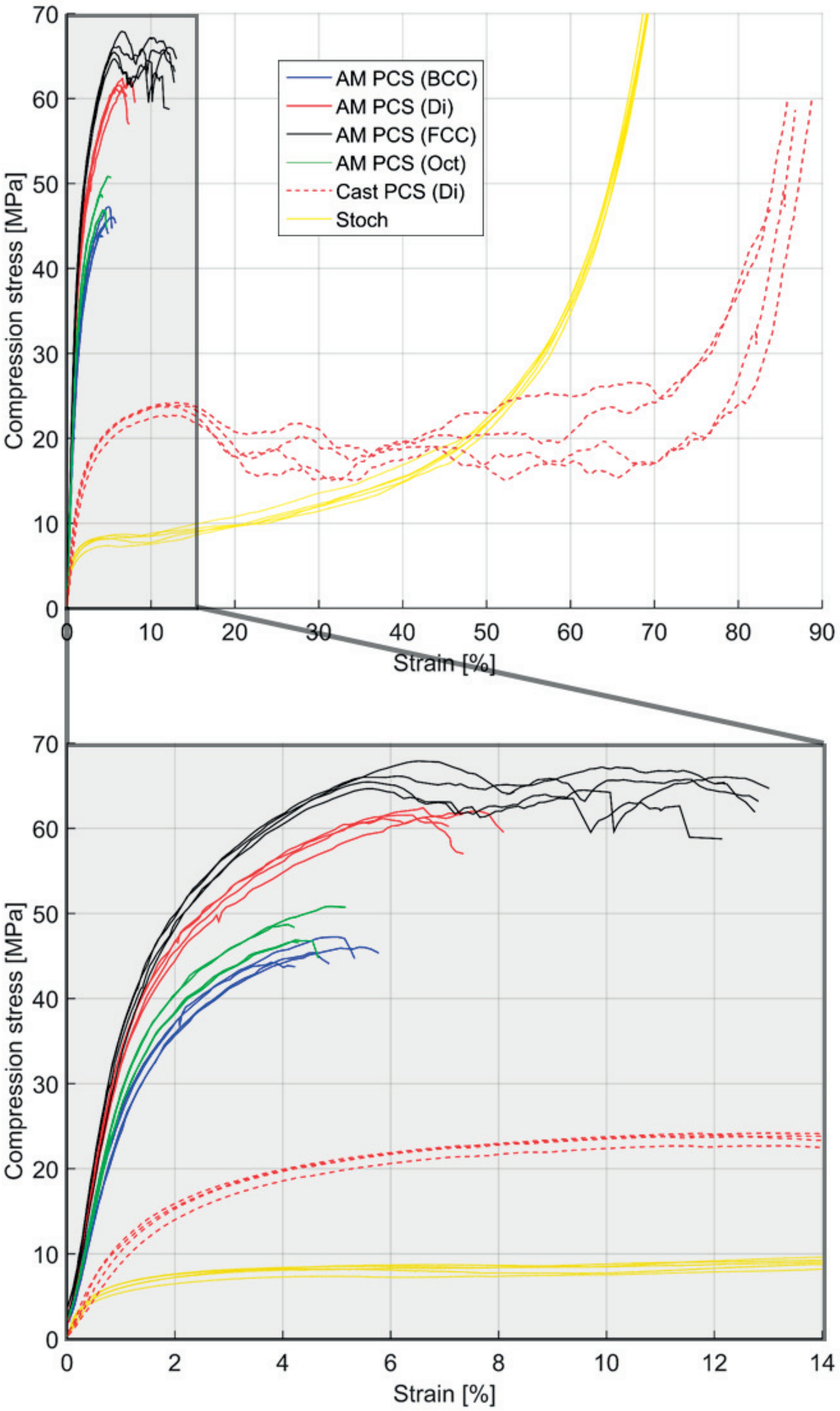

Figure 4.4 – Stress-strain curves of PCS and stochastic structures (top) with focus on the AM samples (bottom)

Samples mechanical properties were added to Ashby plots of cellular metals (Figure 4.5 and 4.6) to estimate their performance compared to other topologies. As seen, PCS structures are close to the ideal bending-dominated behaviour which agrees with the predicted deformation mode by Maxwell's criterion (Equation 1.7), except for the octet-truss. However, Ashby scaling laws are based on beam bending theory and it was reported that care has to be taken while considering structures with relative densities reaching 0.3, which is the case for our samples [42, 111].

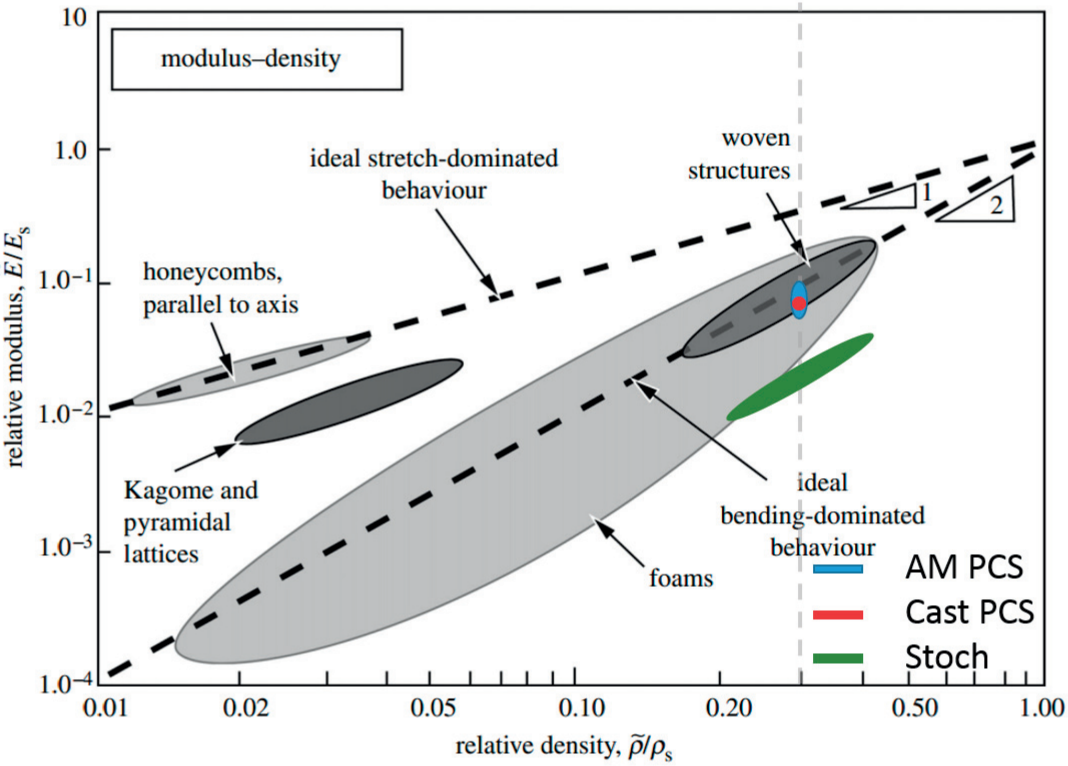

Figure 4.5 – Specific compressive modulus Ashby plots of cellular metals with addition of the properties obtained for the different structures of this study. PCS extrapolated modulus are plotted for comparison (FE predictions are not shown for sake of readibility but are close to the one plotted here). Bulk alloy Young modulus was taken as 70 GPa. Adapted from [42].

4.4.3 Structure topology influence

The influence of structure topology on mechanical properties can be observed by comparing samples with the same bulk alloy properties. We compared the Cast Di to the Stoch samples and AM FCC to AM BCC parts. We are aware that the lower silicon percentage and the magnesium present in the A357 alloy (Stoch) may have improved its mechanical performance somewhat compared to AlSi12. AM FCC and AM BCC were selected as they respectively showed the highest and lowest performance. Table 4.2 shows the comparison of the two previously defined cases. The percentage improvement figures were calculated in a worst-case scenarios, thus representing minimal values.

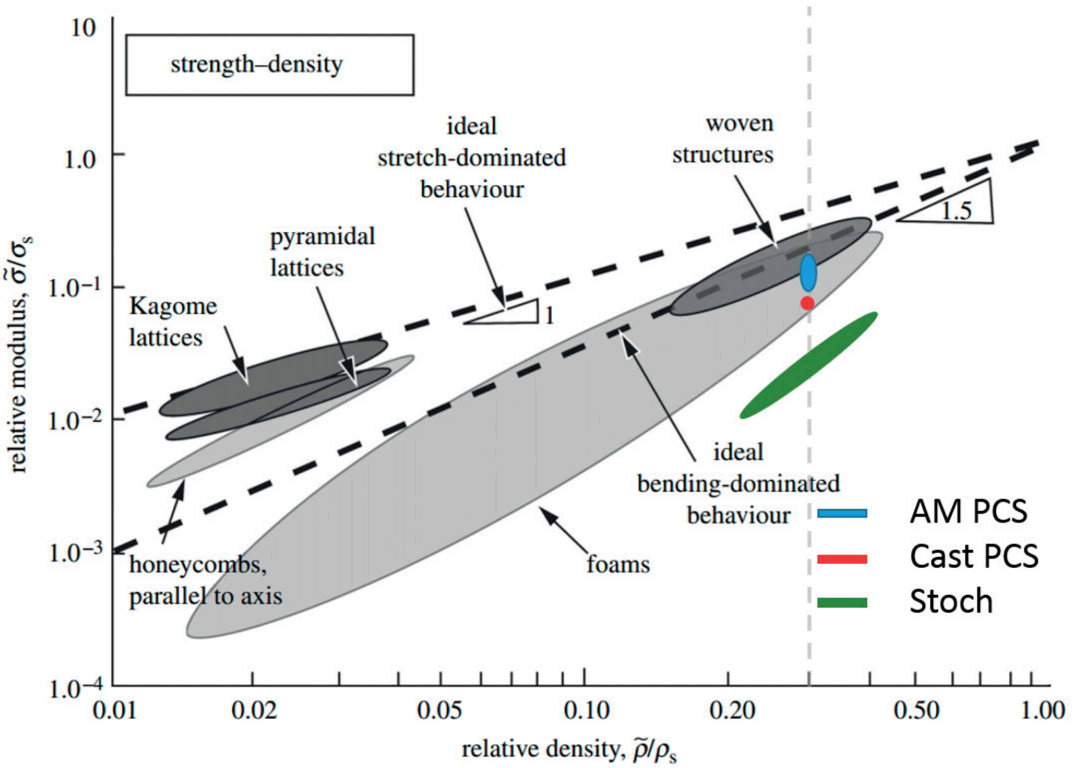

Figure 4.6 – Specific yield stress Ashby plots of cellular metals with addition of the properties obtained for the different structures of this study. PCS extrapolated modulus are plotted for comparison (FE predictions are not shown for sake of readibility but are close to the one plotted here). Yield stress was defined as the mean measured value for AM PCS (280 MPa) while 130 MPa was used for Cast PCS and Stoch. Adapted from [42].

Table 4.2 – Topology influence on the structure mechanical properties.

Casting process		Cast Di	Stoch	Improvement [%] (at least)
Compressive modulus	[GPa]	1 - 1.4	1.3 - 2.1	No significant improvement
Yield stress	[MPa]	11 - 13	4 - 6	85
Plateau stress	[MPa]	18 - 22	11 - 13	40
Densification strain	[%]	71 - 81	45 - 47	50
Absorbed energy	[MJ/m^3]	13.6 - 16	4.6 - 5.6	145
Energy absorption eff.	[%]	78 - 82	60 - 62	25
AM process		FCC	BCC	Improvement [%] (at least)
Compressive modulus	[GPa]	3.7 - 4.3	2.7 - 3.1	20
Extrap Comp. modulus	[GPa]	6.4 - 8.4	3.7 - 5.7	15
Yield stress	[MPa]	36 - 40	27 - 29	25
Maximal stress	[MPa]	64 - 68	44 - 48	35
Failure strain	[%]	12.3 - 13.1	4.3 - 5.7	115
Absorbed energy	[MJ/m^3]	7 - 7.6	1.5 - 2.1	230
Energy absorption eff.	[%]	86 - 88	75 - 77	10

The comparison between the cast samples highlights the importance of mass distribution optimization. Switching from a stochastic to a periodic structure avoids the presence of unconstrained material, which increases the mass with no beneficial effects on the mechanical properties, and emphasizes the importance of the struts connectivity (Equation 1.7). This result is seen as the yield stress and absorbed energy values were improved by a factor 2 and 2.5 respectively. An interesting point is that no stiffness improvement could be observed which emphasizes the importance of microplasticity effects in such structures (later described in Section 4.4.5).

The comparison between FCC and BCC structures shows significant differences, ranging from 15% (extrapolated compressive modulus) to 230% (absorbed energy). However as AM PCS did not complete the full classical deformation pattern (failure before 15% strain), care as to be taken when using absorbed energy figures. This result shows the importance of the topological assembly of the struts.

4.4.4 Bulk alloy influence

The influence of bulk alloy properties on structural performances can be assessed by comparing Diamond structures manufactured by SLM and casting methods. Care was taken while comparing results, as the cell size was 4 mm for AM Di and 6 mm for Cast Di. The literature shows that bigger cell size [183] and higher sample to cell size ratio [163, 182] can be detrimental to mechanical properties. The relative density was kept constant to validate the comparison. Table 4.3 shows results for AM and Cast Di structures. The behavior in compression being different, it was chosen to compare the Cast Di densification strain to AM Di failure strain. Under this assumption, the AM maximal stress is compared to the Cast peak stress.

Table 4.3 – Bulk alloy influence on PCS mechanical properties. Positive (negative) difference shows better performance obtained from the AM (vs. casting) process

Di Structure		AM	Cast	Difference [%] (at least)
Compressive modulus	[GPa]	3.7 - 3.9	1 - 1.4	165
Extrap Comp. modulus	[GPa]	4.5 - 6.5	4.3 - 6.3	No significant difference
Yield stress	[MPa]	35 - 37	11 - 13	170
Maximal/Peak stress	[MPa]	61 - 63	23 - 25	150
Failure/Dens. strain	[%]	7.1 - 7.9	71 - 81	-800
Absorbed energy	[MJ/m^3]	3.5 - 3.9	13.6 - 16	-250
Energy absorption eff.	[%]	79 - 81	78 - 82	No significant difference

AM Di structures are performing at least 150% better for the compressive modulus, the yield stress and the maximal stress, while Cast Di samples exhibited an absorbed energy four times higher than their counterparts. The latter result comes from the large difference in failure strain. The brittle fracture of AM samples might be due to the presence of the microstructure of the metal (melt-pools) acting as a preferential crack growth site [26, 35, 40], a feature not present in Di samples. Another reason might be residual stresses present in the AM parts and induced by the process, whose relaxation may have triggered the observed failure mode [19, 217]. Post-process heat treatment of AM structures might change the failure mode from brittle to plastic at the expense of structural strength (this was not tested, however, for lack of samples). It was reported that heat treatment impacts the failure mode of gyroid structures manufactured in AlSi10Mg by SLM [36].

4.4.5 Microplasticity

An interesting result is observed when comparing the measured and the extrapolated compressive modulus in the Table 4.3. AM Di structures exhibited a measured apparent compressive modulus three times higher than their Cast counterparts while no significant difference could be observed in the extrapolated compressive modulus. The latter gives the stiffness of the structures after erasing any influence of microplasticity [42, 111]. The difference in compressive modulus (between AM and Cast) was due to an uneven level of microplasticity upon initial deformation of the two structures, after this being of a greater extent for the Cast Di samples. Finite element analysis showed that stress concentration occurs during compression at the junction between struts and nodes (Figure 4.7). Stress concentration factors at corners and notches are defined by the local radius of curvature. Figure 4.8 shows optical microscopy images of stress concentration sites for both AM and Cast Di structures. The latter exhibited a smaller radius of curvature with respect to the cell size (by a factor 3) than AM samples resulting in higher local stress during loading. This feature makes the Cast Di structure more susceptible to microplasticity and therefore leading to a lower apparent compressive modulus, which is consistent with the measurements.

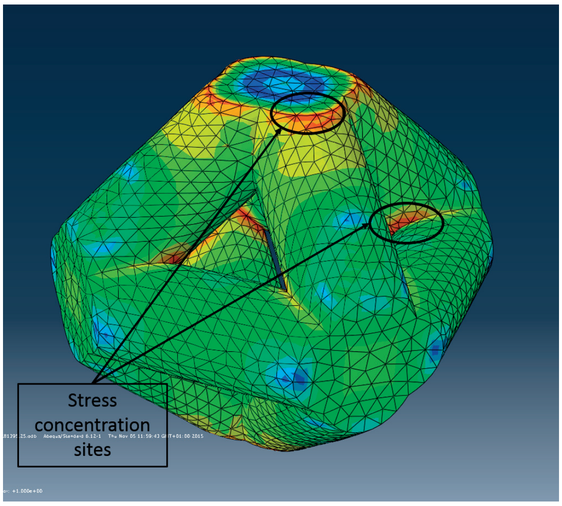

Figure 4.7 – Images extracted from FE analyzis of Di structure with stress concentration sites highlighted.

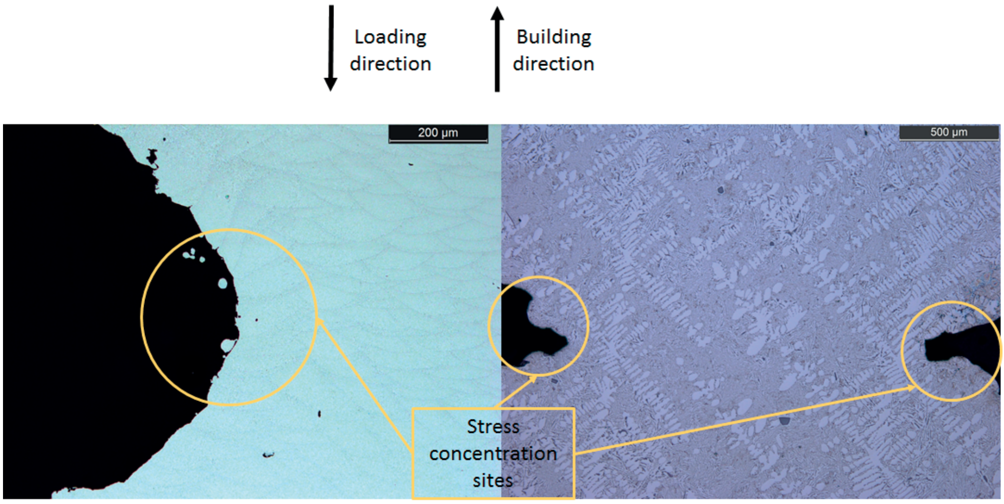

Figure 4.8 – Optical microscopy images of AM Di (left) and Cast Di (right). Stress concentrations sites are highlighted in yellow.

4.5 Deformation mechanism

In Chapter 2, the mechanism of AM PCS deformation under compression was explained based on topological considerations, namely as a sliding between densest planes. It appears that the same mechanism was involved for deformation of cast PCS (Chapter 3) samples emphasizing the conclusion that PCS deformation is driven mainly by the architecture of the PCS, not by the bulk alloy properties. It was shown that two different families of planes, namely {100} and {111}, lead to the failure of Di structures, with a preference for the latter, which exhibits a stiffer Kagome planar lattice [151, 155]. Figure 4.9 shows images of AM and Cast Di during compression tests highlighting the combination of planes inducing global shearing.

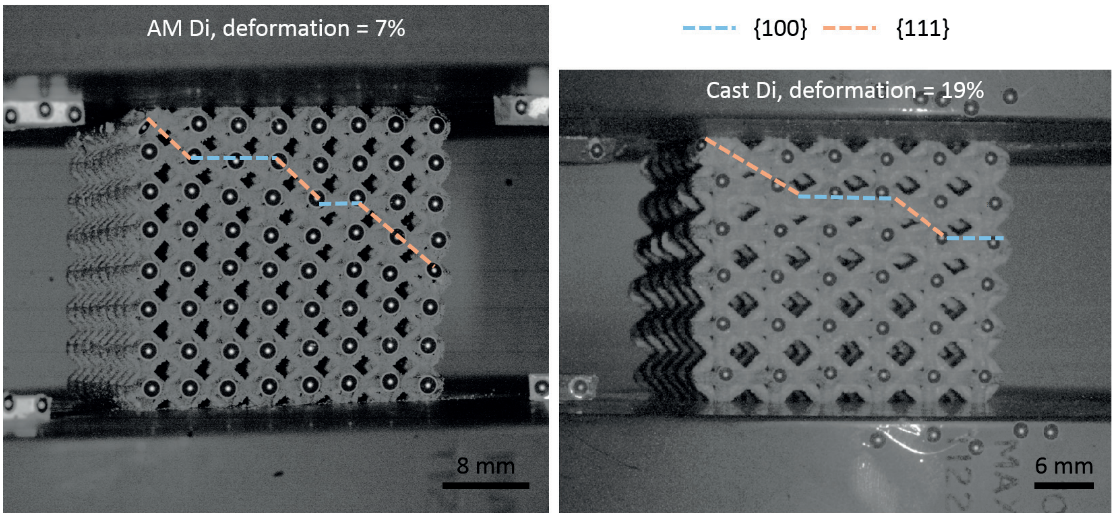

Figure 4.9 – AM Di sample at 7% of deformation (right) and Cast Di sample at 19% of deformation (left). Dash lines highlight the plane of sliding

Going further in the failure criterion validation, it can be confronted from what is observed in the literature.

Some studies show results contradictory with the proposed failure criterion. An octet-truss assembly failed by band-collapse, but was of only two cell layers, which might have prevented the predicted shear failure mechanism from occurring. The structure was designed with rectangular struts cross-section which might also explain the deviation with respect to our samples [175]. Therefore, a minimum number of cells might be required for the structure to follow the criterion, as well as a specific struts topology. It was also reported that a 316L stainless steel alloy octet-truss structure failed in compression by band collapse [179]. A possible explanation would be due to the small struts diameter (less 0.5 mm). This designed strut size would lead to more inhomogeneity between the horizontal and the diagonal struts induced by the manufacturing process which could change the failure mode, as shown by Liu and al. [171]. Thus, a minimal struts diameter might be required to agree with the predicted failure mode. Other studies in contradiction with the criterion were based only on numerical calculations which might not reflect accurately the behavior observed during experiments (as for our calculations in Chapter 2) [177, 179].

This being said, most of the studies reported in the literature appeared to be consistent with the proposed failure criterion, as for BCC structures [13, 161, 162, 165, 181], for octet-truss structures [171, 178], and for simple cubic structures [167].

4.6 Conclusion

Optimizing the mass distribution is crucial to obtain cellular metals with high specific mechanical properties. Topology was the most influential parameter for strength improvement. During this study, two well-distinct behaviors were observed for PCS under compression:

- A high stiffness, a high yield stress and a low failure strain for AM structures, which might be suitable for structural applications.
- A large densification strain at constant pressure for cast samples, which might be of interest for energy absorption applications.

The deformation mechanism of PCS is based on topological considerations, and a failure criterion was established to predict the deformation. Nevertheless, refinement of the model may need to be performed to define the frame in which the criterion applies; determining the required number of cell repetition, the acceptable struts diameter and topology, or the range of relative density. Susceptibility to microplasticity was found to be different for the same PCS topology produced by different processes. The variation was explained by the effect of differences in the curvature radius at stress-concentration sites.

5 Hypervelocity impact testing on aluminum-silicon cellular materials

5.1 Introduction

In this chapter, the behavior of aluminum-silicon alloys cellular materials (stochastic and cast periodic cellular structures) under hypervelocity ballistic impacts is characterized to investigate potential Micro-Meteoroid and Orbital Debris (MMOD) shielding applications. Currently, spacecraft protections are based on advanced Whipple shield configurations consisting of bumpers, high-strength fabrics and interspace to spread and absorb the load, and thus decreasing the debris penetration capacity. This concept was kept for the study, replacing the rear wall with our structures. Tests were performed based on a two-stage light gas gun owned and operated by Thiot Ingénierie (Puybrun, France). This chapter is based on the master thesis done by Régis Voillat [216] from which a paper was submitted [235]. The sample preparation, the metallographic characterization and the entire data analyzis were performed by Mr. Voillat while the PCS sample casting, the test campaign organization and the 3D-tomography recording were achieved by myself. The test plan was established from a common agreement.

5.2 Experimental methods

5.2.1 Samples

Sample components

Each sample can be divided into three parts:

- the core
- the bumper
- the frame structure

Two different structures were tested as a core material. The first is a cast AlSi12 Diamond PCS (6 mm cell-size) produced according to the process described in Chapter 3, with dimensions of 36x36x48 mm^3 (6x6x8 cells) in X, Y, Z and a relative density of 34%. The second is a cast A357 stochastic structure (3 mm cylindrical pores) produced by the Constellium company (Voreppe, France) with a relative density of 21%, machined to the same dimensions as the PCS by electrical discharge machining. For both structures, no post-process heat treatments were performed. Figure 5.1 shows the two different cores used in this study before assembly.

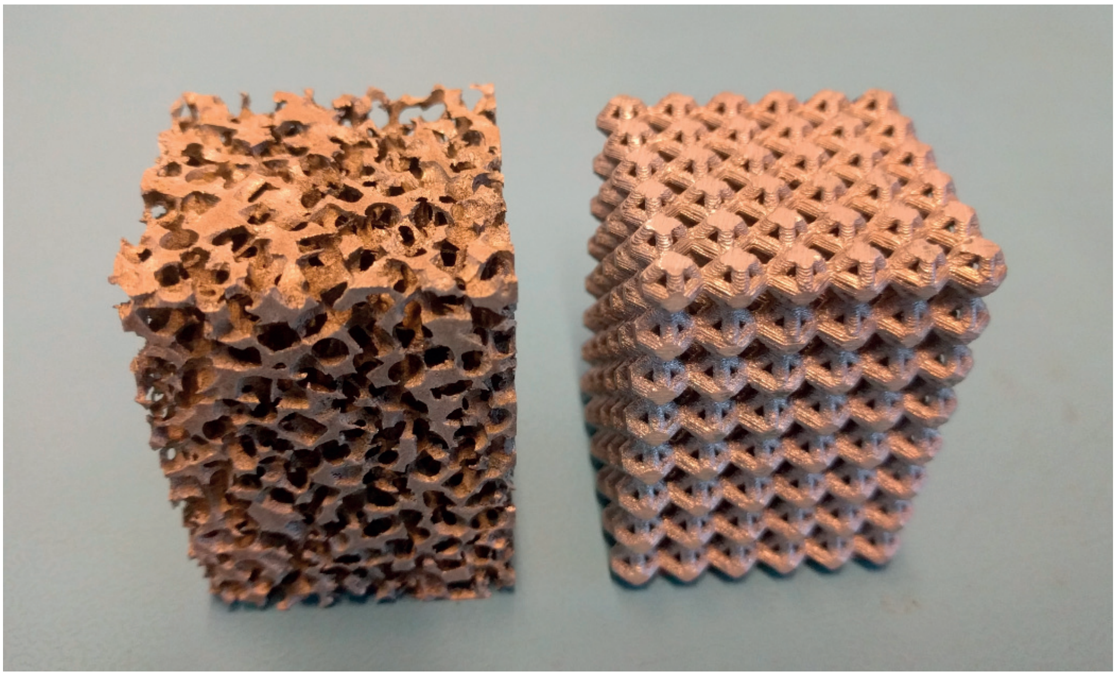

Figure 5.1 – The two different tested core structures, stochastic on the left (A357 cast alloy with 21% of relative density), PCS on the right (AlSi12 cast alloy with 34% relative density). Reproduced from [216].

Bumpers are thin layers of material placed at a certain distance in front of the core to fragment the projectile and spread the resulting debris cloud. Two different bumper materials were tested for debris fragmentation: (i) a 0.15 mm-thick aluminum (98-99.5%) foil (BS EN 546-3 Standard) and (ii) a space-qualified multi-layer insulation (MLI) alternating ten layers of aluminum coated PET films with non-woven ceramic fibers. Their surface densities are 41 mg/cm^2 and 35 mg/cm^2 respectively. According to Piekutowski [199], a 0.15 mm-thick Al foil leads to a confined debris cloud after bumper impact, placing our experiments in a worst-case scenario (the projectile not being fragmented efficiently).

Core and bumper are assembled within a frame structure consisting of a 7 mm-thick stainless steel C-shape clamp with a window cut in the rear face to allow investigations of any through-debris passing. Eight M5 threads holes were drilled, five on the top to maintain the core in place during the test, and three on the bottom to be fixed in the test chamber. The choice was made to manufacture one C-shape per core for preliminary sample preparation and to reduce manipulations and workload of the machine operator.

Sample assembly

The three previously described components were assembled in a specific sequence to obtain a full sample. An aluminum foil (same used for the bumper) was glued to the core rear face to witness any full penetration during the test; the glue was an Araldite Standard ambient curing two-component epoxy adhesive (Bostik SA, La Plaine Saint-Denis, France). The core was then positioned into the C-shape and maintained in place with three M5 fasteners applying a specific 20 cN.m torque to avoid excessive compression which could bias the results. Additional 2 mm-thick aluminum plates were inserted between the frame, the screws and the core to spread the load and avoid any localized deformation. Fastener loosening during manipulation and transportation was prevented by gluing the threads and the tips to the Al plate and the frame with epoxy adhesive. The bumper was then fixed to the C-shape front face, glued for the aluminum foil and taped for the MLI. Figure 5.2 shows a fully assembled sample.

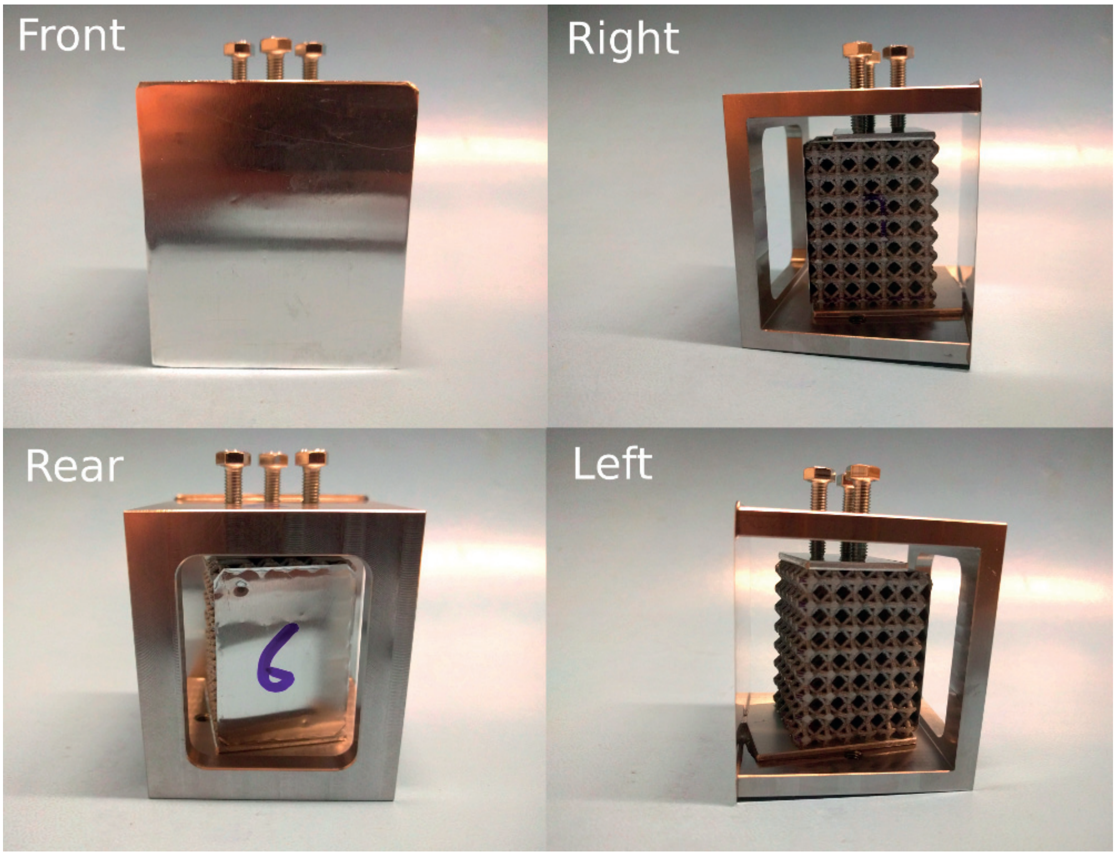

Figure 5.2 – Fully assembled sample. Reproduced from [216].

Sample test configurations

Eight sample configurations were tested during the campaign investigating the influence of four parameters:

1. The core material, either stochastic or structured.
2. The bumper material, either Al foil or MLI.
3. The bumper spacing, either 0 or 10 mm.
4. The core face rotation with respect to the bumper, either 0° or 12°.

The angle of 12° defined for the PCS corresponds to the lowest required angle to avoid any direct open channels from the projectile point of view. Tests were always performed perpendicularly to the bumper to keep the same projectile fragmentation/debris cloud conditions for comparison. Thus, the core was rotated and not the bumper. Table 5.1 shows the eight different configurations tested. The relative density was estimated by dividing the mass by the volume of the core material. One sample per configuration was tested due to the limited number of tests available in the commissioned campaign.

Table 5.1 – Sample configurations used during the test campaign.

ID -	**Core** -	**Core density** [%]	**Bumper** -	**Spacing** [mm]	**Core orientation** [°]
1	Foam	20.3	Al foil	0	0
2	Foam	19.8	Al foil	10	0
3	Foam	23.5	MLI	10	0
4	PCS	34.8	Al foil	0	0
5	PCS	32.2	Al foil	10	0
6	PCS	33.2	Al foil	10	12
7	PCS	32.6	MLI	10	0
8	PCS	33.6	MLI	10	12

5.2.2 Test facilities

The test campaign was performed at the Thiot Ingénierie facilities in Puybrun, France. Thiot Ingénierie design, build and operate numerous light-gas guns allowing ballistic testing over a broad range of mass and velocities. For our case, a two-stage light gas gun nicknamed “Hermes” was used (Figure 5.3). The propulsive gas is Helium compressed to 300 bar and released with a specifically designed fast-valve mechanism. The 2 mm-diameter Al projectile sitting on the polymer sabot was accelerated to velocities up to 7 km/s when reaching the end of the 5 mm-diameter barrel. Residual atmosphere (0.13 Pa) was used to aerodynamically separate the projectile from the sabot. After 1 m of free flight, a 15-20 mm-thick steel plate with a 12 mm-diameter drilled hole in the line of sight stopped the sabot from impacting the target. A 7 mm-thick stainless steel L-shape was manufactured to interface the sample to the test chamber. A 0.75 mm-thick Al plate was taped to the rear face of the C-shape for analysis of debris passing through the sample. Figure 5.4 shows a sample in the chamber after impact.

The velocity was calculated with a Tektronix TDS5054 oscilloscope measuring the time of flight between two optical laser barriers with a known spacing. The integrity of the projectile was verified using RX flash photography. Images of the impact were recorded using a Phantom v2012 high-speed camera operated with infrared (800 nm) light with a framerate of 340000 fps and a field of view of 20-25 mm at the point of impact.

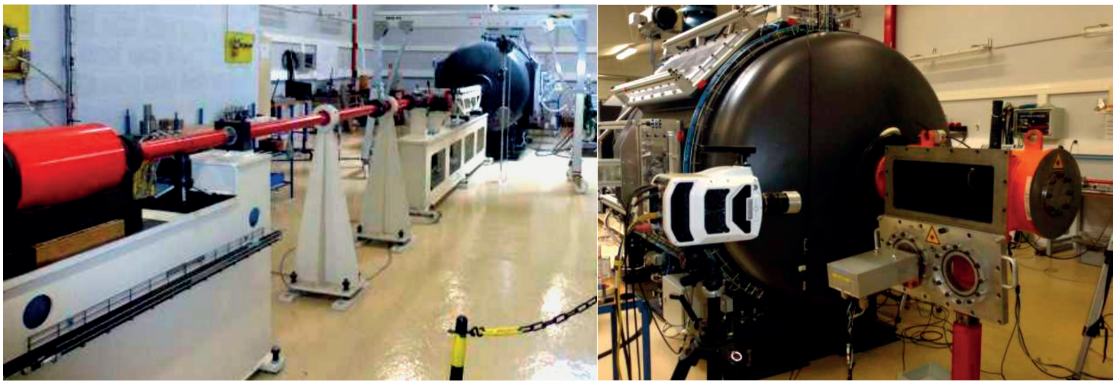

Figure 5.3 – Hermes two-stage light gas gun with pressurized chamber (left) and test chamber with high speed camera visible (right). Courtesy of Thiot Ingénierie.

5.2.3 3D-tomography

3D-tomography was performed on impacted samples to analyze the inner deformation in a non-destructive way. CT-scans were obtained on a Phoenix v|tome|x m300 machine (GE Sensing & Inspection Technologies GmbH) at ESTEC facilities (ESA). Two different machine parameter settings were defined to scan the samples. Full samples (including frame and bumper) and sample cores alone were scanned with a resolution of 75µm per voxel and 30µm per voxel, respectively. Table 5.2 summarizes the machine parameters settings for the two different configurations. No set of parameters led to satisfying results when the bumper was made out of MLI due to excessive density mismatch between the various sample elements; this issue concerned Sample 3, 7 and 8. Auto Optimiser and Switch options were switched on during the scans, and no filters were used. The reconstruction of the 3D volume from the scans was performed using the embedded software Phoenix datos|x reconstruction v.2.1.0 - RTM (GE Sensing & Inspection Technologies GmbH).

5.2.4 Metallography

The effect of impact on sample microstructure was analyzed by optical microscopy. The metallographic preparation was conducted on two sample cores, one stochastic and one structured. Sample core region of interest, extracted by EDM, was embedded into Epofix clear resin. Grinding was then performed in sequence using SiC papers with different Grit sizes (120, 180 and 320). Finally, polishing was achieved with 3µm diamond particle suspension followed by 1µm diamond particles.

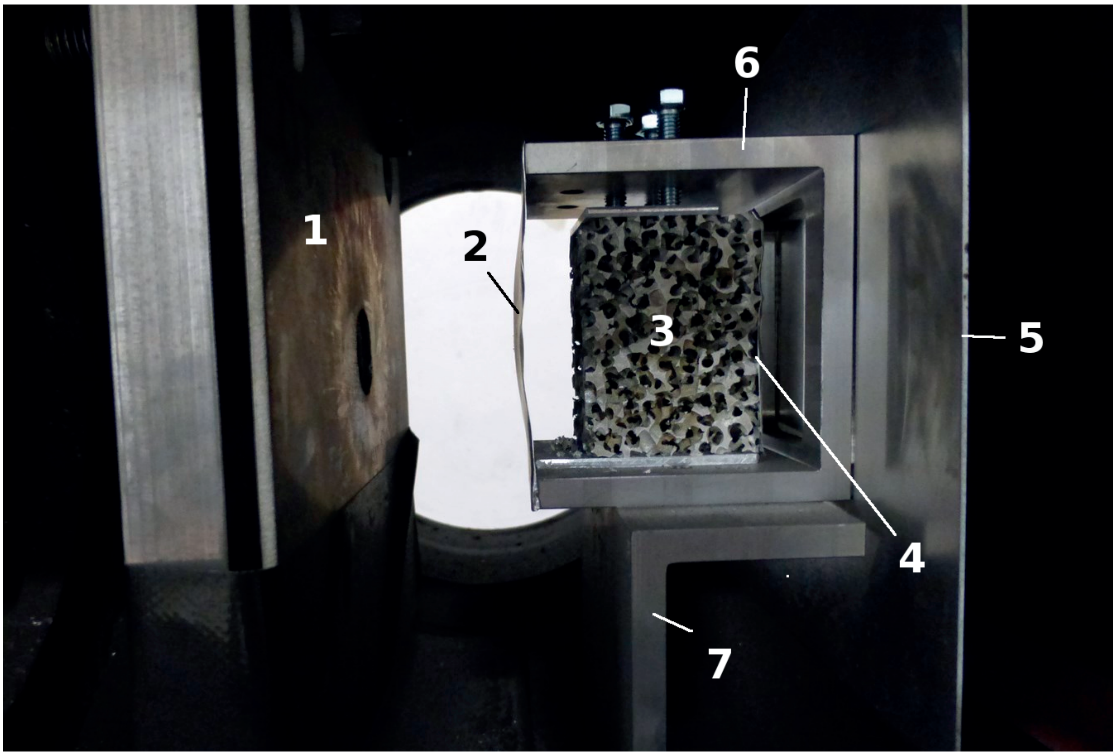

Figure 5.4 – Test chamber configuration (here sample 2 right after impact). 1) Stop plate separating the projectile from the sabot, 2) bumper (aluminum foil), 3) Core material (stochastic foam), 4) rear skin (aluminum foil), 5) witness plate, 6) C-shape support and 7) L-shape support. Reproduced from [216].

Two different microscopes were used to take images of the samples. For the PCS sample, a Zeiss Axioplan 2 was chosen with a coaxial illumination for all the magnifications. For the stochastic sample, a Keyence VHX-5000 was selected with a combination of coaxial illumination and right light diffuse for magnification lower than x500. Higher magnifications used only coaxial illumination. For both microscopes, no filters were used.

Table 5.2 – CT-scan machine parameters for the different tested samples. Full configuration stands for sample including bumper and frame while core configuration corresponds to the sample core alone. One scan corresponds to 1000 frames.

ID	**Configuration**	**Voltage**	**Current**	**Acquisation time per radiograph**
-	-	[kV]	[µmA]	[ms]
1	Full	260	200	500
	Core	230	60	1000
2	Full	260	200	333
	Core	230	60	1000
3	Full	-	-	-
	Core	230	60	1000
4	Full	260	200	500
	Core	230	60	1000
5	Full	260	200	333
	Core	230	60	1000
6	Full	260	200	500
	Core	230	60	1000
7	Full	-	-	-
	Core	230	60	1000
8	Full	-	-	-
	Core	230	60	1000

5.3 Results

5.3.1 Hypervelocity impacts on samples

This section shows the result obtained from the hypervelocity impact test campaign and is divided into sub-sections, each related to a single sample. Three main elements are reported for each sample:

- A table summarizing the configuration parameters with the impact velocity (Table 5.3 to 5.10).
- Pictures of the sample under different point of views, including witness plates when it is relevant (Figure 5.5, 5.7,5.9, 5.11, 5.13, 5.15, 5.17, 5.19).
- Cutaway images extracted from CT-scans showing the crater morphology (Figure 5.6, 5.8, 5.10, 5.12, 5.14, 5.16, 5.18, 5.20).

High-speed images of the tests are shown in Appendix A.

No passing-through debris were observed for the stochastic core whilst all the PCS rear skins were perforated after impact. For sample 8, debris went also through the 0.75 mm-thick Al witness plate.

Sample 1 :

Table 5.3 – Sample 1 configuration used during the test campaign

ID	Core	Core density	Bumper	Spacing	Core orientation	Impact velocity
-	-	[%]	-	[mm]	[°]	[m/s]
1	Foam	20.3	Al foil	0	0	6826

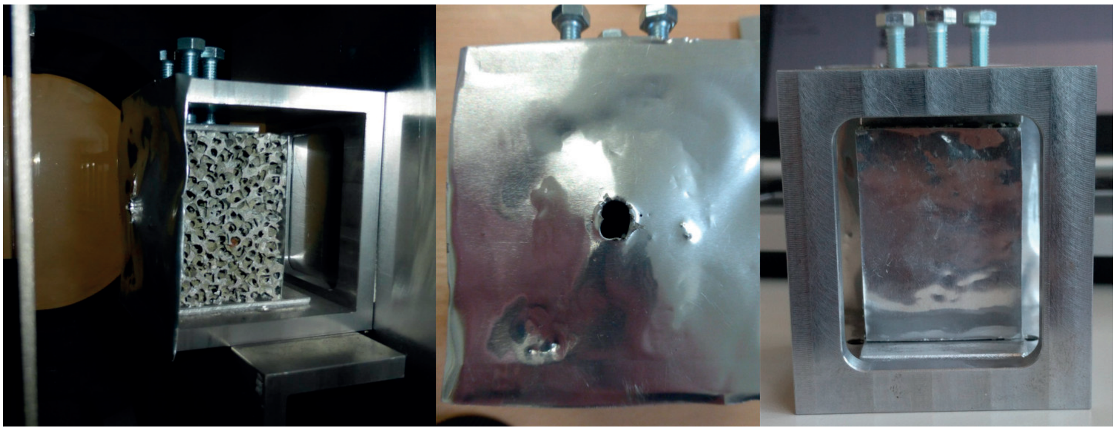

Figure 5.5 – Post-impact pictures of sample 1 in the test chamber (left), from the front (center) and from the back (right). Reproduced from [216].

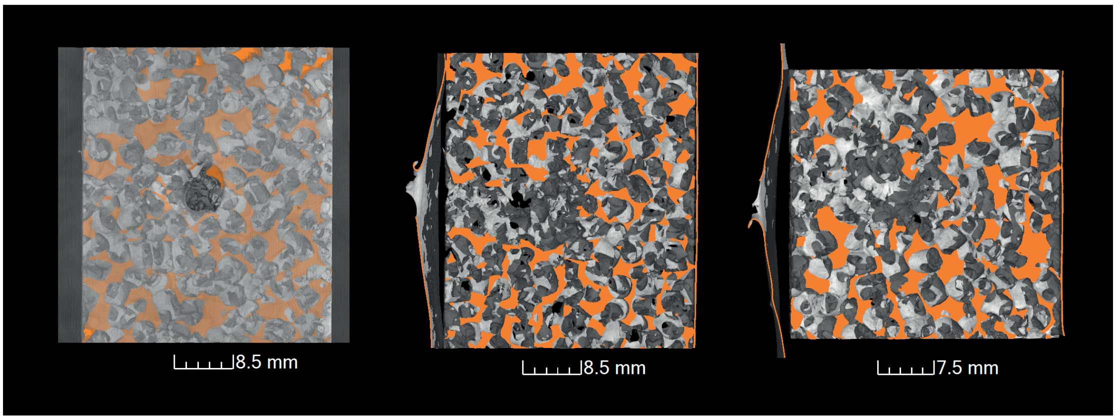

Figure 5.6 – Cross-section of tested sample 1 from the front with transparent bumper (left), from the right (center) and from the top (right). Reproduced from [216].

Sample 2 :

Table 5.4 – Sample 2 configuration used during the test campaign

ID	Core	Core density	Bumper	Spacing	Core orientation	Impact velocity
-	-	[%]	-	[mm]	[°]	[m/s]
2	Foam	19.8	Al foil	10	0	6948

Figure 5.7 – Post-impact pictures of sample 2 in the test chamber (left), from the front (center) and from the back (right). Reproduced from [216].

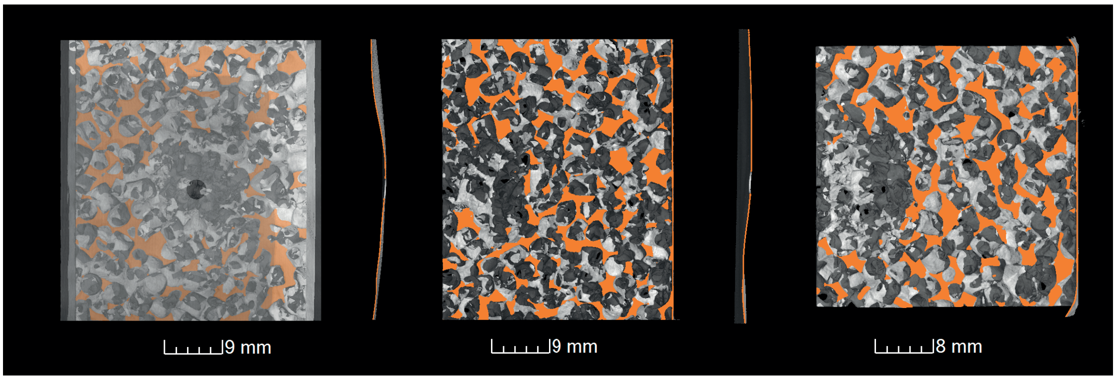

Figure 5.8 – Cross-section of tested sample 2 from the front with transparent bumper (left), from the right (center) and from the top (right). Reproduced from [216].

Sample 3 :

Table 5.5 – Sample 3 configuration used during the test campaign

ID -	**Core** -	**Core density** [%]	**Bumper** -	**Spacing** [mm]	**Core orientation** [°]	**Impact velocity** [m/s]
3	Foam	23.5	MLI	10	0	6733

Figure 5.9 – Post-impact pictures of sample 3 in the test chamber (left), from the front (center) and from the back (right). Reproduced from [216].

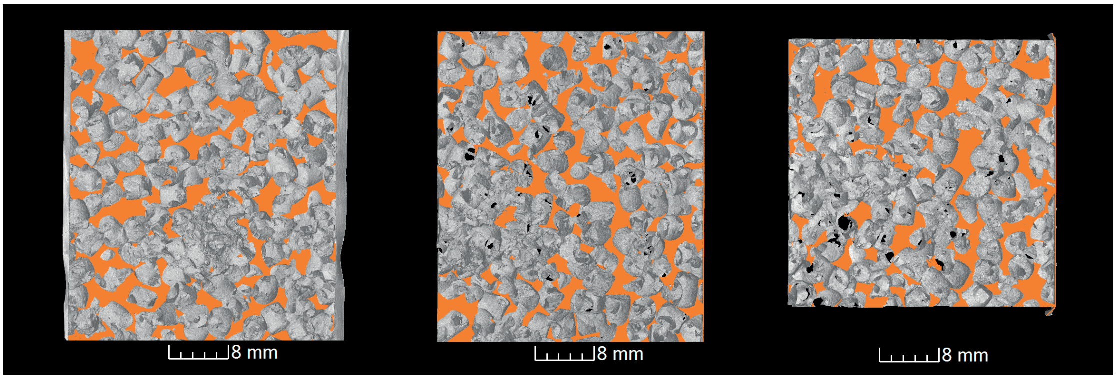

Figure 5.10 – Cross-section of tested sample 3 from the front without the bumper (left), from the right (center) and from the top (right). Reproduced from [216].

Sample 4 :

Table 5.6 – Sample 4 configuration used during the test campaign

ID	Core	Core density	Bumper	Spacing	Core orientation	Impact velocity
-	-	[%]	-	[mm]	[°]	[m/s]
4	PCS	34.8	Al foil	0	0	6907

Figure 5.11 – Post-impact pictures of sample 4 in the test chamber. From left to right: in the test chamber, front view, rear view and witness plate with aluminum deposition. Reproduced from [216].

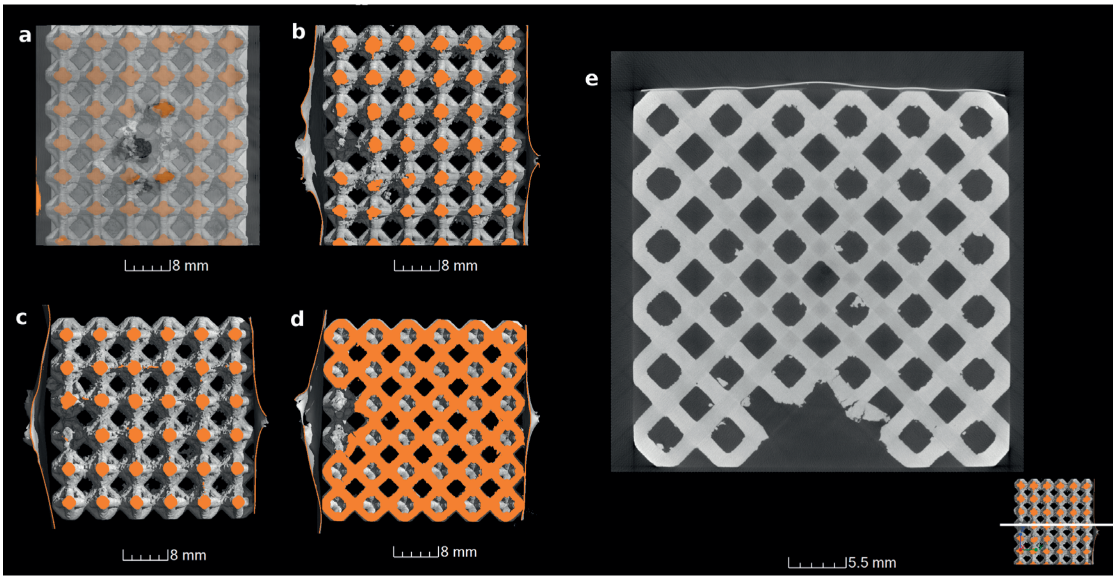

Figure 5.12 – Cross-section of tested sample 4. a) from the front view with transparent bumper, b) from the right, c) from the top view at exit hole level, d) from the top view at impact hole level. e) HD CT-scan image of the top view at the impact hole level (corresponding to the cross-section in d)), cracks can be observed. Reproduced from [216].

Sample 5 :

Table 5.7 – Sample 5 configuration used during the test campaign

ID -	Core -	Core density [%]	Bumper -	Spacing [mm]	Core orientation [°]	Impact velocity [m/s]
5	PCS	32.2	Al foil	10	0	6798

Figure 5.13 – Post-impact pictures of sample 5 in the test chamber. From left to right: in the test chamber, front view, rear view and witness plate with aluminum deposition. Reproduced from [216].

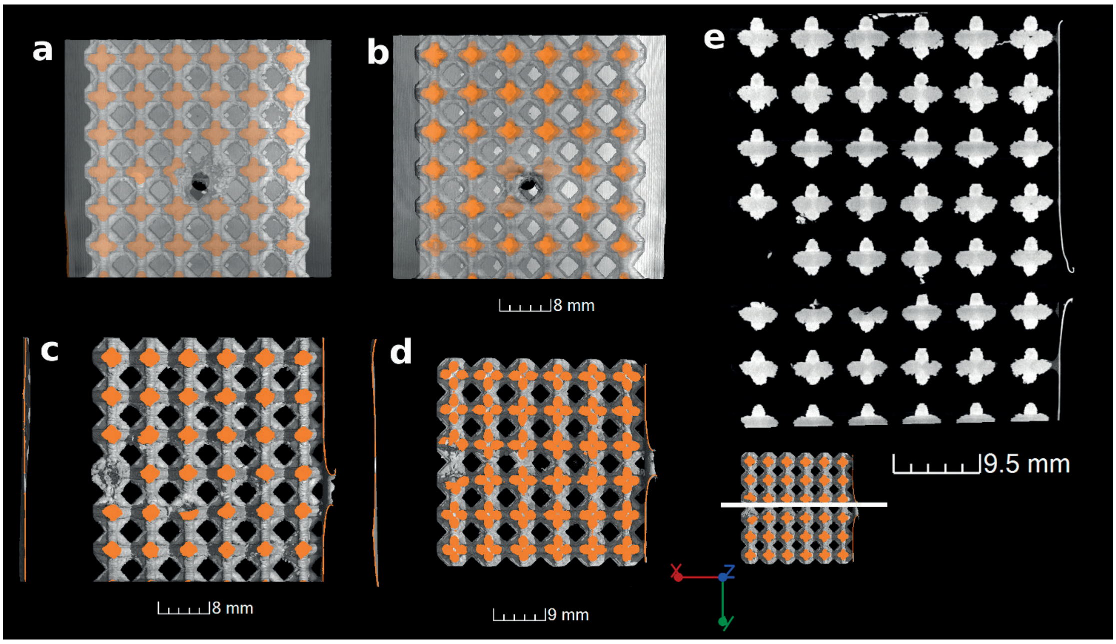

Figure 5.14 – Cross-section of tested sample 5. a) from the front view with transparent bumper, b) from the back with transparent skin, c) from the top view at impact hole level, d) from the top view at impact hole level. e) HD CT-scan image of the right view at the impact hole level (corresponding to the cross-section in c)). Reproduced from [216].

Sample 6 :

Table 5.8 – Sample 6 configuration used during the test campaign

ID -	Core -	Core density [%]	Bumper -	Spacing [mm]	Core orientation [°]	Impact velocity [m/s]
6	PCS	33.2	Al foil	10	12	6760

Figure 5.15 – Post-impact pictures of sample 6 in the test chamber. From left to right: in the test chamber, front view, rear view and witness plate with aluminum deposition. Reproduced from [216].

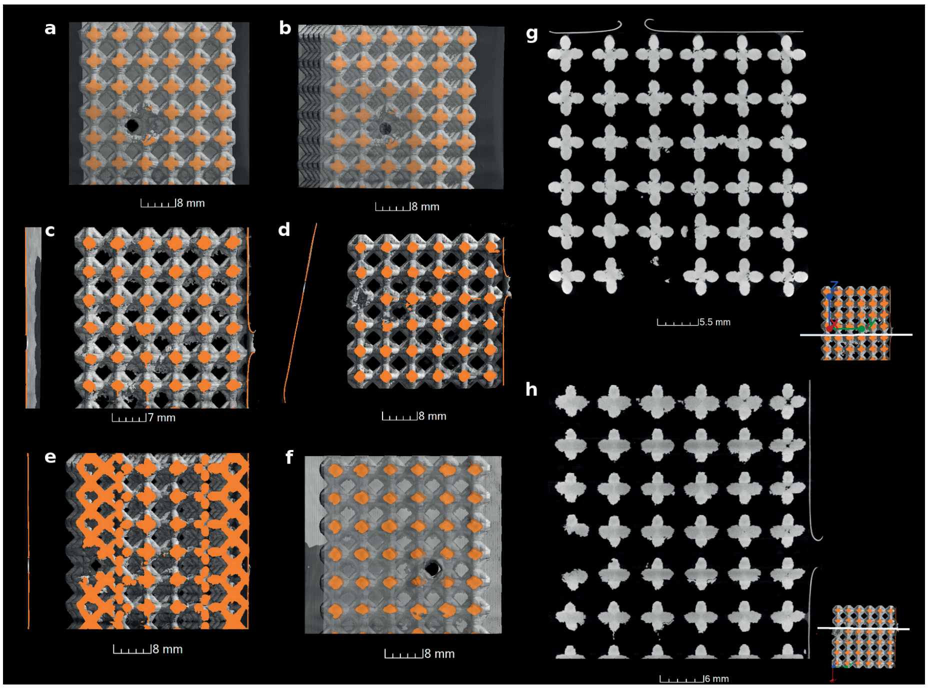

Figure 5.16 – Cross-section of tested sample 6. Front view with transparent bumper aligned to a) lattice main axis and b) projectile trajectory, c) right view aligned to lattice main axes, d) top view, e) right view perpendicular to bumper, f) rear view with transparent skin aligned to lattice main axes, g) HD CT-scan image of the top view at the impact hole level (cross-section in d)), h) HD CT-scan image of the right view at the impact hole level (cross-section in c)). Reproduced from [216].

Sample 7 :

Table 5.9 – Sample 7 configuration used during the test campaign

ID	Core	Core density	Bumper	Spacing	Core orientation	Impact velocity
-	-	[%]	-	[mm]	[°]	[m/s]
7	PCS	32.6	MLI	10	0	6913

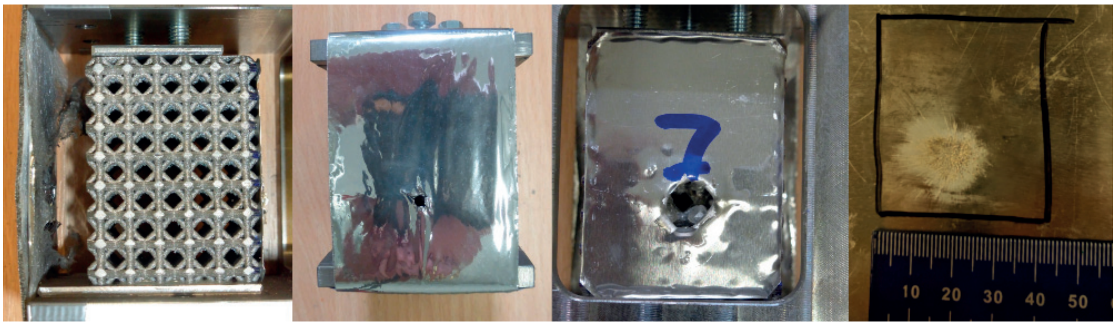

Figure 5.17 – Post-impact pictures of sample 7 in the test chamber. From left to right: in the test chamber, front view, rear view and witness plate with aluminum deposition. Reproduced from [216].

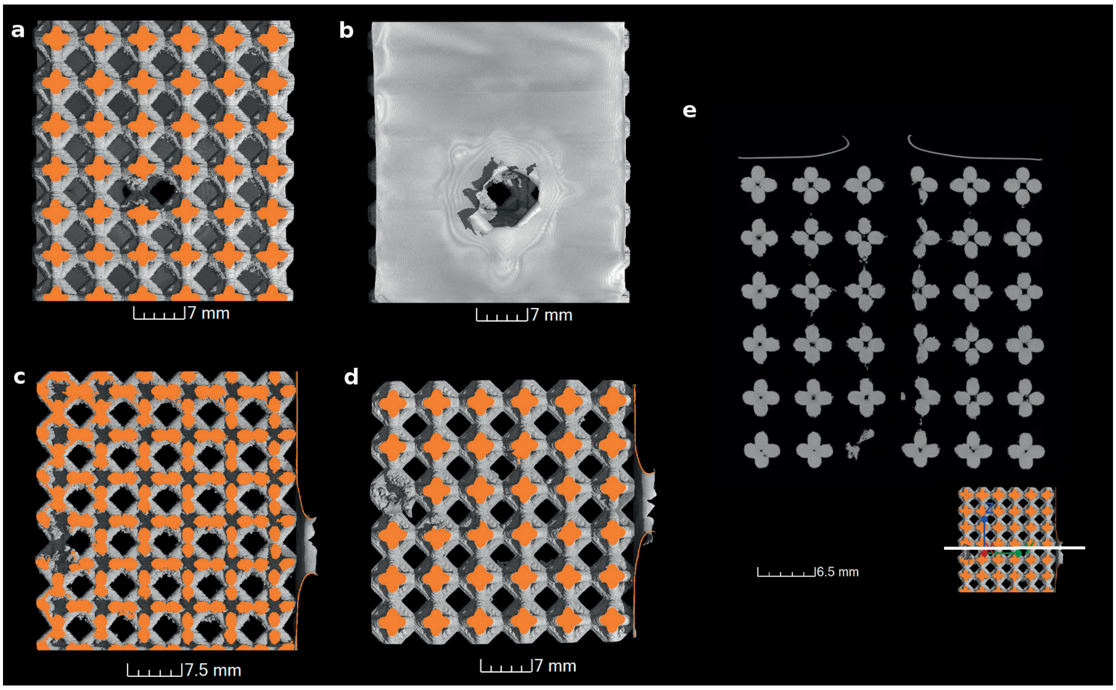

Figure 5.18 – Cross-section of tested sample 7. a) Front view without MLI, b) rear view with aluminum skin, c) right view at impact hole level, d) top view at impact hole level, e) HD CT-scan image of the right view at the impact hole level (cross-section in d)). Reproduced from [216].

Sample 8 :

Table 5.10 – Sample 8 configuration used during the test campaign

ID	Core	Core density	Bumper	Spacing	Core orientation	Impact velocity
-	-	[%]	-	[mm]	[°]	[m/s]
8	PCS	33.6	MLI	10	12	7025

Figure 5.19 – Post-impact pictures of sample 8 in the test chamber. From left to right: in the test chamber, front view, rear view, witness plate with aluminum deposition and secondary impact on witness plate. Reproduced from [216].

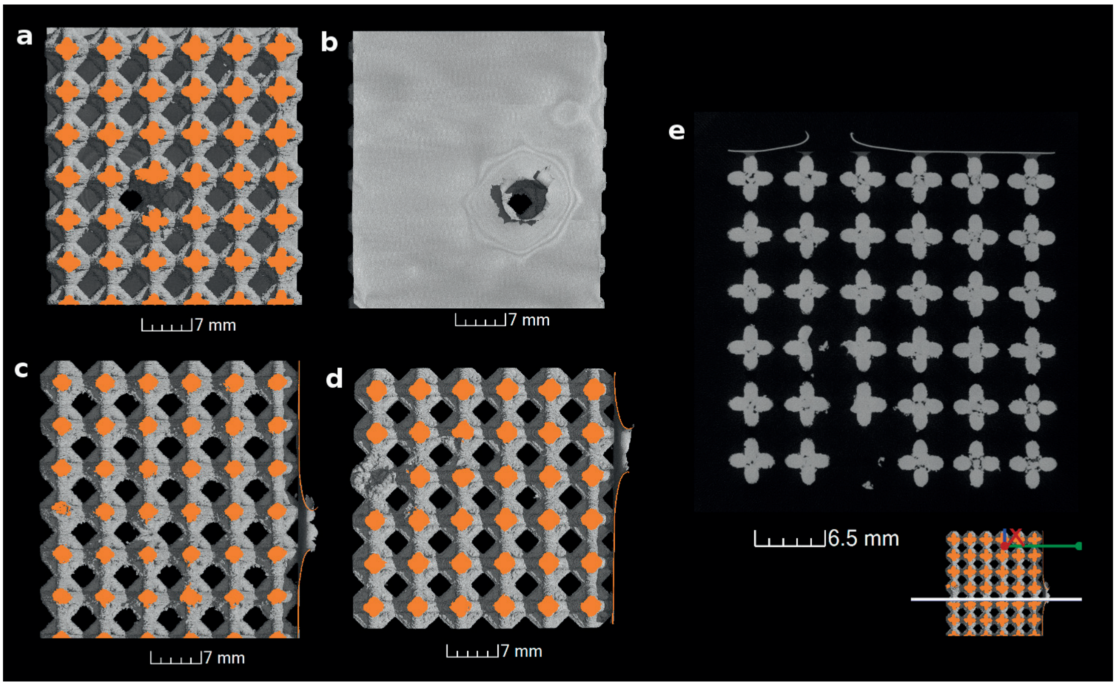

Figure 5.20 – Cross-section of tested sample 8. a) Front view without MLI, b) rear view with aluminum skin, c) right view at impact hole level, d) top view at impact hole level, e) HD CT-scan image of the right view at the impact hole level (cross-section in d)). Reproduced from [216].

5.3.2 Debris cloud morphologies

Whipple shield efficiency is based on the bumper capacity to fragment the debris spreading the load on a larger rear wall surface. The dispersion angles were characterized by high-speed images during the tests. For Al foil bumper, two different debris clouds could be observed and related to their densities, namely (i) a central high-density region with a dispersion angle estimated between 16° and 30° and (ii) a less dense cloud extending to 61°. No relevant measurement could be made on the projectile dispersion after impact on MLI. A possible explanation might be that a significant amount of organic volatiles produced during the impact blurred any observations. Figure 5.21 shows bumper composition effect on the debris clouds after impact.

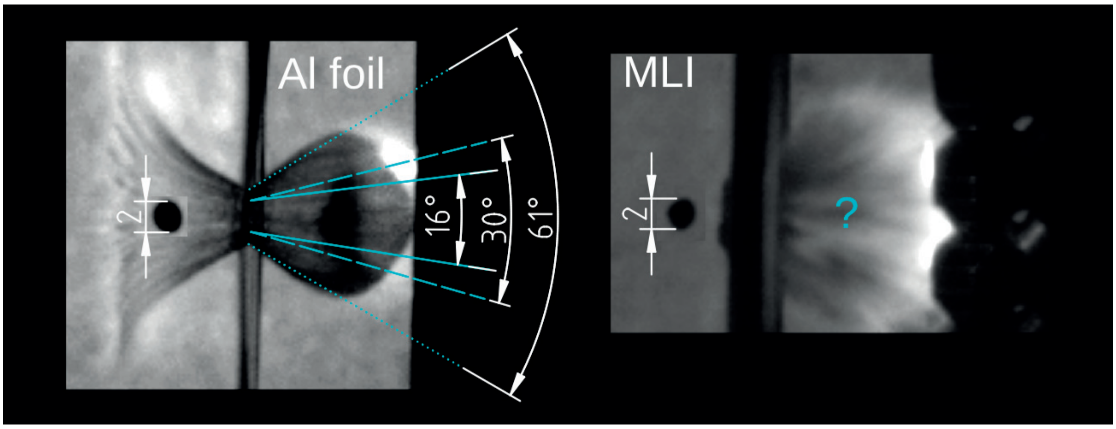

Figure 5.21 – Composite images showing the debris cloud morphology after impact on a 0.15 mm-thick Al foil (left) and MLI (right) bumpers. Reproduced from [216].

5.3.3 Microstructural analysis

Metallographic analyses were performed to assess the effect of high-velocity impact on the Al core microstructures. Figure 5.22 shows the selected surfaces for the investigated stochastic and PCS samples, number 2 and 8 respectively. The focus was set on the front face impact area.

Stochastic samples

Sample 2 was selected for metallographic investigation of stochastic structures. Three main features induced by the impact test could be observed: (i) a layer of deposited material shinier than the A357 bulk alloy and measured to be about tens of microns thick, (ii) broken cell walls and struts, (iii) displaced and reattached chunks of the A357 bulk alloy. Figure 5.23 shows an example of the three features mentioned above.

PCS samples

Sample 8 was chosen for metallographic investigations of periodic cellular structures. Bright material deposition and cracks in the struts could be observed as shown in Figure 5.24. No evidence of displaced bulk material was revealed during microscopy.

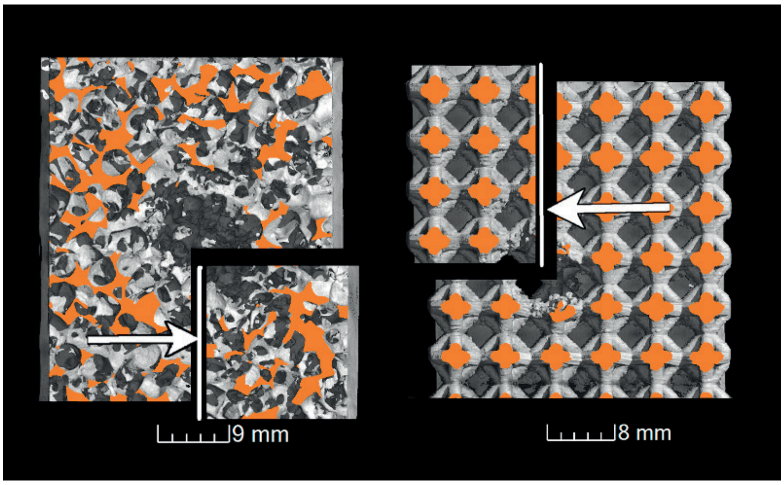

Figure 5.22 – CT-scan front view images of stochastic (left, sample 2) and PCS (right, sample 8) highlighting the analyzed surface during metallography. Reproduced from [216].

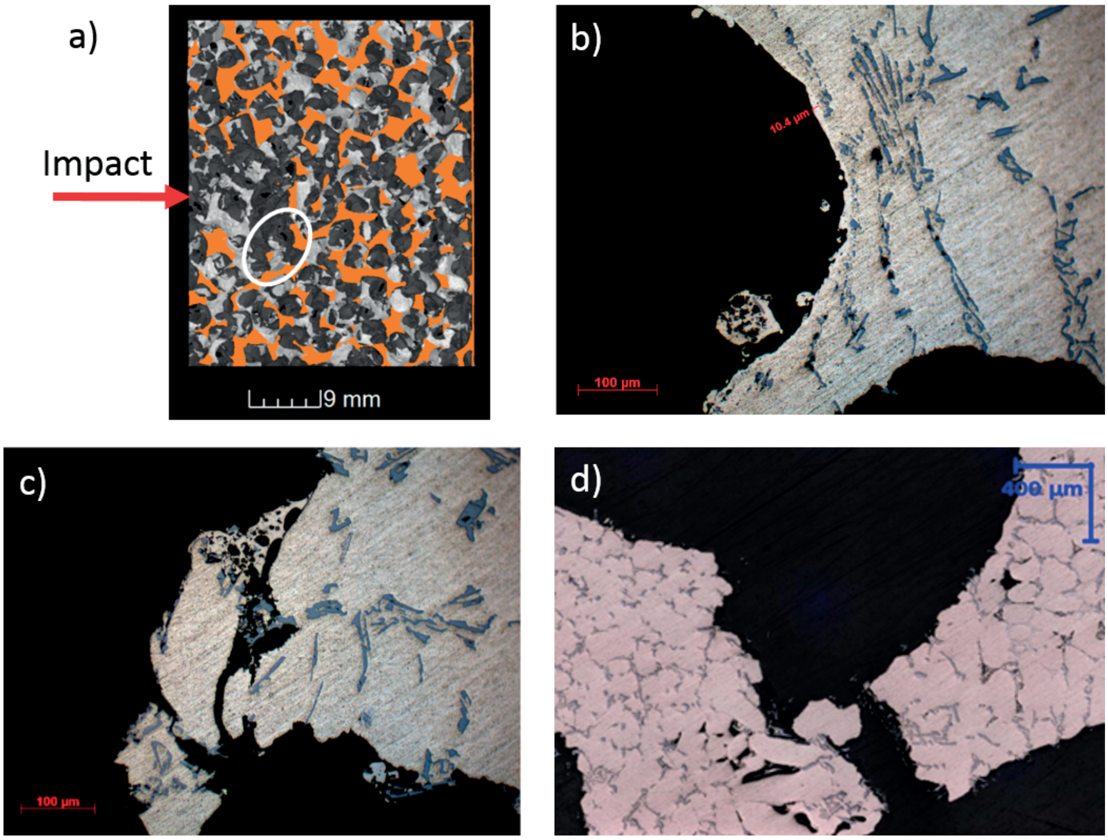

Figure 5.23 – Features induced by hypervelocity impact testing on A357 alloy stochastic structures. a) 3D-scan cutaway right view showing the impact location and the studied area. b) Example of deposited layer (scale bar is 100 µm). c) Example of displaced A357 alloy chunk (scale bar is 100 µm). d) Example of broken cell strut (scale bar is 400 µm). Adapted from [216].

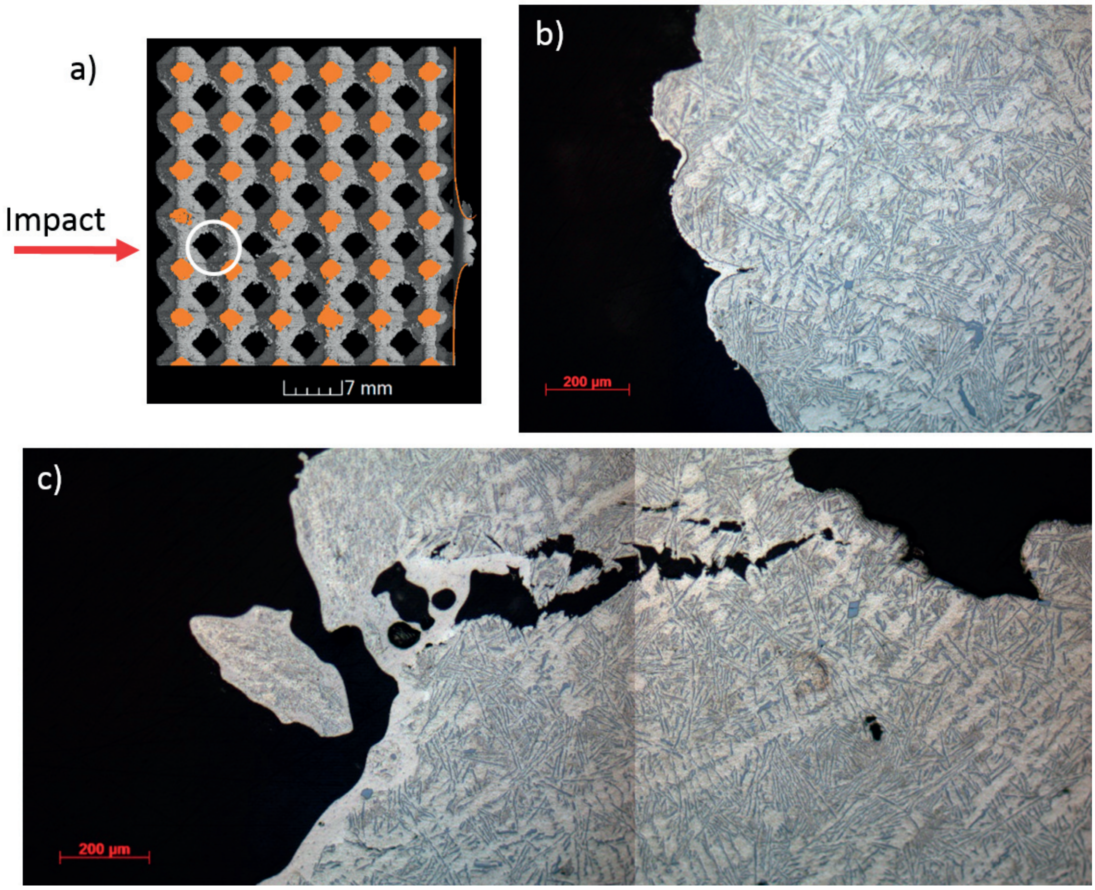

Figure 5.24 – Features induced by hypervelocity impact testing on AlSi12 alloy PCS. a) 3D-scan cutaway right view showing the impact location and the studied area. b) Example of deposited layer (scale bar is 200 µm). c) Example of crack in a cell strut (scale bar is 200 µm). Adapted from [216].

5.4 Discussion

5.4.1 Metallographic analysis

Despite the fact that hypervelocity impact induces high temperature usually leading to melting and vaporization of the encountered material an dthe projectile, no microstructural modification of samples (either stochastic or PCS) could be observed in the crater. The rapidity at which the events occurred regarding heating and cooling rate might explain the observed result.

In addition to some displaced original material and cracks into the structures, another important feature induced by impact is the layer deposition of a brighter material. This feature comes from the solidification of melted and vaporized, nearly pure aluminum, which composes the projectile and the bumper in both sample configurations (Sample 2 and 8).

The main result coming from the combined metallographic and 3D-tomography investigations is that almost no material implied in the impact absorption remained within the core; rather, it was lost as debris and dust. This can be observed on CT-scans and Figure 5.25, which shows a low-magnification picture close to Sample 2's crater. Layer deposition is highlighted in green and displaced material is marked in yellow. Appendix B contains higher magnifications of numbered sectors that can be seen in the overview picture. Therefore, the main energy absorption mechanism implied in the impact absorption is rupture of cell walls and struts instead of plastic deformation or matter change of state.

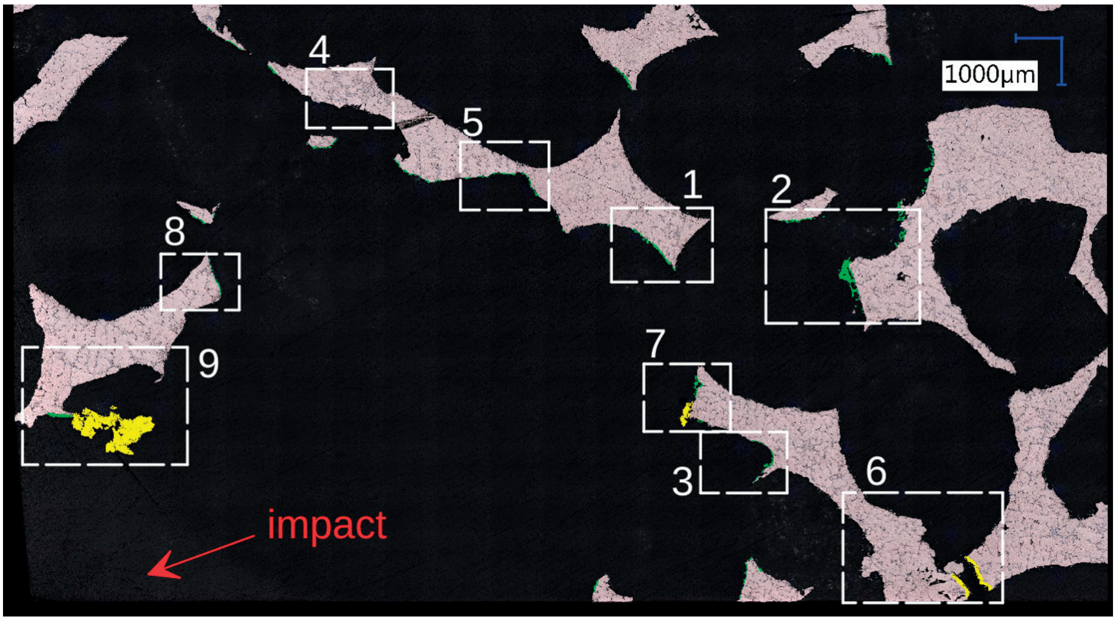

Figure 5.25 – Low magnification picture of crater area on Sample 2. Deposited layers are highlighted in green and displaced material in yellow. Numbered sectors correspond to higher magnification images available in Appendix B. Reproduced from [216].

5.4.2 Stochastic structure impact craters

For all the configurations, stochastic foam cores successfully stopped the projectile. Structural deformations were characterized by the crater depth and the crater volume. For the former, the measurements were performed on CT-scan cross-sections and led to crater depths of 20 mm, 14 mm and 20 mm for Sample 1, 2 and 3 respectively with an uncertainty of 3 mm corresponding to the characteristical pore size (Figure 5.26). The uncertainty was due to the difficulty at some points to set the limit between the crater and the process-induced (initial) porosity.

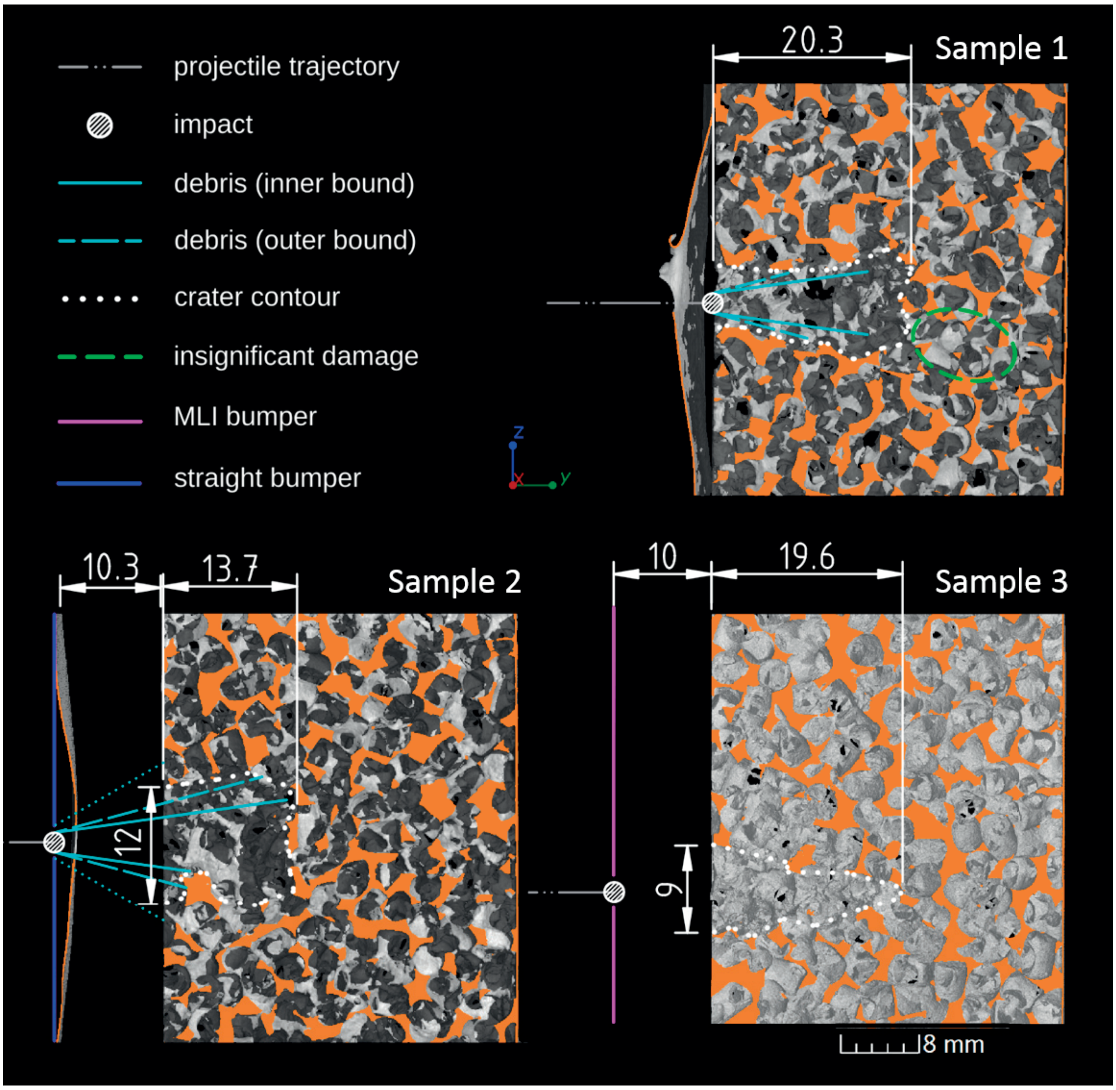

Figure 5.26 – CT-scan cut-away right views of stochastic Sample 1 to 3 at the crater level. Reproduced from [216].

The intricate shape and the difficulty in separating the crater from the pristine porosity made its volume estimation challenging. The evaluation was achieved by image analysis using MATLAB scripts performed on 2D images extracted from the 3D-tomography. A 36x36x36 mm^3 volume was isolated around each crater and subdivided into smaller N mm-side cubes, so-called voxels (N being an integer). Once the mesh was built, the solid fraction of all the voxels was computed and clusters empty of solid were isolated. Clusters were defined as an assembly of at least 6 connected voxels, so as to avoid taking into account rogue voxels located into the original foam porosity. The crater was then defined as the largest cluster and was computed for N values ranging from 14 to 34 (Figure 5.27). Figure 5.28 shows the crater volume evolution for the three stochastic samples as a function of N-factor. A smooth increase in total measured computed macropore (or apparent crater) volume can be observed first, then at a certain threshold volumes start to diverge, around N = 28-29. This limit highlighted the point where voxels were small enough to spread into the foam porosity. Final estimation of the crater volume was then calculated with a conservative N value of 27 leading to 891 mm^3, 1297 mm^3, 757 mm^3 for Sample 1, 2, 3 crater volumes respectively.

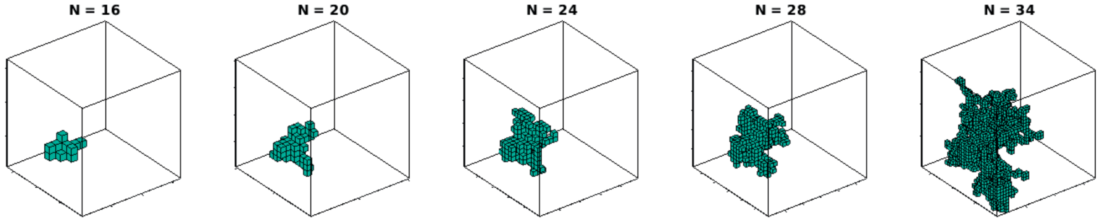

Figure 5.27 – Mesh refinement effect on the computed crater volume by empty cluster aggregation. Reproduced from [216].

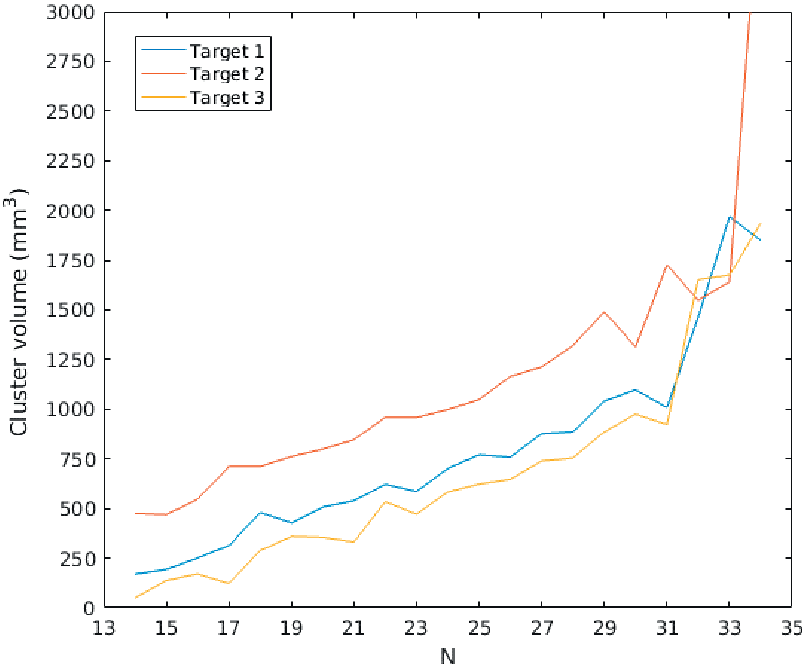

Figure 5.28 – Cluster volume evolution as a function of the N-factor highlighting a divergence for values above 28-29. Reproduced from [216].

Finally, the energy dissipation per volume was estimated for each sample by dividing the impact energy with the crater volume. The impact energy was taken as 90% of the kinetic energy of the projectile, to take into account energy absorption by the residual atmosphere drag and the initial bumper impact. Table 5.11[1] summarizes the different previously defined parameters for all the stochastic samples.

Table 5.11 – Stochastic structures performances at mitigating hypervelocity ballistic impact

Sample (Bumper, Spacing)	**1** (Al foil, 0 mm)	**2** (Al foil, 10 mm)	**3** (MLI, 10 mm)
Crater depth [mm]	20 ± 3	14 ± 3	20 ± 3
Crater volume [mm^3]	891	1297	757
Impact energy [J]	237 ± 12	242 ± 12	245 ± 12
Energy dissipation [J/mm^3]	0.27 ± 0.01	0.19 ± 0.01	0.32 ± 0.01

A deep and narrow crater seems to be more efficient at impact absorption. Nevertheless, the crucial parameter to assess the performance of a shield is its minimum required thickness for no penetration. In this sense, Sample 2 performed 30% better than the others and showed the importance of the bumper and the spacing to improve shielding performances.

The possibility to implement stochastic foam as MMOD protection was assessed by comparing the structure without and with Al bumper (Sample 1 and 2) to a Whipple shield with the same 0.15 mm-thick Al bumper and a spacing of 10 mm. The required A357 rear wall thickness for no penetration was estimated from the equation established by Christiansen [197]. In addition, the necessary thickness for a bulk A357 plate was also computed. Table 5.12 summarizes the results obtained and showed that stochastic foam with a spaced bumper competes with the performance of a Whipple shield with the same configuration regarding surface density. Nevertheless, Whipple shield design used for comparison is the simplest and more complex configurations (Multi-shock with high strength fabrics) are currently in used, outperforming our samples.

Table 5.12 – Thickness and surface density comparison of different shields for no penetration of a 2 mm-diameter Al sphere at 7 km/s

Design Spacing [mm]	**Stochastic** 10	**Stochastic** 0	**Whipple** 10	**Thick wall** 0
Wall thickness [mm]	14	20	2.3	11.1
Overall thickness [mm]	24.2	20.2	12.5	11.1
Surface density [g/cm2]	0.8	1.1	0.7	3.0

5.4.3 PCS structure impact trajectories

The first relevant observation from the impact test campaign performed on PCS is that projectile reached and perforated the sample rear skin for all the configurations. The periodic structures

---

[1] Some differences can be observed from the values exposed here and the one that can be found in Voillat's thesis [216]. The energy absorption values were calculated using a mean crater volume obtained from two methods for Voillat and from one for this work. Therefore, for consistency, calculations were rerun. Concerning the crater depth of Sample 3, the measured 19.6 mm value was rounded to 20 mm instead of 19 mm.

major drawback in impact mitigation is the presence of open channels which can be aligned with the debris trajectories, a feature also observed for aluminum honeycomb structures [211]. A first explanation of the poor shielding properties would then be a direct hit on the rear skin from debris fragments passes along the [100] open channels, especially for Sample 4 and 5. However, this theory doesn't fully explain the damages observed in the rest of the samples due to excessive rear skin deformation (Sample 7) or the absence of direct path in some configurations (Sample 6 and 7). By carefully analyzing the CT-scans, evidence of secondary ejecta ricochets from the impact on the first encountered cells could be observed resulting in localized deformations inside the structures. Figure 5.29 to 5.31 show in red the secondary ejecta trajectories that might be at the origin of the rear skin perforation. Three samples (4, 6 and 8) emphasized characteristics of this spalled material on the protection performances. Sample 4 (Figure 5.30) exposed a case where debris fragments were able to bounce back and perforate a second time the bumper in addition to the rear skin rupture; the event sequence was made evident by observing the high-speed images taken during the test. Sample 6 (Figure 5.31) exhibited a second point of impact on the witness plate which highlighted that secondary ejecta, not only passed through along the [100] direction, but could also make it through the narrower [110] open channel. The Sample 8 witness plate was also perforated after impact, which highlights the fact that a debris has sufficient energy passing through the structure to penetrate a 0.76 mm-thick aluminum plate.

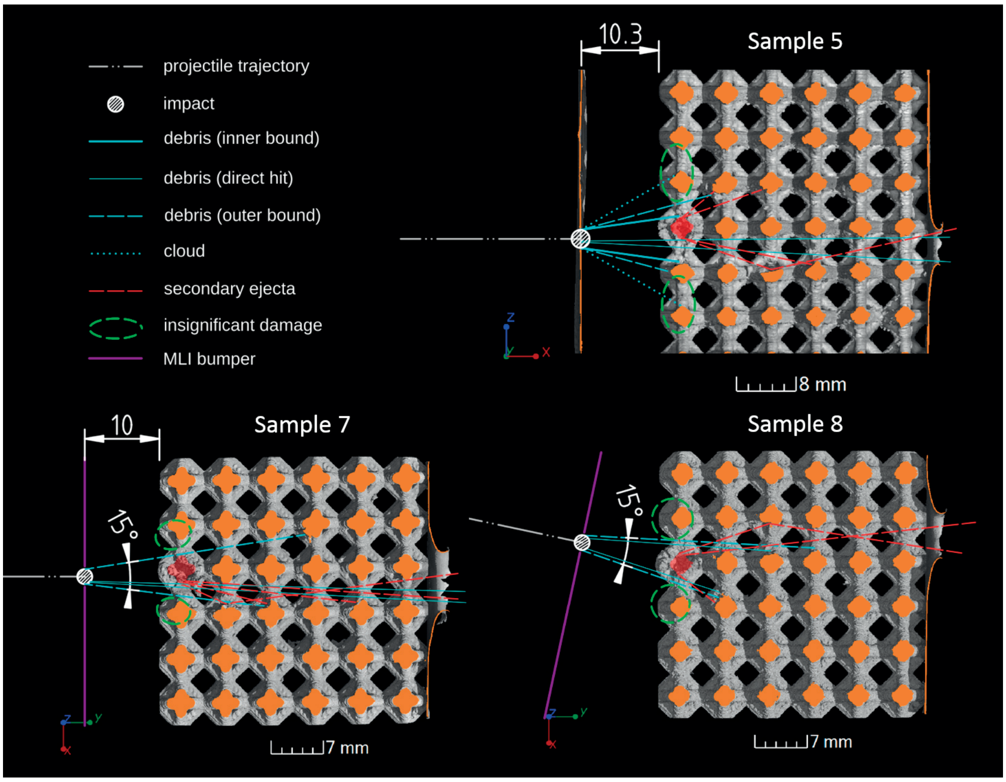

Figure 5.29 – CT-scan cut-away right views of PCS Sample 5, 7 and 8 at the crater level. Attempts to recover secondary ejecta trajectories are shown in red dash lines. Ghost red area shows the location of an entirely destroyed cell during impact. Reproduced from [216].

Figure 5.30 – CT-scan cut-away right views of PCS Sample 4 at the crater level. Bounced back secondary ejecta could be observed. Reproduced from [216]. Adapted from [216].

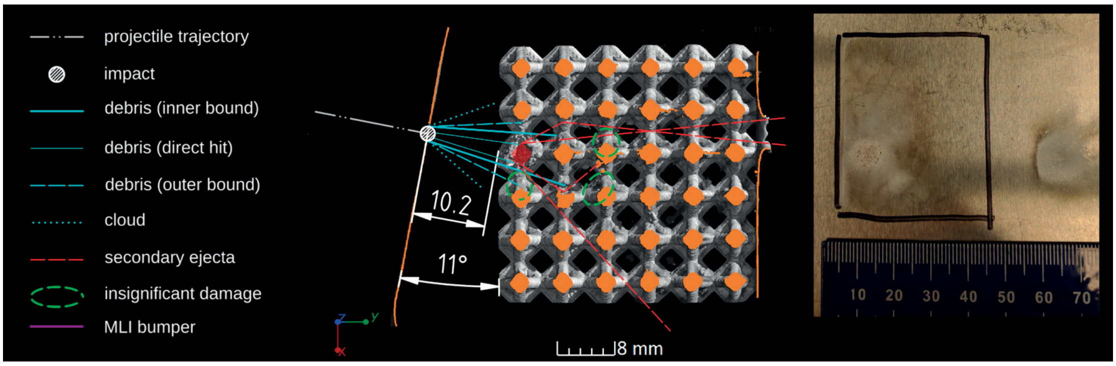

Figure 5.31 – CT-scan cut-away right views of PCS Sample 6 at the crater level. Evidence of secondary preferential path along [110] channels could be observed. Adapted from [216].

5.4.4 Bumper effect on fragmentation debris

From the analysis of the debris cloud after projectile impact on the Al bumper, three different characteristic dispersion angles were measured, a denser part with an angle between 16°-30° and a cloud extending to 61°. Post-impact damage characterization on samples with Al bumper and a 10 mm spacing (Sample 2, 5 and 6) showed that no significant damage could be observed onto the structures for dispersion angle larger than 16°. Therefore, it was considered that the danger zone after bumper impact is located within this angle, which is consistent with the 17° angle estimated by Piekutowsky for a similar configuration [199].

No direct observation could have been made concerning the MLI bumper effect on debris fragmentation. Nevertheless, the damaged area in Sample 7 and 8 and the crater morphology of Sample 3, closer to an impact with no stand-off distance, led to the conclusion that the MLI bumper is less efficient than Al to spread the debris, with an outer bound for the dispersion angle of 15°. On the one hand, MLI could be seen as a multi-shock design which should increase the performance. On the other hand, the organic composition of light elements combined with an interlayer distance less than 0.2 mm might prevent the MLI from efficiently fragmenting the debris, which is consistent with the observations.

5.5 Conclusion

A hypervelocity ballistic impact test campaign was conducted on aluminum structures (stochastic and periodic) with 2 mm-diameter Al projectiles reaching velocities between 6.7 and 7 km/s. Influences of bumper material (Al and MLI), bumper spacing (0 and 10 mm) and impact angle (0° and 11° to normal) were investigated.

Stochastic structures successfully stopped the projectiles independently from the configuration whereas all the PCS failed to complete the task. The importance of the bumper spacing was emphasized in the stochastic structures, improving the performance by 30% with respect to crater depth. Surface density showed that cellular metal could compete with classical Whipple shield design. However, more complex designs are currently in use and probably outperform our samples [186, 187, 197, 200–202, 205]. The poor performances of PCS were explained by a combination of open channels and ricochet of secondary ejecta, which allowed the penetration of the rear skin. Hazardous characteristics of this spalled material were highlighted by the observation of damages far from the projectile line of sight.

Bumper effectiveness for debris fragmentation was assessed and was consistent with reported results concerning the Al bumper [199], although the MLI bumper showed insufficient capacity to break the projectile; this was attributed to its low density.

Despite the high temperatures reached during impact, no modification of the bulk metal microstructure was observed, and the primary energy dissipation mechanism was defined to be the rupture of cell walls and struts instead of plastic deformation and matter change of state.

Cellular metals (stochastic or periodic) may nonetheless be an alternative to MMOD shielding applications if designed accordingly, as this approach would add a structural component that is currently lacking in classical shield concepts.

Conclusion

Results

This thesis was focused on three main research directions, namely (i) the investigation and prediction of the failure mode in additively manufactured AlSi12 periodic cellular structures (PCS) under compression, (ii) the development of an investment casting process to produce such PCS out of AlSi12 alloy, and (iii) the characterization of the behavior of PCS in simulated MMOD impact conditions. The results obtained can be summarized as follow:

Failure mode of additively manufactured periodic cellular structures

- A preliminary tensile test campaign on bulk alloy dogbone samples showed consistency with the literature regarding the mechanical properties, the defects, and the fracture surfaces [6,25–27,35,38–40,225]. The high solidification rate imposed by the process produced a finer microstructure, enhancing the mechanical properties, namely an increase of 100% in the yield stress and 40% in the ultimate tensile stress, than compared to classical cast parts. The importance of process-induced features on the anisotropy and the fracture was highlighted as cracks preferentially propagated along melt-pools interfaces. Numerical models were extracted from the campaign and used in finite element analyzis.
- Varying the topology of periodic cellular structures showed significant differences regarding the performance and deformation mode underlining the importance of the design. At a constant relative density of 30%, face-centered cubic (FCC) structures exhibited higher mechanical properties than body-centered cubic (BCC) structures by at least 20%. The unusual brittle failure observed for these cellular metals was associated with the intrinsic brittleness of the bulk solid material, enhanced by the existence of planes of weakness delimited by melt-pools contours.
- Finite element simulations showed the importance of microplasticity or misalignment in this class of material, responsible for the reduction of the initial compressive modulus by a certain factor between 1.4 and 1.9. The topology dependent uneven side effect was calculated, ranging from a minimum sample-to-cell size ratio required of 2 for diamond (Di) and octet-truss (Oct) structures, and up to a ratio of 6 for FCC structures.
- The observed global shear failure mode of PCS under compression is explained by topological considerations: sliding failure planes are normal to the direction presenting the highest surface density variation and including an interconnected strut network. If more than one

plane family can be identified, the fracture preferentially takes place in the plane exhibiting the highest planar stiffness. This failure criterion is consistent with most observations reported in the literature.

- Fracture occurred by strut bending at the junction with nodes, promoted by a minimum surface density and a preferential alignment to the crack path, along the melt-pool interfaces.

Investment casting of PCS

- An investment casting process using a NaCl salt mold to replicate a sacrificial polymer preform was successfully developed. Di PCS structures with a cell size of 6mm and a relative density of 31% were manufactured this way with the following characteristics: (i) Young's compressive modulus of 1.2 GPa and calculated to be 5.4 GPa without microplasticity effects, (ii) a plateau stress of 20 MPa, (iii) a densification strain of 77%, and (iv) an energy absorption capacity of 15 MJ/m^3 with an efficiency of 80%.
- The main parameter influencing the completed part quality was identified to be the NaCl grain size, with best results obtained for a distribution between 125 and 180 µm. Other important optimized parameters include: drying temperature (80°C), vibration packing time per step (30 s) and infiltration pressure (300 mbar) under 660°C.
- The duration of the drying step could be shortened by a factor 6 through the optimizing of draining and the exposure of the green body surfaces.
- Comparison with AM PCS showed compliance with the previously established failure criterion. The microplasticity effect was enhanced by the radius of curvature at identified stress-concentration sites, the structure exhibiting the smaller radii being the more susceptible to local plasticity.

PCS performance to mitigate MMOD impacts

- Stochastic structure successfully stopped 2-mm diameter Al sphere impacting at 7 km/s. The additional effect of a bumper on the shielding performance was observed in the difference of crater depth, going from 20 mm to 14 mm. The efficiency of MLI thermal insulation was limited as it did not contribute to the fragmentation of the projectile. These results are comparable to a simple Whipple shield design having a similar areal density (0.8 g/cm^2).
- PCS performed poorly at stopping high-velocity projectile, all sample were entirely perforated. This was due to the open-channels present in the structure, creating a preferential direction for the debris to pass through.
- Despite the high temperatures reached during impact, no modification of the bulk metal microstructure was observed. The primary energy dissipation mechanism was defined to be the rupture of cell walls and struts instead of plastic deformation and matter change of state.

The implementation of PCS in space will therefore depend on the specific application. Additively manufactured PCS might be suitable for structural parts due to their higher stiffness and yield stress. A high and effective energy absorption capacity make cast PCS parts good candidates for shock absorbers and dampeners. However, even being structurally optimized, PCS are outperformed by stochastic structures for shields which show promising results for MMOD impact mitigation applications.

Future work

The failure criterion of PCS under compression established during this thesis was consistent with most of the reported results in literature. However, the presence of contradictory observations show this criterion needs to be refined. Further investigations will be required to define the frame in which the criterion applies (such as strut diameter, strut cross-sections, relative density and geometrical defects).

A successful casting process was developed to produce PCS. However, the stereolithography sacrificial preform with the highest resolution could not be used because of its incompatibility with the NaCl mold. Therefore, improvement in reducing the stress imposed by the preform or strengthening the mold might a solution to improve the quality of the cast part. Process steps have to be further optimized to minimize, as example, the uneven mass distribution observed in the cast samples.

The poor performance of PCS at mitigating MMODs impact highlight the necessity to perform further investigations if they want to be used in spacecraft shielding applications. They might be combined with stochastic foam, or their structures might be downgraded to pseudo-periodic, in order to remove the deleterious open-channels. Also, systematic CT-scans before and after impact should be conducted and/or a different material used as projectile to better understand the full historic of the impact phenomena.

A HVIT impacts snapshots

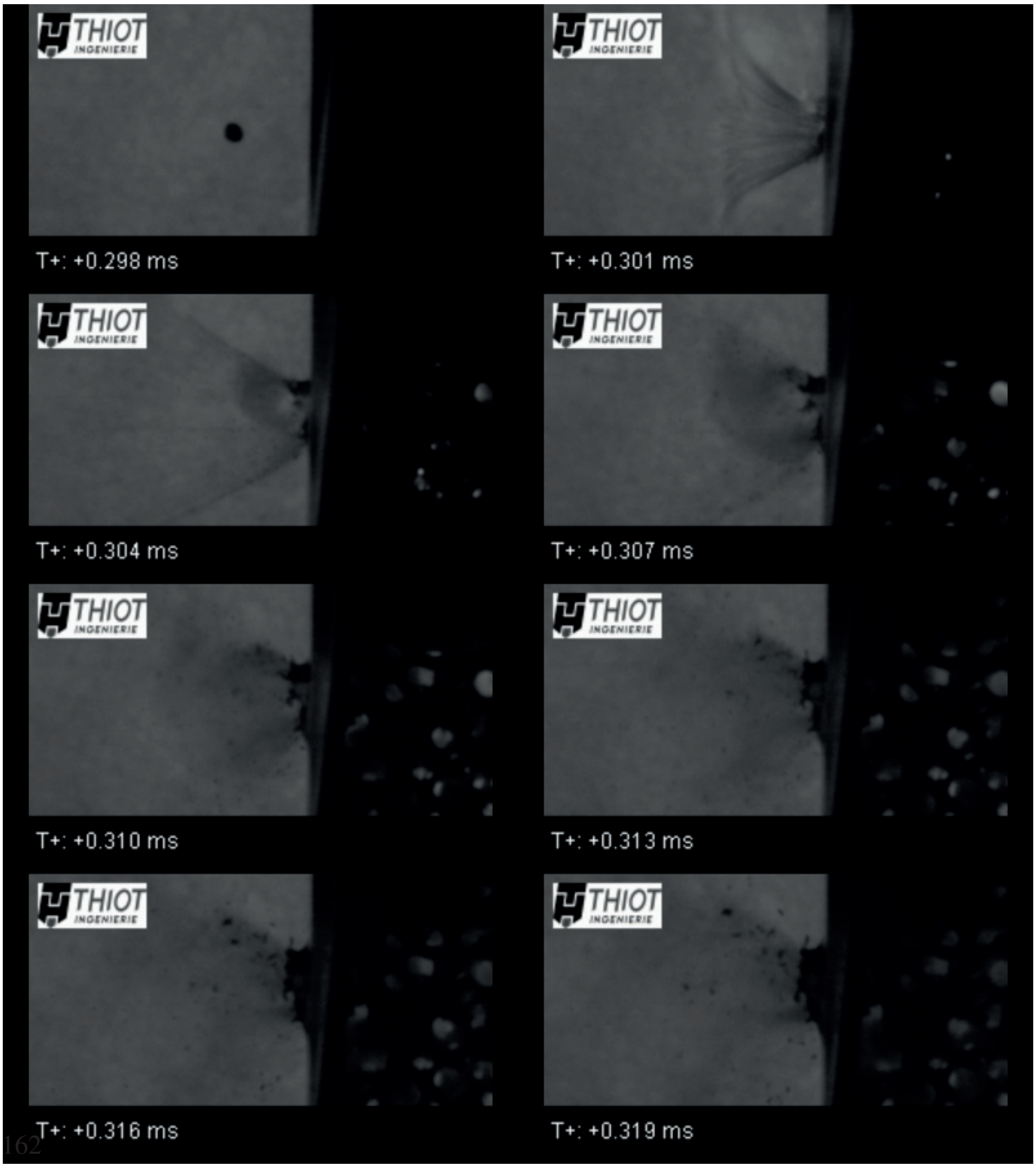

Figure A.1 – High-speed images of impact on sample 1 with a velocity of 6826 m/s. Reproduced from [216].

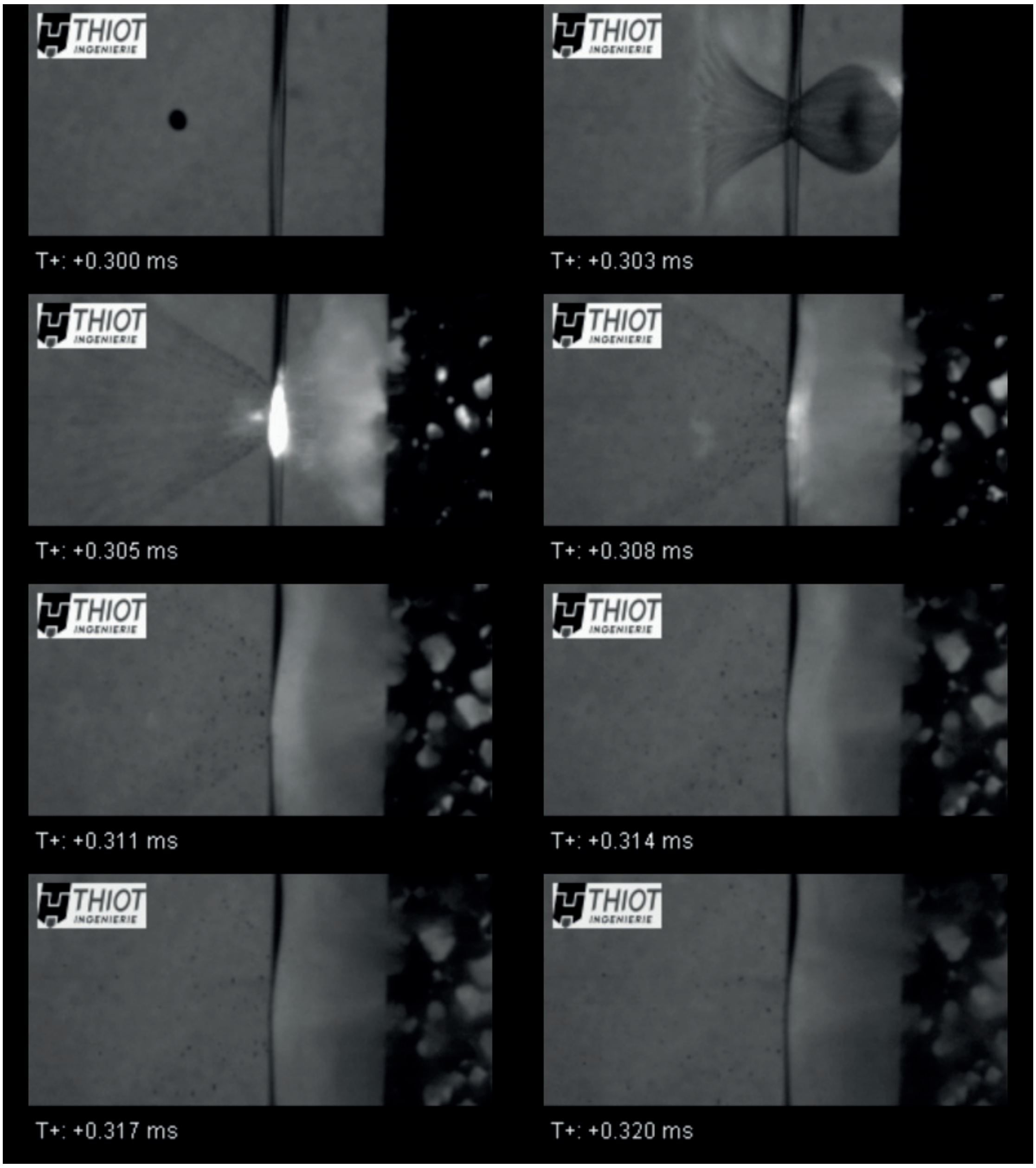

Figure A.2 – High-speed images of impact on sample 2 with a velocity of 6948 m/s. Reproduced from [216].

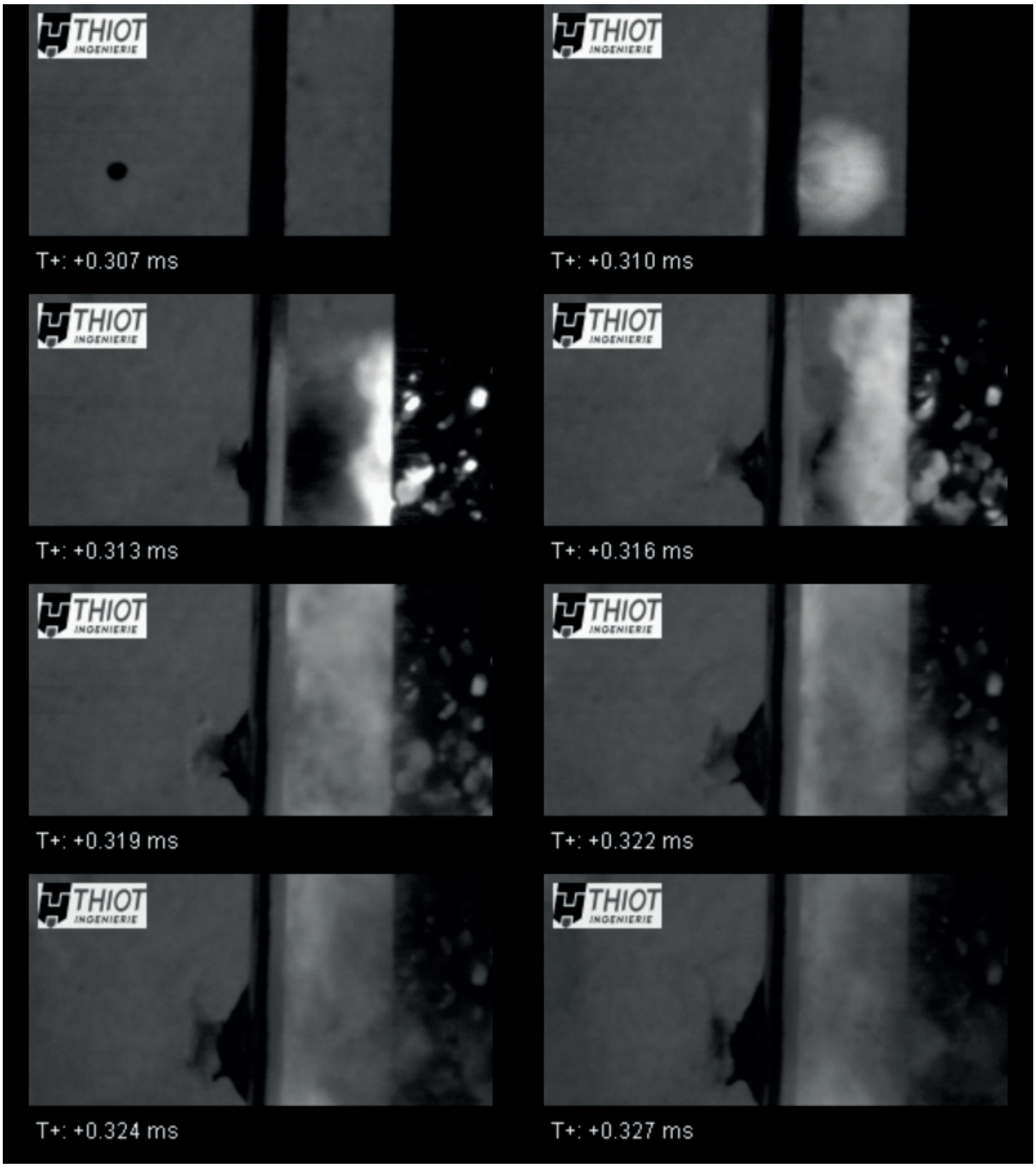

Figure A.3 – High-speed images of impact on sample 3 with a velocity of 6733 m/s. Reproduced from [216].

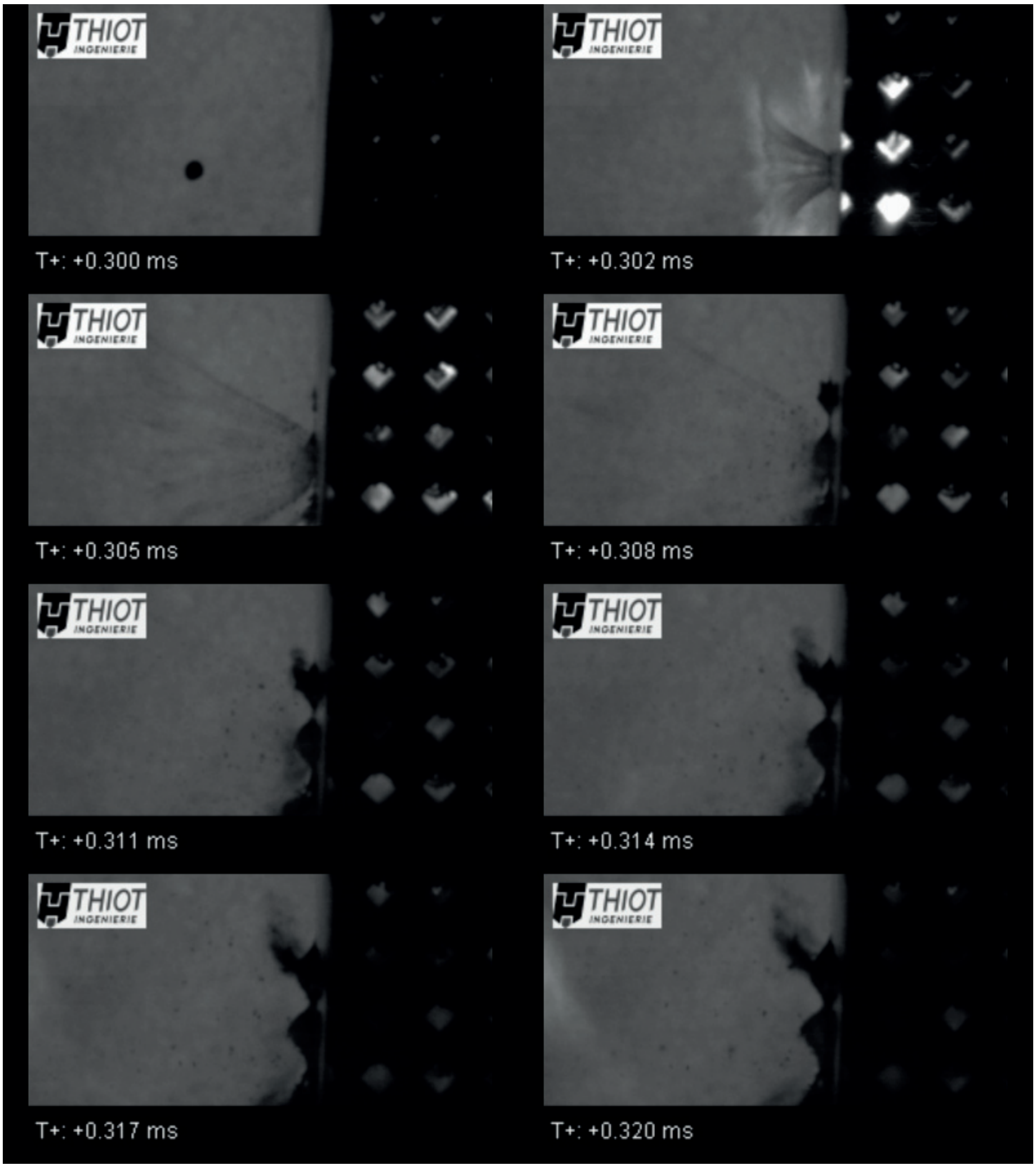

Figure A.4 – High-speed images of impact on sample 4 with a velocity of 6907 m/s. Reproduced from [216].

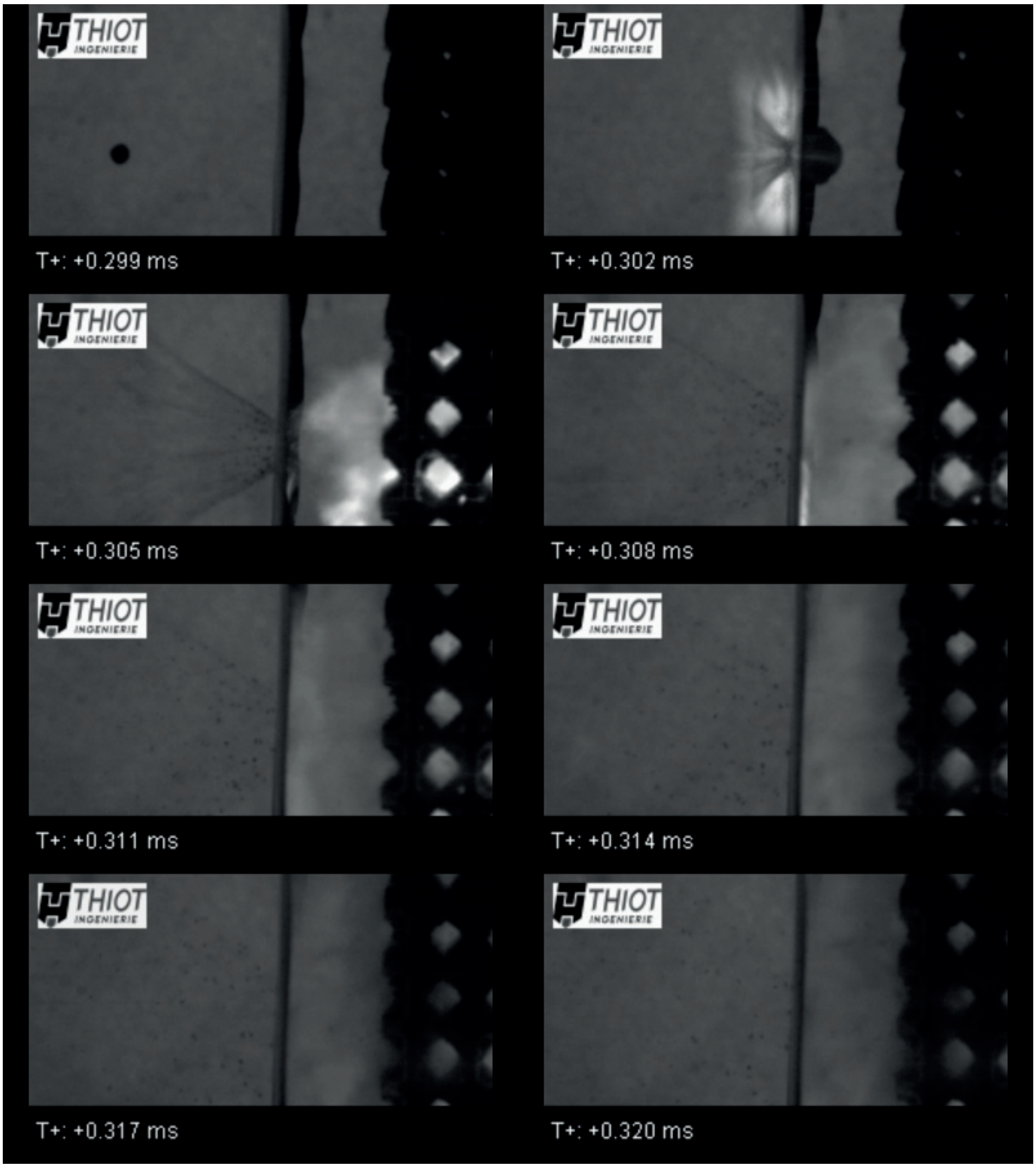

Figure A.5 – High-speed images of impact on sample 5 with a velocity of 6798 m/s. Reproduced from [216].

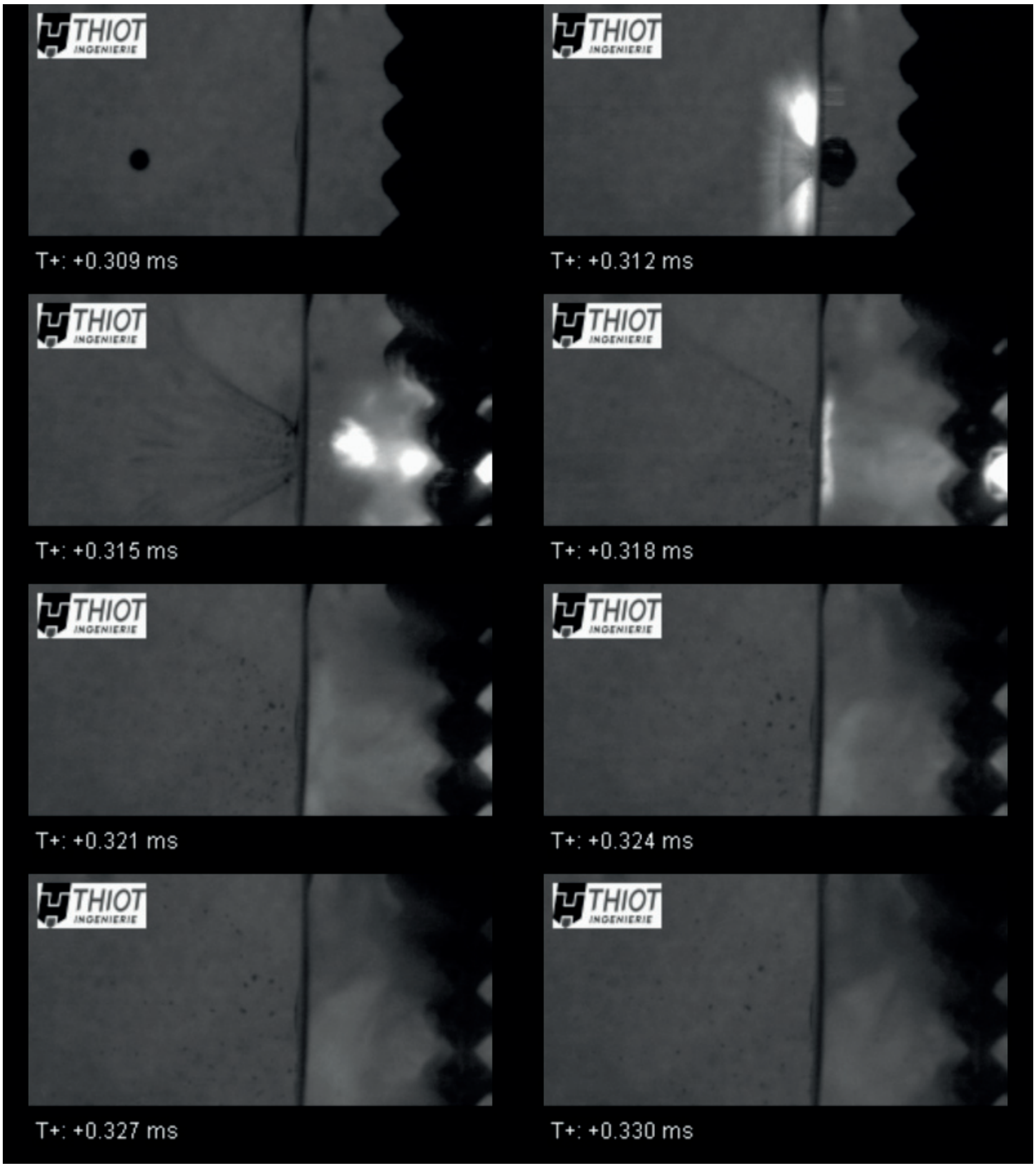

Figure A.6 – High-speed images of impact on sample 6 with a velocity of 6760 m/s. Reproduced from [216].

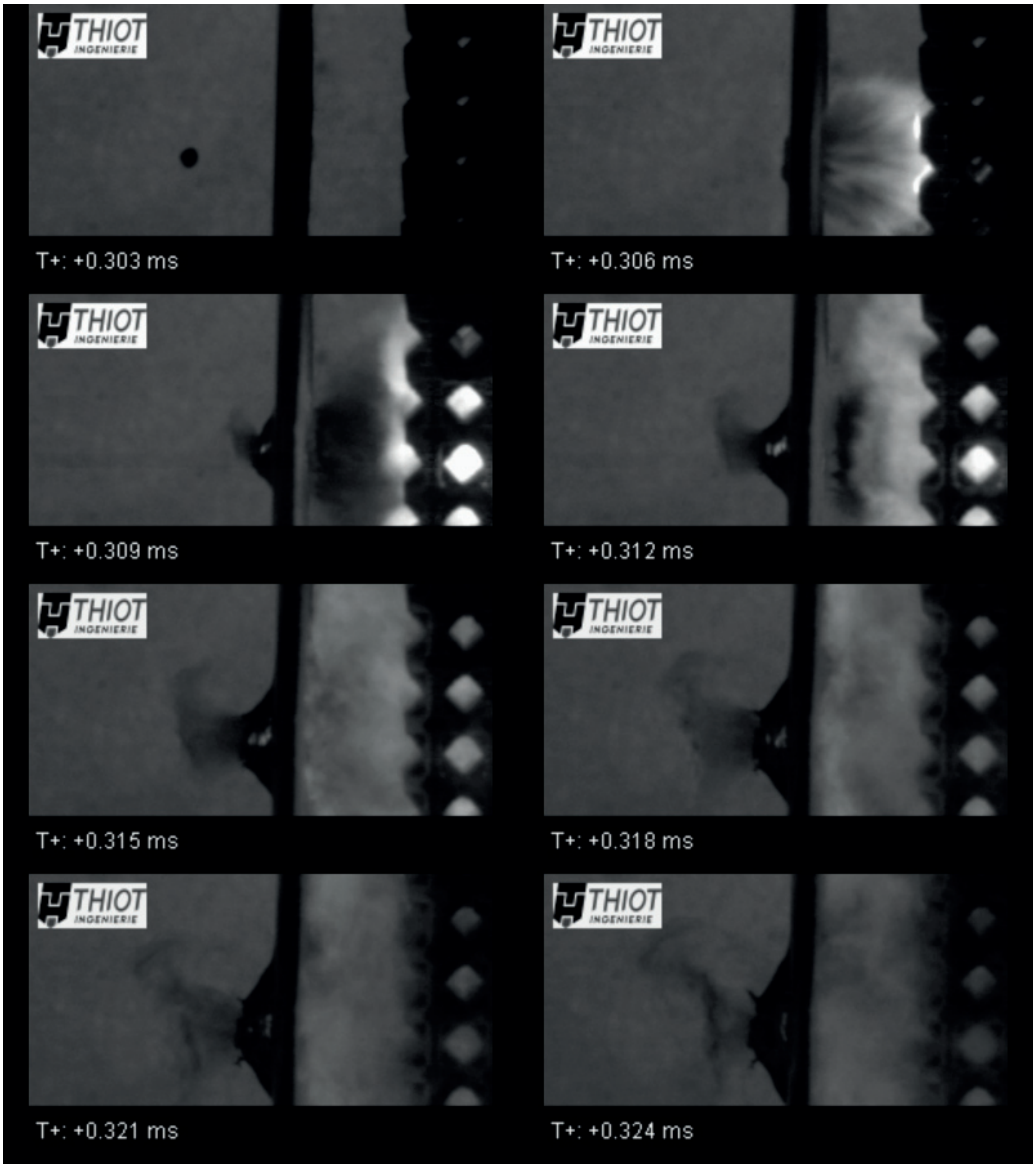

Figure A.7 – High-speed images of impact on sample 7 with a velocity of 6913 m/s. Reproduced from [216].

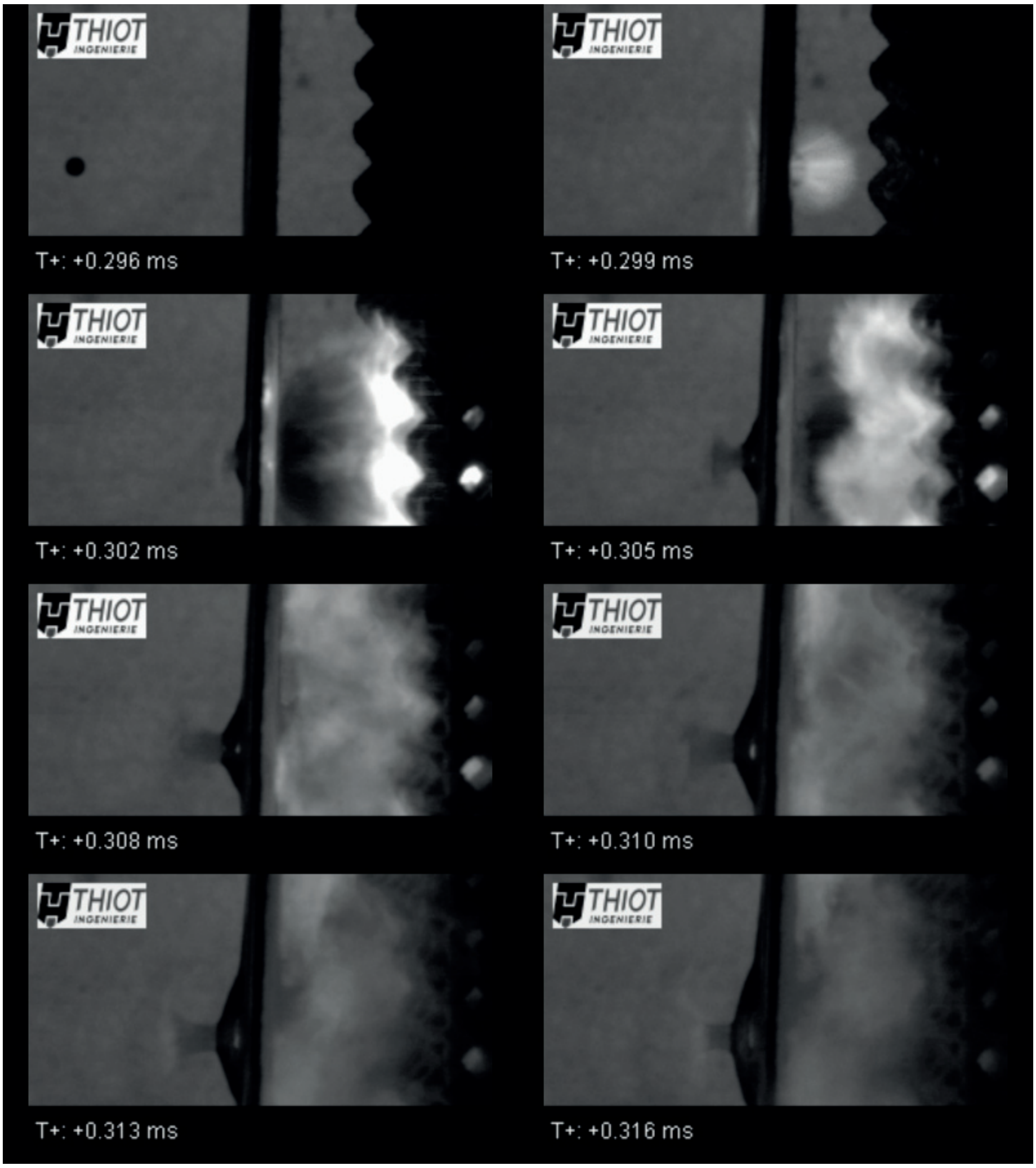

Figure A.8 – High-speed images of impact on sample 8 with a velocity of 7025 m/s. Reproduced from [216].

B Stochastic sample metallography

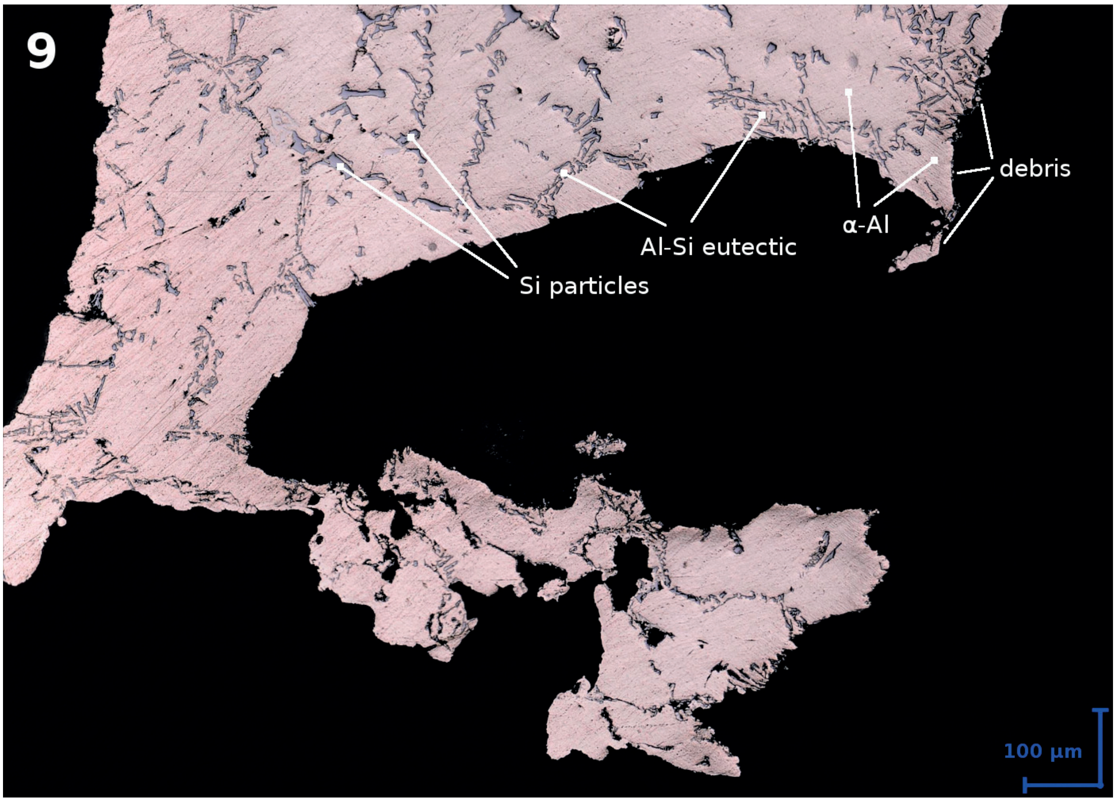

Figure B.1 – Microscopy image showing the three identified features present in stochastic Sample 2 after impact (deposited layer, displaced material, structure crack). Reproduced from [216].

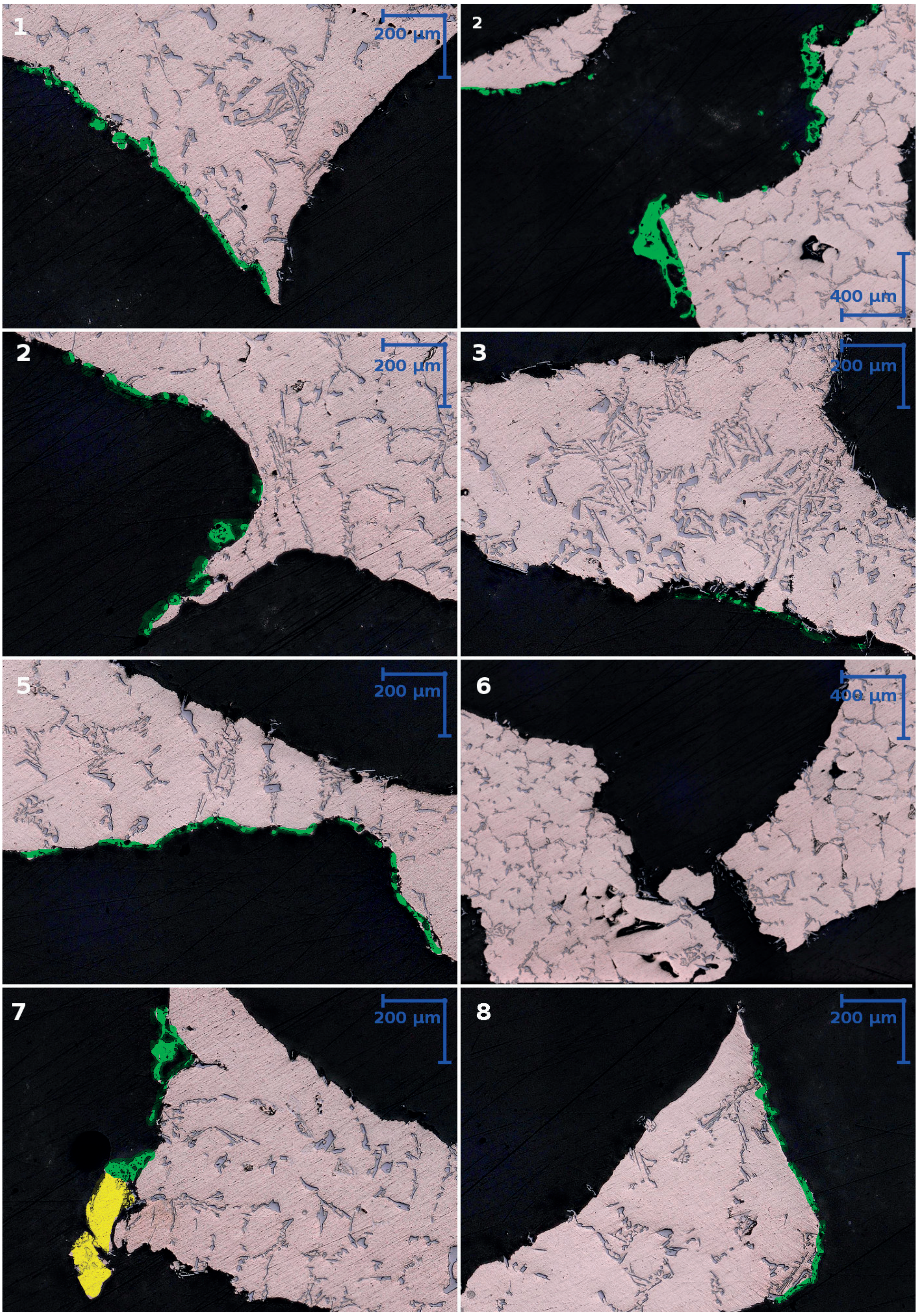

Figure B.2 – Microscopy images of stochastic Sample 2. Deposited layers are highlighted in green and displaced material in yellow. Reproduced from [216].

Bibliography

[1] Claude Nicollier and Volker Gass. *Our Space Environment - Opportunities, Stakes, and dangers*. EPFL Press, New York, NY, 2017.

[2] Ian Gibson, David Rosen, and Brent Stucker. *Additive Manufacturing Technologies*. Springer New York, New York, NY, 2015. DOI: 10.1007/978-1-4939-2113-3.

[3] Cheng-Jui Li, Tsung-Wen Tsai, and Chien-Chou Tseng. Numerical simulation for heat and mass transfer during selective laser melting of titanium alloys powder. *Physics Procedia*, 83:1444 – 1449, 2016. Laser Assisted Net Shape Engineering 9 International Conference on Photonic Technologies Proceedings of the LANE 2016 September 19-22, 2016 Fürth, Germany.

[4] Kai Zeng, D Pal, and Brent Stucker. A review of thermal analysis methods in laser sintering and selective laser melting. pages 796–814, 01 2012.

[5] Adriaan B. Spierings, Nicolaus Herres, and Gideon Levy. Influence of the particle size distribution on surface quality and mechanical properties in AM steel parts. *Rapid Prototyping Journal*, 17(3):195–202, 2011.

[6] L. Lü, J. Y. H. Fuh, and Y. S. Wong. *Laser-induced materials and processes for rapid prototyping*. Kluwer Academic Publishers, Boston, 2001.

[7] Ming. Tang. Inclusions, porosity, and fatigue of alsi10mg parts produced by selective laser melting. Carnegie Mellon University, 2017. Dissertations. 903.

[8] Luke N. Carter, Christopher Martin, Philip J. Withers, and Moataz M. Attallah. The influence of the laser scan strategy on grain structure and cracking behaviour in slm powder-bed fabricated nickel superalloy. *Journal of Alloys and Compounds*, 615:338 – 347, 2014.

[9] Jean-Pierre Kruth, Peter Mercelis, Jonas Van Vaerenbergh, and Tom Craeghs. Feedback control of selective laser melting. In *Proceedings of the 3rd international conference on advanced research in virtual and rapid prototyping*, pages 521–527, 2007.

[10] Ehsan Foroozmehr and Radovan Kovacevic. Effect of path planning on the laser powder deposition process: thermal and structural evaluation. *The International Journal of Advanced Manufacturing Technology*, 51(5-8):659–669, November 2010.

[11] J.P. Kruth, L. Froyen, J. Van Vaerenbergh, P. Mercelis, M. Rombouts, and B. Lauwers. Selective laser melting of iron-based powder. *Journal of Materials Processing Technology*, 149(1-3):616–622, June 2004.

[12] Daniel Thomas. The development of design rules for selective laser melting. 2009.

[13] Martin Leary, Maciej Mazur, Joe Elambasseril, Matthew McMillan, Thomas Chirent, Yingying Sun, Ma Qian, Mark Easton, and Milan Brandt. Selective laser melting (SLM) of AlSi12mg lattice structures. *Materials & Design*, 98:344–357, May 2016.

[14] S. Van Bael, G. Kerckhofs, M. Moesen, G. Pyka, J. Schrooten, and J.P. Kruth. Micro-CT-based improvement of geometrical and mechanical controllability of selective laser melted Ti6al4v porous structures. *Materials Science and Engineering: A*, 528(24):7423–7431, September 2011.

[15] Giovanni Strano, Liang Hao, Richard M. Everson, and Kenneth E. Evans. Surface roughness analysis, modelling and prediction in selective laser melting. *Journal of Materials Processing Technology*, 213(4):589–597, April 2013.

[16] Grzegorz Pyka, Greet Kerckhofs, Ioannis Papantoniou, Mathew Speirs, Jan Schrooten, and Martine Wevers. Surface Roughness and Morphology Customization of Additive Manufactured Open Porous Ti6al4v Structures. *Materials*, 6(10):4737–4757, October 2013.

[17] M. Cloots, A. Spierings, and K. Wegener. Assessing new support minimizing strategies for the additive manufacturing technology SLM. In *Solid Freeform Fabrication Symposium (SFF), Austin, TX, Aug*, pages 12–14, 2013.

[18] F. Calignano. Design optimization of supports for overhanging structures in aluminum and titanium alloys by selective laser melting. *Materials & Design*, 64:203–213, December 2014.

[19] Kozo Osakada and Masanori Shiomi. Flexible manufacturing of metallic products by selective laser melting of powder. *International Journal of Machine Tools and Manufacture*, 46(11):1188–1193, September 2006.

[20] Christian Weingarten, Damien Buchbinder, Norbert Pirch, Wilhelm Meiners, Konrad Wissenbach, and Reinhart Poprawe. Formation and reduction of hydrogen porosity during selective laser melting of alsi10mg. *Journal of Materials Processing Technology*, 221:112 – 120, 2015.

[21] Rongshi Xiao and Xinyi Zhang. Problems and issues in laser beam welding of aluminum–lithium alloys. *Journal of Manufacturing Processes*, 16(2):166 – 175, 2014.

[22] Haijun Gong, Khalid Rafi, Hengfeng Gu, Thomas Starr, and Brent Stucker. Analysis of defect generation in ti–6al–4v parts made using powder bed fusion additive manufacturing processes. *Additive Manufacturing*, 1–4:87 – 98, 2014. Inaugural Issue.

[23] Galina Kasperovich, Jan Haubrich, Joachim Gussone, and Guillermo Requena. Correlation between porosity and processing parameters in tial6v4 produced by selective laser melting. *Materials & Design*, 105:160 – 170, 2016.

[24] W. J. Sames, F. A. List, S. Pannala, R. R. Dehoff, and S. S. Babu. The metallurgy and processing science of metal additive manufacturing. *International Materials Reviews*, 61(5):315–360, 2016.

[25] Ming Tang and P. Chris Pistorius. Oxides, porosity and fatigue performance of alsi10mg parts produced by selective laser melting. *International Journal of Fatigue*, 94, Part 2:192 – 201, 2017. Fatigue and Fracture Behavior of Additive Manufactured Parts.

[26] Francesco Trevisan, Flaviana Calignano, Massimo Lorusso, Jukka Pakkanen, Alberta Aversa, Elisa Ambrosio, Mariangela Lombardi, Paolo Fino, and Diego Manfredi. On the Selective Laser Melting (SLM) of the AlSi10mg Alloy: Process, Microstructure, and Mechanical Properties. *Materials*, 10(1):76, January 2017.

[27] E. O. t Olakanmi, R. F. Cochrane, and K. W. Dalgarno. A review on selective laser sintering/melting (SLS/SLM) of aluminium alloy powders: Processing, microstructure, and properties. *Progress in Materials Science*, 74:401–477, 2015.

[28] Yali Li and Dongdong Gu. Parametric analysis of thermal behavior during selective laser melting additive manufacturing of aluminum alloy powder. *Materials & Design*, 63:856–867, November 2014.

[29] Loong-Ee Loh, Chee-Kai Chua, Wai-Yee Yeong, Jie Song, Mahta Mapar, Swee-Leong Sing, Zhong-Hong Liu, and Dan-Qing Zhang. Numerical investigation and an effective modelling on the Selective Laser Melting (SLM) process with aluminium alloy 6061. *International Journal of Heat and Mass Transfer*, 80:288–300, January 2015.

[30] Bo Song, Xiao Zhao, Shuai Li, Changjun Han, Qingsong Wei, Shifeng Wen, Jie Liu, and Yusheng Shi. Differences in microstructure and properties between selective laser melting and traditional manufacturing for fabrication of metal parts: A review. *Frontiers of Mechanical Engineering*, 10(2):111–125, June 2015.

[31] Sindo Kou. *Basic Solidification Concepts*, pages 143–169. John Wiley & Sons, Inc., 2003.

[32] J. D. Hunt and S. Z. Lu. Numerical modeling of cellular/dendritic array growth: spacing and structure predictions. *Metallurgical and Materials Transactions A*, 27(3):611–623, Mar 1996.

[33] Lore Thijs, Karolien Kempen, Jean-Pierre Kruth, and Jan Van Humbeeck. Fine-structured aluminium products with controllable texture by selective laser melting of pre-alloyed alsi10mg powder. *Acta Materialia*, 61(5):1809 – 1819, 2013.

[34] D. Buchbinder, H. Schleifenbaum, S. Heidrich, W. Meiners, and J. Bültmann. High Power Selective Laser Melting (HP SLM) of Aluminum Parts. *Physics Procedia*, 12:271–278, 2011.

[35] K. Kempen, L. Thijs, J. Van Humbeeck, and J.-P. Kruth. Mechanical Properties of AlSi10mg Produced by Selective Laser Melting. *Physics Procedia*, 39:439–446, 2012.

[36] I. Maskery, N.T. Aboulkhair, A.O. Aremu, C.J. Tuck, and I.A. Ashcroft. Compressive failure modes and energy absorption in additively manufactured double gyroid lattices. *Additive Manufacturing*, 16:24–29, August 2017.

[37] I. Maskery, N.T. Aboulkhair, A.O. Aremu, C.J. Tuck, I.A. Ashcroft, R.D. Wildman, and R.J.M. Hague. A mechanical property evaluation of graded density Al-Si10-Mg lattice structures manufactured by selective laser melting. *Materials Science and Engineering: A*, 670:264–274, July 2016.

[38] X.P. Li, X.J. Wang, M. Saunders, A. Suvorova, L.C. Zhang, Y.J. Liu, M.H. Fang, Z.H. Huang, and T.B. Sercombe. A selective laser melting and solution heat treatment refined Al–12si alloy with a controllable ultrafine eutectic microstructure and 25% tensile ductility. *Acta Materialia*, 95:74–82, August 2015.

[39] Shafaqat Siddique, Muhammad Imran, Eric Wycisk, Claus Emmelmann, and Frank Walther. Influence of process-induced microstructure and imperfections on mechanical properties of AlSi12 processed by selective laser melting. *Journal of Materials Processing Technology*, 221:205–213, July 2015.

[40] I. Rosenthal, A. Stern, and N. Frage. Strain rate sensitivity and fracture mechanism of AlSi10mg parts produced by Selective Laser Melting. *Materials Science and Engineering: A*, 682:509–517, January 2017.

[41] Gencaga Purcek, Onur Saray, and Oktay Kul. Microstructural evolution and mechanical properties of severely deformed Al-12si casting alloy by equal-channel angular extrusion. *Metals and Materials International*, 16(1):145–154, February 2010.

[42] M. F. Ashby, A. G. Evans, N. A. Fleck, L. J. Gibson, J. W. Hutchinson, and H. N.G Wadley. *Metal foams, A design Guide.pdf*. Butterworth Heinemann, June 2000.

[43] John Banhart. Manufacture, characterisation and application of cellular metals and metal foams. *Progress in Materials Science*, 46(6):559–632, 2001.

[44] G. J. Davies and Shu Zhen. Metallic foams: their production, properties and applications. *Journal of Materials Science*, 18(7):1899–1911, July 1983.

[45] J. Banhart and J. Baumeister. Production methods for metallic foams. In *MRS Proceedings*, volume 521, page 121. Cambridge Univ Press, 1998.

[46] C. Körner and R. F. Singer. Processing of metal foams—challenges and opportunities. *Advanced Engineering Materials*, 2(4):159–165, 2000.

[47] Haydn NG Wadley. Cellular metals manufacturing. *Advanced Engineering Materials*, 4(10):726–733, 2002.

[48] J. Banhart. Metal foams: Production and stability. *Advanced Engineering Materials*, 8(9):781–794, 2006.

[49] I. Jin, L.D. Kenny, and H. Sang. Method of producing lightweight foamed metal, November 1990.

[50] Wang Deqing, Meng Xiangjun, Xue Weiwei, and Shi Ziyuan. Effect of processing parameters on cell structure of an aluminum foam. *Materials Science and Engineering: A*, 420(1–2):235–239, March 2006.

[51] D. Leitlmeier, H.p. Degischer, and H.j. Flankl. Development of a foaming process for particulate reinforced aluminum melts. *Advanced Engineering Materials*, 4(10):735–740, October 2002.

[52] A. E. Simone and L. J. Gibson. Aluminum foams produced by liquid-state processes. *Acta Materialia*, 46(9):3109–3123, 1998.

[53] J. C. Elliot. Method of producing metal foam, June 1956. US2751289A.

[54] A. R Kennedy. The effect of TiH_2 heat treatment on gas release and foaming in $AlTiH_2$ preforms. *Scripta Materialia*, 47(11):763–767, 2002.

[55] C. C Yang and H Nakae. Foaming characteristics control during production of aluminum alloy foam. *Journal of Alloys and Compounds*, 313(1–2):188–191, 2000.

[56] L. Drenchev, J. Sobczak, S. Malinov, and W. Sha. Gasars: a class of metallic materials with ordered porosity. *Materials Science and Technology*, 22(10):1135–1147, October 2006.

[57] Hideo Nakajima. Fabrication, properties, and applications of porous metals with directional pores. *Proceedings of the Japan Academy. Series B, Physical and Biological Sciences*, 86(9):884–899, November 2010.

[58] H. Nakajima, T. Ikeda, and S.k. Hyun. Fabrication of lotus-type porous metals and their physical properties. *Advanced Engineering Materials*, 6(6):377–384, 2004.

[59] V. I. Shapovalov and J. C. Withers. Hydrogen technology for porous metals (gasars) production. In Bogdan Baranowski, Svetlana Yu Zaginaichenko, Dmitry V. Schur, Valeriy V. Skorokhod, and Ayfer Veziroglu, editors, *Carbon Nanomaterials in Clean Energy Hydrogen Systems*, NATO Science for Peace and Security Series C: Environmental Security, pages 29–51. Springer Netherlands, January 2008.

[60] M. Jaeckel and H. Smigilski. Process for producing metallic or ceramic hollow-sphere bodies, April 1990. US4917857 A.

[61] T. J. Lim, B. Smith, and D. L. McDowell. Behavior of a random hollow sphere metal foam. *Acta Materialia*, 50(11):2867–2879, 2002.

[62] O. Andersen, U. Waag, L. Schneider, G. Stephani, and B. Kieback. Novel metallic hollow sphere structures. *Advanced Engineering Materials*, 2(4):192–195, 2000.

[63] Y. Yamada, K. Shimojima, Y. Sakaguchi, M. Mabuchi, M. Nakamura, T. Asahina, T. Mukai, H. Kanahashi, and K. Higashi. Processing of an open-cellular AZ91 magnesium alloy with a low density of 0.05 g/cm3. *Journal of Materials Science Letters*, 18(18):1477–1480, September 1999.

[64] A. H. Brothers and D. C. Dunand. Density-graded cellular aluminum. *Advanced Engineering Materials*, 8(9):805–809, September 2006.

[65] T. G Nieh, J. H Kinney, J Wadsworth, and A. J. C Ladd. Morphology and elastic properties of aluminum foams produced by a casting technique. *Scripta Materialia*, 38(10):1487–1494, 1998.

[66] T. G. Nieh, K. Higashi, and J. Wadsworth. Effect of cell morphology on the compressive properties of open-cell aluminum foams. *Materials Science and Engineering: A*, 283(1):105–110, 2000.

[67] B. Bugnet and Denis Doniat. Porous metal structure and method of manufacturing of said structure, November 1989. US4882232 A.

[68] P.S. Liu and K.M. Liang. Preparation and corresponding structure of nickel foam. *Materials Science and Technology*, 16(5):575–578, 2000.

[69] P.S. Liu, K.M. Liang, S.W. Tu, S.R. Gu, Q. Yu, T.F. Li, and C. Fu. Relationship between tensile strength and preparation conditions for nickel foam. *Materials Science and Technology*, 17(9):1069–1072, September 2001.

[70] D. L. Wang, C. S. Dai, N. Wu, Z. H. Jiang, and J. Li. Multiple-step constant current density electrodeposition of continuous metal material with high porosity. *Journal of Applied Electrochemistry*, 33(8):725–732, August 2003.

[71] E. Pinkhasov. Method of making open-pore structures, April 1991. US5011638 A.

[72] V. Paserin, S. Marcuson, J. Shu, and D.s. Wilkinson. CVD technique for inco nickel foam production. *Advanced Engineering Materials*, 6(6):454–459, 2004.

[73] Douglas T. Queheillalt, Yasushi Katsumura, and Haydn N.G. Wadley. Synthesis of stochastic open cell ni-based foams. *Scripta Materialia*, 50(3):313–317, February 2004.

[74] C. S. Y. Jee, Z. X. Guo, J. R. G. Evans, and N. Özgüven. Preparation of high porosity metal foams. *Metallurgical and Materials Transactions B*, 31(6):1345–1352, December 2000.

[75] I. M. Fedorchenko. Progress in work in the field of high-porosity materials from metal powders and fibers. *Soviet Powder Metallurgy and Metal Ceramics*, 18(9):615–622, September 1979.

[76] A. E. Markaki, V. Gergely, A. Cockburn, and T. W. Clyne. Production of a highly porous material by liquid phase sintering of short ferritic stainless steel fibres and a preliminary study of its mechanical behaviour. *Composites Science and Technology*, 63(16):2345–2351, 2003.

[77] Jonah Erlebacher and Ram Seshadri. Hard materials with tunable porosity. *MRS Bulletin*, 34(08):561–568, 2009.

[78] Marie E. Cox and David C. Dunand. Bulk gold with hierarchical macro-, micro- and nano-porosity. *Materials Science and Engineering: A*, 528(6):2401–2406, March 2011.

[79] Takeshi Wada, Kunio Yubuta, Akihisa Inoue, and Hidemi Kato. Dealloying by metallic melt. *Materials Letters*, 65(7):1076–1078, 2011.

[80] Z. Esen and Ş. Bor. Processing of titanium foams using magnesium spacer particles. *Scripta Materialia*, 56(5):341–344, March 2007.

[81] Halil I. Bakan. A novel water leaching and sintering process for manufacturing highly porous stainless steel. *Scripta Materialia*, 55(2):203–206, 2006.

[82] Y. Y. Zhao and D. X. Sun. A novel sintering-dissolution process for manufacturing al foams. *Scripta materialia*, 44(1):105–110, 2001.

[83] C. San Marchi and A. Mortensen. Deformation of open-cell aluminum foam. *Acta Materialia*, 49(19):3959–3969, 2001.

[84] J.-F. Despois, Y. Conde, C. San Marchi, and A. Mortensen. Tensile Behaviour of Replicated Aluminium Foams. *Advanced Engineering Materials*, 6(6):444–447, June 2004.

[85] C. Gaillard, J. F. Despois, and A. Mortensen. Processing of NaCl powders of controlled size and shape for the microstructural tailoring of aluminium foams. *Materials Science and Engineering: A*, 374(1–2):250–262, 2004.

[86] R. Goodall and A. Mortensen. Microcellular aluminium? – child's play! *Advanced Engineering Materials*, 9(11):951–954, November 2007.

[87] J.d. LeMay, R.w. Hopper, L.w. Hrubesh, and R.w. Pekala. Low-density microcellular materials: Introduction. *MRS Bulletin*, 15(12):19–20, 1990.

[88] J. F. Despois, A. Marmottant, L. Salvo, and A. Mortensen. Influence of the infiltration pressure on the structure and properties of replicated aluminium foams. *Materials Science and Engineering: A*, 462(1–2):68–75, 2007.

[89] V. S Deshpande and N. A Fleck. Collapse of truss core sandwich beams in 3-point bending. *International Journal of Solids and Structures*, 38(36–37):6275–6305, September 2001.

[90] S. Chiras, D. R. Mumm, A. G. Evans, N. Wicks, J. W. Hutchinson, K. Dharmasena, H. N. G. Wadley, and S. Fichter. The structural performance of near-optimized truss core panels. *International Journal of Solids and Structures*, 39(15):4093–4115, 2002.

[91] N. T. Kirkland, I. Kolbeinsson, T. Woodfield, G. J. Dias, and M. P. Staiger. Synthesis and properties of topologically ordered porous magnesium. *Materials Science and Engineering: B*, 176(20):1666–1672, 2011.

[92] Thanh Nguyen. Synthesis of topologically-ordered porous magnesium. 2011. PhD thesis, University of Canterbury.

[93] M. V. Nathal, J. D. Whittenberger, M. G. Hebsur, P. T. Kantzos, and D. L. Krause. Superalloy lattice block structures. 2004.

[94] Nicholas A. Meisel, Christopher B. Williams, and Alan Druschitz. Lightweight metal cellular structures via indirect 3d printing and casting. In *Proceedings of the International Solid Freeform Fabrication Symposium*, pages 162–176, 2012.

[95] Jiwon Mun, Byoung-Gwan Yun, Jaehyung Ju, and Byung-Moon Chang. Indirect additive manufacturing based casting of a periodic 3d cellular metal – Flow simulation of molten aluminum alloy. *Journal of Manufacturing Processes*, 17:28–40, January 2015.

[96] D. J. Sypeck and H. N. G. Wadley. Multifunctional microtruss laminates: textile synthesis and properties. *Journal of Materials Research*, 16(03):890–897, 2001.

[97] H Wadley. Fabrication and structural performance of periodic cellular metal sandwich structures. *Composites Science and Technology*, 63(16):2331–2343, December 2003.

[98] Ki-Ju Kang. A wire-woven cellular metal of ultrahigh strength. *Acta Materialia*, 57(6):1865–1874, 2009.

[99] Yong-Hyun Lee, Byung-Kon Lee, Insu Jeon, and Ki-Ju Kang. Wire-woven bulk kagome truss cores. *Acta Materialia*, 55(18):6084–6094, October 2007.

[100] Gregory W Kooistra, Vikram S Deshpande, and Haydn N. G Wadley. Compressive behavior of age hardenable tetrahedral lattice truss structures made from aluminium. *Acta Materialia*, 52(14):4229–4237, 2004.

[101] H. N.G Wadley. Multifunctional periodic cellular metals. *Philosophical Transactions of the Royal Society A: Mathematical, Physical and Engineering Sciences*, 364(1838):31–68, January 2006.

[102] Gregory W. Kooistra and Haydn N. G. Wadley. Lattice truss structures from expanded metal sheet. *Materials & Design*, 28(2):507–514, 2007.

[103] Douglas T. Queheillalt and Haydn N. G. Wadley. Titanium alloy lattice truss structures. *Materials & Design*, 30(6):1966–1975, 2009.

[104] P. Heinl, A. Rottmair, C. Körner, and R. F. Singer. Cellular titanium by selective electron beam melting. *Advanced Engineering Materials*, 9(5):360–364, 2007.

[105] Peter Heinl, Lenka Müller, Carolin Körner, Robert F. Singer, and Frank A. Müller. Cellular Ti6Al4V structures with interconnected macro porosity for bone implants fabricated by selective electron beam melting. *Acta Biomaterialia*, 4(5):1536–1544, 2008.

[106] D. A. Ramirez, L. E. Murr, S. J. Li, Y. X. Tian, E. Martinez, J. L. Martinez, B. I. Machado, S. M. Gaytan, F. Medina, and R. B. Wicker. Open-cellular copper structures fabricated by additive manufacturing using electron beam melting. *Materials Science and Engineering: A*, 528(16–17):5379–5386, 2011.

[107] Chunze Yan, Liang Hao, Ahmed Hussein, Simon Lawrence Bubb, Philippe Young, and David Raymont. Evaluation of light-weight AlSi10mg periodic cellular lattice structures fabricated via direct metal laser sintering. *Journal of Materials Processing Technology*, 214(4):856–864, April 2014.

[108] Chunze Yan, Liang Hao, Ahmed Hussein, and David Raymont. Evaluations of cellular lattice structures manufactured using selective laser melting. *International Journal of Machine Tools and Manufacture*, 62:32–38, November 2012.

[109] T. A. Schaedler, A. J. Jacobsen, A. Torrents, A. E. Sorensen, J. Lian, J. R. Greer, L. Valdevit, and W. B. Carter. Ultralight metallic microlattices. *Science*, 334(6058):962–965, November 2011.

[110] L. J. Gibson and M. F. Ashby. *Cellular Solids - Structure and Properties*. Cambridge Solid State Science Series. 2nd edition, August 1999.

[111] M.F Ashby. The properties of foams and lattices. *Philosophical Transactions of the Royal Society A: Mathematical, Physical and Engineering Sciences*, 364(1838):15–30, January 2006.

[112] Mulalo Doyoyo and Tomasz Wierzbicki. Experimental studies on the yield behavior of ductile and brittle aluminum foams. *International Journal of Plasticity*, 19(8):1195–1214, 2003.

[113] T. C. Triantafillou, J. Zhang, T. L. Shercliff, L. J. Gibson, and M. F. Ashby. Failure surfaces for cellular materials under multiaxial loads—II. comparison of models with experiment. *International Journal of Mechanical Sciences*, 31(9):665–678, 1989.

[114] G Gioux, T. M McCormack, and L. J Gibson. Failure of aluminum foams under multiaxial loads. *International Journal of Mechanical Sciences*, 42(6):1097–1117, 2000.

[115] J. S. Blazy, A. Marie-Louise, S. Forest, Y. Chastel, A. Pineau, A. Awade, C. Grolleron, and F. Moussy. Deformation and fracture of aluminium foams under proportional and non proportional multi-axial loading: statistical analysis and size effect. *International Journal of Mechanical Sciences*, 46(2):217–244, 2004.

[116] I. Sridhar and N. A. Fleck. The multiaxial yield behaviour of an aluminium alloy foam. *Journal of Materials Science*, 40(15):4005–4008, 2005.

[117] D. Ruan, G. Lu, L. S. Ong, and B. Wang. Triaxial compression of aluminium foams. *Composites Science and Technology*, 67(6):1218–1234, 2007.

[118] Zhiwei Zhou, Zhihua Wang, Longmao Zhao, and Xuefeng Shu. Loading rate effect on yield surface of aluminum alloy foams. *Materials Science and Engineering: A*, 543:193–199, 2012.

[119] E. Combaz, C. Bacciarini, R. Charvet, W. Dufour, and A. Mortensen. Multiaxial yield behaviour of al replicated foam. *Journal of the Mechanics and Physics of Solids*, 59(9):1777–1793, September 2011.

[120] E. Combaz, C. Bacciarini, R. Charvet, W. Dufour, F. Dauphin, and A. Mortensen. Yield surface of polyurethane and aluminium replicated foam. *Acta Materialia*, 58(15):5168–5183, September 2010.

[121] H Bart-Smith, A. F Bastawros, D. R Mumm, A. G Evans, D. J Sypeck, and H. N. G Wadley. Compressive deformation and yielding mechanisms in cellular al alloys determined using x-ray tomography and surface strain mapping. *Acta Materialia*, 46(10):3583–3592, 1998.

[122] Y. Sugimura, J. Meyer, M. Y. He, H. Bart-Smith, J. Grenstedt, and A. G. Evans. On the mechanical performance of closed cell al alloy foams. *Acta Materialia*, 45(12):5245–5259, 1997.

[123] U Ramamurty and A Paul. Variability in mechanical properties of a metal foam. *Acta Materialia*, 52(4):869–876, February 2004.

[124] B. Vamsi Krishna, Susmita Bose, and Amit Bandyopadhyay. Strength of open-cell 6101 aluminum foams under free and constrained compression. *Materials Science and Engineering: A*, 452-453:178–188, April 2007.

[125] Wen-Yea Jang and Stelios Kyriakides. On the crushing of aluminum open-cell foams: Part i. experiments. *International Journal of Solids and Structures*, 46(3-4):617–634, February 2009.

[126] E. Andrews, W. Sanders, and L. J. Gibson. Compressive and tensile behaviour of aluminum foams. *Materials Science and Engineering: A*, 270(2):113–124, September 1999.

[127] Xiao-qing CAO, Zhi-hua WANG, Hong-wei MA, Long-mao ZHAO, and Gui-tong YANG. Effects of cell size on compressive properties of aluminum foam. *Transactions of Nonferrous Metals Society of China*, 16(2):351–356, 2006.

[128] J. Zhou, Z. Gao, A.M. Cuitino, and W.O. Soboyejo. Effects of heat treatment on the compressive deformation behavior of open cell aluminum foams. *Materials Science and Engineering: A*, 386(1-2):118–128, November 2004.

[129] Hasan Bafti and Ali Habibolahzadeh. Compressive properties of aluminum foam produced by powder-carbamide spacer route. *Materials & Design*, 52:404–411, December 2013.

[130] Dirk Lehmhus and John Banhart. Properties of heat-treated aluminium foams. *Materials Science and Engineering: A*, 349(1–2):98–110, 2003.

[131] Wen-Yea Jang, Stelios Kyriakides, and Andrew M. Kraynik. On the compressive strength of open-cell metal foams with kelvin and random cell structures. *International Journal of Solids and Structures*, 47(21):2872–2883, October 2010.

[132] O. B. Olurin, N. A. Fleck, and M. F. Ashby. Deformation and fracture of aluminium foams. *Materials science & engineering. A, Structural materials : properties, microstructure and processing*, 291(1-2):136–146, 2000.

[133] D Ruan, G Lu, F. L Chen, and E Siores. Compressive behaviour of aluminium foams at low and medium strain rates. *Composite Structures*, 57(1–4):331–336, 2002.

[134] J. L. Yu, J. R. Li, and S. S. Hu. Strain-rate effect and micro-structural optimization of cellular metals. *Mechanics of Materials*, 38(1–2):160–170, January 2006.

[135] Alethea M. Hayes, Aijun Wang, Benjamin M. Dempsey, and David L. McDowell. Mechanics of linear cellular alloys. *Mechanics of Materials*, 36(8):691–713, 2004.

[136] P. J. Tan, S. R. Reid, J. J. Harrigan, Z. Zou, and S. Li. Dynamic compressive strength properties of aluminium foams. part II—'shock' theory and comparison with experimental data and numerical models. *Journal of the Mechanics and Physics of Solids*, 53(10):2206–2230, October 2005.

[137] Zhihua Wang, Hongwei Ma, Longmao Zhao, and Guitong Yang. Studies on the dynamic compressive properties of open-cell aluminum alloy foams. *Scripta Materialia*, 54(1):83–87, January 2006.

[138] Feng Yi, Zhengang Zhu, Fangqiou Zu, Shisheng Hu, and Pan Yi. Strain rate effects on the compressive property and the energy-absorbing capacity of aluminum alloy foams. *Materials Characterization*, 47(5):417–422, 2001.

[139] R.P. Merrett, G.S. Langdon, and M.D. Theobald. The blast and impact loading of aluminium foam. *Materials & Design*, 44:311–319, February 2013.

[140] G. W. Ma, Z. Q. Ye, and Z. S. Shao. Modeling loading rate effect on crushing stress of metallic cellular materials. *International Journal of Impact Engineering*, 36(6):775–782, 2009.

[141] T. Mukai, H. Kanahashi, Y. Yamada, K. Shimojima, M. Mabuchi, T. G. Nieh, and K. Higashi. Dynamic compressive behavior of an ultra-lightweight magnesium foam. *Scripta materialia*, 41(4):365–371, 1999.

[142] C Park and S. R Nutt. Strain rate sensitivity and defects in steel foam. *Materials Science and Engineering: A*, 323(1–2):358–366, January 2002.

[143] Jiaan Liu, Sirong Yu, Yulai Song, Xianyong Zhu, Ming Wei, Yanru Luo, and Yaohui Liu. Dynamic compressive strength of zn–22al foams. *Journal of Alloys and Compounds*, 476(1–2):466–469, 2009.

[144] H. Zhao, I. Elnasri, and H.j. Li. The mechanism of strength enhancement under impact loading of cellular materials. *Advanced Engineering Materials*, 8(9):877–883, September 2006.

[145] H. Zhao, I. Elnasri, and S. Abdennadher. An experimental study on the behaviour under impact loading of metallic cellular materials. *International Journal of Mechanical Sciences*, 47(4–5):757–774, 2005.

[146] V. S. Deshpande and N. A. Fleck. High strain rate compressive behaviour of aluminium alloy foams. *International Journal of Impact Engineering*, 24(3):277–298, March 2000.

[147] I. Elnasri, S. Pattofatto, H. Zhao, H. Tsitsiris, F. Hild, and Y. Girard. Shock enhancement of cellular structures under impact loading: Part i experiments. *Journal of the Mechanics and Physics of Solids*, 55(12):2652–2671, 2007.

[148] S. Pattofatto, I. Elnasri, H. Zhao, H. Tsitsiris, F. Hild, and Y. Girard. Shock enhancement of cellular structures under impact loading: Part II analysis. *Journal of the Mechanics and Physics of Solids*, 55(12):2672–2686, 2007.

[149] D. D. Radford, V. S. Deshpande, and N. A. Fleck. The use of metal foam projectiles to simulate shock loading on a structure. *International Journal of Impact Engineering*, 31(9):1152–1171, October 2005.

[150] E. W. Andrews, G. Gioux, P. Onck, and L. J. Gibson. Size effects in ductile cellular solids. part II: experimental results. *International Journal of Mechanical Sciences*, 43(3):701–713, 2001.

[151] N. A. Fleck, V. S. Deshpande, and M. F. Ashby. Micro-architectured materials: past, present and future. *Proceedings of the Royal Society A: Mathematical, Physical and Engineering Sciences*, 466(2121):2495–2516, September 2010.

[152] V.S Deshpande, M. F. Ashby, and N. A. Fleck. Foam topology bending versus stretching dominated architectures. *Acta Materialia*, 49:1035–1040, 2001.

[153] J. Clerk Maxwell. On the calculation of the equilibrium and stiffness of frames. *The London, Edinburgh, and Dublin Philosophical Magazine and Journal of Science*, 27(182):294–299, 1864.

[154] C. R. Calladine. Buckminster Fuller's "tensegrity" structures and Clerk Maxwell's rules for the construction of stiff frames. *International Journal of Solids and Structures*, 14(2):161–172, 1978.

[155] R.G. Hutchinson and N.A. Fleck. The structural performance of the periodic truss. *Journal of the Mechanics and Physics of Solids*, 54(4):756–782, April 2006.

[156] N. E. R. Romijn and N. A. Fleck. The fracture toughness of planar lattices: Imperfection sensitivity. *Journal of Mechanics Physics of Solids*, 55:2538–2564, December 2007.

[157] Nicholas A. Meisel, Christopher B. Williams, and Alan Druschitz. Lightweight metal cellular structures via indirect 3d printing and casting. In *Proceedings of the International Solid Freeform Fabrication Symposium*, pages 162–176, 2012.

[158] M. Cholewa, T. Szuter, T. Wróbel, and M. Kondracki. The skeleton castings as a new type of cast lattice structures. *Journal of Achievements in Materials and Manufacturing Engineering*, 54(2):250–259, 2012.

[159] Christopher B. Williams, Joe K. Cochran, and David W. Rosen. Additive manufacturing of metallic cellular materials via three-dimensional printing. *The International Journal of Advanced Manufacturing Technology*, 53(1-4):231–239, March 2011.

[160] Shanqing Xu, Jianhu Shen, Shiwei Zhou, Xiaodong Huang, and Yi Min Xie. Design of lattice structures with controlled anisotropy. *Materials & Design*, 93:443–447, March 2016.

[161] Volker Weißmann, Rainer Bader, Harald Hansmann, and Nico Laufer. Influence of the structural orientation on the mechanical properties of selective laser melted Ti6al4v open-porous scaffolds. *Materials & Design*, 95:188–197, April 2016.

[162] Oraib Al-Ketan, Rashid K. Abu Al-Rub, and Reza Rowshan. The effect of architecture on the mechanical properties of cellular structures based on the IWP minimal surface. *Journal of Materials Research*, 33(03):343–359, February 2018.

[163] L. Yang. A study about size effects of 3d periodic cellular structures. In *Proceedings of the International Solid Freeform Fabrication Symposium, Austin, TX*, 2016.

[164] Eberhard Abele, Hanns A. Stoffregen, Klaus Klimkeit, Holger Hoche, and Matthias Oechsner. Optimisation of process parameters for lattice structures. *Rapid Prototyping Journal*, 21(1):117–127, January 2015.

[165] Chunlei Qiu, Sheng Yue, Nicholas J.E. Adkins, Mark Ward, Hany Hassanin, Peter D. Lee, Philip J. Withers, and Moataz M. Attallah. Influence of processing conditions on strut structure and compressive properties of cellular lattice structures fabricated by selective laser melting. *Materials Science and Engineering: A*, 628:188–197, March 2015.

[166] Rafidah Hasan, Robert A.W. Mines, Eva Shen, Sozohn Tsopanos, and Wesley Cantwell. Comparison on Compressive Behaviour of Aluminium Honeycomb and Titanium Alloy Micro Lattice Blocks. *Key Engineering Materials*, 462-463:213–218, January 2011.

[167] E. Hernández-Nava, C.J. Smith, F. Derguti, S. Tammas-Williams, F. Leonard, P.J. Withers, I. Todd, and R. Goodall. The effect of defects on the mechanical response of Ti-6al-4v cubic lattice structures fabricated by electron beam melting. *Acta Materialia*, 108:279–292, April 2016.

[168] N. Vanderesse, I. Ky, F. Quevedo González, N. Nuño, and P. Bocher. Image analysis characterization of periodic porous materials produced by additive manufacturing. *Materials & Design*, 92:767–778, February 2016.

[169] William van Grunsven, Everth Hernandez-Nava, Gwendolen Reilly, and Russell Goodall. Fabrication and Mechanical Characterisation of Titanium Lattices with Graded Porosity. *Metals*, 4(3):401–409, August 2014.

[170] Li Yang. AN INVESTIGATION OF ANISOTROPY OF OF 3d PERIODIC CELLULAR STRUCTURE DESIGS.

[171] Lu Liu, Paul Kamm, Francisco García-Moreno, John Banhart, and Damiano Pasini. Elastic and failure response of imperfect three-dimensional metallic lattices: the role of geometric defects induced by Selective Laser Melting. *Journal of the Mechanics and Physics of Solids*, 107:160–184, October 2017.

[172] R.G. Hutchinson and N.A. Fleck. Microarchitectured cellular solids - the hunt for statically determinate periodic trusses. *ZAMM*, 85(9):607–617, September 2005.

[173] Jane Chu, Sarah Engelbrecht, Gregory Graf, and David W. Rosen. A comparison of synthesis methods for cellular structures with application to additive manufacturing. *Rapid Prototyping Journal*, 16(4):275–283, June 2010.

[174] David W. Rosen. Computer-Aided Design for Additive Manufacturing of Cellular Structures. *Computer-Aided Design and Applications*, 4(5):585–594, January 2007.

[175] Liang Dong, Vikram Deshpande, and Haydn Wadley. Mechanical response of Ti–6al–4v octet-truss lattice structures. *International Journal of Solids and Structures*, 60-61:107–124, May 2015.

[176] M.R. O'Masta, L. Dong, L. St-Pierre, H.N.G. Wadley, and V.S. Deshpande. The fracture toughness of octet-truss lattices. *Journal of the Mechanics and Physics of Solids*, 98:271–289, January 2017.

[177] ZeZhou He, FengChao Wang, YinBo Zhu, HengAn Wu, and Harold S. Park. Mechanical properties of copper octet-truss nanolattices. *Journal of the Mechanics and Physics of Solids*, 101:133–149, 2017.

[178] Colin Bonatti and Dirk Mohr. Large deformation response of additively-manufactured FCC metamaterials: From octet truss lattices towards continuous shell mesostructures. *International Journal of Plasticity*, 92:122–147, May 2017.

[179] Thomas Tancogne-Dejean, Adriaan B. Spierings, and Dirk Mohr. Additively-manufactured metallic micro-lattice materials for high specific energy absorption under static and dynamic loading. *Acta Materialia*, 116:14–28, September 2016.

[180] V.S Deshpande, N. A. Fleck, and M. F. Ashby. Effective properties of the octet-truss lattice material. *Journal of tje mechanics and physics of solids*, 49:1747–1769, 2001.

[181] S. McKown, Y. Shen, W.K. Brookes, C.J. Sutcliffe, W.J. Cantwell, G.S. Langdon, G.N. Nurick, and M.D. Theobald. The quasi-static and blast loading response of lattice structures. *International Journal of Impact Engineering*, 35(8):795–810, August 2008.

[182] S.J.N. Morrish, M. Pedersen, K.F.W. Wong, I. Todd, and R. Goodall. Size effects in compression in Electron Beam Melted Ti6al4v diamond structure lattices. *Materials Letters*, 190:138–142, March 2017.

[183] Chunze Yan, Liang Hao, Ahmed Hussein, Philippe Young, Juntong Huang, and Wei Zhu. Microstructure and mechanical properties of aluminium alloy cellular lattice structures manufactured by direct metal laser sintering. *Materials Science and Engineering: A*, 628:238–246, March 2015.

[184] Terry A. Ring. Preface. In Terry A. Ring, editor, *Fundamentals of Ceramic Powder Processing and Synthesis*, pages xxi – xxii. Academic Press, San Diego, 1996.

[185] Institute of Medicine (US) Committee on Quality of Health Care in America. *Crossing the quality chasm: A new health system for the 21st century*. National Academies Press, 2001.

[186] Eric L. Christiansen, J. Arnold, A. Davis, J. Hyde, Dana Lear, J. C. Liou, F. Lyons, T. Prior, M. Ratliff, S. Ryan, and others. Handbook for designing MMOD protection. *NASA Johnson Space Center, NASA/TM-2009-214785*, 2009.

[187] Eric L. Christiansen and Lyndon B. Johnson Space Center. *Meteoroid/debris shielding*. National Aeronautics and Space Administration, Lyndon B. Johnson Space Center, 2003.

[188] Christoph R. Englert, J. Timothy Bays, Kenneth D. Marr, Charles M. Brown, Andrew C. Nicholas, and Theodore T. Finne. Optical orbital debris spotter. *Acta Astronautica*, 104(1):99–105, November 2014.

[189] Donald J. Kessler and Burton G. Cour-Palais. Collision frequency of artificial satellites: The creation of a debris belt. *Journal of Geophysical Research: Space Physics*, 83(A6):2637–2646, 1978.

[190] Inter agency Space Debris coordination committee Sterring Group and Working Group 4. Iadc space debris mitigation guidelines. pages 1–10, 2007.

[191] ESA Space Debris Mitigation WG. ESA space debris mitigation compliance verification guidelines. pages 1–95, 2015.

[192] *Protecting the Space Station from Meteoroids and Orbital Debris*. National Academies Press, Washington, D.C., January 1997. DOI: 10.17226/5532.

[193] Jer-Chyi Liou and Lyndon B. Johnson Space Center. *The new NASA orbital debris engineering model ORDEM2000*. National Aeronautics and Space Administration, Lyndon B. Johnson Space Center, 2002.

[194] Robin Putzar and Frank Schaefer. Experimental space debris simulation at EMI's calibre 4 mm two-stage light gas gun. In *Proceedings of the 5th European Conference on Space Debris, Darmstadt, Germany, ESA SP-672*, 2009.

[195] W. J. Nellis, S. T. Weir, and A. C. Mitchell. Minimum metallic conductivity of fluid hydrogen at 140 GPa (1.4 Mbar). *Physical Review B*, 59(5):3434–3449, February 1999.

[196] James D. Walker, Donald J. Grosch, and Scott A. Mullin. A hypervelocity fragment launcher based on an inhibited shaped charge. *International Journal of Impact Engineering*, 14(1–4):763–774, 1993.

[197] Eric L. Christiansen. Design and performance equations for advanced meteoroid and debris shields. *International Journal of Impact Engineering*, 14(1):145–156, 1993.

[198] Karl Rawer, D. Bilitza, and Bodo W. Reinisch. *International Reference Ionosphere-Workshop 1999*. Committee on Space Research, 2001.

[199] Andrew J. Piekutowski. Characteristics of debris clouds produced by hypervelocity impact of aluminum spheres with thin aluminum plates. *International Journal of Impact Engineering*, 14(1-4):573–586, 1993.

[200] Roberto Destefanis, Moreno Faraud, and Marco Trucchi. Columbus debris shielding experiments and ballistic limit curves. *International Journal of Impact Engineering*, 23(1, Part 1):181–192, 1999.

[201] Burton G. Cour-Palais and Jeanne Lee Crews. A multi-shock concept for spacecraft shielding. *International Journal of Impact Engineering*, 10(1):135–146, 1990.

[202] E. L. Christiansen, J. L. Crews, J. E. Williamsen, J. H. Robinson, and A. M. Nolen. Enhanced meteoroid and orbital debris shielding. *International Journal of Impact Engineering*, 17(1):217–228, 1995.

[203] S. Ryan, F. Schaefer, R. Destefanis, and M. Lambert. A ballistic limit equation for hypervelocity impacts on composite honeycomb sandwich panel satellite structures. *Advances in Space Research*, 41(7):1152–1166, January 2008.

[204] M. Lambert. Hypervelocity impacts and damage laws. *Advances in Space Research*, 19(2):369–378, 1997.

[205] E. Beruto, R. Destefanis, M. Faraud, and P. Buchwald. Debris shielding development for the colombus orbital facility.pdf. In *Proceedings of the Second European Conference on Space Debris, Darmstadt, Germany, Mar 17-19, 1997, Noordwijk, Netherlands, European Space Agency*, pages 509–517, 1997.

[206] K. Loft, M.C. Price, M.J. Cole, and M.J. Burchell. Impacts into metals targets at velocities greater than 1 km/s: A new online resource for the hypervelocity impact community and an illustration of the geometric change of debris cloud impact patterns with impact velocity. *International Journal of Impact Engineering*, 56:47–60, June 2013.

[207] Z.-T. Ma, B. Jia, and B.-J. Pang. Behavior of aluminum foams under hypervelocity impact: Validation of numerical simulation. *Advanced Engineering Materials*, 9(10):888–891, October 2007.

[208] S. Ryan and E. L. Christiansen. *Micrometeroid and Orbital Debris (MMOD) Shield Ballistic Limit Analysis Program.pdf*. National Aeronautics and Space Administration, Lyndon B. Johnson Space Center, 2009.

[209] Roberto Destefanis, Frank Schäfer, Michel Lambert, Moreno Faraud, and Eberhard Schneider. Enhanced space debris shields for manned spacecraft. *International Journal of Impact Engineering*, 29(1–10):215–226, 2003.

[210] Shannon Ryan and Eric L. Christiansen. Hypervelocity impact testing of advanced materials and structures for micrometeoroid and orbital debris shielding. *Acta Astronautica*, 83:216–231, February 2013.

[211] S. Ryan, T. Hedman, and E.L. Christiansen. Honeycomb vs. foam: Evaluating potential upgrades to ISS module shielding. *Acta Astronautica*, 67(7-8):818–825, October 2010.

[212] R. Destefanis, F. Schäfer, M. Lambert, and M. Faraud. Selecting enhanced space debris shields for manned spacecraft. *International Journal of Impact Engineering*, 33(1-12):219–230, December 2006.

[213] John Yasensky and Eric L. Christiansen. Hypervelocity impact evaluation of metal foam core sandwich structures. 2007.

[214] Marta B. Bastrzyk, Christopher C. Daniels, Jay J. Oswald, Patrick H. Dunlap Jr, and Bruce M. Steinetz. Material properties of three candidate elastomers for space seals applications. 2010.

[215] Qing Zhen Li, Zhong Hua Du, and Kang Kang Wang. An Experimental Study of High-Velocity Impact on Aluminum Foam Composite Shield Structure. *Advanced Materials Research*, 690-693:20–24, May 2013.

[216] R. Voillat. Hypervelocity impact testing on periodic and stochastic open porosity Al-Si cellular structures for space applications. *Master Thesis - SSC - EPFL*, June 2017.

[217] C.J. Smith, F. Derguti, E. Hernandez Nava, M. Thomas, S. Tammas-Williams, S. Gulizia, D. Fraser, and I. Todd. Dimensional accuracy of Electron Beam Melting (EBM) additive manufacture with regard to weight optimized truss structures. *Journal of Materials Processing Technology*, 229:128–138, March 2016.

[218] Yangli Xu, Dongyun Zhang, Yan Zhou, Weidong Wang, and Xuanyang Cao. Study on Topology Optimization Design, Manufacturability, and Performance Evaluation of Ti-6al-4v Porous Structures Fabricated by Selective Laser Melting (SLM). *Materials*, 10(9):1048, September 2017.

[219] Ji-Eun Choi, Gyoung-Dek Ko, and Ki-Ju Kang. Taguchi method-based sensitivity study of design parameters representing specific strength of wire-woven bulk kagome under compression. *Composite Structures*, 92(10):2547–2553, September 2010.

[220] A. B. Spierings, M. Voegtlin, T. Bauer, and K. Wegener. Powder flowability characterisation methodology for powder-bed-based metal additive manufacturing. *Progress in Additive Manufacturing*, 1(1-2):9–20, June 2016.

[221] Metallic materials – Tensile testing – Part 1: Method of test at room temperature. Standard, International Organization for Standardization, Geneva, CH, August 2009.

[222] Mechanical testing of metals – Ductility testing – Compression test for porous and cellular metals. Standard, International Organization for Standardization, Geneva, CH, December 2011.

[223] Weidong Wu, Joseph Owino, Ahmed Al-Ostaz, and Liguang Cai. Applying periodic boundary conditions in finite element analysis. In *SIMULIA Community Conference, Providence*, pages 707–719, 2014.

[224] Jean-François Despois, Randoald Mueller, and Andreas Mortensen. Uniaxial deformation of microcellular metals. *Acta Materialia*, 54(16):4129–4142, September 2006.

[225] C. Y. Yap, C. K. Chua, Z. L. Dong, Z. H. Liu, D. Q. Zhang, L. E. Loh, and S. L. Sing. Review of selective laser melting: Materials and applications. *Applied Physics Reviews*, 2(4):041101, December 2015.

[226] V. Bersier. Additive layer manufacturing optimization for the production of periodic cellular structure in polymers. *Minor Semester Project - SSC - EPFL*, December 2016.

[227] European Commission. *Ceramic Manufacturing Industry*. 2007.

[228] Richard P. Chartoff and Anil K. Sircar. Thermal analysis of polymers. *Encyclopedia of polymer science and technology*, 2005.

[229] C.H. Cáceres and B.I. Selling. Casting defects and the tensile properties of an AlSiMg alloy. *Materials Science and Engineering: A*, 220(1-2):109–116, December 1996.

[230] C. H. Cáceres and Q. G. Wang. Dendrite cell size and ductility of Al—Si—Mg casting alloys: Spear and Gardner revisited. *International Journal of Cast Metals Research*, 9(3):157–162, September 1996.

[231] Rui Chen, Qingyan Xu, and Baicheng Liu. Cellular automaton simulation of three-dimensional dendrite growth in Al–7si–Mg ternary aluminum alloys. *Computational Materials Science*, 105:90–100, July 2015.

[232] Gallien Florian. Aluminium foam characterization - analysis of test results and outlook. *ESA Frame Contract RFQ/3-13789/13/NL/PA Call-Off Order 2*, March 2014.

[233] John J. Lewandowski and Mohsen Seifi. Metal Additive Manufacturing: A Review of Mechanical Properties. *Annual Review of Materials Research*, 46(1):151–186, July 2016.

[234] Mohammad Zamanzade, Afrooz Barnoush, and Christian Motz. A Review on the Properties of Iron Aluminide Intermetallics. *Crystals*, 6(12):10, January 2016.

[235] Régis Voillat, Florian Gallien, Andreas Mortensen, and Volker Gass. Hypervelocity impact testing on stochastic and structured open porosity cast al-si cellular structures for space applications. *International Journal of Impact Engineering*, February 2018.

Florian Gallien

Material Engineer(PhD) · Metallic materials and advanced manufacturing expert
Rue du Crêt 7, 1006 Lausanne, Switzerland
☎ +41 76 679 7054 | ✉ florian.gallien@epfl.ch | Florian-Gallien

Education

Ph.D. in Materials Science and Space technology November. 2013 - February 2018

EPFL (Swiss Federal Institute of Technology, Lausanne), Switzerland

- 1 year spent at the European Space Agency facilities, ESTEC, The Netherlands

M.S. in Materials science 2010-2012

EPFL (Swiss Federal Institute of Technology, Lausanne), Switzerland

- GPA: 5.4/6.0
- Minor in Space Technology

B.S. in Material Science 2007-2010

EPFL (Swiss Federal Institute of Technology, Lausanne), Switzerland

- GPA: 5.3/6.0
- Last year in exchange at Politecnico di Milano, Italy (2009-2010)

Experience

Swiss Space Center & Laboratory of Mechanical Metallurgy, EPFL, Switzerland Nov. 2013 - present

Doctoral research (Advisors: Prof. Volker Gass & Prof. Andreas Mortensen)

- Mechanical and microstructural characterization of additive manufactured AlSi12 lattice structures for Space applications
- Process development of AlSi12 cast lattice structures by replication of polymer template using water-leachable molds
- 3D printing of polymer lattice structures manufactured by FDM
- Hypervelocity impact testing of cellular AlSi12 alloys structures
- Finite Element analysis for correlation with experimental data
- Mentoring student projects (Bachelor and Master)

European Space Agency (ESA) Technical and Research Center, ESTEC, The Netherlands Nov. 2013 - present

Doctoral research (Advisors: Dr. Tommaso Ghidini & Dr. Andrew Norman)

- Tensile and compression test with digital image correlation for strain-mapping during deformation
- 3D-Tomography for topology and defects inspection
- Metallographic preparation of samples (grinding, polishing and etching)
- Microstructure and fracture surface analysis on optical and scanning electron microscopes.

Swiss Space Center, EPFL, Switzerland Nov. 2012 - Nov. 2013

Materials specialist (Advisor: Prof. Volker Gass)

- Support Swiss Space Center members and projects for any materials related activities
- Mechanical characterization of stochastic A357 cellular structures (ESA frame contract)
- Literature review on space components buit by additive manufacturing
- Mentoring student projects (Bachelor and Minor)

Laboratory of Mechanical Metallurgy, EPFL, Switzerland 2011-2012

Masters research project (Advisor: Prof. Andreas Mortensen)

- Anisotropy characterization of monocristalline silicon tested in bending
- Finite Element analysis validated by experiments

Publications

Voillat R, Gallien F, Mortensen A and Gass V. Hypervelocity impact testing on stochastic and structured open porosity cast Al-Si cellular structures for space applications. Manuscript submitted (December 2017) and in revision (*International Journal of Impact Engineering*).

Skills

Laboratory Skills

- Mechanical characterization of material (traction and compression)
- Optical and scanning electron microscopy
- 3D-tomography
- Sample preparation (grinding, polishing and etching)
- Aluminum-silicon alloy investment casting
- Hypervelocity ballistic impact

Software Skills

- CAD: Solidworks
- Numerical computing: MATLAB
- Finite element analysis: ABAQUS
- Presentation and design: MS Office (Word, Excel, Powerpoint), LaTeX

Project Management and Teaching

- Staff of Swiss delegation during international summer school in Space, Beijing, China
- Trained and mentored Masters students working on research projects
- Project management of mechanical test campaign for ESA

Communication Skills

- Oral presentations and scientific writing
- Point of contact for industrial members of the Swiss Space Center

Languages

- French (native speaker)
- English (advanced)
- Italian (advanced)

Organization

Cubaliente student association

2015-present

- Committee member and teacher of student dance organization

Hobbies and passion

Dancing

- Cuban salsa dancer and teacher (10 years)
- Hip hop (3 years)

Sports

- Skiing (8 years of competition)
- Swimming
- Basketball